INSTABILITY AND TURBULENCE IN A STRATIFIED SHEAR LAYER

UNIVERSITY OF SOUTHERN CALIFORNIA

PREPARED FOR
OFFICE OF NAVAL RESEARCH

JUNE 1976

USCAE 134
JUNE 1976

UNIVERSITY OF SOUTHERN CALIFORNIA

SCHOOL OF ENGINEERING

INSTABILITY AND TURBULENCE IN A

STRATIFIED SHEAR LAYER

C. Gary Koop

National Science Foundation
Grant Number ENG73-04057
and
Office of Naval Research
Contract Numbers N00014-67-A-0269-0031
and N00014-76-C-0211

DEPARTMENT OF AEROSPACE ENGINEERING

Engineering

UNCLASSIFIED

SECURITY CLASSIFICATION OF THIS PAGE (When Data Entered)

REPORT DOCUMENTATION PAGE		READ INSTRUCTIONS BEFORE COMPLETING FORM
1. REPORT NUMBER USCAE REPORT 134	2. GOVT ACCESSION NO.	3. RECIPIENT'S CATALOG NUMBER
4. TITLE (and Subtitle) INSTABILITY AND TURBULENCE IN A STRATIFIED SHEAR LAYER		5. TYPE OF REPORT & PERIOD COVERED Technical Report Sept. 3, 1972 - Sept. 1, 1975 6. PERFORMING ORG. REPORT NUMBER
7. AUTHOR(s) C. Gary Koop		8. CONTRACT OR GRANT NUMBER(s) N00014-76-C-0211 N00014-67-A-0269-0031
9. PERFORMING ORGANIZATION NAME AND ADDRESS University of Southern California Department of Aerospace Engineering Los Angeles, California 90007		10. PROGRAM ELEMENT, PROJECT, TASK AREA & WORK UNIT NUMBERS NR 062-493
11. CONTROLLING OFFICE NAME AND ADDRESS Department of the Navy, Code 438 Office of Naval Research Arlington, Virginia 22217		12. REPORT DATE June 1976 13. NUMBER OF PAGES 263 (including cover)
14. MONITORING AGENCY NAME & ADDRESS(if different from Controlling Office) Department of the Navy, Code 603 Office of Naval Research Branch Office 1030 East Green Street Pasadena, California 91106		15. SECURITY CLASS. (of this report) UNCLASSIFIED 15a. DECLASSIFICATION/DOWNGRADING SCHEDULE
16. DISTRIBUTION STATEMENT (of this Report) "Approved for public release; distribution unlimited."		
17. DISTRIBUTION STATEMENT (of the abstract entered in Block 20, if different from Report)		
18. SUPPLEMENTARY NOTES Ph.D. Dissertation		
19. KEY WORDS (Continue on reverse side if necessary and identify by block number) Stratified Shear Layer Buoyant Mixing Layer Stratified Instability Stratified Turbulence		

20. ABSTRACT (Continue on reverse side if necessary and identify by block number)

The results of an experimental investigation of shear instability and turbulent mixing in a stratified fluid are presented. Two parallel streams of water, moving at different velocities and having different densities (salinities) are produced in an open channel. Dye and shadowgraph techniques are used to visualize the flow, and quantitative measurements of velocity and density are made with hot films and conductivity probes.

Two modes of instability are possible, depending upon the initial value

DD FORM 1 JAN 73 1473 EDITION OF 1 NOV 65 IS OBSOLETE

UNCLASSIFIED

SECURITY CLASSIFICATION OF THIS PAGE (When Data Entered)

0.

f the Richardson number. For small Richardson numbers, large scale vorticies re observed initially, as in the unstratified case, but they are eventually estroyed by the stable stratification. Flow field measurements give a maximum hickness of the mixing region which agree with recent theoretical predictions. he amount of permanent vertical solute transport produced by the turbulent vent varies inversely with the initial Richardson number. As the initial ichardson number increases, a transition to interfacial wave-breaking occurs hich has no unstratified counterpart. These waves eventually decay, and the net ffect on the vertical solute transport becomes vanishingly small at sufficiently igh initial Richardson numbers.

USCAE 134
June 1976

INSTABILITY AND TURBULENCE IN A STRATIFIED SHEAR LAYER

C. Gary Koop

National Science Foundation
Grant Number ENG73-04057
and
Office of Naval Research
Contract Numbers N00014-67-A-0269-0031
and N00014-76-C-0211

Department of Aerospace Engineering
University of Southern California
Los Angeles, California

ACKNOWLEDGMENT

It is with great pleasure that I acknowledge the assistance I received from Professor Frederick K. Browand, who as my Ph.D. Advisor, participated in every phase of this work on almost a daily basis. His support and encouragement in this investigation were extremely beneficial to me, particularly in the early stages when I had somewhat less than a clear understanding of what stratified fluid mechanics was all about.

I would also like to express my sincere gratitude to Professor Larry G. Redekopp, whose excellent teaching ability has been instrumental in shaping my understanding of fluid mechanics and mathematical physics.

Finally, I would like to thank Professor Tony Maxworthy, whose playing of the "devil's advocate" forced me to reevaluate my thinking upon several aspects of this work.

This study was supported by NSF Grant ENG73-04057 and ONR Contract N00014-67-A-0269-0031 and N00014-76-C-0211.

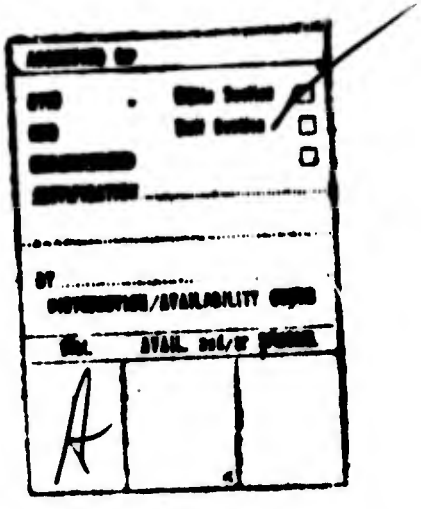

ABSTRACT

The results of an experimental investigation of shear instability and turbulent mixing in a stratified fluid are presented. Two parallel streams of water, moving at different velocities and having different densities (salinities) are produced in an open channel. Dye and shadowgraph techniques are used to visualize the flow and quantitative measurements of velocity and density are made with hot films and conductivity probes.

Two modes of instability are possible, depending upon the initial value of the Richardson number. For small Richardson numbers, large scale vorticies are observed initially, as in the unstratified case, but they are eventually destroyed by the stable stratification. Flow field measurements give a maximum thickness of the mixing region which agree with recent theoretical predictions. The amount of permanent vertical solute transport produced by the turbulent event varies inversely with the initial Richardson number. As the initial Richardson number increases, a transition to interfacial wave-breaking occurs which has no unstratified counterpart. These waves eventually decay, and the net effect on the vertical solute transport becomes vanishingly small at sufficiently high initial Richardson numbers.

TABLE OF CONTENTS

LIST OF TABLES

LIST OF FIGURES

LIST OF SYMBOLS

Symbol	Definition
E_o	$(\Delta U)^4/g(\Delta\rho/\rho_o)$
h_o	Maximum slope thickness of velocity profile at entrance to test section
$h_\rho(x)$	Maximum slope thickness of mean density profile as a function of x
H^*_{max}	Corcos and Sherman (1976) definition of maximum billow amplitude
ΔKE	Change in kinetic energy
ΔPE	Change in potential energy
$M(z)$	Mixedness coefficient defined by eq. 3.4.3.7
M_{max}	Maximum value of M(z)
$P_\rho(\rho, \rho + \delta\rho; z)$	Density probability distribution function, defined by eq. 3.4.3.5
Ra	Rayleigh number = $g \frac{\Delta\rho}{\rho_o} \frac{h^3}{\nu D}$
Re_{h_o}	Reynolds number based on $h_o = (\Delta U h_o)/\nu$
Ri_G	Mean gradient Richardson number $= g \frac{\Delta\rho}{\rho_o \theta_\rho} \frac{1}{(\Delta U/\theta_u)^2}$
Ri_{h_o}	Richardson number based on $h_o = g \frac{\Delta\rho}{\rho_o} \frac{h_o}{(\Delta U)^2}$
Ri_{h_ρ}	Richardson number based on $h_\rho(x)$
Ri_{max}	Maximum value of Ri_{h_ρ}

S_c	Schmidt number, ν/D
T_D	Diffusion time scale subsequent to collapse
T_E	Time scale characterizing entrainment rate in turbulent growth region
T_{mix}	Diffusion time scale prior to the collapse
T_T	Time scale which characterizes the active lifetime of the turbulence after the collapse
$U(z)$	Dimensional mean velocity profile
$\bar{U}(z)$	$= U(z)/\Delta U$
$u_{rms}(z)$	Dimensional rms velocity profile
$\bar{u}_{rms}(z)$	$= U_{rms}(z)/\Delta U$
$\bar{u}^{max}_{rms}$	Maximum value of $\bar{u}_{rms}(z)$
U_T	Top layer velocity
U_B	Bottom layer velocity
U_{ave}	$(U_T + U_B)/2$
ΔU	$(U_B - U_T)$
δ^*	Integral thickness of density profile, defined by eq. 6.4.2
δ^*_F	Value of δ^* at end of test section
δ^*_{max}	Maximum value of δ^*
ϵ	Dissipation rate/unit volume
η	Kolmogorov microscale
η_ρ	Diffusive limit for density fluctuations

θ_o	Momentum thickness at entrance to test section
$\theta_u(x)$	Momentum thickness calculated from mean velocity profile, defined by eq. 3.4.3.3
$\theta_\rho(x)$	Integral thickness of mean density profile, defined by eq. 3.4.3.4
ρ_o	$(\rho_T + \rho_B)/2$
ρ_T	Top layer density
ρ_B	Bottom layer density
$\Delta\rho$	$(\rho_B - \rho_T)$

CHAPTER 1

INTRODUCTION

1.1 Motivation

The study of turbulent mixing in a stratified fluid medium has received a great deal of attention in recent years, particularly within the past decade. Motivation for theoretical investigations and laboratory experiments has been provided by many observations and field measurements of naturally occuring mixing processes within the oceans and atmosphere which show that turbulent mixing occurs under a variety of ambient conditions and over a wide range of length and time scales. Through these investigations, it has become evident that particular attention must be paid to the fine scale features of turbulent mixing and the resulting density structure, if one is interested in making realistic estimates of the vertical transport of important quantities. This is exemplified by the detailed measurements of thermocline structure within the San Diego trough made by Osborne and Cox (1972). Their calculations show that estimates of the entropy production made using an eddy viscosity model in conjunction with the measured mean thermal gradients are an order of magnitude larger than estimates made using a model which incorporates the fine scale structure of the thermocline. In addition to oceanographic applications, these

small scale mixing processes have been shown to be important in meteorology. Fleagle (1969) points out that meteorologists have estimated that perhaps as much as 50% of the total energy losses occuring within the planetary boundary layer are due to such processes. Thus, from a meteorological standpoint, a better understanding of small scale turbulent mixing is essential if more accurate weather predictions are to be made in the future.

Numerous mechanisms for the generation of such naturally occuring turbulence have been proposed. A partial list of these would include such phenomena as resonant interaction and breaking of internal waves, rotor formation due to the presence of lee waves, critical layer absorbtion of internal wave energy in a shear flow, double diffusion processes arising from the difference in diffusivities of salt and heat, formation of turbulent thermals due to surface heating or cooling, mechanical stirring of the ocean's surface by the wind, interleaving of fluid masses due to horizontal gradients of density, and turbulent mixing arising as a result of a dynamic instability. Despite the multitude of various mechanisms cited here as possible means of producing turbulent motions in a natural environment, the list is quite incomplete, and one could include many other means by which such turbulence could be generated and maintained.

Although it is unlikely that any one mechanism is identifiable as being the primary means by which mixing occurs in nature, there is a growing body of evidence suggesting that turbulence which occurs in the atmosphere and ocean is very often the result of a dynamic

instability of the Kelvin-Helmholtz* type. Support for this statement is provided by numerous theoretical, experimental, and field investigations, many of which are discussed in the next section. In light of the importance of such Kelvin-Helmholtz induced turbulence (alternatively called billow turbulence or shortened to K-H induced turbulence), it is essential to understand the dynamics of these processes if one is to successfully deal with such complexities as the dispersion of contaminants within the atmosphere and ocean, the detection and prediction of clear air turbulence (CAT), development of accurate models for weather prediction, analysis of the problems of thermal pollution, or the assessment of the environmental impact of proposed industrial facilities.

Before proceding with a discussion of the present investigation, which is presented in Chapters 2 to 6, a brief survey of the available literature dealing with Kelvin-Helmholtz induced turbulence is given in the remaining portion of this introduction. Section 1.2 presents a review of recent field measurements, section 1.3 deals with theoretical and experimental investigations of the linear K-H instability, and section 1.4 describes work which has been done on nonlinear K-H waves and the turbulence which results from this

---

* Strictly speaking, the classical Kelvin-Helmholtz problem refers specifically to the instability which occurs upon an infinitely thin vorticity interface, or a piecewise continuous shearing region. However, within the literature the Kelvin-Helmholtz instability has become an all inclusive label for almost any type of free shear layer instability, and it is in this context that the term shall be used throughout the remainder of this work.

instability. Finally, section 1.5 outlines the scope of the present investigation, and the goals which are to be attained by this study.

1.2 Review of Recent Field Measurements

It is the intent of this introductory chapter to give a brief survey of recent theoretical and experimental work which has been performed in the interest of understanding some of the mixing processes which occur in stratified fluids as a result of Kelvin-Helmholtz induced turbulence. Before doing so, however, it is beneficial to review some of the pertinent observations and field measurements which have been made in the atmosphere and the ocean, as it is these naturally occurring processes that theoreticians and experimentalists are attempting to simulate in their models. By understanding how mixing proceeds in a natural environment it is felt that one is better able to discern how well such models approximate what occurs in nature. For a more complete discussion of much of the work which has been done in this area, one is referred to the excellent review article by Maxworthy and Browand (1975).

It has become evident within the past 8-10 years, as a result of numerous field observations and high resolution measurements, made in various naturally stratified bodies of water and in the atmosphere above widely scattered geographic locations, that there is almost a universal similarity in the fine scale features of the density structure. Detailed investigations of stratified bodies of water using free-fall devices include measurements made within the world's oceans (Woods (1968), Woods and Wiley (1972), Stommel and Federov

(1967), Osborne and Cox (1972), Osborne and Sidden (1973), Simpson (1972)), lakes (Lazier (1973), Simpson and Woods (1970)), and reservoirs (Browand and Koop (1976)). Such measurements yield continuous vertical profiles of primarily temperature, temperature gradient, and salinity, although there have been a few detailed measurements of velocity structure (Osborne and Sidden (1973), Simpson (1972)). In addition, the horizontal extent of thermocline structure has also been investigated (Woods (1968), Williams and Gibson (1974), Osborne and Cox (1972), Grant, et al. (1962), Naysmyth (1970)).

The atmospheric density structure has been investigated (Browning (1971), Browning and Watkins (1970), Atlas, et al. (1970)) using high power continuous wave high resolution radar in conjunction with traditional meteorological sounding devices.

The common result of all these studies is the appearance of a vertically intermittant density structure consisting of a series of regions having intense density gradient (denoted as "sheets" by Woods (1968)) separated by areas of relatively low gradient ("steps").* Within the ocean, these steps and sheets have characteristic thicknesses of O(1-10 m) and O(1-100 cm) respectively. The horizontal extent of the sheet structures measured by Osborne and Cox (1972) was O(750 m), which is similar to the results obtained

*It is noted that hereafter, the descriptive terms fine scale structure, microstructure, steps and sheets will be used interchangeably to denote the high and low gradient features of the density structure -- this to discriminate between these and the gross features of the medium.

by Stommel and Federov (1967). Within the atmosphere, characteristic sheet thicknesses are 0(200-400 m), but the horizontal extent of such regions is as yet unknown.

Although there appears to be a great deal of similarity between the microstructure observed in the various atmospheric, oceanic, and limnological investigations cited, it would be incorrect to assume that this implies a common mechanism for the generation of such structure. As previously noted, there are many mechanisms whereby mixing may be effected in a stratified fluid, and it is possible that several of these could be responsible for the generation of step-sheet structure. It is believed, however, that one very probable cause of the fine scale density features common to both the atmosphere and ocean is the mixing produced as a result of turbulence induced by the growth of a Kelvin-Helmholtz instability. Documentation to support such a claim is well-provided. Woods (1968), using fluorscene dye for visualization purposes, presents a series of quite spectacular photographs recording the production of a turbulent patch of mixing within the Mediterranean thermocline, which was the result of the nonlinear growth and breaking of a Kelvin-Helmholtz wave. Using measurements of vertical temperature profiles made in conjunction with such flow visualization experiments, Woods and Wiley (1972) estimate that, at any instant in time, between 3 and 10% of the water column may be undergoing such a turbulent event. Woods also performed these experiments near the Bahamas and observed similar results. It is noted that the present

author, using techniques similar to Woods, has photographically recorded what appear to be similar mixing processes in the coastal waters near Santa Catalina Island, although the results are not as easily interpreted as those of Woods and Wiley (1972).

Evidence for the existence of similar mixing events occuring in the atmosphere is provided by the radar echoes of Browning and Watkins (1970) and Atlas, et al. (1970), which show a remarkable similarity to the oceanic observations previously cited.

Briefly, what these aforementioned observations reveal is that initially a linear Kelvin-Helmholtz instability forms in a region where the mean shear is enhanced by some transient phenomenon (such as an internal wave), so that the local value of the Richardson number falls below some critical level. If the duration of this transient shear is sufficiently long, the linear disturbance grows to a finite amplitude. At this point, the fluoroscene dye visualizations of Woods and Wiley (1972), made in the seasonal thermocline, bear a close resemblence to the streakline patterns observed experimentally by Winant and Browand (1974). In later stages of development, small scale irregularities are observed, and subsequently, the once well-organized structure degrades into a patch of turbulence. These turbulent patches or billows have active lifetimes which are limited in duration for primarily two reasons, the first being the time scale associated with the transient shear which augmented the mean shear to trip the instability. However, if this time scale is long, the active lifetime may be determined by how much time is required

for the net rate of extraction of energy from the billows, due to dissipation, entropy generation, or radiation of internal waves, to exceed the rate at which the turbulence extracts energy from the mean flow. Whatever the cause, after some period of time, the large scale turbulent motions begin to subside, the billow is elongated in the horizontal direction due to buoyancy effects or the mean shear, and finally it collapses to form a layer of mixed fluid by merging with adjacent collapsed structures. The small scale residual turbulence decays under the action of viscosity. The density structure within this layer, which presumably depends upon how much molecular mixing has occurred as a result of the turbulence, has not yet been clearly established. Woods and Wiley (1972) suggest that the net effect of the turbulent event is to produce a layer of relatively constant density fluid, thus giving a step-sheet appearance to the density profile through this region. They also speculate that this process could repeat itself with further instabilities occurring on the high-gradient interfacial sheets. They present data showing a region of the thermocline containing a number of closely spaced sheets, and attribute their existance to such multiple sheet formation. It is noted, however, that the aforementioned mechanism for sheet formation has not been supported by laboratory experiments. Further discussion of this point is presented in section 1.4.

1.3 Review of the Linear Kelvin-Helmholtz Instability

The early classical works of Helmholtz (1868), Kelvin (1871), and Rayleigh (1878-1919) dealt with the problem of a linear temporally

growing disturbance upon a discontinuous or piecewise continuous free shear flow. Lamb (1932, paragraph 367) summarizes the history of this problem and presents an analysis showing that for any velocity and density difference, the stratified shear layer of zero thickness is always unstable to small disturbances of some wave number. Rosenhead (1931) extended this analysis to include finite amplitude disturbances on a vortex sheet in a homogeneous fluid, and showed that nonlinearity tends to roll the initially planar vortex sheet into a series of cusped waves.

A relatively recent review article by Drazin and Howard (1966) summarizes much of the work which has been done on linear stability since the 1930's, and in particular they discuss how the stability problem is altered when the velocity and/or the density layers have finite thickness. Perhaps the most significant result presented in the article is the Miles-Howard theorem stating that for a linear disturbance in a Boussinesq fluid, a sufficient condition for stability is that the local Richardson number be everywhere greater than 1/4.

The particular mean profiles of velocity and density presented in the review article of Drazin and Howard are typically of an idealized nature, so that the problem is amenable to exact analytical solutions to linearized equations. Calculations of the stability boundaries for more complicated geometries have been recently made by Hazel (1972) using numerical techniques. One very interesting result of these computations is the dramatic effect that the relative

magnitude of the mean velocity and density length scales has upon the stability problem. Denoting some length scales associated with the mean velocity and density profiles as l_u and l_ρ respectively, Hazel found that if $l_u/l_\rho < 2$, the stability diagram is basically the same as for that case where $l_u/l_\rho = 1$. That is, Hazel's stability diagram for this case consists of a single mode of non-dispersive waves whose amplification rates are a function of their wave length, and the shear layer is stable to disturbances of all wave lengths, provided that the global Richardson number exceeds 1/4. However, if $l_u/l_\rho > 2$, Hazel found that the stability diagram bifurcates into two distinctly different modes. The first mode, hereafter to be called mode I, is entirely composed of nondispersive waves, and is similar to the instability which arises when $l_u/l_\rho < 2$. The second branch of the stability boundary, denoted as mode II, consists of unstable disturbances which are dispersive in nature. In addition, the stability boundary for this mode is open ended, so that regardless of how large the global Richardson number, the shear layer is always unstable for some range of wave numbers. It should be pointed out that prediction of mode II instability for global Richardson numbers greater than 1/4 is not in violation of Miles' sufficiency theorem for stability, since the disparity in length scales insures that the local Richardson number will be less than 1/4 somewhere in the flow field.

This bifurcation in the stability boundary as a consequence of the disparity in the l_u and l_ρ length scales was also

determined in an earlier paper by Holmboe (1962), who presents an interesting physical interpretation to explain this phenomenon. Holmboe analytically solved the stability problem of an infinitely thin density interface imbedded within a region of constant vorticity. Thus, $l_u/l_\rho = \infty$ which, according to Hazel's criterion, yields a bimodal stability boundary. The theory involves considering the stability of two waves propogating upon the upper and lower edges of the vorticity interface, which have an arbitrary phase relationship relative to each other. The results show that for sufficiently long wave lengths, relative to the thickness of the vorticity region, an interaction occurs between the upper and lower disturbances such that the propogation velocity of each wave approaches zero and their relative phase relation becomes fixed. As discussed by Browand and Winant (1973), the mechanism by which these two waves are amplified is due to the pressure perturbation each wave induces upon the other, and this leads to a mutual enhancement of the growth rate of each wave. This process corresponds to the mode I branch of Hazel's calculations. For the dispersive mode II instability, the interfacial waves do not approach a constant phase orientation. The instability evolves because the waves propogate with a wave number dependent phase velocity in such a manner that the disturbances spend the greater portion of a wave period in a phase orientation favorable for growth via the previously described mechanism of mutually interactive pressure fields. Both modes have been observed experimentally by Browand and Wang (1972) and Browand and Winant (1973).

All of the investigations thus far considered have been concerned with the stability of inviscid fluids, and it has been tacitly assumed that for problems of geophysical interest, the effects of viscosity upon the stability and growth rate are negligible. However, attempts to experimentally verify these analyses must, by necessity, deal with flows that are not only affected by viscosity, but normally have Reynolds numbers significantly smaller than the natural phenomena they are modelling. In order to investigate the effects of viscosity, and in particular, determine the minimum Reynolds number for which an experiment can be expected to adequately describe the results of an inviscid theory, Maslowe and Thompson (1971) theoretically considered the stability of an unbounded stratified shear flow with the viscous and heat conduction terms included. The method involves linearizing the full equations of motion to yield a sixth order eigenvalue problem which was solved numerically.

Their results show that the damping effect of viscosity upon small amplitude disturbances in a stratified shear flow is quite small. As a practical limit, their work suggests that, for low Richardson numbers, a Reynolds number greater than about 50* is sufficient to insure negligible viscous stresses. For higher Richardson numbers, however, due to the lower disturbance growth rate, the critical Reynolds number for negligible viscous effects is

*Note that the Reynolds number as defined by Maslowe and Thompson is smaller by a factor of 4 than the present definition. The critical value of 50 incorporates the present definition, which is defined in the list of symbols located in the preface.

larger. It should be noted that Maslowe and Thompson considered the case of a thermally stratified shear layer (Pr = .72) so that the relative values of l_u and l_ρ are approximately equal. To date there has been no theoretical investigation of the effects of viscosity upon a shear layer whose stability diagram has the bimodal structure discussed by Holmboe and Hazel. Clearly, since inviscid theory predicts instability for all wave numbers, there is probably a region in the high wave number portion of stability space where viscosity works to stabilize small disturbances.

Much of the experimental verification of these previously described linear stability theories has been provided by experiments conducted in both wind tunnels and water channels using thermal or saline variations to produce the required density difference. Although most of the work done on linear stability theory is concerned with disturbances which are periodic in space and grow in time, the bulk of experimentation deals with spatially growing disturbances. Thus, it has been necessary to make some appropriate transformation in order to compare the measured spatial growth rates of experiments with the predictions of temporal stability analyses. However, it has been shown by Gaster (1962) that mathematically the two problems are distinctly different, and that in general, such transformations between spatial and temporal growth rates are not valid. Gaster points out, though, that the errors induced by making such a transformation are small, provided the growth rate of the disturbance is not large. Thus, for the purpose

of identifying the neutral stability boundary, this distinction between spatial and temporal stability becomes academic. Hence, with the inclusion of this cautionary note, there follows a discussion which reviews the several experiments that have been performed to investigate the linear Kelvin-Helmholtz instability.

In a carefully designed thermally stratified wind tunnel, which utilized special water jackets on the walls to eliminate thermal boundary layers, Scotti and Corcos (1972) investigated the stability of small amplitude disturbances in a two-layer stratified shear flow. The range of global Richardson numbers examined was between .07 and .7, the Reynolds number varied between 50 and 150, and l_u/l_ρ was slightly less than unity. Using a thin taut wire located in the center of the interface, they generated waves of known frequency and measured the growth (or decay) of these disturbances as they propogated down the channel. An important result of their experiment is verification of the Miles-Howard sufficiency condition for stability. For cases when the Richardson number was sufficiently small, so that the shear layer was unstable, the amplification rates for a number of wave lengths were deduced from measurements of the temperature fluctuations downstream. Using the mean profiles produced in this experiment, Hazel (1972) computed the theoretical growth rates predicted by linear inviscid theory, and the agreement with the measured values was good. This empirical corroboration of the linear inviscid theoretical calculations indicates that the effect of viscous damping upon the disturbances

was minimal, thus indirectly substantiating the work of Maslowe and Thompson.

Although the experiment of Scotti and Corcos agreed well with theoretical predictions, their use of thermal stratification produced a shear layer where $l_u/l_\rho < 1$, thus precluding the possibility of investigating the mode II waves discussed previously. However, Browand and Wang (1972) conducted a similar experiment in a water channel using salt as the stratifying agent so that $l_u/l_\rho \cong 15$. Their experiment also consisted of mechanically exciting small amplitude disturbances at various frequencies and at several values of the Richardson number, and measuring the rate at which these disturbances are amplified. Their results confirm the existance of the mode II interfacial waves, and they showed that such waves grow even when the global Richardson number is as high as .7. However, the growth rates for these disturbances are lower by an order of magnitude than what is predicted by inviscid theory. It is speculated that this is due to viscous damping, since the majority of the mode II stability boundary lies in the high wave number region of stability space.

1.4 Review of Nonlinear K-H Waves and the Resulting Turbulence

In contrast to the considerable volume of both theoretical and experimental work which has been performed upon linear stability problems, there has been relatively little study devoted to the nonlinear aspects of Kelvin-Helmholtz waves, owing to the extreme mathematical difficulties that arise. However, within about the

past five years significant advances have been made in this area, and these are the subject of the following discussion.

Because of the dynamical similarity between nonlinear waves in a stratified and homogeneous shear layer, the study of the stratified problem has been augmented in many ways by research performed on nonlinear waves in the absence of buoyancy. Consequently, before considering the complexities introduced by the inclusion of the density terms, it is useful to review some of the results which have been obtained for the unstratified problem.

In a moderate Reynolds number experiment, Freymuth (1966) used smoke visualization to show how the initially unperturbed streaklines roll up into patterns similar to those calculated by Rosenhead (1932). Michalke (1970) was able to show that these rollers correspond to regions of high vorticity concentration. Recently, Browand and Weidman (1975), using conditional sampling techniques, experimentally measured the vorticity distribution within these structures. They found that in such regions, the local concentrations of vorticity can exceed the mean vorticity across the layer by as much as 70%, thus corroborating Michalke's contention that these are indeed regions of intense vorticity concentration. The interaction of adjacent pairs of these vortical regions was visually detected by Freymuth (1966), who observed that such structures interact by rolling around each other, resulting in the coalescence of the regions into a single larger vortex. This is believed to explain Browand's (1966) observation that subharmonics of the

fundamental mode are generated near the edge of a separated jet. In an analysis of this subharmonic generation, Kelly (1967) showed that there is an exchange of energy between modes, such that the subharmonic grows at the expense of the primary wave. Furthermore, Kelly's theory predicts that the interaction will occur when the amplitude of the primary wave is roughly 10% of the mean shear, and this result is confirmed by Browand (1966). In a recent article, Winant and Browand (1974) showed that, at least at moderate Reynolds numbers, this vortex interaction and subharmonic generation (termed vortex pairing) repeats itself several times, and they contend that this is the primary mechanism by which the shear layer grows.

The motivation for several theoretical papers aimed at providing a detailed description of the nonlinear Kelvin-Helmholtz wave was supplied by Benny and Bergeron (1969), who considered the dynamics of a homogeneous shear layer. Using singular perturbation methods, their results show that the singularity which arises at the critical layer in the linear inviscid theory may be eliminated by the inclusion of either nonlinear or viscous terms within this region, depending upon the disturbance amplitude. Using similar techniques, Kelly and Maslowe (1972) considered the finite amplitude K-H wave in the presence of stratification. Their analysis, which is limited to large Reynolds numbers and small Richardson numbers, yields a structure which is similar to the familiar "cats-eye" pattern discussed by Lamb (1932, paragraph 156), except that the shape is slightly modified by density effects. In a subsequent

paper, Maslowe (1973) extended his previous analysis and eliminated the requirement that the Richardson number be small. An interesting feature of these results is the presence of thin regions of intense velocity and density gradient in the neighborhood of the critical layer located at the edges of the "cats-eye". Maslowe showed that even though the global Richardson number may be quite large, the local Richardson number within this high shear region may be small enough to admit the possibility of secondary instabilities. He presents this result as a possible explanation for the large discrepancy between theoretical predictions and atmospheric observations of the critical value of the Richardson number for which turbulent breakdown occurs.

In another recent study, Patnaik (1973) investigated the temporal growth of the Kelvin-Helmholtz instability in a stratified medium using finite difference techniques to numerically solve the complete Navier-Stokes equations. The results are presented in a series of computer-generated plots which follow the growth of the original infinitesimal disturbance, through the nonlinear growth regime, to the point where the amplitude of the wave equilibrates. In general, the disturbance at its maximum amplitude is very similar to that presented by Kelly and Maslowe (1970), and Patnaik's calculations corroborate their prediction of thin regions of high shear and density gradient in the neighborhood of the critical layer.

In an additional numerical experiment, Patnaik considered the nonlinear interaction between a primary wave and its subharmonic.

His results confirm the analysis of Kelly (1967), the measurements of Browand (1966), and Freymuth's visualizations (1966), and show that the subharmonic grows at the expense of the primary wave.

The major difficulty with using finite-difference schemes for solving the Navier-Stokes equations is that the methods are normally applicable to low Reynolds number problems, or to interaction problems of short duration. Thus, even though Patnaik's results have greatly illucidated many of the details of nonlinear waves, his model is not directly applicable to investigation of the high Reynolds number problems found in nature, or in the interaction problems involving the generation of several subharmonics which have been experimentally observed.

To alleviate some of these shortcomings, Corcos and Sherman (1976) present an analytic model, based in part upon Patnaik's computations, which describes the growth and eventual self-limiting amplitude of nonlinear K-H waves in a high Reynolds number flow. Their analysis considers the periodically spaced regions of vorticity concentration (the cores) which are joined by thin layers (the braids) where vorticity is also concentrated. By examining the scaling in the thin braid region, they show that streamwise variations in vorticity are small relative to changes across the layer. This result is utilized in formulating the governing equations in the braid region. These equations show that the net circulation in the braid region is controlled by the rate at which vorticity is produced by baroclinicity, and the rate at which it is convected out of the braid

into the core region by the core-induced strain field. Finally, noting that the circulation about a single wave length is conserved, Corcos and Sherman show that the wave amplitude equilibrates when the rate of change of braid circulation goes to zero, since at this point the core can no longer entrain fluid and conserve total circulation.

An interesting result of this work is the existence of a preferred wave length for maximum equilibrium amplitude. It is found that, although short wave lengths tend to grow more rapidly than longer wave lengths, they equilibrate at smaller amplitudes. Extremely long wave lengths don't grow at all, and thus there is some particular wave number for which the equilibrium amplitude of the disturbance is maximized.

Corcos and Sherman also investigated the likelihood of secondary instabilities arising in the braid region due to the shear and strain induced by the cores. Because the thickness of the braid region is very dependent upon viscosity, they find that at Reynolds numbers typical of oceanic mixing events, the relatively thick braids are not very suseptible to such secondary motions. However, in the atmosphere, where Reynolds numbers are typically several orders of magnitude larger, they conclude that secondary instabilities must be prevalent.

Experimental studies of nonlinear Kelvin-Helmholtz wave and the resulting turbulence have been confined to primarily three investigations. Delisi and Corcos (1973), using the same apparatus as Scotti and Corcos (1972), externally excited the initial instability

and used periodic sampling techniques to measure detailed structure of the nonlinear wave. Their measurements are consistent with the calculations of Patnaik, and in particular they show the high density gradient regions at the edge of the core. Another interesting feature of their results, as noted by Maxworthy and Browand (1975), is the appearance of small internal waves within the large scale structure having nearly horizontal wave crests and wave lengths a fraction of the maximum layer thickness. Their investigation, however, lacked an adequate method for measuring velocity, and thus valuable information about the vorticity distribution within the core and braid was not measured.

In another mixing layer experiment, Browand and Winant (1973), using the same apparatus as Browand and Wang (1972), investigated the effects of the initial Richardson number upon the growth of the shear layer, and in addition, the structure of the final mixed layer. Their results show that if the initial Richardson number is small (less than about .07), the dynamics are initially similar to those of the homogeneous case, with vortex pairing being the primary mechanism for growth. However, at some downstream location, this pairing process is impaired by buoyancy effects. Beyond this point, the vortex structure collapses to form a layer of mixed fluid with mode II interfacial waves propogating along the sheared region. Browand and Winant also discuss the breaking of these waves, and they show that this leads to additional mixing after the large scale entrainment processes observed upstream have subsided.

The third, and perhaps most comprehensive experimental investigation to date, was performed by Thorpe (1973). Using a unique tilting channel to generate a mean shear with a temporally growing instability, Thorpe made measurements of shear layer growth based upon several flow visualization experiments and a limited amount of velocity and density data. One important result of these measurements is the observation that within the range of initial Richardson numbers investigated ($.04 < Ri_{h_o} < .2$), the final value of the mean gradient Richardson number, defined as $Ri_G = \frac{g\Delta\rho}{\rho} \frac{\ell_u^2}{(\Delta U)^2 \ell_\rho}$, approaches a constant value independent of the initial conditions. This result is significant because it provides information about the permanent modification of the density structure as a result of the turbulence, something which is of great interest in oceanography and meteorology. Garrett and Munk (1972) make use of this result in discussing the likelihood that such shear-induced turbulence is responsible for turbulent mixing observed in the oceanic thermocline.

Thorpe also notes that the shear layer is relatively inefficient at permanently mixing the entrained fluid. He found that between 80-90% of the energy extracted from the mean flow by the turbulence is either dissipated or radiated away in the form of internal waves. The small remaining portion of energy is used to increase the potential energy of the system by mixing the fluid down to molecular scales. However, in contrast to the model proposed by Woods and Wiley (1972), Thorpe observes that the density structure of this molecularly mixed fluid does not have the step-sheet

appearance which has been found in the ocean. Thus, further work is needed before this apparent discrepancy can be resolved.

1.5 Scope of the Present Investigation

It is felt that to date there has not been a single comprehensive experiment performed which provides detailed measurements of both velocity and density structure during all phases of stratified shear layer turbulence including the initial laminar instability, the nonlinear growth regime, the breakdown to turbulence, and the final relaminarization of the layer. Such is the intent of the present investigation in an attempt to provide statistically significant measurements of such turbulent events. It is hoped that our understanding of some of the naturally occurring processes which occur in the atmosphere and ocean will be advanced by this study.

The acquisition and reduction of the data is the subject of the next two chapters. The flow visualization experiments are reported in Chapter 4. The quantitative data is presented in Chapter 5, and a discussion of this data is given in Chapter 6.

CHAPTER 2

EXPERIMENTAL APPARATUS AND TEST CONDITIONS

2.1 Channel and Test Section

Two parallel streams of water having different densities and moving at different velocities are merged at the entrance to the test section. The density of each stream is controlled by varying the concentration of fine-grained kiln-dried salt in aqueous solution, and the density is measured using a Rascher and Betzold hydrometer capable of measuring density differences as small as .0001 gram/cc. A detailed description of the facility may be found in Wang (1971) and Winant (1973), so only a brief summary will be given here.

Both streams are gravity fed from constant head reservoirs located six feet above the channel. The water enters a stilling section designed to remove as much turbulence as possible before entering the test section. The mass flow within a single stream is controlled by two Fischer and Porter flow meters having a range of .5 to 5.5 GPM with an accuracy of roughly 2% of full scale. The test section has a square 10 x 10 cm cross section, is 160 cm long, and has a free surface to allow for the introduction of probes into the flow field at any downstream location. The fluid in each stream leaving the test section is passed through a mechanical

divider which separates the stream into two parts. The mass flow in each of these is again monitored using a Fischer and Porter flow meter and controlled by a diaphram valve. The water is then fed into downstream reservoirs and pumped back into the upstream reservoirs for re-use in the test section. The total volume of fluid within the system is approximately 270 gallons. For velocities typical of the experiment, about 25 minutes are required to pass the entire volume through the test section once. Flow velocities within the channel may be varied from 1 to 15 cm/sec, and the free stream turbulence level at the entrance to the test section is typically .5% of the local mean velocity. For the purpose of flow visualization, dye may be introduced into the boundary layer of the fluid on the upper side of the splitter plate, thus marking the interface between the two streams. The entire apparatus is represented schematically in figure 1, and photographs of the facility are shown in figure 2. The geometry of the flow field near the test section entrance is shown in figure 3.

2.2 Description of Experimental Equipment and Sensors

2.2.1 Air bearing mechanism

Located alongside the channel is a track which supports a carriage that rides on an air bearing. One side of the track is an extruded aluminum angle, while the other side is a 2" by 3/4" bar of stock aluminum with the corners machined to a smooth contour. Teflon tape is applied to the track to reduce irregularities in the surface.

The carriage has two modes of operation, and serves a dual purpose. One use is to tow the carriage at a constant velocity by connecting it to a Minareck variable speed motor via a bead chain. In this manner, a camera (movie or still) may be mounted on the carriage and towed at the mean convection velocity of the fluid in the channel. When the flow is visualized, using dye or shadowgraph, photographs may be taken in a moving reference frame, so that one is able to follow the evolution of a single event as it passes through the test section.

The second manner of operating the air bearing is to raise one end of the track (the downstream end, say), detach the carriage from the bead chain, and simply let gravitational acceleration propel it towards the other end. In this mode, the carriage moves with a minimal amount of vibration, and it is in this manner that the hot-film probes are calibrated (the calibration procedure is described in Chapter 3).

2.2.2 Traversing mechanisms

Two types of probe drives are used in this investigation. The first is a two-degree-of-freedom traversing unit made by Velmex which is driven by two variable speed motors. The vertical location of the probe may be monitored by coupling the vertical drive motor to a ten-turn potentiometer, which yields a voltage proportional to the position of the probe. The vertical traversing speed of this drive can be varied between .0025 cm/sec to 10 cm/sec.

The second device is a homemade one-degree-of-freedom mechanism which simply drops vertically under the action of gravity. The slider, to which probes are attached, is fitted with four Thompson bearings and slides down two 1" stainless steel rods. The slider motion is stopped when it strikes two rubber pads mounted on a retainer plate. The probe drive is triggered using a solenoid switch, and the vertical position of the probe is mointored by coupling the slider to a ten-turn potentiometer via a rack and pinion assembly. This device is primarily used to measure instantaneous profiles of the shear layer density structure, and typical traversing velocities are 80-100 cm/sec as the probe passes through the layer.

2.2.3 Hot-film and conductivity probes

Quantitative measurements of velocity are made using a Thermosystems, Inc., model 1210 NACI .002" cylindrical hot-film. The film is driven using a homemade constant temperature anemometer and bucking amplifier circuit. The probes are typically run at overheats of 6% which yields sufficient velocity sensitivity without causing localized boiling of the water. At such a low overheat, however, the probe is somewhat sensitive to temperature as well as velocity. Thus, as a precaution, the temperature of the working fluid was monitored using a thermometer accurate to .01°C. The water was never observed to changed by more than .25°C during the course of an experiment, and typically it was about .05°C. In addition, to avoid thermal variations between the layers, tap water was never used to make small adjustments to the density, since this

was generally at a different temperature than the water in the channel. If an increase in the density difference was required, salt was added to the heavy layer rather than fresh water being added to the light one.

The homemade conductivity probes used in this experiment are of the type described by Maxworthy and Browand (1975). The particular probe used in this investigation has a tip diameter of .004" which is anodized in a solution of Platinum Chloride to coat the tip with a layer of platinum black, thus increasing its capacitive impedance. The nominal diameter of the tip after anodization is .006". Operation of the conductivity probe relies upon the electrical impedance of a conducting solution to measure the density of a fluid stratified by salt. The probes are run in an AC bridge circuit which is driven by a Hewlett-Packard model 3310A signal generator at 40 khz, and the bridge output is demodulated to yield a voltage which is a nonlinear function of the salt concentration. Although the measured impedance is an integrated function of the fluid resistivity, only fluid near the probe tip contributes significantly to the total resistivity. Thus, for very small tipped electrodes (typically .005" - .01"), good spatial resolution may be achieved, as is described in section 3.3.2.

2.2.4 Tape recorder

After a DC voltage was bucked out, the outputs of the anemometer and conductivity probe demodulator were recorded on a

Hewlett-Packard model 3960b four channel FM tape recorder. For most of the measurements, recording was done at 1-1/2 in/sec, yielding a useful bandwidth of DC to 500 hz. However, when high frequency information was desired, such as in the instantaneous density measurements, recording was done at 15 in/sec, which increased the bandwidth to 5 khz. During analog to digital conversion, the tape was played back at 15 in/sec.

2.2.5 Digital system

The analog outputs of the HP magnetic tape system were digitized and stored on a 9-track 1/2" low density (800 BPI) digital tape for further processing. The digitizing system consists of sixteen Datel SHM-2 sample-and-hold modules, two 8-channel Datel MM-8 analog multiplexer modules, and a Datel ADC-L analog-to digital converter (ADC). The maximum aperture and acquisition times for the sample-and-hold module are 10 ns and 100 ns respectively. The decay rate is 50 $\mu v/\mu sec$. Having an input range of $\pm$ 5 volts and an output of 11 significant bits plus one sign bit, the ADC has a quantization error of 1μv, which is negligible for the types of measurements made in this study. After receiving an external timing impulse from an Interdata 5 minicomputer, the sample-and-hold modules sample all of the channels simultaneously. The analog signals are then multiplexed to be digitized by a successive approximation technique.

The digital tape was then processed on a PDP 10 digital computer using FORTRAN IV programs. The PDP 10 is a time sharing

system which was accessed remotely using a Tektronix model 4010-1 terminal. In addition to creating and running programs, this terminal has the additional feature of being able to display graphical results on the CRT, and hard copies of these plots are generated using a Tektronix model 4610 hard copy unit.

2.2.6 Auxilliary equipment

In addition to the aforementioned apparatus, a variety of electronic equipment was used primarily for the purpose of monitoring data during the course of an experiment. The following is a list of some of this equipment and its basic function.

A Hewlett-Packard model 180A dual beam oscilliscope was used for balancing the AC bridge of the demodulator circuit, and also for visual monitoring of the hot-film and conductivity probe outputs.

Two Hewlett-Packard model 7005B X-Y plotters were used to monitor and make hard copies of raw anemometer and conductivity probe output during the course of an experiment.

A Hewlett-Packard 3400A RMS voltmeter was used to measure the true rms voltage of a fluctuating signal.

A Hewlett-Packard model 34702A digital voltmeter was used to measure various DC levels, especially bucking voltages.

A Hewlett-Packard model 5489A low pass filter was used during digitizing in order to prevent aliasing of the signal.

2.3 Experimental Test Conditions for Measurements of Mean Quantities

2.3.1 Important parameters

A prime objective of this experiment is to conduct a parametric investigation of the flow field over as wide a range of pertinent parameters as is feasible with the existing apparatus. Many practical problems exist which limit the useful range which may be investigated, and careful assessment must be made of these physical limitations in order that optimal use of the facility be realized. Before considering these physical constraints which are inherent to the experimental apparatus, it is useful to consider what parameters are important and over what range they are to be varied. Having obtained this information, one is in a position to determine the experimental running conditions which best suit the apparatus.

Of primary importance in this study is the effect that buoyancy has upon the stability and turbulence of the mixing layer. Thus, one is interested in the relative magnitude of buoyancy and inertial forces, which is measured by the Richardson number. In terms of global quantities, this may be defined as

$$Ri_L = \frac{g\Delta\rho L}{\rho(\Delta U)^2}$$

where L is some characteristic length scale, and the subscript "L" in Ri_L denotes the length scale used to define the Richardson number. The range over which Ri_L is varied should be large enough

to study both modes of the linear instability as discussed by Browand and Wang (1972). Thus, for the purpose of this investigation, it is desired that the Richardson number be varied over the range

$$0 < Ri_{h_o} \leq \text{(roughly) } .20$$

where h_o is the maximum slope thickness of the mean shear at the entrance to the test section (the subscript "o" denotes conditions at the test section entrance). The case $Ri_{h_o} = 0$ is excluded since this corresponds to the unstratified shear layer, and thus is outside the domain of interest of the present experiment.

A second parameter which may be of importance is the Reynolds number defined by

$$Re_{h_o} = \frac{\Delta U h_o}{\nu} .$$

In the oceanic environment, the small scale mixing processes are characterized by Reynolds numbers on the order of $(10^3 - 10^4)$, while in the atmosphere they may be as large as 10^7. This is significantly larger than can be obtained in the present apparatus. Thus, in deciding upon the conditions at which the experiment is to be performed, one must try to maximize the value of the Reynolds number.

A third parameter which is important, particularly in the early states of the mixing, is the velocity ratio $\Delta U/U_{ave}$, where ΔU is the velocity difference across the layer and U_{ave} is the mean convection velocity of the fluid in the channel. From linear temporal stability theory it is known that the initial unstable

wave grows like $\exp(2\pi\Delta U t/\lambda)$, where λ is the wave length of the disturbance, and t is time. If t is interpreted as x/U_{ave}, it can be seen that the velocity ratio enters into the problem because the growth rate of the initial instability is proportional to $\Delta U/U_{ave}$. In addition, it may be shown from dimensional analysis that the growth of the homogeneous turbulent shear layer is also functionally dependent upon the velocity ratio (see Brown and Roshko (1974) for a discussion of this point).

In principle, one could consider a number of other nondimensional quantities such as $\Delta\rho/\rho$ (which would not be a parameter in a Boussinesq fluid), Sc (which is not easily varied), Sc/Pr (which measures the relative diffusion rates of heat and salinity), etc. However, it is clear that an experimental investigation for even as few as three independent parameters represents a formidable task, and generally, is quite unfeasible. In order to limit the parametric investigation to a tractable number of independent variables, it was decided that the main portion of the experiment would be concerned with variations of the Richardson number only, with all other quantities held fixed. This is accomplished by fixing the values of U_T, U_B and h_o, and only varying the density difference across the layer. However, because the Reynolds numbers which may be attained in the present facility are significantly smaller than those of the geophysical processes which are being modelled, a second set of experiments were performed for several values of Re_{h_o} and fixed Ri_{h_o}, to determine the degree to which the experimental results are affected by viscosity.

The next section presents a discussion of how the flow conditions for the Richardson number experiments were determined, and section 2.3.3 presents a similar discussion for the Reynolds number experiments.

2.3.2 Flow conditions for the Richardson number experiments

In attempting to define what the flow conditions should be at the entrance to the test section, the problem arises that there is no convenient, well-defined characteristic length scale present. Thus, in trying to compare experimental data measured at different values of Ri_{h_o} or Re_{h_o}, one is left with the problem of defining h_o. The approach used in this investigation is to define a length scale based upon the velocity profile in the laminar portion of the shear layer at some prescribed location downstream of the splitter plate, as depicted in figure 3. This is a reasonable choice for the length scale, since the wave length of the instability which develops upon the interfacial shear region will scale with this thickness. The horizontal station chosen to make this measurement should be far enough downstream that most of the wake, due to the boundary layer separating off the splitter plate, has been eradicated by viscosity, but not so far downstream that the instability has become manifest. However, measurements made very early in this investigation revealed that the wake of the splitter plate extends well into the test section (10 cm or more), and it is still present when the laminar instability begins to develop. This made the problem of determining h_o quite difficult and somewhat arbitrary.

This nonuniqueness of choice for h_o is depicted in figure 4, where two reasonable definitions are shown. As further evidence of the problem of defining a characteristic length for such a doubly inflectional velocity profile, the momentum thickness defined as

$$\theta_o = \frac{1}{(U_B - U_T)^2} \int_{-\infty}^{\infty} \left[U_B - U(z)\right]\left[U(z) - U_T\right] dz$$

was actually negative for one case measured!

In addition to the ambiguity associated with choosing an appropriate length scale, it is not clear that the instability which develops from this wake-like velocity profile is the same as would develop from a single inflection point profile such as a "tanh z" distribution. Miksad (1972) has investigated the linear unstratified stability problem for profiles whose shape is similar to that shown in figure 4. His results show that, for velocity distributions typical of his experiment, the growth rate of the unstable mode associated with the inflection point "A" in figure 4 is small relative to that corresponding to inflection point "B". However, this result may be sensitive to the shape of the profile being considered, and in particular must depend upon the parameter $(U_T - U_{min})/(U_B - U_T)$, which conceivably could be .1 - .6 in the present experiment. In addition, at high Richardson numbers, where the amount of disturbance amplification is attenuated by the stratification, it is not clear that a wide disparity in the growth rates associated with inflection points "A" and "B" will still exist.

In order to alleviate some of these problems associated with the presence of the splitter plate wake, a fine mesh screen (.0035" wire, 60 mesh/in, 30.5% open area) was placed across the entrance to the test section. The screen acts to create a vertical pressure gradient upstream of the test section entrance which effectively eliminates the boundary layer coming off the splitter plate (this problem is treated analytically by Lau and Baines (1968)). The dramatic effect that the screen has upon the shear layer velocity profile is depicted in figure 5. It can be seen from this figure that a single well-defined definition of the shear layer thickness may be made. However, it is also observed that placing the screen across the test section entrance has significantly reduced the initial length scale. This thinning effect due to the screen has two disadvantages. With the screen in place, the maximum slope thickness of the layer is roughly .1 cm. For typical velocity differences across the layer of 4-10 cm/sec, the initial Reynolds number of the experiment lies between 40 and 100. The results of the linear viscous stability problem investigated by Maslowe and Thompson (1971) indicate that the spatial growth rates of interfacial waves would be somewhat affected by viscosity at such low values of the Reynolds number, particularly at higher values of the Richardson number. Clearly, this is an undesireable situation since the geophysical process being modelled is of sufficiently high Reynolds number to be independent of viscosity.

Another serious problem connected with such a small initial Reynolds number is associated with the spatial growth of the

initially laminar shear layer. By way of example, consider performing the experiment with $Ri_{h_o} = .1$, using $h_o = .1$ cm. At this value of the initial Richardson number, the initial instability is not visually observed until roughly x = 5 cm. Using Locke's (1950) results, the shear layer at this location would have grown by viscous diffusion to a thickness of .35 cm. Thus, at this point, where the instability becomes manifest, the value of the local Richardson number has increased to $Ri_{h_o} \cong .35$ which is 350% larger than the initial value! If a second experiment were performed at a larger value of Ri_{h_o} (but keeping Re_{h_o} fixed), the location of the point where the instability is first visually observed would, presumably, be further downstream, due to the attenuation of the disturbance growth rate by the increased stratification. Consequently, the laminar shear layer would have a longer distance in which to grow, and the local Richardson number where the instability is first observed would be an even larger percentage of the initial value. This would make interpretation of the data obtained from these two experiments extremely difficult.

Thus, even though the placement of a full screen across the test section entrance is an effective means of eliminating the wake of the splitter plate, it was still not considered an acceptable solution to the initial length scale problem. In successive attempts to improve the characteristics of the velocity profile at x = 0, several ideas were tried. These included using contoured screens as described by Lau and Baines (1968), incorporating capillary tube

flow straighteners, and using contoured porous filter beds made from soft and rigidized reticulated foam as described by Clark and Stoeffler (1973). None of the aforenamed provided an acceptable solution to the problem.

The final approach, which was used in all successive experiments, was to place a flat screen across only the upper slower moving layer. The net effect is to remove the thick, and quite pronounced, boundary layer from the upper low Reynolds number layer, while retaining the thinner boundary layer separating off of the bottom of the splitter plate. Thus, the plate wake is significantly thinner and is quickly eradicated by viscosity, while the bottom boundary layer adds thickness to the profile. This process is conceptually depicted in figure 6. Figure 7 shows a comparison of the velocity profiles obtained for the case of having no screen, half screen, and full screen for the conditions U_T = 3.2 cm/sec, U_B = 10.95 cm/sec and x = 1 cm. It is noted that the use of the half screen configuration produces a threefold increase in the initial length scale over the full screen case.

Figure 8 shows conditions for the half screen case at x = 1.5 cm for several values of U_T. It may be seen from this figure that at larger values of U_T, the upper layer screen becomes less effective at removing the boundary layer. In order to minimize this effect, one would try to keep U_T as small as possible and maximize the velocity difference across the layer. However, extremely small values of U_T yield unduly thick boundary layers

along the side wall of the channel in the test section of the upper layer. As a compromise between screen effectiveness and test section boundary layer growth, it was decided to fix U_T at 3.2 cm/sec (i.e., 20% on the flow meter scale) for that portion of the investigation concerned with the parametric investigation of Ri_{h_o}.

From the preceding discussion, the best value for U_T has been established, but the optimum value of U_B is, as yet, undetermined. One would like to make U_B as large as possible in order to maximize ΔU, and thus the initial Reynolds number. However, a practical constraint upon the magnitude of U_B is the fact that at high values of Ri_{h_o}, a large ΔU requires a very large density difference across the layer. If the density difference becomes too big, the character of the flow in the channel changes from supercritical to subcritical operation. In the subcritical mode, disturbances created far downstream in the channel (in the exit valves, for example) can propogate upstream and modify conditions within the test section. In practice, it is found that by careful matching of the entrance-exit mass flux within each stream, density differences of .035 g/cc may be used. For larger values of $\Delta\rho/\rho$, the flow conditions within the channel may not be predetermined, due to the subcriticality of the flow. Hence, using $\Delta\rho/\rho_o = .035$ as a practical upper limit on the density difference, and assuming that $Ri_{h_o} = .20$ is the largest initial Richardson number of interest, a velocity difference of 7.75 cm/sec is required, thus setting the lower layer velocity at 10.95 cm/sec. The initial Reynolds number

is about 300, which should be large enough to avoid the effects of viscous damping upon the linear instability.

The final problem is to determine the smallest value of Ri_{h_o} such that the layer thickness is everywhere significantly smaller than the dimensions of the channel. Using the results of Spencer and Jones (1971) for the unstratified mixing layer, the maximum slope thickness varies linearly with x and is given by

$$h = .08 \frac{(\Delta U)x}{U_{ave}}$$

Stratification can only work to decrease this spatial growth rate, and hence use of this formula places an upper bound upon the thickness of the stratified shear layer. The above expression may also be written as

$$h/h_o = \frac{.08(t/\tau)}{Ri_{h_o}}$$

where τ is the Brunt-Vaisala period and $t = x/U_{ave}$. Measurements reported by Thorpe (1973) indicate that for low initial Richardson numbers, the stratified shear layer grows very much like its homogeneous counterpart until roughly $t/\tau = 8$. Beyond this point, the turbulence production is suppressed by the buoyancy, and the layer gets no thicker. Using this result, and specifying that the maximum acceptable thickness of the shear layer is 4 cm, the lowest value of the initial Richardson number which will "fit" in the test section is $Ri_{h_o} = .05$.

Thus, by requiring that the Reynolds number be maximized, the characteristics of the initial shear layer optimized, the

channel always be in supercritical operation, and the length scales for low values of Ri_{h_o} be small relative to the dimensions of the channel, one arrives at the following test conditions which make optimal use of the experimental facility:

$$.05 \leq Ri_{h_o} \leq .20$$

$$.0075 < \Delta\rho/\rho_o < .035$$

$$Re_{h_o} = 300$$

$$U_T = 3.2 \text{ cm/sec}$$

$$U_B = 10.95 \text{ cm/sec}$$

2.3.3 Flow conditions for the Reynolds number experiments

The second phase of the mean velocity and density measurements is to systematically vary the initial Reynolds number at some fixed value of the Richardson number, so that an assessment of the viscous effect upon the data may be obtained. The value of the Richardson number at which this test is to be performed was chosen to be $Ri_{h_o} = .06$, for which vortex pairing is still the mechanism for growth.

It is desireable to fix the upper layer velocity at 3.2 cm/sec for the same reasons that are stated in the previous section. Hence, the maximum value of the Reynolds number which may be obtained in the channel is achieved by running the bottom layer at its maximum velocity, which yields an initial Reynolds number of about 350.

The minimum value of the Reynolds number is controlled primarily by how small a density difference can be measured (using the Rascher and Betzold hydrometer) and maintained within a reasonable tolerance. In practice, it is found that density differences of less than about .003 - .004 gram/cc are difficult to maintain, and this places the lower bound on the Reynolds number at $Re_{h_o} = 200$.

2.3.4 Variability of the prescribed test conditions

In concluding this section on how the test conditions were prescribed, it is useful to examine how closely these conditions may be maintained.

In section 2.1 it is noted that the Fischer and Porter flow meters have an accuracy of about 2% of full scale, or about .1 GPM. A .1 GPM increase in the flow rate of both meters supplying a single layer would increase the velocity of the fluid in that layer by about .25 cm/sec. Thus, in the worst possible case, where the upper layer velocity is fast by .25 cm/sec and lower layer is slow by that amount, the total error would be about 6% of the nominal velocity difference across the layer. However, such a case is rather unlikely, and it is felt that the velocity difference can be maintained to between 1 - 3%.

It is also of interest to determine how closely the prescribed density difference across the layer can be maintained. The amount of density degradation which occurs during the course of an experiment is primarily dependent upon the duration of the run, how much mixing occurs within a run, and the total amount of fluid

within the system. Without significant modification to the facility, the total volume of fluid can be considered fixed. The duration of a run is determined primarily by the length of time required to insure a good statistical sample. Finally, the amount of mixing which occurs within the test section is a function of the boundary conditions at the entrance to the channel which have already been prescribed. It is concluded, therefore, that there is very little control over how much of the original density difference is lost during the course of an experiment. Fortunately, however, it is found that the buoyancy loss is less than 10% of the initial $\Delta\rho/\rho$ for the most severe case which corresponds to the lowest value of Ri_{h_o}, and this decreases to about 0 - 2% for larger values of the initial Richardson number. Some compensation for this density degradation was accomplished by starting an experiment at too large a density difference (typically 3 - 5%), so that at the conclusion of the experiment, the measured density difference across the layer was too small by roughly the same amount.

CHAPTER 3

CALIBRATION, EXPERIMENTAL PROCEDURE AND DATA PROCESSING

3.1 Introduction

The investigation is divided into three phases. The first part of the experiment consists of a flow visualization study using dye and shadowgraph techniques. These observations, made in both moving and Eulerian coordinate systems, provide a qualitative description of how the flow field evolves, and the results are extremely useful for interpreting many of the measurements which are made in the channel. During the second phase of the experiment, "instantaneous" measurements of the vertical distribution of density are made at several stations. These data are used in conjunction with the results of the flow visualization experiments to provide a more quantitative description of the various stages of the mixing process. The main thrust of the experiment is embodied in the third part of the investigation in which averages are made over long time periods to determine the mean distributions of both the velocity and density fields through the several stages of mixing. By varying the boundary conditions at the test section entrance, it is felt that such mean measurements will supply information about how buoyancy affects the turbulent mixing in a free shear layer.

3.2 Channel Coordinate System

The coordinate system used for measurements is shown in figure 9. The origin is fixed in the middle of the splitter plate, the x-axis points downstream, the z-axis points vertically upwards, and the y-axis lies along the edge of the splitter plate.

3.3 Calibration

3.3.1 Hot-film calibration

A Thermosystems, Inc. model 1210 NACL .002" quartz coated hot-film anemometer was used for velocity measurements during this investigation. The film, operating at an overheat of 6%, was calibrated preceding and following each 15-30 minute data acquisition period during phase III of the experiment. The method of calibration involves the use of the air bearing supported carriage in the free-fall mode (described in Chapter 2), which was chosen because it minimizes anemometer vibration. Attempts to calibrate the hot-film by towing the carriage using the DC motor and bead chain were ruled out due to excessively noisy anemometer output.

The velocity of the carriage during calibration is measured by attaching a .005" wire which is coupled to a ten-turn potentiometer that turns as the carriage moves (see figure 10). By connecting a power supply across the potentiomer, a voltage proportional to the position of the carriage is obtained. This is differentiated in an anlog manner, and the output along with the

anemometer signal is recorded on the FM tape recorder for digital processing. Only data acquired while the carriage is accelerating are used for the calibration, so that there is no risk of the probe running into its own thermal wake.

Parenthetically, it is noted that one distinct advantage to using this free-falling device is that a single run provides a complete calibration over all velocities of interest. Thus, the time consuming practice of towing the probes at several different velocities is avoided. This is particularly useful when hundreds of such calibrations are required, such as in phase III of this experiment.

This calibration procedure is repeated five times preceding and following each period of data acquisition. A least-squares fit of the resulting data to a King's law formulation of the form

$$e^2 = A + BU^n$$

is used to correlate the anemometer output with the velocity of the carriage. Various values of the exponent n have been quoted in the literature, depending upon the flow velocities of interest. A tabulation of these given by Winant (1973) shows that the values of n which have been used lie in the range of $.25 < n < .45$. Winant, using the present facility and a similar hot-film, used a value of $n = .25$. In order to determine a reasonable value of the exponent for the present experiment, a short investigation was conducted to determine the value of n which minimizes the average variance of the data to the least squares fit of the King's law formulation.

The results, which are shown in figure 11, show that the average variance is rather insensitive to the value of n, and that the data is well-fitted for values of n lying in the range .2 to .3. For conveneince, and for consistency with Winant, a value of n = .25 was used for the remainder of this investigation. For this value of the King's law exponent, the average variance of the data is about .15 cm/sec. For velocities typical of the experiment, this error corresponds to about 1-2% of the velocity difference across the layer.

Two typical calibration curves are shown in figures 12 and 13, one being taken prior to an experiment, and the other obtained at the conclusion of the experiment 25 minutes later. The solid lines in this figure are the least-squares fit through the data. At a velocity of 10 cm/sec the amount of drift which has occurred during the interim corresponds to an error in velocity of .3 cm/sec. However, since the values of the King's law constants are known both at the beginning and end of an experiment, a linear interpolation in time may be used for A and B in the data reduction program to compensate for this probe drift.

3.3.2 Conductivity probe calibration

The conductivity probe described in section 2.2.3 is calibrated before an experiment using constant salinity baths. In general, the output voltage of the probe is a nonlinear function of density, but a parabolic least squares fit of the form

$$(e - e_o) = k(\rho - \rho_o)^2 \qquad 3.3.2.1$$

fits the data reasonably well, provided the range of density does not exceed about .03 g/cc. Two such calibrations made within an hour of each other are shown in figure 14.

One of the bothersome aspects of conductivity probe operation is the low frequency drift associated with the contamination and removal of the capacitive platinum black coating on the tip of the sensor. However, successive calibrations similar to the ones shown in figure 14 show that the basic nonlinearity of the probe, which is measured by the parameter k in eq. 3.3.2.1, is not changed in time. Instead, the drift appears to affect only the origin of the calibration curve, or more specifically, the values of e_o and ρ_o. To alleviate this drift problem, a two point in situ calibration is made prior to and following each experiment using the known salinities (measured by hydrometer) of the upper and lower layers to determine the values of e_o and ρ_o. The value of k is determined from the salinity bath calibration. As in the case of the hot-film, the variation of e_o and ρ_o are compensated for by a linear interpolation in time.

Another important facet of conductivity probe operation is the spatial resolution of the sensor. The frequency response of a conductivity probe is limited by the time required to convect fluid across that volume surrounding the probe tip which contributes significantly to the measured impedance. This spatial resolution is measured by traversing the probe through the salinity interface 2 mm downstream of the splitter plate. The results are presented in

figure 15. An interesting feature shown in this figure is the fact that the probe senses the presence of the interface before it physically arrives there, this being due to the finite averaging volume surrounding the probe tip. It is also interesting to note that the probe responds to 80% of the density change in .008", or roughly 1.5 diameters, but that almost 6 diameters are required for the probe to respond to 95% of this density difference.

During one portion of this investigation, which is discussed in Chapter 6, a second, smaller conductivity probe was used to make high resolution measurements. This probe, which was specially constructed for this part of the study, has a tip diameter of roughly .0002 - .0004", and its spatial resolution is better than .002". In subsequent discussions, this sensor is referred to as the microconductivity probe.

3.4 Experimental Procedure

3.4.1 Phase I: flow visualization

The first stage of the investigation is a flow visualization experiment undertaken to provide physical insight into how the stratified mixing layer evolves in space and time. Two techniques are used to visualize the flow field. The first method uses dye injection into the laminar boundary layer on the top side of the splitter plate. If the boundary layer leaving the splitter plate at the entrance to the test section is thinned using a fine mesh screen, this injected dye effectively marks that part of the flow field

containing vorticity. The second method of visualization uses a 500 watt mercury lamp (manufactured by Illumination Industries, Inc.) in conjunction with a 4" diameter f/3.5 columnating lens to produce a shadowgraph image which is projected against an opaque surface. The shadowgraph method yields a description of the density structure by providing a shadow pattern whose light intensity is proportional to the second derivative of the instantaneous distribution of density. Thus, in the resulting photographs it is to be expected that the fine scale features are going to be more pronounced than the large scale structures.

Both methods of flow visualization are used to produce 16 mm movies of the evolution of the shear layer in a moving coordinate system using the towing mechanism described in section 2.2.1. The intent of this stage of the experiment is to provide photographic documentation of the effects of the initial Richardson number and Reynolds number upon the turbulent mixing processes.

3.4.2 Phase II: instantaneous density measurements

Using the conductivity probe mounted on the high speed probe traverse (described in section 2.2.2) measurements of the "instantaneous" density distribution are made at various downstream stations. The conductivity probe passes through the shear layer (typically 1-3 cm thick) in roughly .01 seconds, during which time a fluid parcel is convected about .1 mm downstream. The time scale associated with the large scale motions is roughly $h/\Delta U = .2$ sec, and hence, the measurements reflect very closely the instantaneous structure of

the shear layer. The raw data output is recorded on the FM tape recorded at the highest tape speed of 15 in/sec. At this speed, the recorder has a bandwidth of 0-5 khz. This corresponds to roughly .02 cm spatial resolution which is better than the measured resolution of the probe itself (see section 3.3.2). The measurements of instantaneous density structure are supplemented by having the traverse trip a microswitch during its descent that results in a photograph being taken of the shadowgraph image of the density field.

The intent of this second phase of the experiment is twofold. First of all, it is of interest to investigate the density structure of the large scale vortex motions observed early in the mixing process. This yields valuable information about the entrainment process and how mixing of this fluid proceeds. Secondly, it is important to know how much of this entrained fluid has had its density permanently altered by the turbulent mixing, and whether such mixing produces the step-sheet structure observed in the ocean and atmosphere. This latter question is investigated by examining the instantaneous density profiles obtained far downstream in the channel where the turbulence has subsided. Because the Reynolds number may be important in these molecular mixing processes, these experiments are performed at four different initial Reynolds numbers for a fixed value of the Richardson number. The particular Richardson number and Reynolds numbers chosen for these four cases are presented in table 2, and are discussed in section 3.4.3. The downstream stations chosen for these measurements are $x = 25$ cm,

where large scale vortex motions are observed, x = 60 cm, where the large scale motions have collapsed to form a turbulent layer, and x = 130 cm, where most of the turbulence has subsided and the layer is approaching a laminar state.

3.4.3 Phase III: mean velocity and density measurements

During the final phase of this experiment, mean profiles of velocity and density are measured at 12-15 downstream locations for six initial values of the Richardson number and four different Reynolds numbers. The intent of this phase of the experiment is to study the response of the turbulent mixing to changes in the boundary conditions at the test section entrance. It is desired that these variations be over as wide a range possible, subject to the physical constraints of the facility as discussed in section 2.3. The six initial Richardson numbers and four initial Reynolds numbers chosen for these measurements are identified and tabulated in tables 1 and 2, respectively. In addition, a schematic of the test matrix is shown in table 3. A point of explanation of these tables is in order. As will be subsequently discussed, a convenient measure of length scales in the mixing layer is the momentum thickness, which is more accurately calculated than the maximum slope thickness frequently used in the literature. This is due to the fact that integration of measured data is a more precise operation than is differentiation. Thus, in many of the subsequent measurements, the momentum thickness is used to measure the length scales associated with mean quantities. For consistency, this same length scale

definition is used to define the initial conditions at x = 0. Thus, the initial values of the Richardson number and Reynolds number quoted in tables 1 and 2 are based upon measurements of the momentum thickness, θ_o, in the laminar shear layer downstream of the splitter plate. However, in order that comparisons may be made with theoretical and experimental work reported in the literature, the values of these parameters based upon a maximum slope thickness definition are also presented in tables 1 and 2.*

Also presented in these tables are two nondimensional quantities x/θ_o and t/τ where

$$t/\tau = \frac{x}{\theta_o} \frac{Ri_{h_o} \Delta U}{U_{ave}} \quad .$$

The latter quantity is the same nondimensionalization used by Thorpe (1973), and is included here so that comparison may be made with his data.

The measurements, obtained over an eight-month period, were made by slowly traversing a hot-film and conductivity probe (located side by side and separated by 1 cm) through the mixing layer at a rate between .03 - .1 mm/sec using the Velmex probe drive. The descent rate of the traversing unit was adjusted so that typically 1800 large-scale vortex structures were sampled for determination of the mean velocity and density profile. The anemometer and

*The maximum slope thickness was empirically determined to be about 5 times larger than the momentum thickness.

conductivity probe outputs, and the probes' vertical position were recorded at 1-1/2 in/sec on channels 1-3 of the FM tape recorder, and channel 4 was used for vocal annotations and to record a control signal which located the data on the tape. Following each period of data acquisition (generally lasting between 15-30 minutes), the hot-film calibration and in situ conductivity probe calibration were performed using the procedure described in section 3.3, and these data were also recorded on the tape recorder. Upon completing a traverse and sensor calibration, the densities of the reservoirs were adjusted using salt to compensate for the mixing that occurred during the course of the experiment. After having mixed the reservoirs supplying each layer to a uniform density, the sensors were once again calibrated, and the procedure was repeated at the next downstream station.

The analog data are subsequently converted to digital form using the analog-to-digital converter unit described in section 2.2.5. Digitizing is performed at a rate of 50 samples/sec, which results in about 45,000 samples for a typical traverse. The raw digital data are then converted to velocity and density using the results of the anemometer and conductivity probe calibration.

The mean density (and similarly mean velocity) profiles are computed in the data reduction program by evaluating

$$\rho(z) = \frac{1}{N} \sum_{i=1}^{N} \rho_i \qquad 3.4.3.1$$

where ρ_i represents a density sample.* Similarly, root mean square quantities are obtained from

$$\rho_{rms}(z) = \frac{\sum_{i=1}^{N} \left[(\rho_i - \rho(z))^2\right]^{1/2}}{N} \quad . \qquad 3.4.3.2$$

N is typically about 2000, which corresponds to an averaging interval of about 40 seconds for each value of z. During this time, about 80 large-scale structures pass the probe. This is somewhat smaller than what would be desired for forming a good statistically significant ensemble average, and the resulting data, particularly the root mean square quantities, are somewhat noisy. However, because of the previously discussed constraint upon the maximum allowable running time before excessive degradation of the density difference is encountered, the problem is intrinsic to the facility, and one must accept this small amount of statistical uncertainty as an inherent experimental error.

Another function performed by the data reduction program is the calculation of the momentum thickness θ_u, defined as

$$\theta_u = \frac{1}{(U_B - U_T)^2} \int_{-\infty}^{\infty} \left[U_B - U(z)\right]\left[U(z) - U_T\right] dz \qquad 3.4.3.3$$

where U_B and U_T are the bottom and top layer velocities. This is a convenient measure of the shear layer thickness, and as

*Note: although z is slowly varying over the N samples, this definition assumes that z is fixed at the average value during the interval.

previously noted, it is felt that such a quantity is more representative of the thickness of the layer than is the maximum slope thickness. In a similar fashion, it is useful to define a second parameter θ_ρ, which is an integral measure of the thickness of the mean density profile. This is defined as

$$\theta_\rho = \frac{1}{(\rho_B - \rho_T)^2} \int_{-\infty}^{\infty} \left[\left(\rho_B - \rho(z) \right) \left(\rho(z) - \rho_T \right) \right] dz \qquad 3.4.3.4$$

where ρ_B and ρ_T are the bottom and top layer densities.

One more quantity which yields useful information about the structure of the turbulent shear layer is the probability distribution function P_ρ defined as

$$P_\rho(\rho, \rho + \delta\rho; z) = \frac{1}{N} \sum_{i=1}^{N} \left\{ H(\rho_i - \rho) - H\left[\rho_i - (\rho + \delta\rho) \right] \right\} \qquad 3.4.3.5$$

where H is the Heaveside step function. This probability distribution function defines the amount of time that the density lies within a certain window defined by ρ and $\rho + \delta\rho$. Using an isometric projection graphics routine to plot this function, semi-quantitative information about the character of the individual samples which form the time averaged mean density distribution is obtained.

One final parameter calculated by the data reduction program which proved to be of some interest in this investigation is the quantity $M(z)$* which is defined as

*This definition was suggested by Strom, Konrad and Roshko (1974).

$$M(z) = \frac{2}{(\rho_B - \rho_T)} \frac{1}{N} \sum_{i=1}^{N} \left[H(\rho_{ave} - \rho_i)(\rho_B - \rho_i) + H(\rho_i - \rho_{ave})(\rho_i - \rho_T) \right]$$

$$\rho_{ave} = \frac{\rho_T + \rho_B}{2} \qquad 3.4.3.6$$

An interpretation of this quantity is that on the centerline (where $\rho(z) = \rho_{ave}$) $M(z)$ measures the degree to which the density of entrained fluid has been altered by molecular processes. This is made clear by examination of figure 16, where a function $\rho(t)$ is shown to be bounded at all times between the values ρ_T and ρ_B. The parameter M(z) measures the cross hatched area shown in this figure. Clearly, if $\rho(t)$ has the step function distribution shown in figure 16b, corresponding to totally unmixed fluid, then M(z) = 0. On the other hand, if $\rho(t)$ is fixed at the mean density, meaning that the fluid has been totally mixed, then M(z) = 1. It is noted that at locations other than the shear layer centerline, where $\rho(z) \neq \rho_{ave}$, the upper bound of M(z) is no longer unity.

It is worth noting that the mixedness parameter may also be calculated from the probability distribution function P_ρ via the relation

$$M(z) = \frac{2}{\rho_B - \rho_T} \frac{1}{N} \sum_{i=1}^{N} \left[H(\rho_{ave} - \rho^i)\, P_\rho(\rho^i, \rho^i + \delta\rho;\, z)(\rho_B - \rho^i) + H(\rho^i - \rho_{ave})\, P_\rho(\rho^i, \rho^i + \delta\rho;\, z)(\rho^i - \rho_T) \right] \delta\rho \qquad 3.4.3.7$$

where

$$\rho^i = \rho_T + \left(\frac{i - 1}{N - 1}\right)\left(\rho_B - \rho_T\right)$$

and $\delta\rho$ is the width of the window used in eq. 3.4.3.5.

CHAPTER 4

PHASE I: FLOW VISUALIZATION

4.1 Introduction

Following the procedure described in section 3.4.1, the flow is visualized for photographic documentation using dye injection at the interface or by the shadowgraph. The visualization experiments are conducted in such a fashion as to isolate the effects of Richardson number and Reynolds number.

The qualitative results presented in this chapter suggest that the laminar instability which develops within the first few centimeters of the test section has an important influence upon the growth characteristics of the mixing layer, even in the turbulent regime. This is because the linear theory predicts two modes of instability, and the nonlinear behavior of these modes are distinctly different. As previously noted in Chapter 1, the linear temporal stability problem analogous to this spatially evolving flow has been treated analytically by Holmboe (1962). Because many of the observed features of the shear layer may be interpreted in terms of Holmboe's model, a brief discussion of that work is presented in section 4.2.

Section 4.3 presents the results of the flow visualization study conducted by Winant and Browand (1974) in the present facility

for the case of zero density difference across the layer. This documentation is presented here because it is essential to understand, at least qualitatively, how the unstratified shear layer evolves, so that the effects of stratification may be properly assessed.

The results of the present flow visualization experiment are presented in section 4.4, where it is shown that the addition of a statically stable density difference across the mixing layer dramatically alters the flow field from what Winant and Browand observed for the homogeneous problem.

Finally, in section 4.5, documentation is presented to qualitatively describe how variations in the initial Reynolds number affect the dynamical processes of the mixing layer.

4.2 Review of Holmboe's Stability Model

4.2.1 Unstratified shear layer

Holmboe (1962) first considered the linear temporal stability of two streams moving antiparallel with a region of constant shear in between, as depicted in figure 17a.

Consider two wavy disturbances $z_1(t)$ and $z_2(t)$ propogating along the two vorticity interfaces. If z_1 and z_2 are permitted to have an arbitrary phase relationship with respect to one another (that could vary in time), then they may be represented as

$$z_1(x,t) = A(t)\ \mathrm{Cos}\ [kx - \sigma(t)]$$

$$z_2(x,t) = -A(t)\ \mathrm{Cos}\ [kx + \sigma(t)]$$

where k is the wave number of the disturbances, and $\sigma(t)$ measures their relative phase orientation. Solving Laplace's equation in the irrotational regions, utilizing the circulation theorem, and imposing kinematical constraints upon the system yields

$$\xi_{tt} + \frac{1}{4} n_r^2 \xi = 0 \qquad 4.2.1.1$$

where,

$$n_r^2 = (kh - 1 - e^{-kh})(kh - 1 + e^{-kh}) \qquad 4.2.1.2$$

$$\xi = A(t) \text{ Cox } \sigma(t)$$

It may be seen from these results that for sufficiently small wave numbers, n_r^2 becomes negative, and the disturbances are destabilized. Figure 18 sketches qualitatively how $\sigma(t)$ and $A(t)$ vary for the unstable case. Perhaps the most interesting feature of figure 18 is that as $t \to \infty$, the waves approach a constant phase orientation relative to each other. In this phase-locked configuration, pressure fluctuations from the lower disturbance tend to amplify the upper wave and visa versa, and the mechanism for growth is this mutually interacting pressure field. Batchelor (1970, p. 516) presents a simple argument which shows how such an instability tends to spatially redistribute the originally uniform vorticity concentrations. Browand and Winant (1973) extrapolate these linear results and present a heuristic picture of how the linear instability affects the character of the nonlinear wave. They speculate that the vorticity field

becomes so spatially discretized under the action of the initial instability, that the wave eventually "pinches off" to form a series of discrete vorticies. This process is depicted in figure 19. That these vortex structures have been observed experimentally in their flow visualization experiments lends some amount of credance to this rather simplistic conceptualization.

4.2.2 Stratified shear layer

Holmboe (1962) next examined how the addition of a statically stable density difference imbedded in the center of the vortical region (see figure 17b) affects the dynamics of the stability problem. The dynamical difference between this and the preceding problem is that now the distortion of the interface acts to produce vorticity locally due to baroclinicity, rather than to simply redistribute it.

Following a procedure analogous to the unstratified case, Holmboe solves for the stream function in regions 1, 2 and 3 shown in figure 17b, utilizes the circulation theorem to evaluate aribtrary constants, and looks for solutions for $z_1(t)$ and $z_2(t)$ of the form

$$A(t) = A_o e^{ct}$$

to yield the eigenvalue problem given by

$$c^4 + \frac{1}{4}\left[(kh - 1)^2 - e^{-2kh} + 2kh\, R_i\right] c^2 + \frac{1}{8}\left[(kh - 1) + e^{-kh}\right]^2 = 0 \qquad 4.2.2.1$$

where,

$$R_i = g \frac{\Delta\rho}{\rho} \frac{h}{(\Delta U)^2} \; ; \; c = c_r + i\, c_i$$

Depending upon the relative magnitudes of kh and Ri, Eq. 4.2.2.1 admits three classes of solutions for z_1 and z_2:

a) both waves are neutrally stable.

b) both waves grow exponentially and their relative phase orientation is fixed.

c) both waves grow expontially and their relative phase orientation varies with time.

Cases (b) and (c) are the mode I and mode II waves alluded to previously in Chapter 1. The solution curves for eq. 4.2.2.1 have been calculated by Browand and Wang (1972), and their results are reproduced in figure 20.

Examination of this figure shows that for Ri less than about .07, the mode I branch of the instability predominates. This is the stratified analog to the phase-locked solution obtained for the homogeneous case. The primary affect of buoyancy is to alter the phase orientation of the two waves to a value which is less favorable for growth. However, the mechanism by which the instability grows is the same. Thus, it may be anticipated that the nonlinear character of this mode will again be the generation of a series of discreet vortical regions, as are observed in the unstratified mixing layer.

For Ri > .07, the mode II wave (denoted as the Holmboe mode by Browand and Winant (1973)) predominates. This mode has no counterpart in the homogeneous problem, and it has the peculiarity that wave numbers which are stable in the absence of buoyancy become destablized when a statically stable density difference is present. For this branch of the eigenvalue solution, the two waves move anti-parallel to each other, and their amplitude grows exponentially. However, their rate of change of phase is not constant, but varies in such a manner that the waves spend the greater portion of the wave period in phase orientations favorable for growth via the mechanism of mutually interactive pressure fields. For the remainder of the wave period, the waves rapidly change their phase orientation by 2π, spending only a small amount of time in phase orientations unfavorable for growth, and the process repeats itself.

Browand and Winant (1973) present another heuristic argument to show how this second mode of instability may lead to turbulent mixing by interfacial wave breaking, as opposed to the vortex generation mechanism previously discussed. This is shown in figure 21.

4.3 Review of Visualization Experiments for the Unstratified Shear Layer (from Winant and Browand (1974))

Using the same facility as the present experiment, Winant and Browand (1974) investigated the dynamical behavior of the unstratified shear layer. A description of the flow field in a moving coordinate system was obtained by towing the camera at the

mean convection speed of the two streams, and dye was used as the means of visualizing the fluid. A typical sequence of the photographs thus obtained is shown in figure 22. For this case, U_{ave} = 2.75 cm/sec, $\Delta U/U_{ave}$ = .95. The Reynolds number varies between 30 near the origin to about 1200 some 60 cm downstream. The horizontal lines in the background are 2.5 cm apart, and the vertical lines are separated by .5 cm. The flow is moving towards the right, with the faster moving layer on the bottom.

It is observed from figure 22 that small waves develop on the interface within the first few centimeters of the test section, as a result of the linear instability. After two or three wave lengths, it is seen that the spatial distribution of the dye is such that it becomes concentrated into discreet regions. These regions of intense dye concentration are, presumeably, regions where the vorticity is localized. This is because initially all of the vorticity is confined to the interfacial region dividing the two streams where the dye is injected. This supposed correspondence between dye concentration and vorticity is also supported by the conditional sampling measurements of the vorticity distribution in a plane homogeneous mixing layer by Browand and Weidman (1975).

Beyond about x = 5 cm, all of the vorticity which was initially confined to the interfacial region has been rolled up into discreet elements. Between x = 10-15 cm, it can be seen that adjacent vorticies tend to interact by rolling around each other and coalescing into a single larger vortex with viscous diffusion and/or small scale turbulence tending to "smear out" the identities of the original

vorticies. Winant and Browand (1974), using Stuart's (1967) model for an infinite row of vorticies of finite extent, show that this interaction or pairing of adjacent structures is due to an instability arising from the irregularities in spatial distribution of such structures. This pairing process is observed to continue downstream until the scale size of the vorticies becomes comparable to the dimensions of the channel.

By following the trajectories of adjacent structures, Winant and Browand estimate the growth rate (i.e., the change in vortex diameter divided by the distance traveled) to be about .08. This is in very close agreement with the measurements of Spencer and Jones (1971) for their much higher Reynolds number experiment. Subsequent hot-film measurements made by Winant and Browand confirm this qualitative result, and show that the mean thickness of the layer varies linearly with downstream distance.

4.4 Effects of Stratification Upon the Shear Layer

As has been discussed in section 4.2, when buoyancy effects are important, two modes of instability are possible. The mode I wave occurs for values of the Richardson number less than about .07, and is the stratified counterpart to that instability which arises in the homogeneous problem. The mode II instability, which arises for values of the Richardson number greater than about .07, has no counterpart in the unstratified shear layer. Because many of the essential features of the layer structure are influenced by which mode of instability predominates in the early stages of growth,

the two cases are treated separately in the following discussions.

4.4.1 Initial Richardson number less than .07

Figures 23 and 24 show the evolution of the shear layer for the case where the mode I instability predominates initially. For the case shown, $Ri_{h_o} = .04$, $U_{ave} = 6$ cm/sec, and $\Delta U/U_{ave} = .8$. Figure 23 depicts the case where dye is used as the visualization agent, whereas in figure 24, the shadowgraph technique is used.

At this fairly low value of the Richardson number, the initial development is very similar to the early growth stages of the unstratified mixing layer discussed in the previous section. In figure 23, one may see the small amplitude waves developing in the first few centimeters of the test section, and these grow to finite amplitude within several wave lengths. The character of this non-linear disturbance is interesting, because it is clearly evident that the streak lines are asymetrical with respect to the centerline of the shear layer. Very sharp cusps, similar to breaking surface waves near a beach*, are observed on the bottom part of the disturbance. At later times, these cusps are observed to envelope a larger quantity of fluid from the lower layer and form a large scale vortex structure. It is noteworthy, therefore, that the vortices observed at x = 7.5 - 15 cm are composed primarily of high density fluid, due

*The analogy with breaking surface waves should not be carried too far, since in such cases the asymmetry is due to the large density difference between air and water. The present experiment deals with a Boussinesq fluid, so that the density gradient across the layer may not create a preferred direction.

to this initial asymmetry. If the sign of the mean shear is reversed, so that the top layer has the higher velocity, the cusp forms into the upper layer, indicating that the phenomena is not introduced by some asymmetry associated with the apparatus. This same type of structure for the nonlinear wave is also observed in the pictures of Brown and Roshko (1974), where cusping into the faster moving layer is seen. However, this is not observed in the experiments of Thorpe (1973), where it is found that the nonlinear wave cusps into both layers. Hence, there is a curious distinction between these experiments, and since this may have an important effect upon the dynamics of the mixing, it deserves further comment.

Thorpe's (1973) experimental apparatus produces two streams of fluid moving antiparallel to each other, so that the instability which forms varies in time rather than space. That this experiment, does not yield an asymetrical nonlinear wave is not unexpected, since it may be shown that the equation governing the finite amplitude disturbance possesses skew symmetry, provided that the mean shear possesses such symmetry. Thus, in Thorpe's experiment as well as the numerical calculations of Patnaik (1973), it is observed that there is no preferred direction associated with the finite amplitude disturbance.

The present experiment, however, involves spatially rather than temporally growing disturbances, and unfortunately, this nonlinear stability problem has not been solved theoretically. However, it is known from linear stability theory (see Michalche, 1970) that for a homogeneous shear layer, the eigenfunction

corresponding to a spatially growing disturbance is asymetrical with respect to the centerline, with larger root mean square fluctuations occurring on the high speed side. Thus, it is not unreasonable to expect that the nonlinear outgrowth of this linear instability will also be asymetrical, and this is believed to be the cause of the "one-sidedness"* of the entrainment observed in the early stages of the mixing layer development.

Returning again to figure 23, it is found that starting at about x = 16 cm, the regions of concentrated dye (or vorticity) interact as in the unstratified case, via the mechanism of vortex pairing, to produce a larger length scale and a subharmonic of the fundamental frequency. However, subsequent to this first vortex interaction, the similarity ceases between the stratified mixing layer and its homogeneous counterpart. Beyond about x = 45 cm, the large scale vortex structure is observed to become somewhat disorganized with many small scale irregularities appearing (this is particularly evident in the shadowgraph pictures shown in figure 24). Further downstream, these large scale structures are observed to "collapse" and amalgamate with adjacent structures to form a layer of turbulent fluid. The shadowgraph pictures show that a great deal of fine scale turbulence is generated by this collapse, due to the static instabilities which arise in the entrained fluid.

---

* This descriptive term was first used by Maxworthy and Browand (1975).

As the flow proceeds further downstream, this fluid becomes mixed by molecular diffusion, and the fine scales are observed to become elongated in the horizontal direction due to the mean shear and to buoyancy effects. At x = 120 (the last station observed), the layer is approaching a laminar state. Thus, the net effect of this turbulent event is to produce a laminar shear layer with a characteristic thickness that is significantly larger than the original layer thickness. The ratio of this final thickness to initial thickness is a measure of how effective the turbulence is at entraining and mixing fluid. This efficiency of the turbulence to enhance vertical transport is of some interest to meteorologists and oceanographers, and will be discussed at great length in Chapters 5 and 6.

Figure 25 presents the results of a similar experiment performed at a higher value of the density difference. For the case shown, the original Richardson number is .06, so that the mode I wave still dominates in the laminar shear region. The early growth stages are observed to be quite similar to the previously discussed case, with the nonlinear outgrowth of the laminar instability tending to roll up all of the available vorticity into discreet lumps. However an important distinction which arises between the two experiments is that now there is no interaction between the structures to form subharmonics of the fundamental mode. Thus, the collapse of this large scale structure occurs at a smaller amplitude, and the resulting mixed layer thickness found far downstream is smaller

than that which is observed in figure 24 for the lower Richardson number experiment.

4.4.2 Initial Richardson number greater than .07

Figure 26 presents an example of how the shear layer evolves when the mode II instability predominates in the laminar region. For the case shown, $Ri_{h_o} \tilde{=} .2$, $Re_{h_o} = 300$, and $\Delta U/U_{ave} = 1.1$. It is immediately obvious from figure 26 that the increased stratification has dramatically altered the dynamical processes prevalent in the early mixing stages. The localization and discretization of the vorticity which is initially uniformly distributed is not observed for this case. Presumably, this is due to the dispersiveness of the present system, so that amplification of the initial instability by mutual interaction of stationary interfacial waves is no longer possible. Thus, entrainment by large scale structures and vortex interactions are no longer the mechanisms for growth of the mixing region at high initial Richardson numbers. Instead, it appears that mixing proceeds by breaking at the crests of interfacial waves. This is particularly evident at about x = 15 cm in figure 26, where several jets of fluid are observed to be ejected from the crests of the waves into the lower layer. This ejected fluid is subject to the vertical acceleration due to buoyancy while being accelerated horizontally by the faster moving layer, and this results in the orbital trajectory observed. It is interesting that such breaking occurs almost exclusively into the lower (faster moving) layer. This type of asymmetry is similar to

that which is observed for the lower Richardson number case, and it too may be due to the spatial rather than temporal nature of the initial linear instability, as discussed in section 4.4.1.

A more detailed description of the structure of these interfacial waves is presented in figure 27, where dye is used for visualization. The time spacing between successive pictures in this figure is roughly .15 seconds, and the camera moves a total distance of about 15 cm during the entire sequence. Clearly seen in this figure are the two branches of the mode II instability, corresponding to positive and negative phase speeds in this moving coordinate system, so that one wave appears to be propogating upstream and the other downstream. Of course, in lab coordinates, both waves are being swept downstream. It is observed that certain phase orientations of the two waves result in extremely large wave slopes, such as at t = .15 sec where a wave slope of order unity is encountered. It is believed that such regions of large wave slope provide sites for breaking, although this breaking is better visualized in the shadowgraph pictures of figure 26.

4.5 Effects of the Initial Reynolds Number

Figures 28 to 31 present the results of flow visualization experiments performed at $Ri_{h_o} = .06$, $\Delta U/U_{ave} = 1.1$, and initial Reynolds numbers of $Re_{h_o} = 200$, 250, 300 and 350. At the maximum thickness of the layer, the local Reynolds numbers for these four cases are roughly 800, 1000, 1200 and 1400, respectively. It is noted that these photographs were obtained in a Eulerian coordinate

system, so that one is not looking at the same fluid particles between successive frames.

Figure 28 presents the results of the lowest Reynolds number experiment, where Re_{h_o} = 200. At x = 25 cm, the initial nonlinear roll-up may be observed. (The structures shown here are in the process of pairing.) It is seen, however, that the core of the vortex region is almost completely homogeneous, suggesting that the finite amplitude disturbance simply engulfed a patch of fluid with very little mixing. At x = 45 cm, the large scale structure has collapsed to form a turbulent layer, and at x = 112.5 cm, the layer has become almost completely laminar.

Figure 29 shows the appearance of the flow field for the case of Re_{h_o} = 250. At x = 25 cm, the initial roll-up is similar to the preceding case, but significantly more fine scale structure is observed, particularly within the vortex core. At x = 45 cm, a turbulent layer is again observed, but the fine scales of the turbulence tend to be smaller at this increased Reynolds number. Finally, at x = 126 cm, most of the turbulence has been suppressed.

Figure 30 presents the photographs taken for the experiment performed with Re_{h_o} = 300. At x = 25 cm, the large scale vortex structure is again observed, but there is significantly more fine scale structure than in either of the two preceding examples. It is also observed that such fine scale turbulence is found not only within the core regions, but between the cores as well. The picture at x = 45 cm shows the collapsed state of the layer, where a further decrease in the scale size over the previous cases is

seen. However, at x = 126 cm, there is little difference between the three cases.

Finally, figure 31 presents the results of the highest Reynolds number experiment. At x = 25 cm, it is observed that the fine scale turbulence envelopes the entire large scale structure, so that it is difficult to identify the vortex cores. At x = 45 cm, the collapsed layer is seen to have significantly finer scales than any of the other experiments. However, at x = 126 cm, the picture is quite similar to all three of the preceding cases.

A note of caution is in order at this point. It has already been stated that, owing to its intrinsic nature, the shadowgraph is very sensitive to small scale fluctuations. This effect is compounded by the fact that the shadowgraph image is an integrated average of all the structure across the channel. Consequently, these photographs give a distorted picture of the relative importance of the fine scale turbulence to the large scale structure. This point is dramatically demonstrated in the next chapter, where actual density profiles through these regions are presented.

CHAPTER 5

EXPERIMENTAL RESULTS

5.1 Introduction

Quantitative measurements of the flow field, using a hot-film anemometer and a conductivity probe, are presented herein. A majority of the data were obtained and reduced over an eight-month interval in approximately 125 separate runs. The experimental conditions at which these tests were performed, and the procedure followed, are as described in Chapter 3. Section 5.2 is devoted to the results of phase II of this investigation, where profiles of the vertical distribution of the instantaneous density field are measured at various stages of the mixing process. The main portion of this chapter is embodied in section 5.3, which deals with the measurements of the mean and the root mean square of the velocity and density fields which were obtained in the third phase of operation.

5.2 Phase II: Instantaneous Density Distribution

The measurements of the instantaneous vertical distribution of the density field are presented in figures 32 to 34. The flow conditions at the test section entrance for this data are such that Ri_{h_o} is fixed and Re_{h_o} assumes the three values corresponding to

cases G, C, and I as identified in table 2. The horizontal stations chosen to make these measurements are roughly x = 25, 65, and 125 cm downstream of the splitter plate. It is noted that the density probe used for these measurements is somewhat larger than the one which is described in Chapter 3. This is because that smaller, more delicate sensor, cannot withstand the large accelerations and decelerations imposed by the high speed traversing unit without breaking. The spatial averaging volume of the sensor used in this portion of the investigation is roughly twice that of the probe described in Chapter 3.

Figure 32 shows the measurements made at the three prescribed initial Reynolds numbers for x = 25 cm, which is a region where the large scale vortex structure is prevalent. Also shown in this figure are the shadowgraph images photographically recorded at the instant of the measurement, so that one may observe the type of structure through which the sensor passed. In figure 32a is shown the data for the lowest Reynolds number case. An interesting feature depicted here is the relative homogeneity of the fluid density within the core of the vortex. This is consistent with the flow visualization experiments described previously, where it was seen that the initial nonlinear wave tends to entrain large parcels of fluid with little subsequent turbulent mixing. A somewhat surprising result, however, is shown in figure 32b, which presents the measurements made at the next higher Reynolds number. An examination of the photograph for this case would indicate that the core of the

vortex is fairly turbulent, with a great deal of fine scale mixing present. The measured density profile, on the other hand, shows no such mixing, but rather, that the core is comprised of relatively constant density fluid, not unlike the previous case. This same feature is similarly demonstrated in figure 32c, which shows the measurements made at the highest Reynolds number. Here it is seen that, although some mixing has occurred as a result of the turbulence in the core, the density of the entrained fluid is significantly more uniform than the shadowgraph image would suggest. This apparent discrepancy between the photographs and the actual density measurements is attributable to the increased sensitivity of the shadowgraph to small scale fluctuations. In addition to this, the recorded image reflects the integrated average of all the density structure across the channel, thus yielding a further distortion of the density field through which the probe is passing. Thus, caution is required when interpretting such photographic documentation.

Figure 33 shows the measurements made in the region of the flow field following the collapse of the large scale vortex structure. The essential features of the three cases are roughly the same, in that no coherent large scales are observed, and a great deal of fine scale mixing is apparent in both the measurements and the photographs. The somewhat larger fluctuation levels seen in the data of figure 32b are perhaps due to the fact that the measuring station is about 20 cm closer to the splitter plate than the other two cases shown.

Finally, figure 34 shows the data for the last station at which measurements are made. Again, there does not appear to be a great deal of dissimilarity between the three cases, except that the irregularities in the highest Reynolds number experiment appear to be somewhat smaller than the other two cases shown. This is, perhaps, because at higher Reynolds numbers, the scale sizes are reduced which results in an increase in the amount of molecular diffusion that occurs. The general appearance of the measurements made at this value of the longitudinal coordinate is that of an almost linear dependance of the density in the mixing region upon the vertical coordinate, with fairly smooth transitions to the uniform densities above and below the layer. Similar results are reported by Thorpe (1973) for his experiments which were performed at Reynolds numbers comparable to oceanic mixing processes.

The data shown in figure 34 represent only a small portion of the total number of such measurements made during this phase of the investigation. In examining all of this data it is found that the gross alteration of the density profile to produce step-sheet structure, as measured by Woods and Wiley (1972), is never observed in any of the experiments. This is also consistent with Thorpe's results. It is noted, however, that there are often observed to be small scale irregularities that might be interpreted as microstructure, but these have length scales of roughly 10% of the layer thickness, and their appearance is apparantly intermittant both in time and in vertical location. The degree to which such structure is intermittant

may be investigated by performing an ensemble average of several of these profiles, and examining whether any characteristic features of the fine scales emerge in the mean profile. This was accomplished by measuring thirty instantaneous density profiles at x = 120 cm for case C. Because the mixing region at this station is observed to exhibit a slight sinuous motion, one cannot determine the mean profile by simply averaging all of the data at each value of z and expect any characteristic structure to survive. To overcome this difficulty, a second method is employed whereby the vertical coordinate of each run is shifted (by computer) relative to all the other profiles such that the average variance from the mean profile is minimized. The result of this calculation is shown in figure 34d, where it is seen that all trace of the fine scale features observed in the individual profiles has been eliminated. It is noted that this procedure for forming the ensemble is not unique, and one could pursue other means of averaging the data, such as lining up all of the locations of maximum slope, for example. This has not been done for the present data, but on the basis of figure 34d, one would conclude that the fine scale structure observed in the individual instantaneous profiles are truly intermittant phenomena, and cannot be considered to be a repeatable signature of the mixing event.

Another point to be made is that the physical limitations of the facility preclude the examination of the final state of the system, where no time dependent fluctuations are present. Hence, it is not known whether these fine scale features of the instantaneous

density profiles survive the complete relaminarization process, or whether diffusion acts to smooth out these irregularities.

5.3 Phase III: Measurements of Mean and Root Mean Square Quantities

The contents of this section are divided into two parts. The first is concerned with the hot-film and conductivity probe measurements for those cases where buoyancy effects are studied by varying the value of the Richardson number at the entrance to the test section. In section 5.3.2, a similar discussion is found for those cases where the Reynolds number is varied so that viscous effects may be investigated. The two sections are devoted primarily to simply presenting the results of these measurements, with very little interpretation given as to the physical significance of the data. This is reserved for Chapter 6, where a discussion is presented of how these results lead to an increased understanding of the physical processes important for turbulent mixing in a stratified environment.

5.3.1 Variation of the initial Richardson number

Following the procedure outlined in Chapter 3, measurements of the mean and the root mean square of the velocity and density fields are obtained by slowly traversing a hot-film anemometer and a conductivity probe (separated laterally by 1 cm) across the mixing region. Figures 35 and 36 present typical examples of the raw data which was monitored on two X-Y plotters at the time of the

measurement. The data presented here are from case C which is identified in table 1. The three longitudinal coordinates chosen for presentation are representative of the early mixing region, where a great deal of large scale coherent structure is present, the region following the decimation of this structure due to buoyancy, and the furthest downstream station, which is characterized by (almost) laminar flow. Figure 35 shows the raw anemometer output, while figure 36 presents the signal from the conductivity probe. Examination of this raw data is interesting. From figure 36a it is seen that in the early stages of mixing, at $x/\theta_o = 343$, the density of the fluid at any instant is almost exclusively either that of the upper stream or the lower stream, and is rarely anything in between. The implication of this is that the density of a significant portion of the fluid which has been entrained into the layer by the turbulence has not been altered by diffusive mechanisms. At the second measuring station, $x/\theta_o = 691$, it is seen that the amplitudes of both the velocity and density fluctuations have significantly diminished from those of the previous station. The conductivity probe data show that even though large scale fluctuations still exist, there is a must higher probability that the density will lie at some value intermediate to the top and bottom stream density. Also noted at this station in figure 35b, is a peculiar change in the shape of the anemometer output, such that there appears to be a larger velocity defect than what was observed at the previous station. This is not a spurious result, and it will be shown that

this change in profile shape is a characteristic feature of the later stages of mixing.

The data at the furthest downstream station, presented in figures 35c and 36c, show that much of the turbulence has decayed by this point. Relatively low level density fluctuations are seen in figure 36c, and the data appear to be concentrated about some mean distribution. The anemometer data in figure 35c similarly show small amplitude fluctuations. However, it is also observed that the boundary layer on the bottom of the channel has made the transition to turbulence, as can be seen from examining the lower portion of the anemometer signal. Clearly, this is an undesirable situation, as it is not known how such externally produced turbulence will affect the dynamics of the free shear layer being investigated. Hence, when such situations arise, the data are either discounted entirely, or indication is given that the results may be contaminated by mixing from the bottom boundary layer.*

A quantitative means of displaying the character of the density data just described is provided by examining the probability distribution function $P_\rho(\rho, \rho + \delta\rho; z)$ defined by eq. 3.4.3.5. An isometric projection of this function is plotted in figure 37 for case C at several downstream stations. Inspection of this figure confirms much of what was qualitatively established in the previous discussion. At the first downstream location shown, it may be seen

*The convention to be used in the remainder of this work is that open symbols represent good data, while solid symbols indicate that the validity of the data is in question.

that both above and below the mixing region, there is a probability of unity (i.e., a certainty) that at any instant in time the density of a fluid parcel will be that of the top and bottom stream, respectively. Within the mixing region, however, the probability function is bimodal, such that the fluid which is entrained into the layer has a very small probability of having a density in between that of the top and the bottom stream. It is also significant that there is a greater probability of finding heavy fluid in the top half of the layer than there is of finding light fluid in the bottom half. As discussed in the previous chapter, this is presumably due to the preference of the initial nonlinear wave to entrain fluid from the lower (higher velocity) stream.

As one examines the data at subsequent longitudinal coordinates, it is seen that this original bimodal structure gradually evolves into a single peaked probability function. At the last station shown, for any value of z within the mixing region, the probability appears to be roughly symmetric about the maximum value. Thus, at this station the locus of probability peaks approximately describes the mean density profile. The density fluctuations are fairly closely concentrated about this mean distribution, and within the mixing region there is a relatively small probability of the density being that of either the top or the bottom stream.

Using data similar to those shown in figures 35 and 36, profiles of the mean velocity and density distribution are

calculated by the data reduction program for all of the longitudinal coordinates and test conditions described in table 1. Typical examples of these mean density and velocity profiles are presented in figures 38 and 39, respectively, where the ordinate and abscissa are normalized by

$$\bar{\rho}(\bar{z}) = \frac{2[\rho(z) - \rho_T]}{\rho_B - \rho_T} - 1 \; ; \; \bar{z} = z/\theta_\rho$$

$$\bar{U}(\bar{z}) = \frac{2[U(z) - U_T]}{U_B - U_T} - 1 \; ; \; \bar{z} = z/\theta_U$$

In each case, the profile has been shifted so that the ordinate is zero at $z = 0$. The data shown are from case C. Figure 38 presents the mean density profiles measured at x stations between $x/\theta_o = 115$ to $x/\theta_o = 862$. It may be seen that these normalized profiles possess a similar form, with very little spread in the data. It is noteworthy that such similarity exists, even though the physical appearance of the streak lines in the flowfield have been shown in figures 23 to 25 to differ greatly over this range of x. Thus, the similarity of the mean distributions does not imply that the physical processes which are occurring are of a similar nature.

Figure 39 presents the mean velocity data. These are divided into the two regions $x/\theta_o < 300$ and $x/\theta_o > 300$. From figure 39a it is seen that for $x/\theta_o < 300$, the velocity profiles as well as the density have a similar form with very little spread in the data noted. Also shown in this figure is the classic mean profile measured by Liepmann and Laufer (1947) for a high Reynolds

number homogeneous shear layer. Except at the edges of the mixing region, there is excellent agreement with the present mean velocity data. From figure 39b it is noted that for $x/\theta_o > 300$, the mean velocity profile is described by a distinctly different shape from that just discussed. This suggests that the important physical processes prevalent in the mixing region have a different character, depending upon whether x/θ_o is less than or greater than 300. This change in mean velocity profile shape is also observed in the raw anemometer data of figure 35c, where the increased velocity defect at this station has already been noted.

An observation which should be made at this point is that any length scale based upon the mean velocity profile is, perhaps, not a good measure of the thickness of the mixing region. This is made clear by considering that a parameter such as θ_u (defined by eq. 3.4.3.3) may vary from station to station due to increases in the velocity defect, even though the thickness of the layer* remains unchanged. This isn't to suggest that θ_u is not a useful quantity, since this parameter has an important physical interpretation other than its being a convenient integral length scale. The point is that one should not use θ_u and the concept of thickness interchangeably. It has been shown in figure 38, however, that the mean density distribution does not exhibit this changing

*The term "layer thickness" as used here refers to the vertical extents between which all of the turbulent mixing is confined.

profile shape. Thus, θ_ρ can change only by variations in the physical dimensions of the mixing region, and hence, provides a good quantitative integral measure of the layer thickness.

The distributions of the root mean square of the density and velocity fluctuations for case C are presented in figures 40 and 41, respectively. The coordinates for these figures are normalized as

$$\bar{\rho}_{rms}(\bar{z}) = \frac{\rho_{rms}(z)}{\rho_B - \rho_T} \; ; \; \bar{z} = z/\theta_\rho$$

$$\bar{u}_{rms}(\bar{z}) = \frac{u_{rms}(z)}{U_B - U_T} \; ; \; \bar{z} = z/\theta_u$$

One feature clearly distinguishable from these figures is that, although the mean density and velocity profiles exhibit some degree of similarity, this is certainly not true for the fluctuating quantities. This is not an unexpected result, since the Reynolds numbers at these stations are roughly 800 - 2000, and hence, not extremely large. It is noted that typically in free shear layer turbulence experiments, Reynolds numbers of roughly $Re_h = 60{,}000$ (Fiedler, 1974) are required before the turbulence becomes self-preserving for second order correlations, and even larger Reynolds numbers are needed for self-preservation of the higher order correlations. However, this lack of similarity for the fluctuating quantities is not necessarily attributable to difficulties associated with the experimental apparatus, since it is buoyancy itself, the physical quantity being modelled in this experiment, which limits

the spatial extent over which the turbulence can persist, and hence, how large a value the Reynolds number may achieve. In oceanic mixing events, at the point of collapse of the large-scale structure the Reynolds numbers are typically about 20,000 (Thorpe, 1973), and thus are also well below that which is required for self-preserving turbulence. In the atmosphere, however, where Reynolds numbers are significantly larger (of order 10^7, Thorpe, 1973) such mixing events can be expected to produce fully developed turbulence, and hence, are not well modelled by this experiment.

Using data similar to that shown in figures 38 and 39, calculations of the integral parameters θ_ρ and θ_u, as defined by eqs. 3.4.3.4 and 3.4.3.3, respectively, are made in the data reduction program for all of the cases identified in table 1. The results are presented in figure 42a and 42b. Much of what was qualitatively established in the flow visualization experiments is corroborated and quantified in the θ_ρ data shown in figure 42a.

For the four lowest Richardson number experiments (cases A, C, D, E), the following description of this θ_ρ data is applicable. Initially, the shear layer is characterized by a linear dependence of θ_ρ upon the longitudinal coordinate, independent of Ri_{h_o}. Comparison of these data with the high Reynolds number experiments of Spencer and Jones (1971) for the unstratified mixing layer shows excellent agreement. This is not a totally unexpected result, since the flow visualization studies reveal that the dynamics of the early growth stage of the present experiment are very similar

to those of the homogeneous mixing layer. It is found, however, that the spatial extent of this linear growth region is very dependent upon the initial Richardson number, it being smaller for larger values of Ri_{h_o}. This too is to be expected, since the photographs reveal that buoyancy increases tend to destroy the large scale coherent structures, which are responsible for growth, at positions closer to the entrance to the test section. Once the effects of buoyancy have become manifest, the growth rate of the shear layer diminishes, and θ_ρ achieves a maximum value. Beyond this point, θ_ρ declines from the peak value, with greater decreases observed at the larger Ri_{h_o}, until a final asymptotic state is approached. It is noted that the data shown in solid circles are for those cases where the boundary layer on the bottom of the channel is observed to become turbulent from the raw anemometer data. This externally produced turbulence has the effect of spreading the density fluctuations throughout the bottom stream, thus yielding an apparent increase in θ_ρ. This is clearly evident in the last x station of figure 36, where density variations are observed throughout much of the bottom stream, but appear to be relatively confined to the shear layer region in the upper stream. Thus, it is believed that the increase in θ_ρ beyond about $x/\theta_o = 800$ for cases A, C, and D is a spurious result.

The appearance of the data corresponding to the two highest values of Ri_{h_o} differs somewhat from what has just been described. For these cases, θ_ρ/θ_o initially grows to a value of about .8 at

x/θ_o = 200, and this feature is relatively insensitive to the Richardson number. At subsequent values of x/θ_o, the shear layer thickness appears to either remain constant or increase slightly to a value of about 1 at x/θ_o = 600 to 800, whereupon θ_ρ gradually decreases with increases in the longitudinal coordinate. This continued growth of the shear layer thickness for large portions of the channel length is consistent with the visualization experiments conducted at the high initial Richardson numbers. These show how the mixing appears to proceed by interfacial wave breaking, rather than by large scale vortex formation, and that this type of mixing is observed to persist for distances of 50 to 70 cm (x/θ_o = 700 to 1000), before the mixing subsides.

Figure 42b presents the measurements of the momentum thickness θ_u for the identical cases which are shown in figure 42a. Although many of the same trends are observed for θ_u as are seen for θ_ρ, in general the picture is more complicated, and hence, more difficult to interpret. In the early stages of mixing, the growth rate of θ_u compares well with the Spencer and Jones (1971) data, particularly for the four smallest values of Ri_{h_o}. However, at the point of maximum shear layer thickness, as defined by the θ_ρ data, the momentum thickness continues to increase before a maximum value is achieved. This continued increase in θ_u beyond the point of maximum θ_ρ is attributable to the mean velocity profile shape change noted earlier, but further interpretive discussion for why this change occurs is

deferred to Chapter 6. Beyond the point of maximum θ_u, the momentum thickness appears to decrease, but much of this data is contaminated by the transition to turbulence of the bottom boundary layer. It is interesting to note that the maximum value of θ_u is not nearly as sensitive to Ri_{h_o} as is θ_ρ.

Using data similar to that shown in figures 40 and 41, the maximum value of the root mean square of the density and velocity fluctuations, defined as $\bar{\rho}^{\max}_{rms}$ and $\bar{u}^{\max}_{rms}$, respectively, are determined for all the cases listed in table 1. These are plotted versus x/θ_o in figures 43a and b, respectively. Examination of this figure indicates that any discussion concerning the important features of this data must consider separately the results of the three lowest (cases A, C, and D) and the three highest (cases E, J, and L) Richardson number experiments, since a clear distinction between the two groups of data exists. For the three lowest Ri_{h_o} cases, it is observed that $\bar{\rho}^{\max}_{rms}$ increases to a maximum of about .45 at $x/\theta_o = 300$. Further downstream, the fluctuations are observed to decay monotonically with x/θ_o, until at the last station $\bar{\rho}^{\max}_{rms} \cong .1$. It is noteworthy that all of the data in this Richardson number group tend to follow the same trend. The character of the rms measurements for the high Ri_{h_o} cases is distinctly different. These data show that early in the mixing, $\bar{\rho}^{\max}_{rms}$ still attains a value of about .43 - .45, but that this rms level is maintained to about $x/\theta_o \cong 700$, before a very slight attenuation is noticed. The data for case E, for which Ri_{h_o}

lies in between these two groups, is observed to have rms magnitudes intermediate to the low and the high Richardson number experiments. The significance of the data shown along the dashed line in this figure is discussed in Chapter 6.

Figure 43b presents the peak rms velocity fluctuations. Again, the features of the data depend upon whether one is considering the low or the high Ri_{h_o} cases. For the four lowest Ri_{h_o} experiments, the peak magnitude of $\bar{u}^{\,max}_{rms}$ starts out at about .05 and increases to about .15 at $x/\theta_o \cong 300$. Beyond this point, a monotonic decay with x/θ_o is observed, and at the last measuring station $\bar{u}^{\,max}_{rms}$ equals about .05. For the high Richardson number group, the rate of increase of the peak $\bar{u}^{\,max}_{rms}$ with the longitudinal coordinate is initially smaller than the aforementioned data, but this increase in $\bar{u}^{\,max}_{rms}$ persists much further downstream to about $x/\theta_o \cong 700$, whereupon it too begins to decay monotonically with x.

It has already been remarked in discussing the probability distribution function $P_\rho(\rho, \rho + \delta\rho; z)$, that in the initial growth stages, very little molecular mixing is observed as a result of the turbulent motions. However, at distances far removed from the entrance to the test section, the shear layer appears to be approaching a laminar state with characteristic thickness significantly larger than that with which it started. Clearly, then, at some time during the course of the mixing event, the physical properties of a certain amount of entrained fluid had to be altered by molecular processes. From the oceanographer's and meteorologist's standpoint

this final amount of mixed fluid is the parameter of primary importance, since this reflects upon the ability of the turbulence in a stratified fluid medium to enhance the vertical transport of such important physical quantities as heat, momentum, salinity, dissolved oxygen, contaminants, etc. As a first step in trying to understand how this mixing proceeds, it is of interest to determine where in the mixing process does the greatest amount of molecular diffusion occur. This is important to know, since possible mechanisms which may be proposed to explain this mixing are dependent upon where such mixing occurs. Thus, if a great deal of molecular diffusion occurs in the early turbulent growth region, one would appeal to typical shear induced turbulence theories for ideas and explanations. If the mixing occurs subsequent to the collapse, though, one might do better to model the process as mixing produced by high Rayleigh number free convection turbulence, since in this region buoyancy may be expected to be the dominant factor.

A quantitative means of characterizing how mixing proceeds in the shear layer is provided by considering the mixedness parameter $M(z)$, which is defined by eq. 3.4.3.7. As noted in Chapter 3 and depicted in figure 17, on the shear layer centerline the value of this parameter is bounded between $M = 0$, corresponding to the case where the density at any instant is either ρ_B or ρ_T but never anything in between (totally unmixed), and $M = 1$, where the density is at all times equal to the mean value $(\rho_T + \rho_B)/2$ (totally mixed). The distribution of $M(z)$ is calculated for all the cases listed

in table 1, and the maximum value of this parameter at each x station, M_{max}, is plotted in figure 44. As is the case with the rms measurements, the features of the data depend upon whether one is considering the low or the high Richardson number regions.

For experiments corresponding to the three lowest Richardson numbers, one can see that in the early growth region of the layer M_{max} decreases to a value of about .2 at $x/\theta_o = 200$, and then monotonically increases to a value of about .85 at the end of the channel. It is noted that the anomolous behavior of the data, where M_{max} is observed to decrease for $x/\theta_o < 200$, is not believed to be correct. Further discussion of this point and the data shown along the dashed line in figure 44 is presented in the following chapter.

Considering the variation of M_{max} for the high Richardson number cases J and L, one sees that the characteristics of the mixing process have been considerably altered by the increased stratification. For these experiments, the fluid within the shear region is considerably less mixed than the low Ri_{h_o} data for $x/\theta_o > 200$. It is seen that M_{max} maintains a magnitude of about .2 for almost half the test section length before a slight increase in the mixing is observed. This corresponds to the same region where the rms fluctuations maintain the relatively high level of about .4.

Summarizing the results presented in this section, one observes the following. For the low initial Richardson number

experiments in the early growth region of the layer, the thickness, as measured by θ_ρ, increases linearly with downstream distance, and the growth compares well with that of the unstratified shear layer. During this period the momentum thickness increases, the rms velocity fluctuations increase, the rms density fluctuations increase, and the maximum mixedness M_{max} decreases to a minimum (these last two results are qualified in the next chapter). At some Richardson number dependent longitudinal location, buoyancy forces disrupt the turbulent growth, and beyond this point the large scale vortex structures observed in the visualization studies collapse to form a turbulent layer, the density length scale θ_ρ decreases slightly, the momentum thickness θ_u continues to increase to a maximum value further downstream, the rms fluctuations decrease in magnitude, and the degree of mixing as measured by M_{max} increases. At the furthest end of the channel, neglecting spurious effects introduced by the bottom boundary layer, θ_ρ appears to asymptote to a constant value, the rms fluctuations become very small, and the maximum mixedness approaches 1.

For the high initial Richardson number experiments, the layer thickness initially grows to a value which is fairly independent of Ri_{h_o}, and then increases slightly for roughly half the length of the channel to $x/\theta_o = 700$. During this period, the momentum thickness continually increases to values significantly greater than θ_ρ, the density fluctuations achieve a very large and relatively constant value, the velocity fluctuations slowly increase in

magnitude to a much smaller maximum than that of the density fluctuations, and the mixedness is maintained at a value much smaller than the low Ri_{h_o} data. At about $x/\theta_o = 700$, the layer thickness θ_ρ begins to decrease slightly, as do the rms fluctuations, and the mixedness increases slightly. However, at the end of the channel, the flow is much further from being in an asymptotic state than what is observed at this location for the low Ri_{h_o} experiments.

5.3.2 Variation of the initial Reynolds number

The mean and root mean square data obtained for those cases where the initial Reynolds number is varied is presented in this section. It is noted at the outset, however, that these experiments are not undertaken to provide a complete study of how Reynolds number affects the stratified shear layer. Such a program would not be feasible in the present facility. Rather, the intent of these measurements is to determine whether any of the salient features of the data presented in the previous section would be significantly altered by changes in the relative importance of viscosity.

Before presenting the results of these measurements, it is of interest to briefly discuss some of the practical difficulties which were encountered in performing the experiments, and how these affect the resulting data. For the experiments reported in the previous section, the test conditions at the end of the splitter plate are maintained in the simple manner of keeping the velocity of the upper and lower

layer fixed and controlling the value of the Richardson number using different concentrations of salinity. However, varying the initial value of the Reynolds number proves to be more troublesome. Because the value of the initial length scale in the laminar portion of the shear layer is not easily varied, the value of the Reynolds number is controlled by the velocity difference across the layer. This has two disadvantages. First of all, the initial length scale in the laminar shear region, θ_o, is frequently used for normalization purposes. This thickness is relatively small, typically .7 - .8 mm, and the determination of θ_o could easily be off by 5 - 10%. For the Richardson number experiments, this is not significant, since the same value of θ_o is used for normalization of all the data, and so at most, a level shift of a few percent is encountered. For the Reynolds number experiments, however, θ_o is different for each prescribed value of Re_{h_o}, so that errors in the determination of this initial length scale become important when comparing the results obtained for different values of Re_{h_o}. The second disadvantage of using the velocity difference to control the Reynolds number is that changes in the absolute velocities alter the boundary layer growth along the bottom and sidewall of the channel. Thus, in some cases the boundary layer becomes turbulent three quarters of the way down the test section, while in others it remains laminar but gets very thick. For these reasons, somewhat more data scatter is to be expected for these

experiments than is observed in the previously presented data, particularly in the region near the end of the test section.

The experimental test conditions consist of four different initial Reynolds numbers for a prescribed value of Ri_{h_o} as defined in table 2. It is noted here that due to a faulty calibration of the gain on channel 3 of the tape recorder, the absolute magnitude of the vertical position of the sensors during the traverse across the mixing region are erroneous for the highest Reynolds number case. This error only affects the calculation of θ_u and θ_ρ in case I.

Figure 45 presents the measurements of the length scales θ_ρ and θ_u. From the density length scale data, shown in figure 45a, it is seen that the initial growth rate of the layer is fairly independent of Re_{h_o}, a result not uncommon for free turbulent shear layers. In addition, the maximum value of θ_ρ is not observed to be much affected by the value of the Reynolds number. One does notice, however, that the ratio of the final layer thickness (as measured at the furthest downstream station) to the maximum value of θ_ρ is Reynolds number dependent, with the greatest value of this ratio occurring at the highest Re_{h_o}. It is believed that this is because increased molecular diffusion occurs at the higher Reynolds numbers, but further discussion of this point is deferred to Chapter 6.

The momentum thickness, θ_u, is shown in figure 45b. Here it is observed that the data from the two highest Reynolds number experiments agree fairly well, but the lowest Reynolds number case

shows a slightly decreased growth rate.

The peak values of the root mean square of the density and velocity are shown in figure 46 as a function of x/θ_o. It is seen from the density fluctuation data in figure 46a that the results of the three highest Reynolds number experiments appear to be very similar, with only a slight trend towards lower rms values at increased Re_{h_o}. The data for the lowest Reynolds number, however, show significantly larger rms magnitudes, indicating that much less molecular diffusion has occurred to smear out these density irregularities for this case. The measurements of the peak velocity fluctuations, however, which are shown in figure 46b, exhibit very little difference for all four cases.

The maximum mixedness parameter, M_{max}, is presented in figure 47. Once again, it is seen that the data from the three highest Reynolds number experiments agree fairly well, except for a very slight trend towards increased mixedness at larger Re_{h_o}. The lowest Reynolds number data, however, show a marked decrease in the degree to which entrained fluid is mixed. This is consistent with the density fluctuation data, and shows that less molecular diffusion occurs at low Reynolds numbers.

On the basis of the data presented in this section, it is concluded that the Reynolds number, for which the Richardson number experiments reported in the previous section are performed, is sufficiently high to insure some degree of Reynolds number independence in the early growth stages. Following the collapse

of the large scale, however, the amount of molecular diffusion does appear to be affected by the Reynolds number, but possibly these effects may be accounted for, as is subsequently discussed. This insensitivity to Re_{h_o} in the early growth stages is not an implication that the present data may be quantitatively applied to mixing phenomena in the atmosphere, however. This, perhaps, would be too large an extrapolation in Reynolds number, and could not be justified using the results presented in this section. It is felt, though, that the results of the early stages could be extended to describe mixing processes prevalent in the ocean without fear of being too much in error. Further support for this contention is presented in the next chapter, where some of the present results are compared with the somewhat higher Reynolds number experiments of Thorpe (1973), and good agreement is found.

CHAPTER 6

DISCUSSION OF RESULTS AND CONCLUSIONS

6.1 Introduction

The measurements which have been presented and discussed in the previous chapter exhibit many interesting features which may be useful in understanding some of the important turbulent mixing processes that arise in oceanographic and atmospheric situations. It is only necessary to provide a proper interpretation of these measurements, and such is the topic of the present chapter. In essence, the discussion presented herein deals with some of the gross features of these mixing phenomena, such as how rapidly does the mixing layer grow initially, how long does this growth persist, how large does the layer become before buoyancy destroys the primary turbulent entrainment mechanism, what is left after the mixing has occurred, and how much vertical transport has resulted. From a geophysical standpoint, these are the essential features which must be understood if one is to have the ability to adequately model such mixing processes in nature.

The next section deals with some measurements which were obtained in this investigation that are believed to be anomolous. Sections 6.3 and 6.4 deal with how molecular diffusion affects the shear layer development. This is an important part of the mixing

phenomenon, because these diffusive processes are ultimately responsible for the vertical transport of heat, salinity, and momentum. Section 6.5 deals with a related problem of how energy is dissipated during the mixing, and section 6.6 discusses some of the gross features of the shear layer. The results of this investigation are summarized in section 6.7, and recommendations for future work are given in section 6.8.

6.2 Qualification of Fluctuating Data

If one examines the $\bar{\rho}^{\,max}_{rms}$ data for the four lowest Richardson number experiments shown in figure 43, a somewhat puzzling situation is revealed. It is observed that a peak exists in the distribution of this quantity, such that $\bar{\rho}^{\,max}_{rms}$ increases to a value of about .45 between $0 < x/\theta_o < 200$, after which a monotonic decay with the longitudinal coordinate is found. This appears to be a rather anomolous result, since one would think that very close to the splitter plate, the density probe would simply see the very thin interface "flapping" up and down. Such a situation would produce root mean square density fluctuations close to the maximum possible value of .5.

A second piece of questionable behavior is encountered in figure 44, which presents the distribution of M_{max} versus x/θ_o. Here it is seen that between $0 < x/\theta_o < 200$, the value of M_{max} decreases to a minimum, and then increases monotonically beyond this station. This is even more difficult to rationalize than the rms data, since it is not physically realistic to suggest that the

fluid entrained into the layer becomes less mixed as it moves down the channel.

Clearly, then, something is not correct, and the most plausible explanation is that, due to the finite spatial resolving capability of the conductivity probe, very close to the test section entrance the sensor is simply not fully responding to the very sudden changes in density as the very thin interface moves across the averaging volume of the probe. This spatial resolving capability of the probe then assumes special significance, because one needs to know how much of the flow is being resolved, not only close to the splitter plate, but throughout the entire test section. In particular, one could ask whether the decrease in rms levels downstream of $x/\theta_o = 300$ is due to actual attenuation of the fluctuations, or whether the fluctuation level remains constant but the turbulence is creating scales beyond the resolution of the instrument.

In order to ascertain how well the conductivity probe resolves the flowfield, a brief experiment was conducted using the microconductivity sensor described in Chapter 3. This specially constructed probe has a spatial resolving capability at least an order of magnitude better than the probe used to obtain the previously discussed data. Although such an instrument is inapplicable for use in measurements of long duration, due to poor drift stability, it may be used on a short-term basis to establish how well the larger probe is actually responding to changes in the

density. The procedure followed is to reexamine case C by placing the microconductivity probe at the shear layer centerline and recording five minutes of data at seven values of x/θ_o. This was subsequently digitized at a rate of 1 khz for numerical processing.

Before discussing the results of this experiment, it is of interest to examine samples of the raw density record as a function of time for these seven measurements. These are shown in figure 48 (a to g), where sixteen seconds of each five minute record are presented. Figure 48a shows the data obtained at $x/\theta_o = 200$. The fluid at this station can be seen to be remarkably unmixed, and the root mean square level for this station is calculated to be $\bar{\rho}^{\,max}_{rms} = .4951$. Figure 48b shows the data at $x/\theta_o = 300$, where the average period appears to have increased (probably the result of a pairing), but the fluid is still very much unmixed. Figure 48c shows the appearance of the density field at $x/\theta_o = 400$. Small scale irregularities are seen to be present; but as a whole, there does not appear to be a great deal of turbulent mixing. The data at this particular value of x/θ_o are significant for two reasons. First, from figure 42a it is known that at this value of x/θ_o, the shear layer has achieved its maximum thickness, and beyond this point the layer thickness decreases due to the collapse of the large scale structure. Secondly, the instantaneous vertical distributions of density reported in section 5.2 for the early mixing region are obtained at roughly this station. Thus, the present data corroborate the earlier instantaneous measurements by

showing that at the point of collapse of the large scales, only a small portion of the entrained fluid has experienced the effects of diffusion of salinity.

Figure 48d shows the microconductivity probe data at $x/\theta_o = 500$, where it can be seen that much more fine scale turbulence is present. The measurements at the three remaining stations $x/\theta_o = 600$, 800, and 1000 show that increased amounts of such turbulence is observed as the flow proceeds downstream.

Using the results of this brief experiment, the values of $\bar{\rho}_{rms}^{max}$ and M_{max} are calculated, and these are shown along the dashed lines of figures 43a and 44, respectively. Directing ones attention to figure 43a, it may be seen that the actual magnitudes of the root mean square of the density fluctuations, as measured by the microconductivity probe, for $x/\theta_o < 600$ are somewhat greater than the larger probe would indicate. The maximum difference amounts to a discrepancy in $\Delta\bar{\rho}_{rms}^{max}$ of about .1. However, beyond $x/\theta_o = 600$, there is good agreement between the two probes. Similarly, if one examines the values of M_{max} shown in figure 44, it is seen that the microconductivity probe yields a more plausible description of the flowfield, with no decrease in mixedness observed for increasing longitudinal coordinate. Beyond $x/\theta_o = 600$, there is again seen to be good agreement between the two probes.

From examining both of these figures, it is clear that for $x/\theta_o < 200$, the rms and mixedness data obtained using the larger

density probe are not correct, and should be discounted. For $x/\theta_o > 600$, however, it is felt that this data provides an accurate description of the flow, since an examination of the flow with an increased spatial resolution yields the same result. Between $200 < x/\theta_o < 600$, the data is questionable. Clearly, the flow within this region is not accurately described using the larger probe, since discrepancies as large as $\Delta\bar{\rho}^{\,max}_{rms} = .1$ and $\Delta M_{max} = .2$ are observed. Despite these somewhat erroneous levels, however, the large sensor data do appear to be at least qualitatively correct, in that the decrease in $\bar{\rho}^{\,max}_{rms}$ and the increase in M_{max} beyond $x/\theta_o = 300$ are both observed using this larger sensor. It is felt, though, that such qualitative agreement does not provide a sound basis for proper interpretation of the dynamical processes important in this mixing problem, and any further discussion regarding this low Ri_{h_o}, $\bar{\rho}^{\,max}_{rms}$ and M_{max} data within this region of x/θ_o will allude to the microconductivity measurements only.

6.3 Molecular Diffusion in the Turbulent Growth Region

One point clearly established in the present investigation is that the early turbulent stage of growth, prior to the collapse, is characterized by very little molecular mixing of the entrained fluid. This point is demonstrated in the probability distribution function shown in figure 37a. Here it is seen that a well-defined bimodal structure exists, indicating that the density of fluid entrained into the mixing region has a high probability of being

either ρ_T or ρ_B, but a low probability of being anything in between. This is an indication that the volume of molecularly mixed fluid within the shear region is negligible when compared to the total volume of entrained fluid. These results are corroborated by the microconductivity probe data shown in figures 48 (a to d), where it is observed that the flowfield is dominated by large regions of relatively unmixed fluid. This information is quantified in the mixedness parameter, shown in figure 44, where M_{max} for the microconductivity probe is found to be less than about .2 prior to $x/\theta_o = 400$. Finally, examination of the instantaneous vertical distribution of density within a vortex, as shown in figure 32, substantiates all of the preceding results by showing that the fluid constituting the vortex is relatively unmixed.

It is clear, therefore, that in the present experimental apparatus, molecular diffusion severely lags entrainment during the early turbulent growth stage. It is of interest to determine why this is so, and in addition, to decide whether flows of geophysical interest should exhibit similar behavior. In attempting to answer this question, one could begin by trying to model the diffusive processes occurring in this region so that the volume of mixed fluid could be estimated. Comparing this to the volume of fluid entrained into the layer by the turbulence would demonstrate the conditions under which molecular processes could be considered negligible.

Before proceeding, it is useful to postulate a conceptual model of the appearance of the flowfield within the mixing region. This is shown in the following sketch, where one envisions diffusive processes acting on the contact surfaces dividing fluids of different density. The length scale L is, as yet, not prescribed.

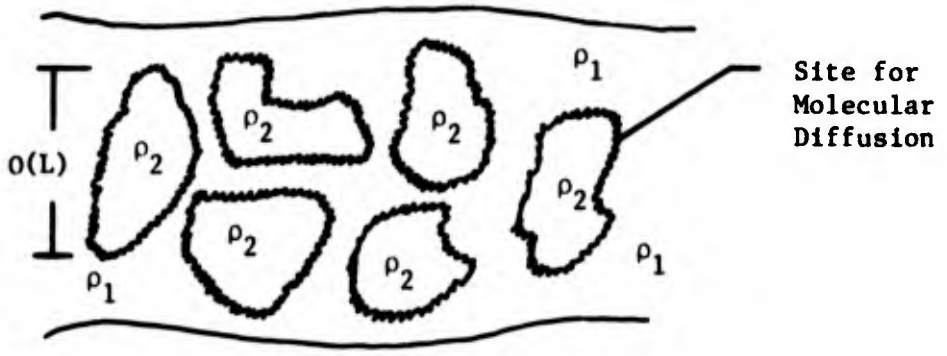

The difficulty which arises at this point is deciding upon some appropriate scaling of the "characteristic eddy" denoted by the length scale L. It is not immediately obvious what scales the quantity L, but one may gain some insight into the question by considering the related problem of turbulence involving diffusion-limited, non-premixed reacting constituents. The analogy to be made is that the region of the fluid over which molecular diffusion occurs, defined by the contact surface dividing materials 1 and 2, is the same as that region where a chemical reaction between the two materials occurs. Thus, by considering the amount of chemical products which are formed in a given length of time, one may infer some information about the scales over which the reactions are occurring (assuming the chemistry is sufficiently rapid).

In this regard, Libby and Williams (1976) present a particularly enlightening spark shadowgraph, taken by Wohl, et al. (1949), which qualitatively reveals the instantaneous structure of such a contact surface. The physical configuration consists of an axisymmetric jet ($Re_D \cong 8600$) exiting into quiescent air. The observed instantaneous flame front, which defines the region of flow where the butane and air are in contact, is described by a cellular structure similar to what is depicted in the previous sketch. The interesting feature of this photograph is that the length scale which characterizes this cellular structure is visually approximated to be about 10 to 20% of the jet diameter. Thus, this qualitative result would suggest that the chemical reaction (and molecular diffusion in the case of a non-reacting flow) is occurring upon turbulent patches with length scales comparable to the integral scale of the jet.

A second, somewhat more quantitative, piece of information related to this problem is given by Bush and Fendell (1974) in their discussion of an earlier experiment performed by Hottel and Hawthorne (1949). The experiment simply consisted of measuring the flame length of a circular turbulent fuel jet exiting into quiescent air. The Reynolds number was varied over a wide range (Bush and Fendell do not specify how large). The results show that the length of the flame region is independent of the Reynolds number. It is well known that a change in the Reynolds number has a significant effect upon the size of the microscale, but that the integral scale (normalized by the jet diameter) is relatively

insensitive to such a change. Thus, to quote Bush and Fendell, "the rate controlling processes occur on the macroscale, rather than the microscale, and many properties of the chemically reacting turbulent shear layer are describable without detailed knowledge of microscale phenomena." This simple experiment tends to support the earlier supposition that chemical reactions occur upon length scales comparable with some integral length.

Based upon this discussion of chemically reacting flows, it will be assumed for the present model that in the early turbulent growth stage, molecular diffusion occurs upon patches of fluid whose characteristic size is determined by the integral scale of the mixing layer. On this basis, one may estimate the amount of time required for molecular diffusion to act across the entire eddy structure as

$$T_{mix} = O\left(\frac{L^2}{D}\right) = O\left(\frac{1}{100}\,\frac{h^2}{D}\right)$$

where,

D = diffusion coefficient

L = integral length scale

$\tilde{=}$ h/10

If this time scale is short relative to a time scale characteristic of the entrainment processes, then one would anticipate the fluid contained in the layer to be well-mixed on a molecular scale. If the opposite is true, however, then it would be expected that the

shear region should be largely heterogeneous.

A time scale which measures the entrainment processes is given by

$$T_E = h/\Delta U$$

so that

$$\frac{T_{mix}}{T_E} = O\left(\frac{R_e S_c}{100}\right)$$

For the present experiment, this ratio is typically $10^3 - 10^4$, which indicates that the order of magnitude analysis is consistent with the experimental results discussed at the beginning of this section. It is also of interest to note that for the experiment performed by Brown and Roshko (1975),

$$\frac{T_{mix}}{T_E} = O\left[\frac{(250,000)(1)}{100}\right]$$

$$= O(10^3) \qquad (S_c \cong 1 \text{ assumed})$$

Thus, the fact that their experiment is characterized by a great deal of unmixed fluid is not inconsistent with the present scaling analysis.

Finally, if one extrapolates these crude arguments to flows of geophysical interest, one concludes that, for natural mixing processes similar to the type studied in the present investigation fluid entrained into the mixing region in the early turbulent growth stage will be relatively unaffected by diffusive processes. This conclusion will have important consequences in the discussion of

the mechanisms by which permanent vertical transport is effected. This is presented in the following section.

6.4 Molecular Diffusion in the Region Following the Large Scale Collapse

From the discussion of the previous section, one concludes that at the point of collapse, most of the entrained fluid is relatively unmixed in a molecular sense. One may wonder, therefore, at what point do diffusive processes play an important role in bringing about the permanent increase in the shear layer thickness observed at the end of the test section. Some insight into this question may be gained by considering the microconductivity probe data shown in figures 43a and 44.

In figure 43a it is seen that prior to the point of maximum shear layer thickness, at $x/\theta_o = 400$ for case C (as determined from the distribution of θ_ρ) the peak rms density fluctuations are very large, typically about .45 and greater. However, just after the collapse of the large scale coherent structure, between $400 < x/\theta_o < 600$, a dramatic 30% decrease in the rms level is observed, such that $\overline{\rho}^{\,max}_{rms}$ changes from .45 to about .3. Secondly, from figure 47 it is seen that between $0 < x/\theta_o < 400$ the value of M_{max} is very small, typically less than .1, but increases to $M_{max} = .46$ between $400 < x/\theta_o < 600$.

These observations are very important because they are the first indications since the start of the mixing event at $x/\theta_o = 0$ that the physical properties of the fluid entrained into the layer

have been altered by diffusion. It is significant that this occurs subsequent to the demise of the vortex structure. The implication is that the shear induced turbulence generated in the early growth stages is responsible for the entrainment of fluid from the upper and lower streams, but not for the mixing of this fluid down to molecular scales. This, apparently, occurs in the turbulent layer just downstream of the point of collapse, where, from figure 48, it is seen that a great deal of small-scale fluctuations exist. Because there is no obvious mechanism by which energy may be directly transferred from the mean shear into these small scales in the absense of the large-scale motions, it is not unreasonable to assume that the energy source for this turbulence lies in the high Rayleigh number free convective motions arising from the static instabilities created during the collapsing process. For the present experiment, the billow Rayleigh number defined as

$$R_a = g \frac{\Delta\rho}{\rho} \frac{h^3}{\nu D} = Ri_h Re_h^2 S_c$$

is about 2×10^8 at the point of collapse. This is to be compared with typical values in the ocean and atmosphere of (Thorpe, 1972) 1.6×10^7 and 2.8×10^{19}, respectively. Rossby (1969) has suggested that the critical Rayleigh number for which free convection turbulence may be expected is given by

$$Ra_{crit} = 14{,}000\ S_c^{.6}$$

which is about 6×10^5 for Sc = 600. Based upon these results, it is

concluded that once the large scale breaks down due to the buoyancy, turbulence induced by free convection is going to be important. Thus, fluid which was entrained upstream by the large scale processes apparently becomes molecularly mixed by free convection turbulence during the time when the shear layer is relaxing to its final state.

During this relaxation period, it is of interest to estimate how much molecular diffusion occurs. One may conceive of two cases which characterize the limiting extremes of this mixing process:

a) So little molecular diffusion occurs during the active lifetime of the turbulence that essentially all of the entrained fluid seeks its own level of neutral buoyancy within the stream from which it originated. For this case, little or no permanent vertical transport of salinity results from the mixing event. An example of such a situation would be a shear layer comprised of two immiscible fluids, where momentum but not specie is permanently transported.

b) So much molecular diffusion occurs during the relaxation process that all of the fluid which was entrained upstream seeks its neutral buoyancy level within the confines of the mixing region. For this case, the thickness of the layer following the demise of the large scale structure would not decrease, since the total volume of fluid within the mixing region remains fixed.

In order to decide how closely a given mixing layer resembles either of these two extremes, one could carry out a scaling analysis similar to that of the preceding section. Before proceeding, however, two questions must be resolved, viz, what limits the active lifetime of the turbulence after the collapse, and what is the "characteristic eddy" size upon which diffusion is occurring. The first question may be resolved by reasoning that since the turbulence has been presumed to be driven by high Rayleigh number convective instabilities, the active lifetime should be limited by the time required for the statically unstable fluid to settle out and seek its own level of neutral buoyancy. This turbulence time scale, which limits the amount of time for which significant molecular diffusion occurs, may be estimated as

$$T_T = \sqrt{\frac{h}{g\frac{\Delta\rho}{\rho}}}$$

The question regarding a characteristic length scale within this collapsed layer is not easily resolved, and only a tentative formulation is presented here. Browand (private communication) has used the results of Holmboe's (1962) linear stability analysis to calculate the stability diagram for a shear flow with a statically unstable density difference. The results show that all wave numbers are amplified, and that the amplification rate increases monotonically as the wave number increases. Clearly, this result is not correct at extremely large wave numbers, and such anomolous behavior is believed to be due to the neglect of diffusion in the model. However,

these calculations do suggest that such a convective instability is likely to produce extremely small length scales that are highly amplified. On this basis, it may not be unreasonable to presume that the turbulent motions prevalent in the shear layer following the destruction of the large scales are characterized by a great deal of fine scale eddys. The high wave number limit of this structure would then scale with the diffusive limit η_ρ, where η_ρ is analogous to the Kolmogorov microscale η.

Assuming the above discussion to be correct, one may proceed in an analysis similar to that of section 6.2. Thus, one could ask whether the amount of time required for diffusion to occur across a structure of scale η_ρ is long or short relative to the active lifetime of the turbulence T_T. This relative measure of the diffusion time will ascertain which of the two limiting extremes of mixing cited earlier will more closely characterize the amount of vertical transport resulting from a mixing event.

One may estimate the diffusion time, T_D, as follows. The amount of time required for diffusion to act across an entire eddy of length scale η_ρ is given by

$$T_D = O(\eta_\rho^2/D)$$

The diffusion length scale η_ρ may be related to the Kolmogorov microscale as (Tennekes and Lumley, 1972)

$$\eta_\rho = \frac{1}{\sqrt{S_c}}\,\eta$$

where η is defined as

$$\eta = \left(\frac{\nu^3}{\varepsilon}\right)^{1/4}$$

and ε is the dissipation rate. As is typical in such scaling arguments, one is left with the problem of estimating the order of the dissipation rate. One reasonable choice for this quantity is given by

$$\varepsilon = 0\left(\frac{u'^3}{L}\right)$$

where u' scales the velocity fluctuations and L is the integral length scale. For the present experiment, these quantities are typically

$$u' \cong \Delta U/10$$

$$L \cong h/10$$

Combining all of the above expressions, one arrives at a relative measure of the diffusion time, T_D, given by

$$\frac{T_D}{T_T} = 0\left[10 \frac{R_{i_h}}{R_{e_h}}\right] \qquad 6.4.1$$

For small values of this ratio, the diffusion time is short compared with the lifetime of the turbulence following the collapse. For these cases, the final layer thickness near the end of the test section should be comparable to the thickness at collapse. For $T_D/T_T >> 1$, however, the reverse is true and one would expect the final amount of mixing to be relatively small.

To test these notions in a quantitative manner using the data obtained in this investigation, it is instructive to examine the quantity δ^* which is defined as*

$$\delta^* = \frac{1}{\rho_B - \rho_T}\left[\int_{-\infty}^{0} \left(\rho_B - \bar{\rho}(z)\right)dz + \int_{0}^{\infty} \left(\bar{\rho}(z) - \rho_T\right)dz \right] \qquad 6.4.2$$

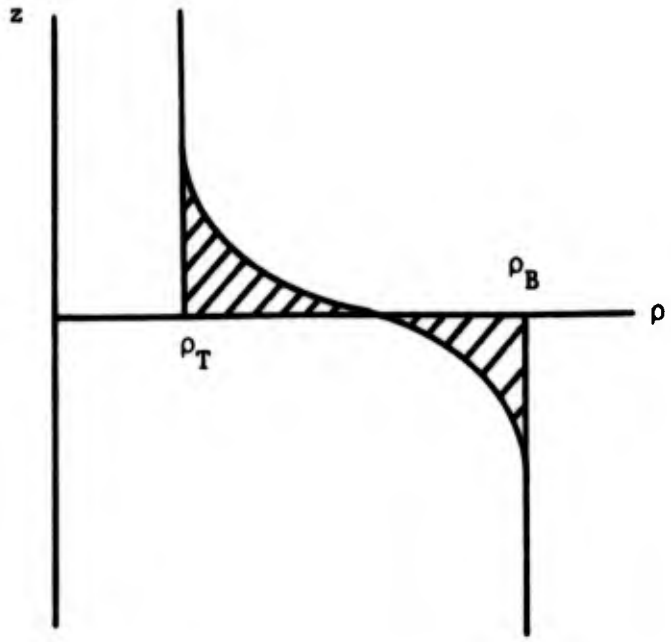

Referring to the sketch, it is seen that δ^* is a measure of the cross hatched area shown here, and this characterizes the amount of mass per unit cross sectional area which has been entrained

*It is noted that in the absence of time dependent density fluctuations, δ^* is related to the mixedness via the relation

$$\delta^* = \frac{1}{2}\int_{-\infty}^{\infty} M(z)dz$$

(but not necessarily mixed) into the layer by the turbulence. δ^*, which is analogous to a displacement thickness, is calculated for all of the cases listed in table 1, and this is shown in figure 49. It is seen that the character of this data is quite similar to that of figure 43a, where the θ_ρ distribution with x/θ_o is shown. One sees, for example, that for the low Ri_{h_o} experiments, δ^* increases to a peak value δ^*_{max} at the point where the large scale collapse occurs, and then relaxes to a somewhat smaller final value of δ^*_F, before the spurious effects of the bottom boundary layer are encountered. The value of δ^*_F is very important, because this is a measure of the total vertical transport of salinity which has resulted from the mixing event. The variation of this quantity with the initial Richardson number is shown in figure 50a. As might be expected intuitively, it is seen that proportionately more transport occurs at lower Richardson numbers. This is because at decreased stratification the large scale entrainment mechanisms have longer lifetimes, and hence, more fluid is entrained in the early growth stages of the mixing. For the four lowest Richardson number cases, it is interesting that there is almost a linear dependence of δ^*_F upon Ri_{h_o}. At the two highest values of Ri_{h_o}, it is seen that the vertical transport is much smaller than that previously discussed, and is relatively insensitive to density difference across the layer.

A quantity readily available from figure 49 which measures the effectiveness of the turbulent diffusion subsequent to the large scale collapse is given by $\delta^*_F/\delta^*_{max}$. It is of interest to study how

this quantity scales with the aforementioned parameter T_D/T_T. This is shown in figure 50b. Also shown in figure 50b is the similar data obtained for the Reynolds number experiments (cases F and G). It is also useful to include some of the high Reynolds number results of Thorpe (1973), and this is done by scaling his figure 4, which presents the density layer thickness deduced from photographs plotted as a function of normalized time. Examination of this data shows that $\delta_F^*/\delta_{max}^*$ is a monotonically decreasing function of T_D/T_T. Thus, as anticipated previously, as the time available for diffusion increases, the molecular mixing process is carried to a further state of completion. It is seen from Thorpe's data that at the larger Reynolds numbers of his experiment, the mixing is so effective that more than 95% of the fluid entrained by the turbulence in the early mixing stages is retained in the mixing region in the final state. On this basis, it is anticipated that for oceanic mixing, assuming that heat is the quantity being transported, $T_T >> T_D$ and the relaxation of the layer from the point of collapse to the final state should proceed in a manner such that the total mass within the mixing region is conserved. There is even more reason to believe that this is true for atmospheric mixing, since

$$(T_D/T_T)_{atmosphere} << (T_D/T_T)_{ocean}$$

This contention is supported by the high power radar measurements of Atlas, et al. (1970), which show that during the atmospheric

mixing event that they witnessed, the thickness of the mixing region subsequent to the destruction of the nonlinear Kelvin-Helmholtz billow did not decrease with time.

In conclusion, therefore, on the basis of what has been presented in this section, it is believed that the final state of the mixing layer, i.e., how much vertical transport of specie has resulted, is dependent upon:

a) how much fluid is initially entrained (but not mixed) during the early turbulent growth period.

b) what percentage of this entrained fluid is retained in the mixing region after all the turbulence has subsided.

Part (a) merely reflects how large the initial vortex structure becomes before being destroyed by buoyancy, and this is directly related to the initial Richardson number. The (b) portion of this process is dependent upon how much time is available for diffusion after the collapse, as well as the magnitude of a typical diffusion time. For problems of geophysical interest, it is anticipated that almost all of the fluid entrained by the turbulence in the early stages of mixing is retained in the layer after the turbulence has subsided.

6.5 Energy Dissipation

A problem related to molecular diffusion of specie is the energy dissipation which occurs during the turbulent mixing event. The amount of energy which is dissipated by this process is also a measure of the efficiency of the turbulence to enhance vertical

transport, since very little transport may result if most of the energy which is extracted from the mean shearing motion is converted into heat. The manner in which the energy dissipation is calculated is not a trivial matter, and a brief elaboration of this point ensues.

6.5.1 The method for calculating energy dissipation

In considering the energy which is dissipated by the turbulent mixing process, one may start with the integral form of the energy equation for a Boussinesq fluid which is written in laboratory fixed corrdinates as

$$\frac{\partial}{\partial \tilde{t}} \int_{\tilde{V}} \left[\frac{1}{2} \rho_o \tilde{u}_i \tilde{u}_i + \rho \tilde{g}_i \tilde{x}_i \right] d\tilde{V} + \int_{\tilde{A}} \left[\frac{1}{2} \rho_o \tilde{u}_i \tilde{u}_i + \rho \tilde{g}_i \tilde{x}_i \right] (\tilde{u}_i \tilde{n}_i) d\tilde{A}$$

$$+ \int_{\tilde{A}} \tilde{u}_i \tilde{\tau}_{\alpha i} \ell_\alpha d\tilde{A} = - \int_{\tilde{V}} \tilde{\epsilon} d\tilde{V} \qquad 6.5.1.1$$

where the tilde refers to a coordinate system fixed in space, $\tilde{V}$ is some fixed volume whose surface area is defined by $\tilde{A}$, and

n_i = outward - drawn normal to $\tilde{A}$

ℓ_α = direction cosines of n_α

$\tau_{\alpha i}$ = surface stress tensor

ϵ = energy dissipation rate/unit volume

ρ_o = some reference density

and

$$-\frac{\Delta\rho}{\rho_o} < \rho < \frac{\Delta\rho}{\rho_o} *$$

*Note that the hydrostatic term has already been integrated out of the equation.

Let us suppose that one is interested in the dynamics of a purely temporal event which is characterized at times $t = 0$ and $t = T_F$ by steady, parallel, two-dimensional flow. Then, taking the volume $\tilde{V}$ to be a thin slab of thickness δx and of infinite extent in the y-z plane, equation 6.5.1.1 may be formally integrated with respect to time, and the volume and surface integrals evaluated to yield

$$\int_{-\infty}^{\infty} \left[\frac{1}{2} \tilde{u}_1 \tilde{u}_1 + \rho \tilde{g} \tilde{z} \right] d\tilde{z} \Big|_{\tilde{t}=0}^{\tilde{t}=T_F} = - \int_{\tilde{t}=0}^{T_F} \left[\int_{-\infty}^{\infty} \tilde{\epsilon} d\tilde{z} \right] d\tilde{t} \qquad 6.5.1.2$$

This may be interpretted as

$$\Delta KE_T + \Delta PE_T = -D_T \qquad 6.5.1.3$$

The subscript T denotes a temporal event. ΔKE_T and ΔPE_T are respectively the change in kinetic and potential energy in the volume $\tilde{V}$ between $t = 0$ and T_F, and D_T is the amount of dissipation which occurs during this time. Thus, by knowing the vertical distributions of the density and horizontal velocity before and after a temporal mixing event, one may use eq. 6.5.1.2 to ascertain the total amount of energy dissipated during the mixing process.

It is also of interest to carry out this analysis for the case where the flowfield is steady in time but varies in the spatial coordinates. Before doing so, however, it is instructive to verify that the energy equation is invariant to a Galilian transformation, since portions of the spatial analysis will involve energy calculations in a moving coordinate system.

If one examines the energy equation in laboratory fixed coordinates, but this time considering the differential form of the equation, one may write

$$\frac{\partial}{\partial\tilde{\tau}}\left(\frac{1}{2}\,\tilde{u}_i\tilde{u}_i\right) + \tilde{u}_j\,\frac{\partial}{\partial\tilde{x}_j}\left(\frac{1}{2}\,\tilde{u}_i\tilde{u}_i\right) = -\frac{1}{\rho_o}\,\tilde{u}_i\,\frac{\partial\tilde{p}}{\partial\tilde{x}_i}\,\frac{\rho\tilde{u}_i}{\rho_o}\,\frac{\partial\tilde{\Omega}}{\partial\tilde{x}_i}$$

$$+ \nu\tilde{u}_i\,\frac{\partial}{\partial\tilde{x}_j}\,\frac{\partial}{\partial\tilde{x}_j}\,\tilde{u}_i \qquad 6.5.1.4$$

where, $\tilde{\Omega} = \tilde{g}\tilde{x}_3$

Now, a Galilian transformation, defined by

$$x_i = \tilde{x}_i - U_i\tilde{t}\ ;\ U_i = \text{constant} \qquad 6.5.1.5$$
$$t = \tilde{t}$$

may be introduced, so that

$$\frac{\partial}{\partial\tilde{t}} = \frac{\partial}{\partial t} - U_i\,\frac{\partial}{\partial x_i}$$

$$\frac{\partial}{\partial\tilde{x}_i} = \frac{\partial}{\partial x_i}$$

where the variables without tildes refer to quantities in the moving coordinate system. Denoting $u_i = \tilde{u}_i - U_i$, and noting that $\tilde{p} \equiv p$ and $\tilde{g} \equiv g$, eq. 6.5.1.4 may be written in the moving reference frame as

$$\frac{\partial}{\partial t}\left(\frac{1}{2}\,u_iu_i\right) + u_j\,\frac{\partial}{\partial x_j}\left(\frac{1}{2}\,u_iu_i\right) + \frac{u_i}{\rho_o}\,\frac{\partial p}{\partial x_i} + \frac{\rho u_i}{\rho_o}\,\frac{\partial\Omega}{\partial x_i} - \nu u_i\,\frac{\partial}{\partial x_j}\,\frac{\partial}{\partial x_j}\,u_i$$
$$= -U_i\left[\frac{\partial u_i}{\partial t} + u_j\,\frac{\partial}{\partial x_j}\,u_i + \frac{1}{\rho_o}\,\frac{\partial p}{\partial x_i} + \frac{\rho}{\rho_o}\,\frac{\partial\Omega}{\partial x_i} - \nu\,\frac{\partial}{\partial x_j}\,\frac{\partial}{\partial x_j}\,u_i\right]$$

6.5.1.6

But the right hand side of eq. 6.5.1.6 is identically zero by virtue of the momentum equation (which is clearly invariant to a Galilian transformation). Thus, the energy equations in the moving and fixed coordinate systems are identical, and hence, energy has been conserved by this transformation.

One may pursue this analysis one step further by recasting eq. 6.5.1.6 in an integral representation to yield an equation which is the same as eq. 6.5.1.1, except that the variables are written without the tildes. The important point to note is that now the volume V over which the integration is to be performed is fixed with respect to the moving coordinate system, rather than being fixed in laboratory coordinates.

Returning, again, to the problem of determining the amount of dissipation in a spatially varying experiment, it is now clear that one may take as the control volume a thin slab of thickness δx and of infinite extent in the y-z plane, which moves at the mean convection speed of the fluid, U_{ave}. Again, it is supposed that at $t = 0$ and $t = T_F$, the flow within the moving volume V is steady, parallel, and two dimensional, and that the surface A is stress-free. Then, integrating the energy integral equation, eq. 6.5.1.1, with respect to t and carrying out the various volume and surface integrations yields

$$\int_{-\infty}^{\infty}\left[\frac{1}{2}\rho_o u_1 u_1 + \rho g z\right]dz \Big|_{t=0}^{T_F} + \frac{\partial}{\partial x}\int_{t=0}^{T_F}\left[\int_{-\infty}^{\infty}\frac{1}{2}\rho_o u_1 u_1 + \rho g z\, u_1 dz\right]dt = -\int_{t=0}^{T_F}\left[\int_{-\infty}^{\infty}\epsilon dz\right]dt \qquad 6.5.1.7$$

The flux term (underlined) is arrived at by considering a Taylor series expansion of the integrand between x and $x + \delta x$ when performing the surface integral over the faces of the slab. One may simplify this term by reintroducing the Galilian transformation

$$\left(\frac{\partial}{\partial \tilde{t}}\right)_{\tilde{x}} = \left(\frac{\partial}{\partial t}\right)_{x} - \left(U_{ave}\frac{\partial}{\partial x}\right)_{t}$$

or alternatively,

$$\left(\frac{\partial}{\partial x}\right)_{t} = \frac{1}{U_{ave}}\left[\left(\frac{\partial}{\partial t}\right)_{x} - \left(\frac{\partial}{\partial \tilde{t}}\right)_{\tilde{x}}\right]$$

Note, however, that for this spatially evolving problem,

$$\left(\frac{\partial}{\partial \tilde{t}}\right)_{\tilde{x}} \equiv 0$$

Thus, the flux term in eq. 6.5.1.7 may be formally integrated with respect to time to yield

$$\frac{1}{U_{ave}} \int_{-\infty}^{\infty} \left[\frac{1}{2}\rho_o u_1 u_1 + \rho g z\right] u_1 dz \Bigg|_{t=0}^{T_F} \qquad 6.5.1.8$$

Examination of this term is interesting, since it does not arise in the temporal problem, and thus represents a fundamental difference between spatially and temporally varying phenomena. If conditions are chosen at $t = 0$ such that, in the moving coordinate system, the velocity and density are $-\Delta U/2$ and $-\Delta\rho/2$, respectively, for $z > 0$, and $+\Delta U/2$ and $+\Delta\rho/2$ for $z < 0$, then the value of the above integral evaluated at $t = 0$ is identically zero. However, in general this is not true at $t = T_F$, except for the

special case where both u and ρ possess skew symmetry about $z = 0$. For arbitrary profiles, this integral has a net contribution in the dissipation calculation.

Incorporating eq. 6.5.1.8 into eq. 6.5.1.7, the energy equation may be written as

$$\int_{-\infty}^{\infty} \frac{1}{2} \rho_o u_1^2 \left[1 + \frac{u_1}{U_{ave}}\right] dz \Bigg|_{t=0}^{T_F} + \int_{-\infty}^{\infty} \left[\rho g z \left(1 + \frac{u_1}{U_{ave}}\right)\right] dz \Bigg|_{t=0}^{T_F}$$

$$= -\int_0^{T_F} \left[\int_{-\infty}^{\infty} \varepsilon dz\right] dt \qquad 6.5.1.9$$

or, written symbolically in a form analogous to eq. 6.5.1.3

$$\Delta KE_s + \Delta PE_s = -D_s \qquad 6.5.1.10$$

where the subscript s implies spatial evolution. Hence, by considering the energy dissipation in a volume moving at the mean convection speed U_{ave}, one arrives at a formulation which is directly comparable to the dissipation determined for a temporally varying problem.

6.5.2 Total energy dissipation during the mixing event

Referring to the previous discussion, if one chooses the value of T_F such that

$$T_F = \frac{\theta_o}{U_{ave}} (x/\theta_o)_F$$

where $(x/\theta_o)_F$ is the furthest location downstream of the splitter plate for which the data for a particular case are unaffected by the

boundary layer on the channel wall, then one may calculate the energy dissipation which occurs during the entire mixing process by using the measured velocity and density data at this station in the integration of eq. 6.5.1.9. It is noted that implicit in this calculation is the assumption that the flow at this longitudinal coordinate is both steady and parallel, so that $\rho(z)$ and $u_1(z)$ may be approximated by the measured mean density and horizontal velocity profiles, respectively.

Considering eq. 6.5.1.10, a quantity of interest is given by (dropping the subscript s)

$$-\left(\frac{\Delta PE}{\Delta KE}\right)_F = \left[1 + \frac{D}{\Delta KE}\right]_F \qquad 6.5.2.1$$

where the F denotes the total change in energy between $t = 0$ and $t = T_F$. This ratio is significant, because it measures how much of the kinetic energy which has been extracted from the mean flow by the turbulence is used to increase the potential energy of the system. This calculation is performed for all of the cases listed in table 1, and the results are shown in figure 51. Also shown here are the similar data for a temporally growing mixing layer experiment which were obtained by Thorpe (1973) using eq. 6.5.1.4.

Several points need to be made explicit when considering the data from these two experiments. First of all, from examination of the $\bar{\rho}^{\,max}_{rms}$ and the M_{max} measurements shown in figures 43a and 44, it is found that for cases E, J, and L the density fluctuation level at the end of the test section is quite large. Hence, the

assumption of steady flow is certainly violated, and the energy calculation made at this station does not, in reality, characterize the actual final state of the mixing.

A second point to bear in mind is that due to the manner in which the mean shear is produced, Thorpe's experiment should not exhibit the mode II wave structure observed in the present experiment at high initial Richardson numbers. This is because those velocity and density profiles initially have the same length scale, and hence the criterion of Hazel (1972) for instability of the mode II wave is not satisfied. Thus, because the physical processes are distinctly different in this Richardson number regime, a disparity between Thorpe's data and the present experiment is not unexpected.

One final, and somewhat philisophical note to be made is that it is not clear whether a comparison of the two sets of data is anything more than an academic exercise, since there is no justification a priori to support the contention that there should be any agreement at all between the two investigations. This is due to the unmistakable distinction that one experiment evolves in space and the other in time, and hence in no way can they be considered the same problem. However, because of the great similarity in many of the physical features of the two investigations, the temptation to compare the results is almost overwhelming. It is noted, however, that a problem of definition arises when comparing the two results for $Ri_{h_o} \geq .125$. In calculating the relative changes in potential

and kinetic energy, Thorpe defines the end state of the mixing event as $t/\tau \geq 12$ (the precise value of t/τ used for each calculation is not made explicit). The present results (e.g., figures 43 and 44) show that for case E the flow field is still evolving at the last longitudinal station $x/\theta_o = 1035$, which corresponds to $t/\tau = 30$. In comparing the present data at this Richardson number with the similar data of Thorpe, it is important that the comparison be made at the same value of t/τ. Thus, figure 51 also shows the value of $(\Delta PE/\Delta KE)_F$ for the present experiment evaluated at $t/\tau = 12$.*

The data presented in figure 51 show that, for the four lowest Richardson number experiments, the relative increase in potential energy is a decreasing function of Ri_{h_o}. Hence, at higher Richardson numbers, the turbulence is less efficient at effecting vertical transport, and thus more energy is dissipated. It is also found that these results compare very well with the measurements of Thorpe, particularly when one uses the datum point for case E evaluated at $t/\tau = 12$. This is quite a remarkable result when one considers the order of magnitude disparity in Reynolds number between the two experiments. The implication of this is that, although the present experiment is performed at Reynolds numbers well below those of Thorpe, the increased importance of viscosity does not impose an undue constraint upon the important dynamical

*This same procedure could also be applied to cases J and L, although this has not been done.

processes, and this supports the contention that the present work has applicability in the investigation of oceanic mixing events.

It is also observed from figure 51 that the mixing mechanisms prevalent for the high Richardson number regime have a very dissipative character. It is seen here that by the time the fluid has been convected to the end of the test section, only about 2-5% of the energy extracted from the mean flow by the turbulence has been used to increase the mean potential energy of the system. This is to be compared with the low Richardson number experiments where 15-25% of the extracted kinetic energy goes into potential energy. Between cases D and E, where the growth mechanisms are believed to change from vortex formation and pairing to mode II wave breaking, the relative potential energy increase changes from about 16% to about 6%, indicating that the former means of mixing fluid is almost three-fold more effective at adding potential energy to the system.

6.5.3 Energy dissipation as a function of longitudinal coordinate

Following a procedure analogous to that used in the previous section to compute total energy dissipation, one may also investigate the dissipation as a function of the longitudinal coordinate. This is a useful exercise, because it is felt that the curious change in shape of the mean velocity profile observed in figure 39b is somehow associated with the dissipation of energy at certain stages of the mixing process. However, the results of such a calculation are not as easily interpreted as those of

section 6.5.2. This is because those measurements are concerned with the conditions at the end states of the mixing event, and hence the assumption of steady parallel flow is acceptable. For the present case, one must account for the turbulent energy as well as the mean kinetic and potential energy, and thus the problem is more difficult.

The equation governing the mean kinetic energy in a turbulent Boussinesq fluid is given by Hinze (1959, p. 65) (minus the buoyancy term) as

$$\frac{\partial}{\partial t}\left(\frac{1}{2}\bar{U}_j\bar{U}_j\right) + \frac{\partial}{\partial x_i}\bar{U}_i\left(\frac{\bar{p}}{\rho_o} + \frac{1}{2}\bar{U}_j\bar{U}_j\right) = \bar{U}_i\frac{\partial}{\partial x_j}\left[\frac{\partial\bar{U}_i}{\partial x_j} + \frac{\partial\bar{U}_j}{\partial x_i}\right]$$

$$- \bar{U}_i\frac{\partial}{\partial x_j}\overline{u_i'u_j'} + \text{Density Term} \qquad 6.5.3.1$$

where the instantaneous velocity vector U_j is decomposed into $U_j = \bar{U}_j + u_j'$, so that the overbar denotes an ensemble average term and primed variables refer to fluctuating quantities.

The density term is obtained by multiplying the momentum equation by $\bar{U}_i$ to yield

$$(\text{density term}) = -\frac{1}{\rho_o}\bar{U}_i\,\rho\frac{\partial\Omega}{\partial x_i}\;;\quad \Omega = \Omega(x_3)$$

Using the continuity equation, and noting that $\bar{U}_i = U_i - u_i'$ yields

$$(\text{density term}) = -\frac{1}{\rho_o}\left\{\left[\frac{\partial}{\partial t} + \frac{\partial}{\partial x_i}\bar{U}_i\right](\rho\Omega) - \Omega\left[\frac{\partial}{\partial t} + (U_i - u_i')\frac{\partial\rho}{\partial x_i}\right]\right\}$$

Incorporating the incompressibility condition, letting $\rho = \bar{\rho} + \rho'$

and ensemble averaging yields

$$\text{(density term)} = -\frac{1}{\rho_o}\left\{\left[\frac{\partial}{\partial t} + \frac{\partial}{\partial x_i}\bar{U}_i\right](\bar{\rho}\bar{\Omega}) + \frac{\partial}{\partial x_i}(\overline{\rho' u_i' \Omega}) - \overline{\rho' u_i'}\frac{\partial \bar{\Omega}}{\partial x_i}\right\} \qquad 6.5.3.2$$

This density term may be included in eq. 6.5.3.1 to yield the differential form of the energy equation for a Boussinesq fluid. As has already been shown, the energy equation is invariant to a Galilian transformation, so that one may consider eqs. 6.5.3.1 and 6.5.3.2 to define quantities in a coordinate system translating at velocity U_{ave}, provided that $\bar{U}_i$ is interpreted as the velocity measured in the moving frame of reference. Considering the integration of eq. 6.5.3.1 over some volume V which is fixed in the moving frame, and using Green's theorem, the energy integral equation may be written as

$$\frac{\partial}{\partial t}\int_V \left[\frac{1}{2}\bar{U}_j\bar{U}_j + \frac{\bar{\rho}}{\rho_o}\Omega\right]dV + \int_A \bar{U}_i \ell_i\left[\frac{1}{2}\bar{U}_j\bar{U}_j + \frac{\bar{\rho}\bar{\Omega}}{\rho_o}\right]dA$$

$$= \int_V \frac{\overline{\rho' u_i'}}{\rho_o}\frac{\partial \Omega}{\partial x_i}\,dV - \int_A \ell_j \frac{\overline{\rho' u_i'}}{\rho_o}\Omega\,dA - \int_V \tau_{ij}\frac{\partial \bar{U}_i}{\partial x_j}\,dV$$

$$+ \int_A \ell_j \bar{U}_i \tau_{ij}\,dA - \int_A \ell_i \frac{\bar{p}}{\rho_o}\bar{U}_i\,dA \qquad 6.5.3.3$$

when,

$$\tau_{ij} = \nu\left[\frac{\partial \bar{U}_i}{\partial x_j} + \frac{\partial \bar{U}_j}{\partial x_i}\right] - \overline{u_i' u_j'}$$

and l_j are again the direction cosines.

This equation may be specialized for the case where $\overline{U}_i = U_1(x_3) \equiv U(z)$. Then, again considering the volume V to be a thin slab with thickness δx, of infinite extent in the y-z plane, assuming $\frac{\partial}{\partial y}(\overline{\quad}) = 0$, and evaluating the surface integrals over the faces of the slab in the same manner as for eq. 6.5.1.7, the energy equation may be expressed as

$$\frac{\partial}{\partial t}\int_{-\infty}^{\infty}\left[\frac{1}{2}U^2 + \frac{\bar{\rho}}{\rho_o}gz\right]dz + \frac{\partial}{\partial x}\int_{-\infty}^{\infty}U\left[\frac{1}{2}U^2 + \frac{\bar{\rho}}{\rho_o}gz\right]dz = \int_{-\infty}^{\infty}\frac{\overline{\rho' w'}}{\rho_o}g\,dz$$

$$- \frac{\partial}{\partial x}\int_{-\infty}^{\infty}\frac{\overline{\rho' u'}}{\rho_o}gz\,dz - \nu\int_{-\infty}^{\infty}\left(\frac{\partial U}{\partial z}\right)^2 dz + \int_{-\infty}^{\infty}\overline{u'w'}\frac{\partial U}{\partial z}\,dz$$

$$- \frac{\partial}{\partial x}\int_{-\infty}^{\infty}U\,\overline{u'^2}\,dz - \frac{\partial}{\partial x}\int_{-\infty}^{\infty}\frac{\bar{p}}{\rho_o}U dz \qquad 6.5.3.4$$

Finally, this may be integrated with respect to time, accounting for the flux terms in the same manner as for eq. 6.5.1.8 to yield

$$\int_{-\infty}^{\infty}\frac{1}{2}U^2\left[1 + \frac{U}{U_{ave}}\right]dz\Bigg|_{t=0}^{T} + \int_{-\infty}^{\infty}\frac{\bar{\rho}}{\rho_o}gz\left[1 + \frac{U}{U_{ave}}\right]dz\Bigg|_{t=0}^{T}$$

$$\equiv \overline{\Delta KE} + \overline{\Delta PE} = \int_{t=0}^{T}\Bigg\{\int_{z=-\infty}^{\infty}\Bigg[\underbrace{-\nu\left(\frac{\partial U}{\partial z}\right)^2}_{\text{I}} + \underbrace{\overline{u'w'}\left(\frac{\partial U}{\partial z}\right)}_{\text{II}}$$

$$\underbrace{+\frac{\overline{\rho' w'}}{\rho_o}g}_{\text{III}}\Bigg]dz\Bigg\}dt - \int_{-\infty}^{\infty}\Bigg[\underbrace{\frac{U}{U_{ave}}\overline{u'^2}}_{\text{IV}} + \underbrace{\frac{\overline{\rho' u'}}{\rho_o U_{ave}}gz}_{\text{V}}$$

$$\underbrace{+\frac{\bar{p}}{\rho_o}\frac{U}{U_{ave}}}_{\text{VI}}\Bigg]dz\Bigg|_{t=0}^{T}$$

$\overline{\Delta KE}$ and $\overline{\Delta PE}$ are respectively the change in the mean kinetic and potential energy in the volume V during the interval t = 0 and t = T. In examining the individual terms on the right hand side of eq. 6.5.3.5, it is seen that I represents the direct dissipation of the mean velocity profile by viscosity. II is the extraction of mean kinetic energy by the Reynolds stress. This same term appears in the $\overline{u'^2}$ equation with the opposite sign, indicating that it is a production term in that equation. III is a production or loss term, depending upon the sign of the correlation $\overline{\rho' w'}$, and arises due to the work done by the fluctuating velocity and density field. IV represents the flux of $\overline{u'^2}$ through the volume due to the mean velocity U_{ave} (it is curious that this term does not also include the quantity $U_{ave}(\overline{v'^2} + \overline{w'^2})$ as well). V is the flux of fluctuating potential energy through the volume due to the u' component of the turbulent velocity, and VI is the pressure work term.

Using the measured mean velocity and density profiles for all the conditions in table 1, the change in mean kinetic and potential energy in eq. 6.5.3.5 are calculated for all the measuring stations by interpreting T as x/U_{ave}. The results are presented in figure 52a, where both $\overline{\Delta KE}$ and $\overline{\Delta PE}$ have been normalized by the quantity $E_o = (\Delta U)^4/g(\Delta\rho/\rho_o)$.

Directing ones attention to the potential energy data in figure 52a, it is seen that for the three lowest Richardson number experiments, $\overline{\Delta PE}/E_o$ is an increasing function of x/θ_o prior to

the point where the demise of the vortex structure occurs. After the collapse, $\overline{\Delta PE}/E_o$ maintains a relatively constant value of about .003 - .004. Thus, the layer achieves its maximum potential energy at the point of collapse, and beyond this the dynamical processes are such that further increases in $\overline{\Delta PE}/E_o$ are precluded. For the two highest Richardson number cases, the mean potential energy increase is diminished significantly, with $\overline{\Delta PE}/E_o$ achieving a maximum of about .0006.

Contrasted with this is the mean kinetic energy loss, also shown in figure 52a, which has somewhat of a different character. It is seen that in the early growth stages, $\overline{\Delta KE}/E_o$ decreases with x/θ_o, but beyond the point where the layer achieves its maximum potential energy, kinetic energy is still being extracted from the mean flow. Since this energy no longer is used to increase $\overline{\Delta PE}/E_o$, it is not clear as yet what happens to this energy. At about $x/\theta_o \cong 300$, the kinetic energy associated with the mean shear flow is observed to approach a minimum.

The sum of $(\overline{\Delta KE} + \overline{\Delta PE})/E_o$ is equal to the right hand side of eq. 6.5.3.5 normalized by E_o, and this represents the total amount of energy which has been extracted from the mean flow. This is shown in figure 52b. It is observed that the total mean energy is a decreasing function of x/θ_o until $x/\theta_o \cong 800$, and that proportionately more energy is lost as the Richardson number is increased.

It is significant that the mean flow continues to lose kinetic energy beyond the point at which the layer achieves its maximum potential energy. This is somewhat of an unexpected result, because one would think that once the large scale entrainment mechanism has been disrupted by the buoyancy, there would no longer be a means by which energy could be extracted from the mean shearing motion. As a first step in trying to understand the cause of this phenomenon, one may examine the individual mean velocity profiles which are used to calculate the change in kinetic energy. In doing so, it is observed that prior to the collapse of the large scale vortex structure, the velocity profiles for all cases are quite similar to the data shown in figure 39a which agrees well with the Liepmann and Laufer (1947) data. Subsequent to the collapse, however, it is found that the character of the mean velocity field more closely resembles the data shown in figure 39b, where an increased velocity defect is noted. It is this feature of the mean velocity profile which accounts for the continuous increase in the kinetic energy loss beyond the point where the layer achieves its maximum potential energy, and hence, ceases to grow.

It is apparent, therefore, that the mean profile shape change noted in figures 39a and 39b is somehow related to the destruction of the large scales, and thus, it is of interest to study how the dynamical processes of the mixing layer are altered by this collapsing process. One might do so by investigating the various terms on the right hand side of eq. 6.5.3.5, in order

to determine which may be responsible for this curious nature of the mean velocity profile. Once it is known which is the dominant term in the energy extraction subsequent to the collapse, one is in a better position to propose a physical model to explain the observed phenomenon.

The first term of eq. 6.5.3.5 to be evaluated is I, which represents the direct diffusion of the mean shear by viscosity. This is readily calculated from the mean velocity profiles, and as one might suspect, this term is negligible. For case C, it is found that after the collapse, the direct viscous dissipation of the mean kinetic energy accounts for less than 1% of the total energy loss.

The second term in this equation which may be evaluated from the measurements is IV. It is noted, though, that because the integrand changes sign across the layer, the possibility exists for area cancellation, with the result that term IV may have only a small contribution to the energy balance. Again for case C, it is found that, although IV is more important than the viscous term, it only accounts for 3-5% of the total energy loss, and hence is also too small to be responsible for the mean kinetic energy decrement.

Similarly, it is found that V is extremely small, accounting for typically .1% of the observed energy loss.

The three remaining terms to be examined are II, III, and VI; but, unfortunately, these involve quantities which are not

measured in this investigation, and hence, one may only speculate upon their behavior. As has been noted, term II, which involves the extraction of mean energy by the Reynolds stress $\overline{u'w'}$, shows up with opposite sign in exactly the same form in the turbulent kinetic energy equation, but only as a production term for $\overline{u'^2}$. Thus, only the $\overline{u'^2}$ component of the turbulent energy spectrum receives energy directly from the mean flow under the action of the Reynolds stresses, and it is the pressure terms (alternatively called the isotropic terms) which act to equipartition this energy into the v' and w' components. Turner (1973, p. 146) points out, though, that experiments indicate the pressure terms are relatively inefficient at repartitioning this energy, and hence, one might expect the $\overline{u'^2}$ fluctuations to contain most of the energy. However, if one examines the peak $\bar{u}^{\,max}_{rms}$ data shown in figure 43b, it is seen that subsequent to the collapse, the magnitude of $\overline{u'^2}$ decreases with x/θ_o. This has the implication that the mean kinetic energy loss which is observed in this region of the flow is not attributable to the turbulence production by the Reynolds stresses, for if it were, $\overline{u'^2}$ would presumably be increasing. It is noted, though, that this argument has a serious flaw. It has been suggested that because $\bar{u}^{\,max}_{rms}$ is a decreasing function of x/θ_o, this implies that the Reynolds stress term is not extracting mean kinetic energy. It is conceivable, however, that the Reynolds stress term <u>is</u> important following the collapse, but that the energy dissipation rate exceeds the rate at which turbulent energy

is being created by this production term. However, such is not believed to be the case. If one plots the $\bar{u}^{\,max}_{rms}$ data on logarithmic graph paper, it is found that the magnitude of the velocity fluctuations decays as $x^{-3/4}$. This decay rate is larger than the $x^{-1/2}$ decay observed by Lin and Veenhuizen (1974) for grid generated turbulence in a linearly stratified fluid. Because the Reynolds stress production term for their experiment is known to be unimportant, it is argued that the faster decay rate for the present experiment is not inconsistant with the assumption that term II is negligibly small. It is worth noting that $\bar{\rho}^{\,max}_{rms}$ also decays as $x^{-3/4}$, which is the same decay rate observed by Lin and Veenhuizen for the density fluctuations. Thus, although these arguments do not constitute conclusive proof that the production term in eq. 6.5.3.5 is unimportant in the overall energy balance, at least there is strong suspicion that this is so.

In considering term VI, it is noted that although $\bar{p}$ was not measured in this investigation, experiments performed in a homogeneous mixing layer indicate that the pressure work term has an extremely small contribution to the overall energy balance (Spencer and Jones, 1971).

Thus, one is left with only a single term which may explain how energy is extracted from the mean shearing motion after the large scale entrainment mechanism has been disrupted by the buoyancy. This is given by

$$\int_0^T \left[\int_{-\infty}^{\infty} g \frac{\overline{\rho' w'}}{\rho_o} \, dz \right] dt$$

As is true for the Reynolds stress term, there is insufficient data available to attempt an evaluation of this quantity, but one may speculate as to how it might be important in the mixing process. In considering the state of the flow field once the large scale structures have succumbed to the buoyancy, it is reasonable to assume that a great deal of the fluid is in positions where it is statically unstable. This is evident in the shadowgraph pictures of Chapter 4 and the instantaneous density profiles of Chapter 5. Subsequent to this point, as the flow settles out, the light fluid in the lower portion of the layer is accelerated vertically upward by the buoyancy forces until it reaches its equilibrium point. For this process, $\rho' < 0$ and $w' > 0$ yielding a negative correlation. Similarly, for the heavy fluid found in the upper portion of the layer the settling process is characterized by having $\rho' > 0$ and $w' < 0$, again yielding a negative correlation. Thus, this settling of the fluid to its neutral buoyancy position after the collapse produces a negative $\overline{\rho' w'}$ correlation across the entire mixing region, and this process introduces a mechanism by which energy may be extracted from the mean flow. Furthermore, in the later stages of mixing, when most of the fluid has settled out, the shadowgraph pictures reveal that the isopycnal surfaces become elongated and evolve into internal waves. But for internal wave motion, w' and ρ' are 90^{o} out of phase, and hence have zero correlation. This is consistent with the observation that at about $x/\theta_o \cong 800$, the extraction of kinetic energy from the mean profile ceases.

It is also interesting to note that term III shows up in the diffusion equation for $\overline{\rho'^2}$ with the same sign, indicating that $\overline{\rho'w'}$ also acts to decrease the density fluctuation level. Examination of the microconductivity probe data, shown in figure 43a, shows that subsequent to the collapse the $\bar{\rho}_{rms}^{max}$ level does indeed decrease with x/θ_o.

It is still not clear, though, what happens to the energy which is extracted from the mean shear. If one examines the turbulent kinetic energy equation it is found that the $\overline{\rho'w'}$ correlation acts as a production term only in the $\overline{w'^2}$ equation. Hence, the extracted mean energy shows up initially as $\overline{w'^2}$ "energy," but little more can be said about how this energy is eventually dissipated, since the turbulent kinetic energy equation is far too complex to allow for a simple interpretation with such a limited amount of data.

The conclusion to be drawn from the results presented in this section is that subsequent to the collapse the mean potential energy of the system is relatively constant, but the dynamics associated with the large scale destruction produces a large negative $\overline{\rho'w'}$ correlation which continues to extract energy from the mean flow. Because the physical dimensions of the layer are no longer increasing, this loss in mean kinetic energy can show up only as an increase in the mean velocity defect, which accounts for the mean velocity profile shape change noted in figure 39a and 39b. This $\overline{\rho'w'}$ correlation also works to reduce the rms level

of the density fluctuations, and this is also observed subsequent to the collapse in figure 43a. In the final stages of mixing, the layer is characterized by predominantly internal wave motion, yielding a small $\overline{\rho' w'}$ correlation, and the rate of change of both ρ_{rms}^{max} and $\overline{\Delta KE}/E_o$ are observed to diminish.

6.6 Character of the Gross Features of the Shear Layer

In addition to understanding some of the dissipative processes which occur during the evolution of a mixing event, as discussed in the previous section, one is also interested in characterizing some of the gross properties of the shear layer.

A quantity which yields information about the initial turbulent growth phase of the mixing process is given by

$$Ri_{h_\rho} = g \frac{\Delta\rho}{\rho_o} \frac{h_\rho}{(\Delta U)^2} \cong g \frac{\Delta\rho}{\rho_o} \frac{5\theta_\rho}{(\Delta U)^2}$$

where h_ρ is the maximum slope thickness of the mean density distribution.* This is shown plotted in figure 53 versus the normalized time t/τ given by

$$t/\tau = \frac{x}{U_{ave}} g \frac{\Delta\rho}{\rho_o} \frac{1}{\Delta U} = \frac{x}{\theta_o} Ri_{\theta_o} \frac{\Delta U}{U_{ave}}$$

This choice of the abscissa is used so that direct comparison may be made with the similar data of Thorpe (1973), which were obtained at

*The empirically determined relation $h \cong 5\theta_\rho$ is used to convert from θ_ρ (which is the quantity actually determined from the mean density profile) to the maximum slope thickness h_ρ.

Reynolds numbers roughly an order of magnitude larger than the present experiment.

It is important to note how this comparison is made. Thorpe's data is obtained by integration of the area contained in the mixing region, as determined from photographs. This method tends to overestimate the thickness of the region since, in addition to being somewhat subjective as to what one calls the mixing region, all parts of the layer are weighted equally. It has been empirically determined in this investigation that such a definition of the shear layer thickness is roughly six times larger than the thickness θ_ρ, or 6/5 times larger than the maximum slope thickness h_ρ. Thus, for comparison with the present experiment, Thorpe's data have been scaled by a factor of 5/6.

As has been common for much of the previously presented data, one must discriminate between the low and the high initial Richardson number experiments when discussing the character of the data shown in figure 53. For the three lowest Ri_{h_o} cases, it is seen that for $t/\tau < 4$, Ri_{h_ρ} for the present data is significantly smaller than what Thorpe observed. This is to be expected, since there is a difference in initial conditions between the two experiments, in that Thorpe's initial density profile at $t/\tau = 0$ has a finite thickness, whereas in the present experiment the density interface at $x = 0$ is very thin. However, at later times it is seen that the present data fall within Thorpe's error band, and tend to achieve roughly the same maximum value of

$Ri_{h_\rho} = .32$ at $t/\tau = 6\text{-}8$. This is an interesting result, because it supports the previously expressed contention that many of the gross features of the present experiment are unaffected by moderate changes in the Reynolds number.

Further examination of figure 53 shows that, once again case E appears to mark the demarcation between the low and the high Ri_{h_o} experiments, and for cases J and L it is seen that Ri_{h_ρ} is significantly smaller than the aforementioned data, with a value of $Ri_{h_\rho} = .15$ at $t/\tau = 9$, and Ri_{h_ρ} is still increasing with longitudinal coordinate at this point.

Some of the salient features of this data are replotted in figure 54. The value of $(t/\tau)_{crit}$, defined as the point where Ri_{h_ρ} is maximized, is shown as a function of the initial Richardson number in figure 54a. The error bars shown indicate the distance of the nearest longitudinal measuring stations to this value of t/τ. The two highest Ri_{h_o} cases are deleted, since the point of maximum thickness is somewhat subjective. It is seen from this figure that the point of maximum thickness is achieved at roughly $t/\tau = 6$, which is consistent with the high Reynolds number results of Thorpe.

Figure 54b presents the maximum value of Ri_{h_ρ}, defined as Ri_{max}, for all six experiments. As noted in figure 53, Ri_{max} is roughly .32 for the three lowest Ri_{h_o} cases, but falls to a value of about .15 for the high Richardson number experiments. Thorpe's data, for two values of Ri_{max}, are also shown in figure 54b. It is observed that at the lower initial Richardson

number, Thorpe is in agreement with the present results, but at increased buoyancy the present data are significantly lower than his measurements. However, this disparity between the two experiments at high initial Richardson numbers is not unexpected, because of the predominance of the mode II interfacial waves in the present experiment for these cases.

Parenthetically, it is worth noting that Hopfinger (1972) observes for a cold plane wall jet exiting into heated ambient air, the maximum Richardson number obtained before the entrainment process stops is $Ri_{max} \tilde{=} .32$. Although the physical configuration of his experiment was somewhat different from either that of Thorpe or the present setup, the agreement of the measured maximum value of Ri_{max} between the three investigations is reassuring.

The mechanisms which act to control the maximum amplitude of the Kelvin-Helmholtz billows, and hence limit Ri_{max}, are extremely complex and not well understood. Corcos and Sherman (1976) have attempted to model the situation by considering the dynamics of vorticity transport between the cores, which are periodically spaced regions of vorticity concentration, and what they refer to as the braids, which are the high strain regions between the cores. Their model predicts that, in the absence of vortex interactions, the nonlinear wave amplitude will equilibriate when the rate of vorticity transport out of the braids due to the core induced strain is equal to the baroclinic generation of vorticity within the braid. The resulting limiting amplitude of

the billow structure (Sherman, 1975) is given by

$$H^*_{max} = \pi\lambda^*(1 - \lambda^*) \qquad 6.6.1$$

where,

$$H^*_{max} = g\frac{\Delta\rho}{\rho_o}\frac{H_{max}}{\left(\frac{\Delta U}{2}\right)^2}$$

$$\lambda^* = g\frac{\Delta\rho}{\rho}\frac{\lambda}{4\pi\left(\frac{\Delta U}{2}\right)^2}$$

and H_{max} and λ are identified in the sketch of isopycnal surfaces shown below.

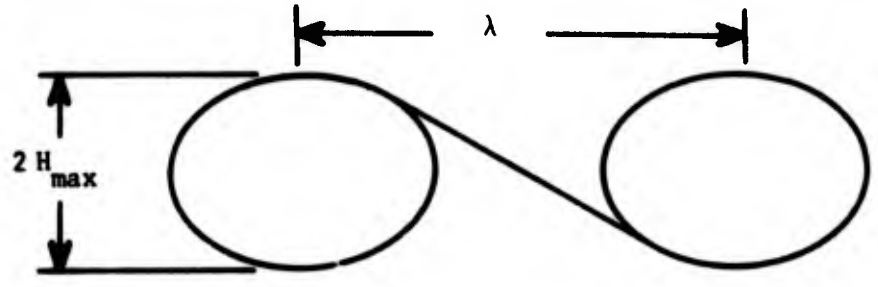

Thus, for a given wavelength, density difference, and shear, one may use eq. 6.6.1 to calculate how large a certain core-braid structure will grow before its amplitude equilibrates. As noted earlier, though, this model does not address itself to the effects of nonlinear interactions between adjacent structures. Clearly, for Ri_{h_o} sufficiently small such interactions will occur as has been demonstrated in the dye visualization study shown in figure 23. To alleviate this shortcoming, Corcos (private communication) has made some numerical studies of the interaction process using

algorithms developed by Patnaik (1974) to investigate how the limiting amplitude of the nonlinear wave is affected by subharmonic generation. The results of these calculations are quite interesting, and may be interpretted within the framework of the core-braid model. The numerical simulations predict that interactions and subharmonic generations will proceed until a point is reached where the maximum amplitude of the subharmonic, as predicted by eq. 6.1.1, is smaller than that of the fundamental structure. Physically, this implies that interactions which result in a decrease in the mixing layer thickness are precluded, a result which is intuitively plausable. Thus, for example, a core-braid structure having $\lambda^* = .25$ could grow via the Corcos and Sherman vorticity transport model to a maximum amplitude of $H^*_{max} = \frac{3\pi}{16}$, at which point a pairing could occur yielding a structure characterized by a wavelength of $\lambda^* = .5$. This subharmonic could then grow, again via the vorticity transport model, to $H^*_{max} = \pi/4$. However, a further pairing would be precluded, as the resulting maximum amplitude H^*_{max} of the subharmonic of $\lambda^* = .5$ would be less than that of the fundamental. Similarly, a structure having $\lambda^* = .35$ could grow to a maximum amplitude of $H^*_{max} = .13\pi$, but Corcos' numerical results would indicate that such a structure could not pair.

The point of demarcation between pairing and no pairing, based upon the Corcos and Sherman model and the numerical calculations of Corcos, occurs at $\lambda^* = 1/3$. Thus, one envisions situations where the vortex structure grows to a maximum amplitude H^*_{max} as predicted

by the core-braid model, and then pairs if $\lambda^* < 1/3$. The resulting subharmonic will then also grow to a new value of H^*_{max}. This process may repeat itself several times until a situation is achieved where $\lambda^* > 1/3$. At this point, further interactions are precluded, and the shear layer has truly reached its maximum amplitude. Using these arguments, one may conclude that for an arbitrary initial value of λ^*, the amplitude which characterizes the state of the mixing layer at the point of equilibration lies between $\frac{2\pi}{9} < H^*_{max} < \pi/4$, which corresponds to $1/3 < \lambda^*_{max} < 2/3$. This spread in maximum amplitude is only about 10% of the maximum permitted value of H^*_{max}. Hence, for most practical situations Corcos and Sherman's model in conjunction with the numerical calculations suggest that the maximum shear layer thickness is characterized by a critical value of H^*_{max} (which may be related to Ri_{max}) roughly equal to $\pi/4$.

The results presented in the foregoing discussion may be tested using the experimental findings of the present study. Some qualitative support for these ideas is given in the photographic documentation of the dye visualization study presented in figures 23 and 25. In figure 23 at $x = 7.5$ cm, the core-braid structure has achieved its maximum amplitude but no interactions have as yet occurred. At this point, $\lambda^* \cong .25 - .3$, and hence Corcos and Sherman's work would predict that a pairing is possible. This, in fact, is what occurs, as can be seen in the next two photographs at $x = 10$ and 12.5 cm. However, the subharmonic produced by

this interaction should not be able to pair, and this too is what is observed to happen. Referring to figure 25, it is seen that at x = 17 cm, the core-braid amplitude has equilibrated, and no interactions have occurred. The value of λ^* at this point is about .4 - .45, and thus the theory would predict that a pairing is not possible. Examination of figure 25 at x = 22 and 25 cm shows that the model has again correctly predicted the outcome of the experiment.

A more quantitative test of the theoretical analysis would be to compare the value of H^*_{max} with that of Ri_{max} which has been measured in the present experiment. One must be aware, however, that although Ri_{max} and H^*_{max} are related, the length scales upon which each is based are slightly different; Ri_{max} being defined by the maximum slope thickness of the density profile while H^*_{max} is based upon the maximum vertical displacement of the isopycnal surfaces (note also that Ri_{max} is normalized by the total shear, while H^*_{max} is defined in terms of $\Delta U/2$). In general, there is no simple relation between the two lengths, but it is anticipated that the disparity between 2H and the maximum slope thickness will not be large. Thus, it will be assumed that such a relation between the two lengths exists. The results of the model (accounting for the factor of 2 difference in definition) are shown in figure 54b. It is seen here that the maximum predicted value of Ri_{max} lies between $.35 < Ri_{max} < .39$. This is in excellent agreement with the measured data of cases A, C and D, where vortex formation

and pairing are believed to be occurring, which show that $.32 < Ri_{max} < .35$. Considering the simplifications inherent in the model and the difference in length scales used to define the equilibrium amplitude, such close agreement is quite remarkable. Thus, the theory and the results of three independent experiments all predict the very important result that when vortex formation and subharmonic interactions are the mechanisms by which the stratified mixing layer grows, the maximum attainable thickness is characterized by a critical value of the quantity Ri_{max} equal to about .35. It is worth noting that for Ri_{h_o} greater than about .12, the above mechanisms of shear layer growth are replaced by interfacial wave breaking, as observed in figure 26, and no adequate theory has as yet been developed which can predict the limiting thickness of the mixing region for these cases.

Before concluding this section on the gross features of the mixing layer development, it is felt that the subject of a mean gradient Richardson number, a quantity frequently found in the literature, should be discussed. Thorpe (1973) has suggested that the final state of his mixing layer experiment is characterized by a critical value of the parameter

$$Ri_G = \frac{g}{\rho_o} \frac{\Delta\rho}{h_\rho} \frac{1}{\left(\frac{\Delta U}{h_u}\right)^2}$$

which is found to be equal to $.322 \pm .063$, based upon 15 observations for $t/\tau > 12$. This result has been used by Garrett and Munk (1972)

while investigating the predominance of such Kelvin-Helmholtz induced turbulence in the oceanic thermocline.

Because of the many similarities between the present experiment and that of Thorpe's, it is naturally of interest to investigate the behavior of this parameter in the present study. It is anticipated at the outset, however, that based upon much of the previous discussion, the character of Ri_G is going to be difficult to interpret. It has been noted already that both θ_u and θ_ρ are very much affected by dissipative mechanisms subsequent to the collapse of the large scale structure. In particular, it has been shown that the length scale associated with the density profile decreases after the collapse, due to the action of buoyancy upon unmixed fluid within the mixing region. It has also been discussed how in this same stage of the mixing process, the momentum thickness continues to increase due to the energy transfer from the mean flow to the turbulence (which must be dissipated eventually). It is not clear, therefore, that a parameter which measures θ_u^2/θ_ρ in the final stage of the turbulent event should be characteristic of this mixing process independent of the Reynolds number and Rayleigh number in the turbulent layer following the collapse, or the diffusion rate measured by the Schmidt number. Clearly, for immiscible fluids ($S_c = \infty$), this result must be invalid.

With these comments noted, the quantity Ri_G, defined for the present experiment as

$$Ri_G = \frac{g}{\rho_o} \frac{\Delta\rho}{\theta_\rho} \frac{1}{\left(\frac{\Delta U}{\theta_u}\right)^2}$$

is presented in figure 55 plotted versus t/τ. It is seen here that very close to the splitter plate, Ri_G is large, due to the initial disparity in length scales in the laminar portion of the shear layer. However, once the mixing begins, Ri_G achieves a local minimum and begins to increase. At about $t/\tau = 6$ it is seen that there is no characteristic feature of the Ri_G distribution which identifies this point as the location where the large scale vortex structure is destroyed by buoyancy. To the contrary, it is observed that Ri_G continues to increase well past this point, as a result of θ_ρ decreasing and θ_u increasing subsequent to the colapsed. It is also found that at the last usable measuring station, before the bottom boundary layer becomes troublesome (typically at $t/\tau = 15$-20), the local value of Ri_G varies between the extremely wide range of about .2-1.2, over the range of initial Richardson numbers investigated. Thus, it is found that the end state of the present experiment is not at all characterized by a critical value of the mean graident Richardson number. As a point of reference, Thorpe's result (scaled by a factor of 1/5 to roughly convert from the maximum slope thickness to momentum thickness) is found to be significantly smaller than all of the present data.

It is not at all unreasonable that the present high Richardson number experiments (cases E, J and L) should be in disagreement with the data of Thorpe, due to the difference in important physical processes prevalent in this Richardson number regime, as has been noted numerous times. However, up to this point, there has been

fairly good agreement between the low Richardson number experiments (cases A, C and D) and Thorpe's work, and it is interesting that so large a discrepancy in Ri_G should exist. It is clear that the disparity must lie in the value of the velocity length scale, since from figure 54b it is seen that the density length scales for the two studies are fairly compatible. Figure 56 presents the ratio θ_u/θ_ρ plotted versus t/τ, along with the similar data of Thorpe. It is seen here that for the low Ri_{h_o} experiments, the velocity scale may be nearly three times as large as that of the density, while at the higher Richardson numbers, θ_u/θ_ρ can be as large as 10. Contrasted with this is Thorpe's results which show that for all of his measurements, the velocity scale never exceeds the density scale by more than 40%. The explanation for this difference in velocity scales between the two experiments is not known, but it is almost certainly related to the turbulence production and diffusion processes prevalent in the mixing layer following the demise of the large scale vorticies.

The point to be made from all of these results is that, for the present experiment, Ri_G is not a very useful way of describing either the point of large scale collapse or the final state of the mixing region. It is felt that more understanding of the character of the mixing process results from investigating how θ_u and θ_ρ individually evolve by vortex generation and interactions prior to the collapse, and after this point by the dissipative mechanisms which have been discussed.

6.7 Summary of Principle Findings

Because of the distinct dynamical difference between the low Richardson number cases, where vortex formation and pairing are predominant, and the high Richardson number experiments, where the mixing proceeds by interfacial wave breaking, the two processes are summarized separately in sections 6.7.1 and 6.7.2, respectively.

6.7.1 Low Richardson number experiments

On the basis of the results obtained in this investigation, the following description of the evolution of the mixing layer applies for low initial Richardson numbers.

Very close to the end of the splitter plate, where the two streams are merged, the shear layer is in a laminar state. Within this region, due to the disparity in diffusion rates, the momentum thickness grows more rapidly than does the salinity layer. In addition to this, the geometry of the experimental apparatus at the test section entrance introduces a large difference in velocity and density length scales. As a result of this initial difference in length scales, the instability which develops in this laminar region is well-described by the linear theories of Holmboe (1962) and Hazel (1972). This instability becomes nonlinear within 1-3 of the initial wavelengths, and the character of these finite amplitude waves is to roll up and form a series of discreet vorticies. For sufficiently small Richardson numbers, the vorticies may interact, or pair. For these cases, the growth of the mixing

layer is very similar to the unstratified mixing layer, in that the mean velocity profile compares well with the Liepmann and Laufer (1947) data, and the growth rate compares well with that of Spencer and Jones (1971). However, during this early turbulent growth period very little molecular diffusion occurs, so that the probability distribution function $P_\rho(\rho, \rho + \delta\rho; z)$ in this region has a bimodal character. In addition, the density fluctuation level in this region is almost as large as the maximum possible value of .5, and the mixedness parameter is quite small. During this phase of the mixing, both the mean kinetic energy loss and the mean potential energy gain are increasing with the longitudinal coordinate.

After roughly 6-7 buoyancy periods, the large scale entrainment mechanisms responsible for the initial growth are disrupted by the stratification at a point where $Ri_{max} \cong .35$. This critical value of Ri_{max}, which characterizes the maximum shear layer thickness, is in very good agreement with the theoretical analysis of Corcos and Sherman (1976) and the numerical calculations of Corcos (private communication), and the experimental results of Thorpe (1973) and Hopfinger (1972).

Beyond this location, the layer ceases to grow, and θ_ρ decreases from its maximum value at a rate which is controlled by diffusive processes. It is at this point that the mixedness increases substantially, and the density fluctuation amplitude decreases due to the $\overline{\rho' w'}$ correlation generated by the collapsing process. This term is also responsible for the continued mean energy

loss beyond the collapse point, which results in a change in shape of the mean velocity profile. However, as the layer relaxes to its final state, the turbulence created by the destruction of the large scale structures evolves into a flow field more closely characterized by an internal wave field, so that the $\overline{\rho' w'}$ correlation decreases, and the mean kinetic energy decrement approaches a constant value. The final state of the density field is determined by how much molecular diffusion has occurred since the large scale collapse, and this is affected by the buoyancy which acts to limit the amount of time available for such diffusion to occur.

6.7.2 High Richardson number experiments

For the high Richardson number experiments, the laminar shear layer which forms downstream of the splitter plate is not really affected by the increased buoyancy, and hence evolves in much the same manner as in the low Ri_{h_o} cases. However, the instability which develops from this laminar region is distinctly different from what has been previously described, and this has been identified as the mode II branch of the linear stability problem. For these cases, the mixing is seen to proceed by breaking at the crests of interfacial waves, rather than by vortex pairing. The layer thickness, as defined by the density field, increases initially, but beyond about $x/\theta_o \cong 200$, this length scale is more or less maintained at a constant value. This behavior is contrasted with the momentum thickness which continues to increase until $x/\theta_o = 800$,

indicating that this interfacial wave breaking is constantly extracting kinetic energy from the mean flow. Also in this region, the density fluctuations are found to be quite large (about .4), and the mixedness remains at the relatively low level of about .2. These conditions do not change a greal deal as the end of the test section is approached, although there is a slight tendancy toward increased mixedness and decreased rms level of the density fluctuations. It is noted, however, that for these cases the amount of mean potential energy gained is quite small, and it is believed that about 95-98% of all the kinetic energy lost by the shearing motion is dissipated.

6.8 Recommendations for Future Work

One of the interesting results to emerge from this study is the observation that a critical value of Ri_{max} exists which characterizes how large the shear layer can grow by the mechanisms of vortex generation and pairing. That this observation is in good agreement with theoretical models is extremely interesting, and further experimental study in this area would be useful. In particular, it would be very enlightening to use the conditional sampling techniques employed by Browand and Weidman (1975) to determine the density and vorticity field at the point of collapse. These results could be used in conjunction with the numerical calculations to give a detailed account of what limits the growth of finite amplitude Kelvin-Helmholtz structures in the presence of stratification.

Secondly, the diffusive mechanisms which persist subsequent to the collapse appear to be very important in determining the structure of the final mixed layer. The detailed dynamical processes important within this region of the flow are extremely complex, due to the interaction of viscous effects, molecular diffusion, shear driven turbulence and turbulence produced as a result of free convection. In addition, these processes are not decoupled from the large scale vortex interactions just discussed. However, in oceanographic and meteorological problems, the extent of permanent vertical transport of important physical quantities as a result of a "turbulent event" like the one studied in this investigation, is of ultimate significance. Thus, it is felt that further study of the details of the diffusive processes prevalent in the collapsed structure is warranted. Careful attention should be paid to the length scales which are produced in this region of the flow field, so that one has sufficient information to estimate the amount of mixed fluid which will result from a particular "turbulent event."

Finally, the means by which mixing occurs at high Richardson numbers has not been explored in great detail in this study. Much more work remains before adequate understanding of these processes will be obtained.

REFERENCES

(1) Atlas, D., Metcalf, J., Richter, J. and Gossard, E. (1970), The Birth of 'CAT' and Microscale Turbulence," J. Atmos. Science, 27, p. 903.

(2) Batchelor, G. K. (1970), An Introduction to Fluid Mechanics, Cambridge University Press, London.

(3) Benney, D. J. and Bergeron, R. F. (1969), "A New Class of Nonlinear Waves in Parallel Flows," Studies in App. Math., 48, p. 181.

(4) Browand, F. K. (1966), "An Experimental Investigation of the Instability of an Incompressible, Separated Shear Layer," J. Fluid Mechanics, 26, p. 281.

(5) Browand, F. K. and Koop, C. G. (1976), In preparation.

(6) Browand, F. K. and Wang, Y. H. (1972), "An Experiment on the Growth of Small Disturbances at the Interface Between Two Streams of Different Densities and Velocities," International Symposium on Stratified Flows, Novosibirsk.

(7) Browand, F. K. and Weidman, P. D. (1976), "Large Scales in the Developing Mixing Layer," To appear in J. Fluid Mechanics.

(8) Browand, F. K. and Winant, C. D. (1973), "Laboratory Observations of Shear-Layer Instability in a Stratified Fluid," Boundary Layer Met., 5, p. 67.

(9) Brown, G. and Roshko, A. (1974), "On Density Effects and Large Structure in Turbulent Mixing Layers," J. Fluid Mechanics, 64, p. 775.

(10) Browning, K. A. (1971), "Structure of the Atmosphere in the Vicinity of Large-Amplitude Kelvin-Helmholtz Billows," Quart. J. Roy. Met. Soc., 97, p. 283.

(11) Browning, K. A. and Watkins, C. D. (1970), "Observations of Clear Air Turbulence by High Power Radar," Nature, 227, p. 260.

(12) Bush, W. and Fendell, F. (1974), "On Diffusion Flames in Turbulent Shear Flows," J. International Academy of Astronautics, 1, p. 645.

(13) Clark, J. W. and Stoeffler, R. C. (1972), "Fluid Mechanics and Meteorological Studies Directed Toward Improved Understanding of CAT," IUCRM Symposium, Scripps Institute, La Jolla, California.

(14) Corcos, G. and Sherman, F. (1976), "Vorticity Concentrations and the Dynamics of Unstable Free Shear Layers," To appear in J. Fluid Mechanics.

(15) Delisi, D. and Corcos, G. (1973), "A Study of Internal Waves in a Wind Tunnel," Boundary Layer Met., 5, p. 121.

(16) Drazin, P. and Howard, L. (1966), "Hydrodynamic Stability of Parallel Flow of Inviscid Fluid," Adv. App. Math., 9, p. 1.

(17) Fiedler, H. (1974), "Transport of Heat Across a Plane Turbulent Mixing Layer," Adv. in Geophysics, 18, p. 93.

(18) Fleagle, R. G. (1969), "The Significance of Clear Air Turbulence in Large Scale Meteorology," Clear Air Turbulence and its Detection, Plenum Press, N.Y., p. 1.

(19) Freymuth, P. (1966), "On Transition in a Separated Boundary Layer," J. Fluid Mechanics, 25, p. 683.

(20) Garrett, C. and Munk, W. (1972), "Oceanic Mixing by Breaking Internal Waves," Deep Sea Research, 19, p. 823.

(21) Gaster, M. (1962), "A Note on the Relation Between Temporally-Increasing and Spatially-Increasing Disturbances in

Hydrodynamic Stability," J. Fluid Mechanics, 14, p. 222.

(22) Gibson, C. H. and Swartz, W. H. (1963), "Detection of Conductivity Fluctuations in a Turbulent Flow Field," J. Fluid Mechanics, 16, p. 357.

(23) Grant, H. L., Moilliet, A. and Vogel, W. M. (1962), "Some Observations of the Occurrence of Turbulence in and Above the Thermocline," J. Fluid Mechanics, 34, p. 443.

(24) Hazel, P. (1972), "Numerical Studies of the Stability of Inviscid Stratified Shear Flows," J. Fluid Mechanics, 51, p. 39.

(25) Helmholtz, H. (1868), "Ueber Discontinuirliche Flüssigkeitsbewegungen," Berl. Monatsber.

(26) Hinze, J. O. (1959), Turbulence: An Introduction to its Mechanism and Theory, McGraw-Hill Book Co., N.Y.

(27) Holmboe, J. (1962), "On the Behavior of Symmetric Waves in Stratified Shear Layers," Geofys. Publ., 24, p. 67.

(28) Hopfinger, E. S. (1972), "Development of a Stratified Shear Flow," International Symposium on Stratified Flows, Novosibirsk, U.S.S.R.

(29) Hottel, H. and Hawthorne, W., "Diffusion Flames and Their Breakdown," Third Symposium on Combustion, Flame, and Explosion Phenomena, Williams and Wilkins, Baltimore, Maryland, p. 254.

(30) Kelly, R. E. (1967), "On the Stability of an Inviscid Shear Layer which is Periodic in Space and Time," J. Fluid Mechanics, 27, p. 657.

(31) Kelly, R. E. and Maslowe, S. A. (1972), "The Nonlinear Critical Layer in a Slightly Stratified Shear Flow," Studies in App. Math., 49, p. 301.

(32) Kelvin, Lord (1887), "Rectilinear Motion of Viscous Fluid Between Two Parallel Planes," Phil. Mag., 24, p. 188.

(33) Lamb, Sir Horace (1932), Hydrodynamics, 6th edition, Dover Publications, N.Y.

(34) Lau, Y. L. and Baines, W. D. (1968), "Flow of Stratified Fluid Through Curved Screens," J. Fluid Mechanics, 33, p. 721.

(35) Lazier, J. (1973), "Temporal Changes in Some Fresh Water Temperature Structures," J. Phys. Ocean., 3, p. 226.

(36) Libby, P. and Williams, F. (1976), "Turbulent Flows Involving Chemical Reactions," Ann. Rev. Fluid Mech., 8, p. 351.

(37) Liepmann, H. W. and Laufer, J. L. (1947), "Investigation of Free Turbulent Mixing," N.A.C.A. Tech. Note No. 1257.

(38) Lin, J. T. and Veenhuizen, S. (1974), "Measurements of the Decay of Grid Generated Turbulence in a Stably Stratified Fluid," Bull. Am. Phys. Soc., 19, p. 1142.

(39) Locke, R. C. (1950), "The Velocity Distribution in the Laminar Boundary Layer Between Parallel Streams," Quart. J. Mech. and App. Math., 4, p. 42.

(40) Maxworthy, T. and Browand, F. (1975), "Experiments in Rotating and Stratified Flows - With Oceanographic Applications," Ann. Review Fluid Mech., 7, p. 273.

(41) Maslowe, S. A. (1973), "Finite-Amplitude Kelvin-Helmholtz Billows," Boundary Layer Met., 5, p. 43.

(42) Maslowe, S. A. and Thompson, J. M. (1971), "Stability of a Stratified Free Shear Layer," Phys. Fluids, 14, p. 453.

(43) Michalke, A. (1970), "The Instability of Free Shear Layers: A Survey of the State of the Art," Deutsche Forschungs und Versuchsanstalt Für Luft-und Raumfahrt.

(44) Miksad, R. W. (1972), "Experiments on the Nonlinear Stages of Free-Shear-Layer Transitions," J. Fluid Mechanics, 56, p. 695.

(45) Naysmyth, P. W. (1970), "Ocean Turbulence," Ph.D. Thesis, University of British Columbia.

(46) Osborne, T. and Cox, C. (1972), "Oceanic Fine Structure," Geophys. Fluid Dynamics, 3, p. 321.

(47) Osborne, T. and Sidden, T. (1973), Proc. Third Biennial Sym. on Turbulence in Liquids, Rolla, Mo.

(48) Patnaik, P. (1973), "A Numerical Study of Finite-Amplitude Kelvin-Helmholtz Waves," Ph.D. Dissertation, University of California, Berkeley.

(49) Prych, E. A., Harty, F. R. and Kennedy, J. F. (1964), "Turbulent Wakes in Density Stratified Fluids of Finite Extent," Hydrodynamics Laboratory Report No. 65, NIT.

(50) Rayleigh, Lord (1878-1919), Scientific Papers, 1, p. 286.

(51) Rosenhead, L. (1931), "The Formation of Vorticies From a Surface of Discontinuity," Proc. Roy. Soc. A, 134, p. 170.

(52) Rossby, H. T. (1969), "A Study of Benard Convection with and Without Rotation," J. Fluid Mechanics, 36, p. 309.

(53) Scotti, R. S. and Corcos, G. M. (1973), "Measurements of the Growth of Small Disturbances in a Stratified Shear Layer," Radio Sci., 4, p. 1309.

(54) Sherman, F. S. (1975), "The Dynamics of Unstable Free Shear Layers - Effects of Buoyancy and Nonlinear Interaction," Survey Lecture for XII Symposium in Fluid Mechanics, Bialowieza, Poland.

(55) Spencer, B. W. and Jones, B. G. (1971), "Statistical Investigation of Pressure and Velocity Fields in the Turbulent Two-Stream Mixing Layer," AIAA 4th Fluid and Plasma Dynamics Conference, Paper Number 71-613, Palo Alto, California.

(56) Simpson, J. H. (1972), "A Free-Fall Probe for the Measurement of Velocity Microstructure," Deep-Sea Research, 19, p. 331.

(57) Simpson, J. H. and Woods, J. D. (1970), "Temperature Microstructure in a Fresh Water Thermocline," Nature, 226, p. 832.

(58) Stommel, H. and Federov, K. N. (1967), "Small Scale Structure in Temperature and Salinity Near Timor and Mindanao," Tellus, 19, p. 306.

(59) Storm, E., Konrad, J. and Roshko, A. (1974), "Unmixedness in Turbulent Mixing Layers," Bull. Am. Phy. Soc., 19, p. 1151.

(60) Stuart, J. T. (1967), "On Finite Amplitude Oscillations in Laminar Mixing Layers," J. Fluid Mechanics, 29, p. 417.

(61) Tennekes, H. and Lumley, J. L. (1972), A First Course in Turbulence, MIT Press, Cambridge, Mass.

(62) Thorpe, S. A. (1972), "Turbulence in Stably Stratified Fluids: A Review of Laboratory Experiments," Boundary Layer Met., 5, p. 95.

(63) Thorpe, S. A. (1973), "Experiments of Instability and Turbulence in a Stratified Shear Flow," J. Fluid Mechanics, 61, p. 731.

(64) Turner, J. S. (1973), Buoyancy Effects in Fluids, Cambridge University Press, London.

(65) Wang, Y. (1971), "An Experimental Study of a Discontinuously Stratified Shear Layer," Ph.D. Dissertation, Dept. Aerospace

Eng., University Southern California, Los Angeles.

(66) Williams, R. B. and Gibson, C. (1974), "Direct Measurements of Turbulence in the Pacific Equitorial Undercurrent," J. Phys. Ocean, 4, p. 104.

(67) Winant, C. (1973), "Vortex Pairing in a Turbulent Shear Layer at Moderate Reynolds Numbers," Ph.D. Dissertation, Dept. Aerospace Eng., University Southern California, Los Angeles.

(68) Winant, C. D. and Browand, F. K. (1974), "Vortex Pairing: The Mechanism of Turbulent Mixing-Layer Growth at Moderate Reynolds Numbers," J. Fluid Mechanics, 63, p. 237.

(69) Wohl, K., Gazley, C. and Kapp, N., "Diffusion Flames," Third Symposium on Combustion, Flame, and Explosion Phenomena, Williams and Wilkins, Baltimore, Md., p. 258.

(70) Woods, J. D. (1968), "Wave Induced Shear Instability in the Summer Thermocline," J. Fluid Mechanics, 32, p. 791.

(71) Woods, J. D. and Wiley, R. L. (1972), "Billow Turbulence and Ocean Microstructure," Deep-Sea Res., 19, p. 87.

TABLE 1

EXPERIMENTAL TEST CONDITIONS FOR

RICHARDSON NUMBER EXPERIMENTS

U_T = 3.2 cm/sec
U_B = 10.95 cm/sec

θ_o = .0763 cm
$h_o \cong$ .38 cm

Re_{θ_o} = 60
Re_{h_o} = 300

Case A		Case C		Case D		Case E		Case J		Case L	
$\frac{\Delta\rho}{\rho}$ = .0085		$\frac{\Delta\rho}{\rho}$ = .0128		$\frac{\Delta\rho}{\rho}$ = .0170		$\frac{\Delta\rho}{\rho}$ = .0213		$\frac{\Delta\rho}{\rho}$ = .0255		$\frac{\Delta\rho}{\rho}$ = .034	
Ri_{θ_o} = .010		Ri_{θ_o} = .015		Ri_{θ_o} = .020		Ri_{θ_o} = .025		Ri_{θ_o} = .030		Ri_{θ_o} = .040	
Ri_{h_o} = .050		Ri_{h_o} = .075		Ri_{h_o} = .100		Ri_{h_o} = .125		Ri_{h_o} = .150		Ri_{h_o} = .200	
x/θ_o	t/τ	x/θ_o	t/τ	x/θ_o	t/τ	x/θ_o	t/τ	x/θ_o	t/τ	x/θ_o	t/τ
173	2	115	2	87	2	104	3	57	2	91	4
258	3	173	3	130	3	138	4	86	3	114	5
343	4	229	4	173	4	173	5	115	4	137	6
430	5	287	5	216	5	207	6	144	5	171	7.5
516	6	343	6	259	6	259	7.5	173	6	205	9
646	7.5	430	7.5	324	7.5	311	9	215	7.5	240	10.5
775	9	516	9	388	9	362	10.5	259	9	274	12
904	10.5	603	10.5	453	10.5	414	12	345	12	342	15
1121	13	691	12	519	12	518	15	431	15	457	20
1291	15	862	15	646	15	691	20	575	20	685	30
		1149	20	864	20	1035	30	862	30	1027	45
		1723	30	1291	30			1436	50	1370	60

TABLE 2

EXPERIMENTAL TEST CONDITIONS FOR

REYNOLDS NUMBER EXPERIMENTS

$Ri_{\theta_o} = .015$				$Ri_{h_o} = .075$			
Case G $\frac{\Delta\rho}{\rho} = .0037$ $\theta_o = .0902$ cm $U_T = 1.90$ cm/sec $U_B = 6.50$ cm/sec $Re_{\theta_o} = 40$ $Re_{h_{max}} \cong 1000$		Case F $\frac{\Delta\rho}{\rho} = .0084$ $\theta_o = .080$ cm $U_T = 2.68$ cm/sec $U_B = 9.18$ cm/sec $Re_{\theta_o} = 50$ $Re_{h_{max}} \cong 1250$		Case C $\frac{\Delta\rho}{\rho} = .0128$ $\theta_o = .0763$ cm $U_T = 3.2$ cm/sec $U_B = 10.9$ cm/sec $Re_{\theta_o} = 60$ $Re_{h_{max}} \cong 1500$		Case I $\frac{\Delta\rho}{\rho} = .0238$ $\theta_o = .064$ cm $U_T = 4.25$ cm/sec $U_B = 14.6$ cm/sec $Re_{\theta_o} = 70$ $Re_{h_{max}} \cong 1750$	
x/θ_o	t/τ	x/θ_o	t/τ	x/θ_o	t/τ	x/θ_o	t/τ
118	2	117	2	115	2	130	2
177	3	176	3	173	3	194	3
236	4	234	4	229	4	259	4
294	5	293	5	287	5	324	5
353	6	351	6	343	6	389	6
442	7.5	439	7.5	430	7.5	486	7.5
530	9	527	9	516	9	583	9
618	10.5	615	10.5	603	10.5	680	10.5
707	12	702	12	691	12	777	12
883	15	878	15	862	15	972	15
1178	20	1171	20	1149	20	1295	20
1766	30	1756	30	1723	30	1943	30

TABLE 3

MATRIX OF TEST CONDITIONS FOR RICHARDSON NUMBER AND REYNOLDS NUMBER EXPERIMENTS

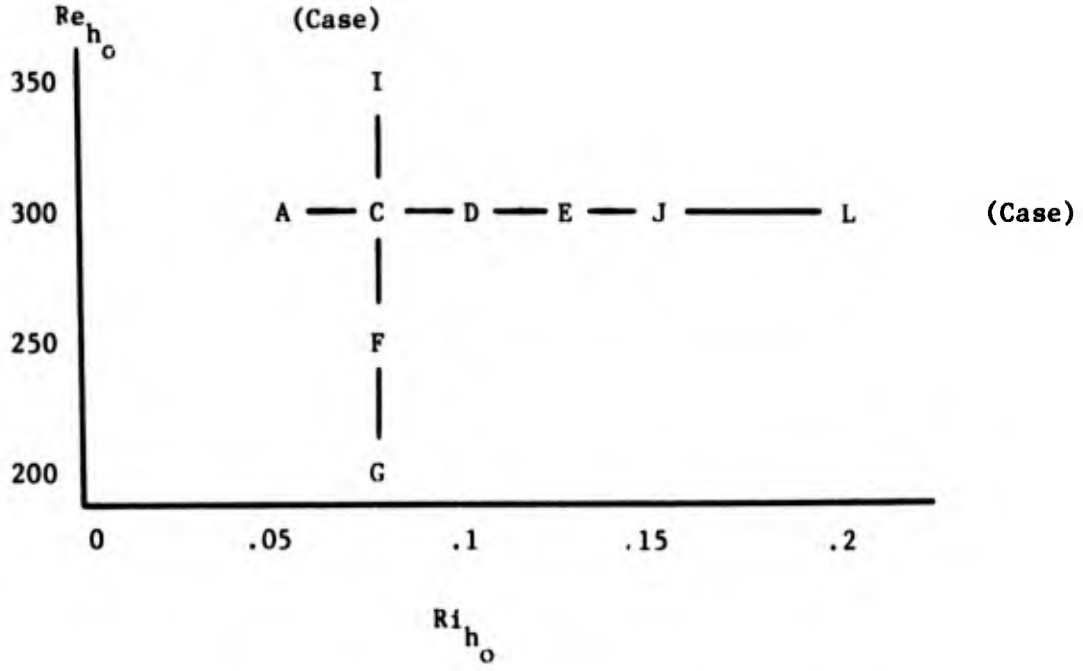

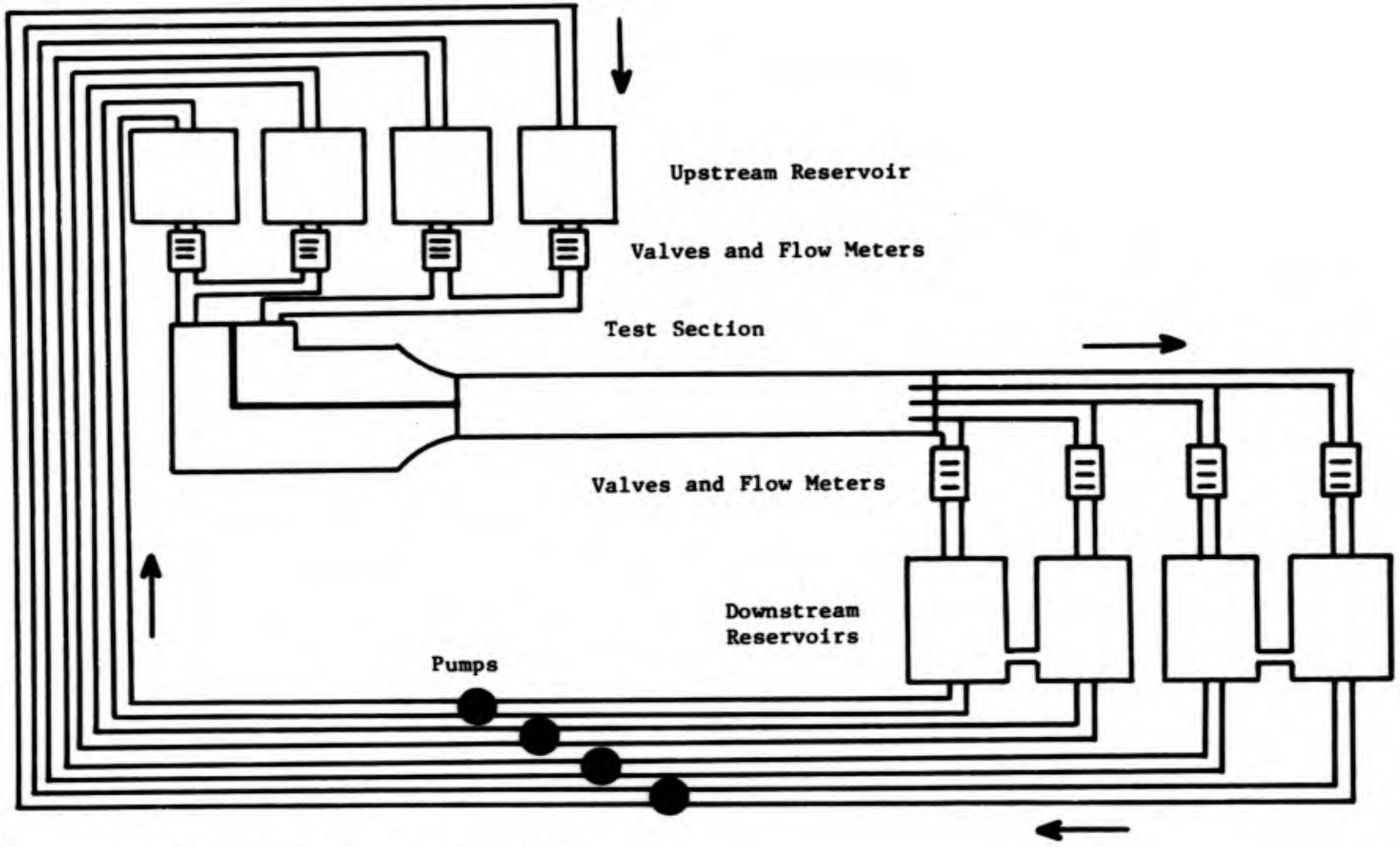

Figure 1: Schematic of Facility

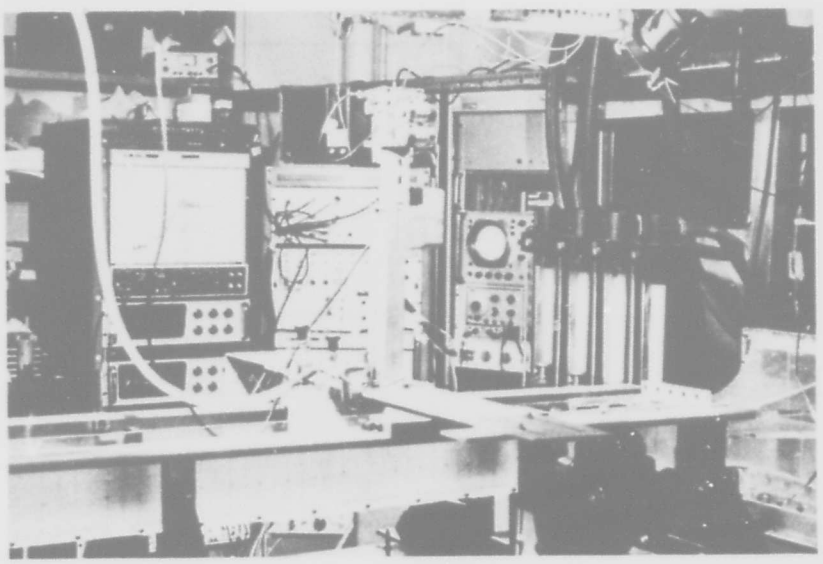

(a) Test Section

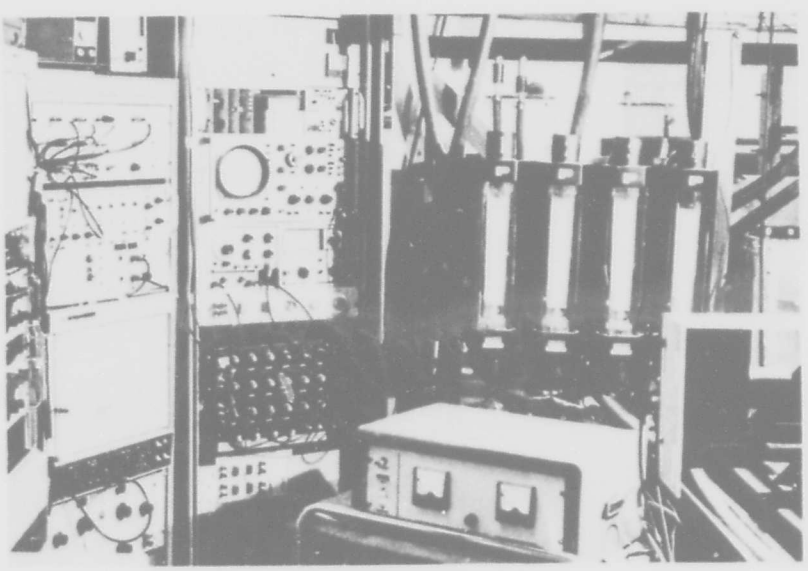

(b) Instrumentation

Figure 2: Photographs of Facility.

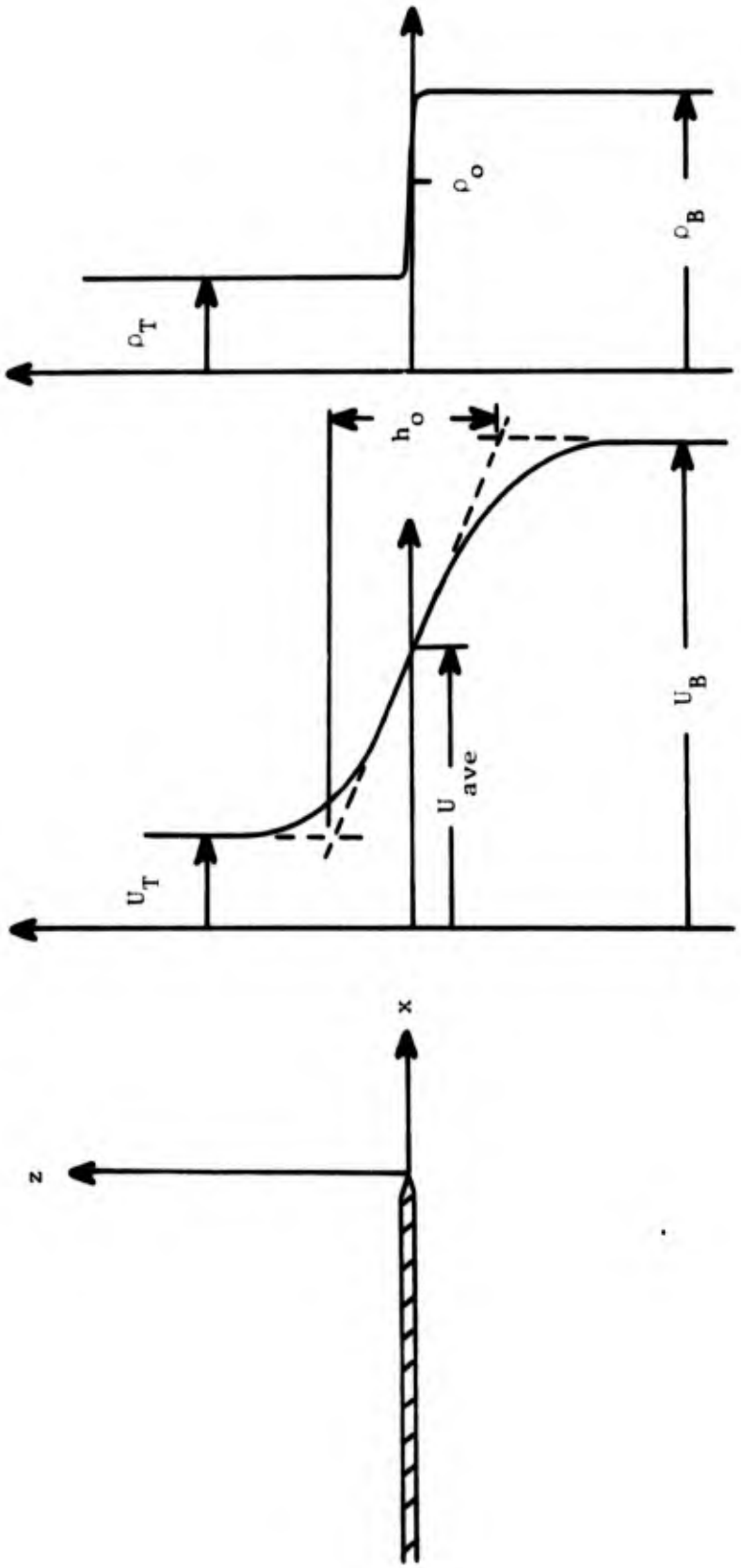

Figure 3: Initial Shear Layer Geometry.

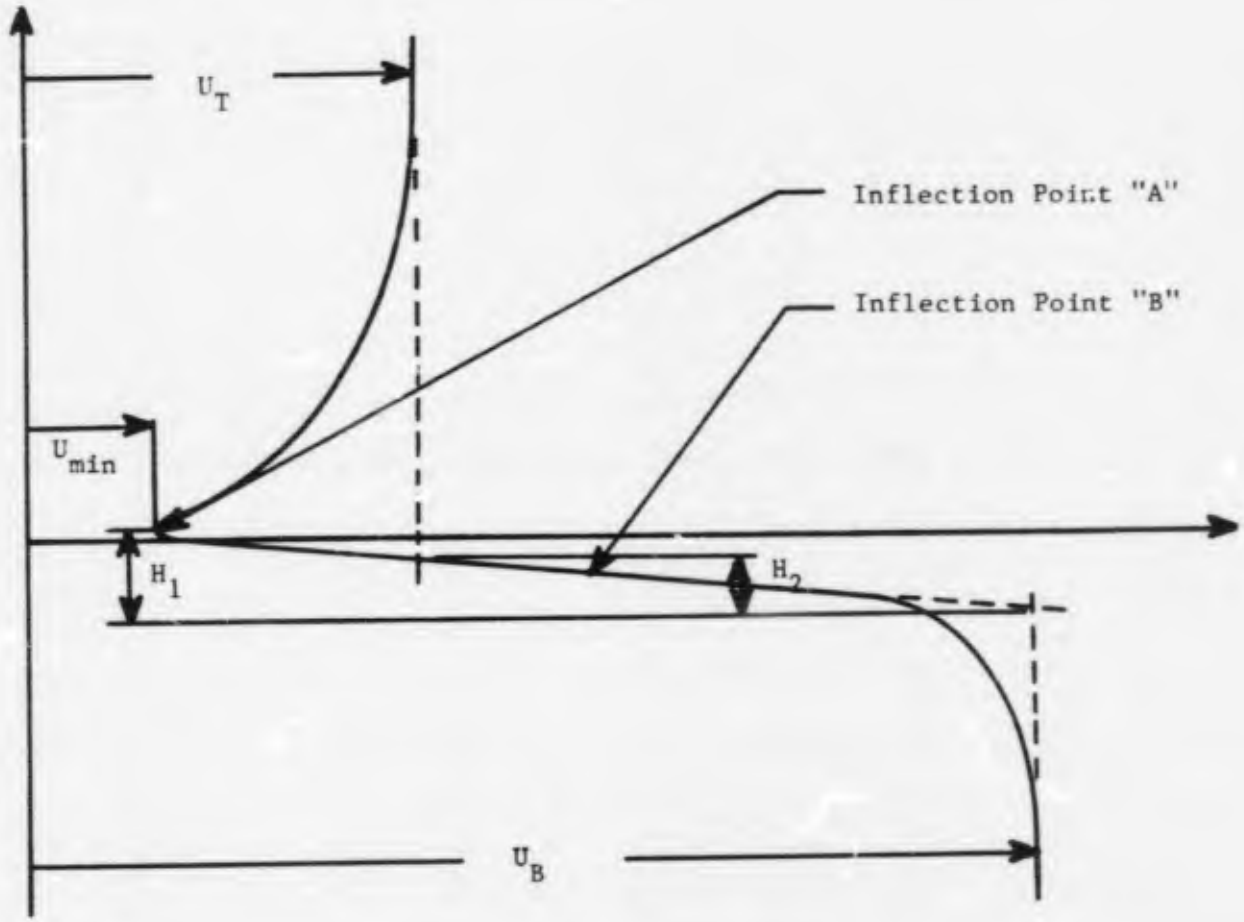

Figure 4: Sketch of a Doubly Inflectional Velocity Profile

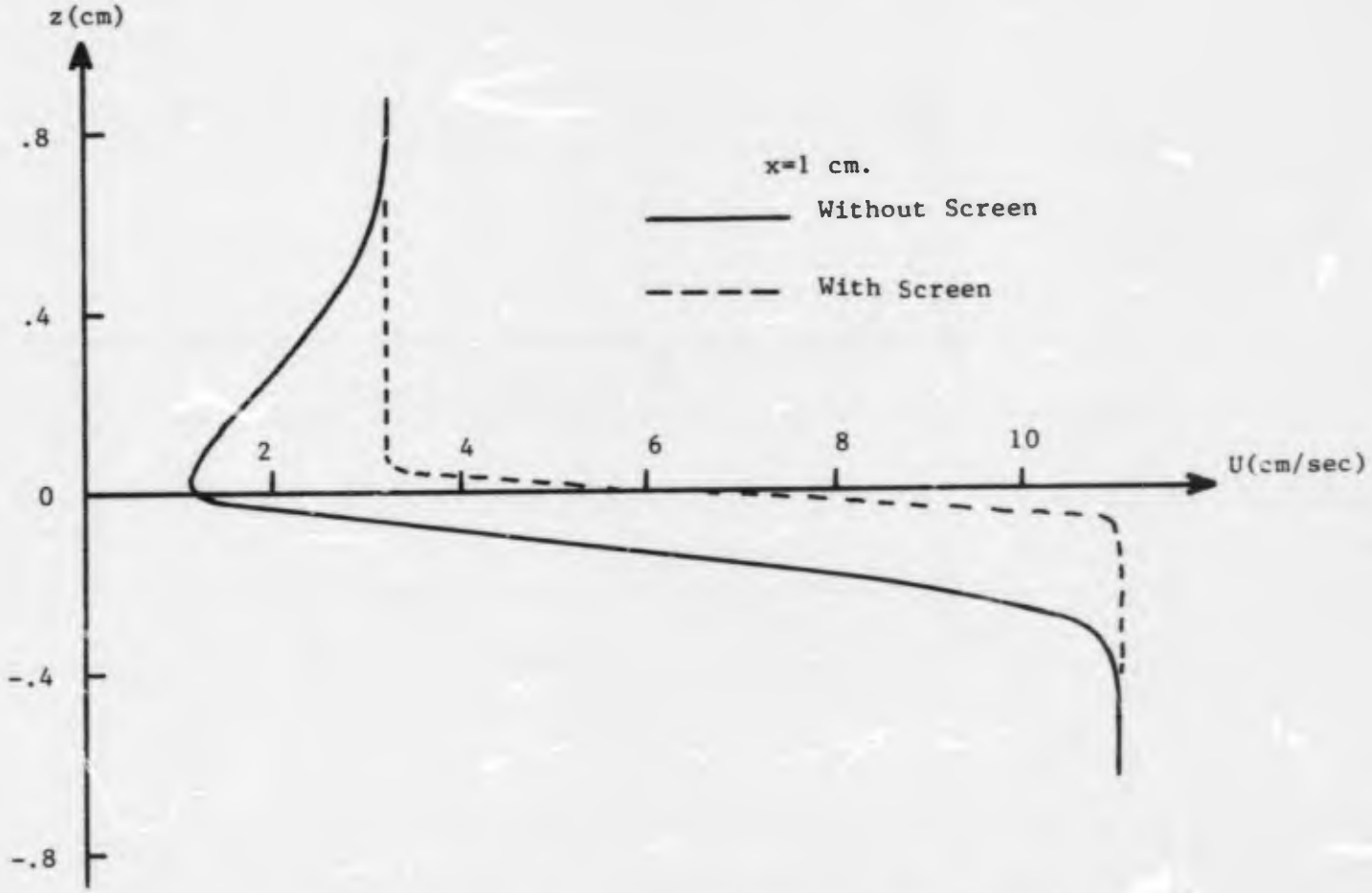

Figure 5: Effect of Fine Mesh Screen Upon Initial Shear Layer Velocity Profile.

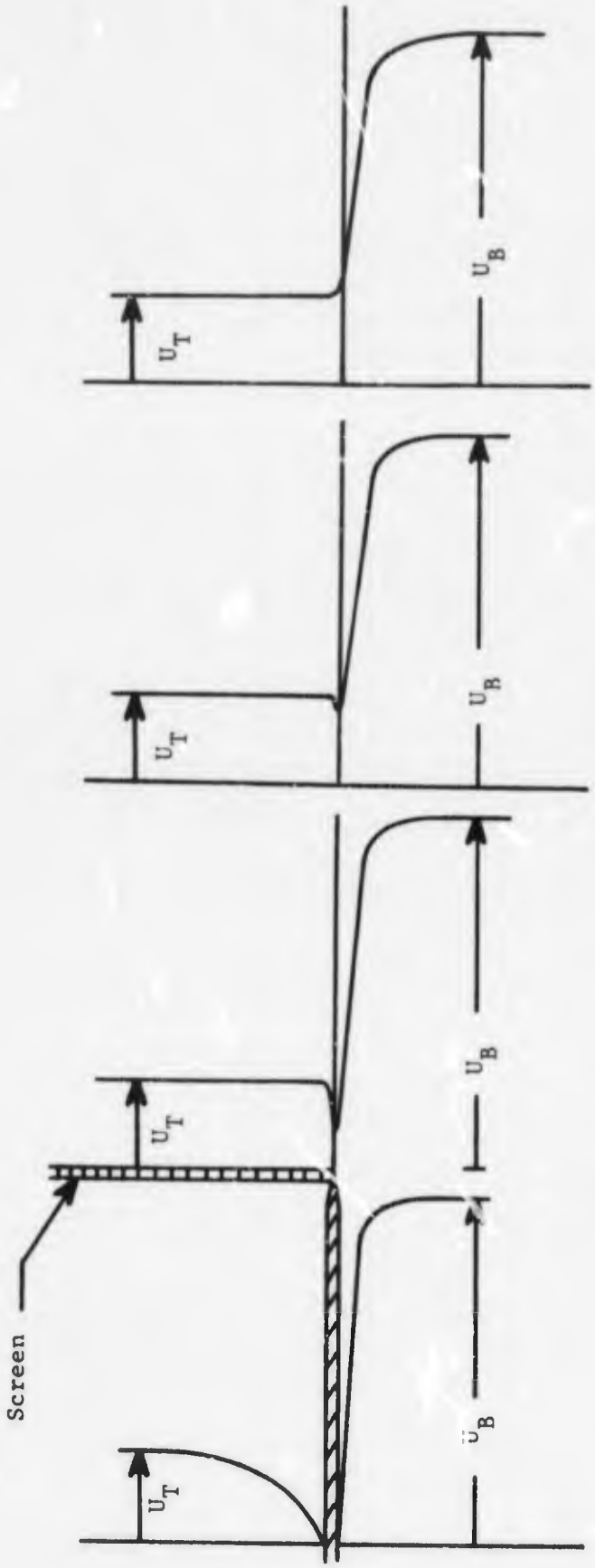

Figure 6: Effect of Half Screen Configuration
(a conceptualization)

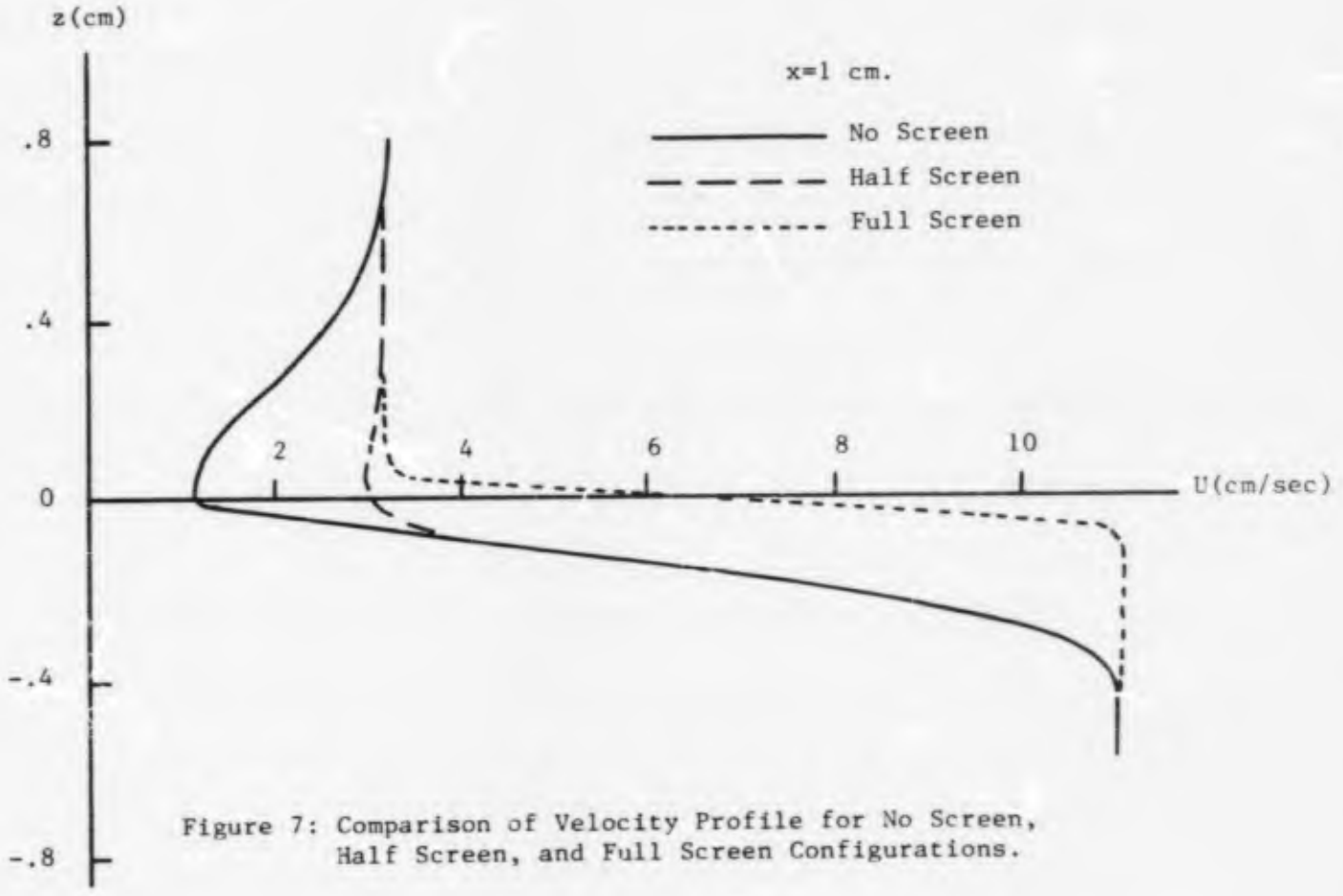

Figure 7: Comparison of Velocity Profile for No Screen, Half Screen, and Full Screen Configurations.

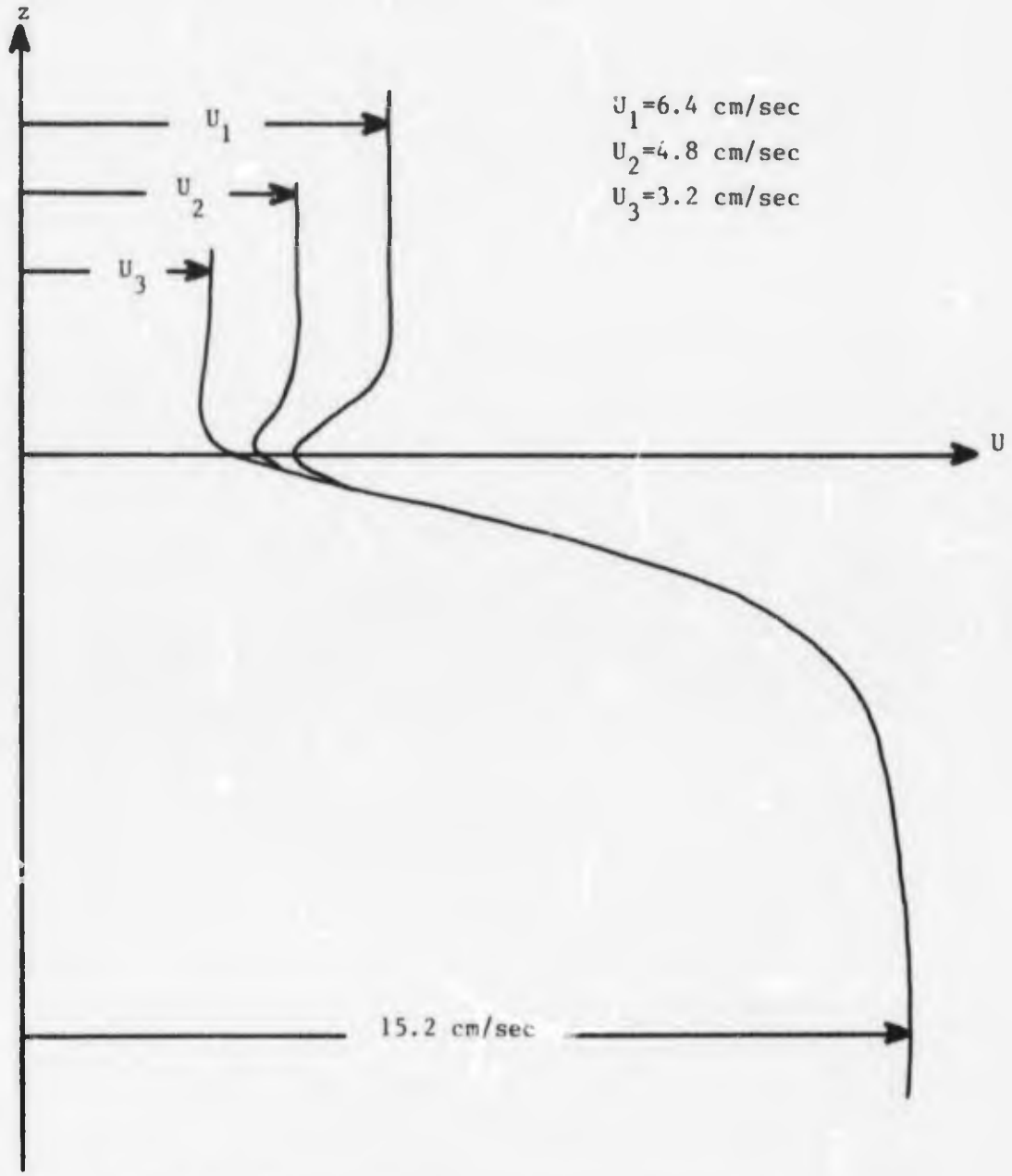

Figure 8: Effect of U_T Upon Velocity Profile for Half Screen Configuration.

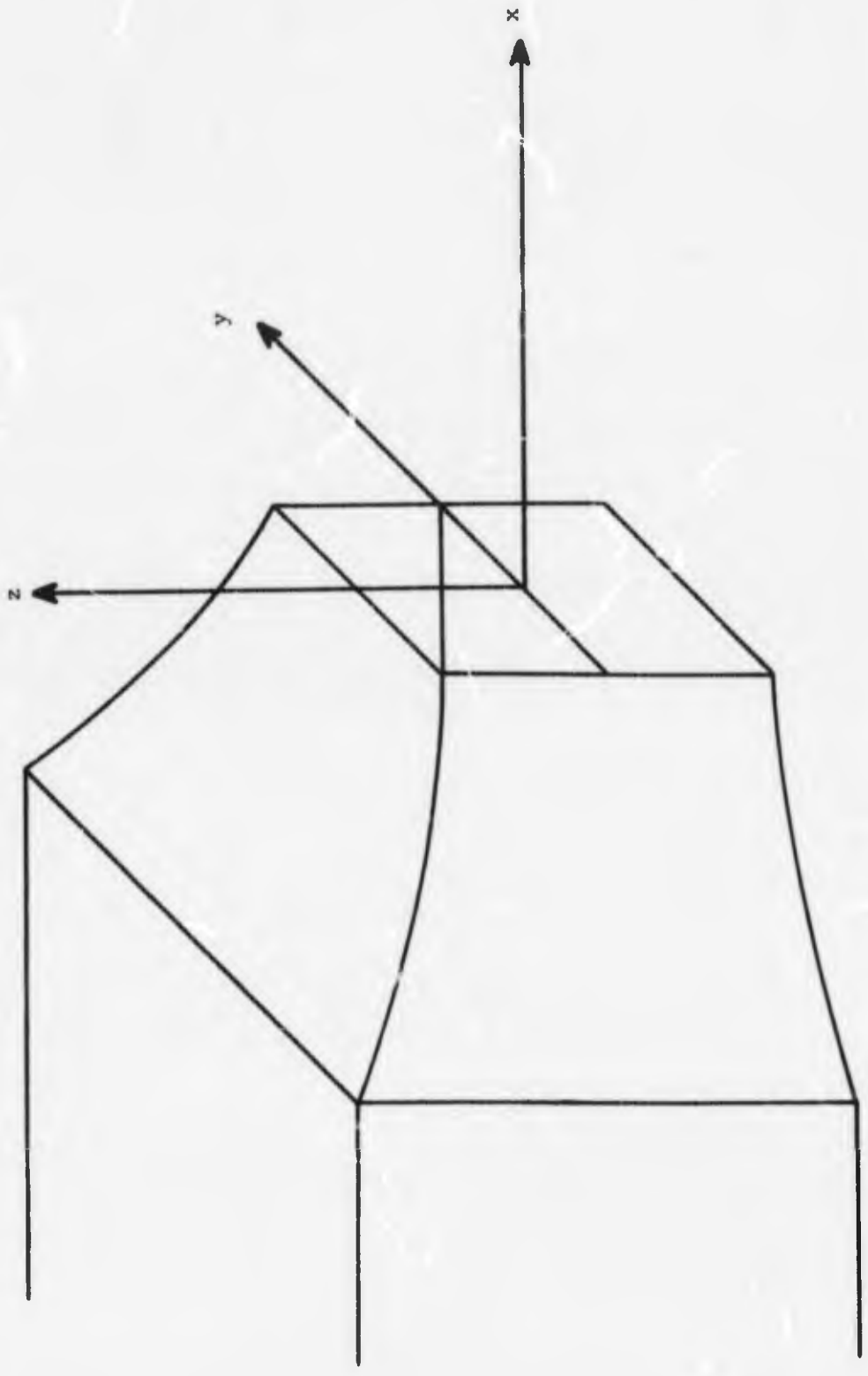

Figure 9: Coordinate System

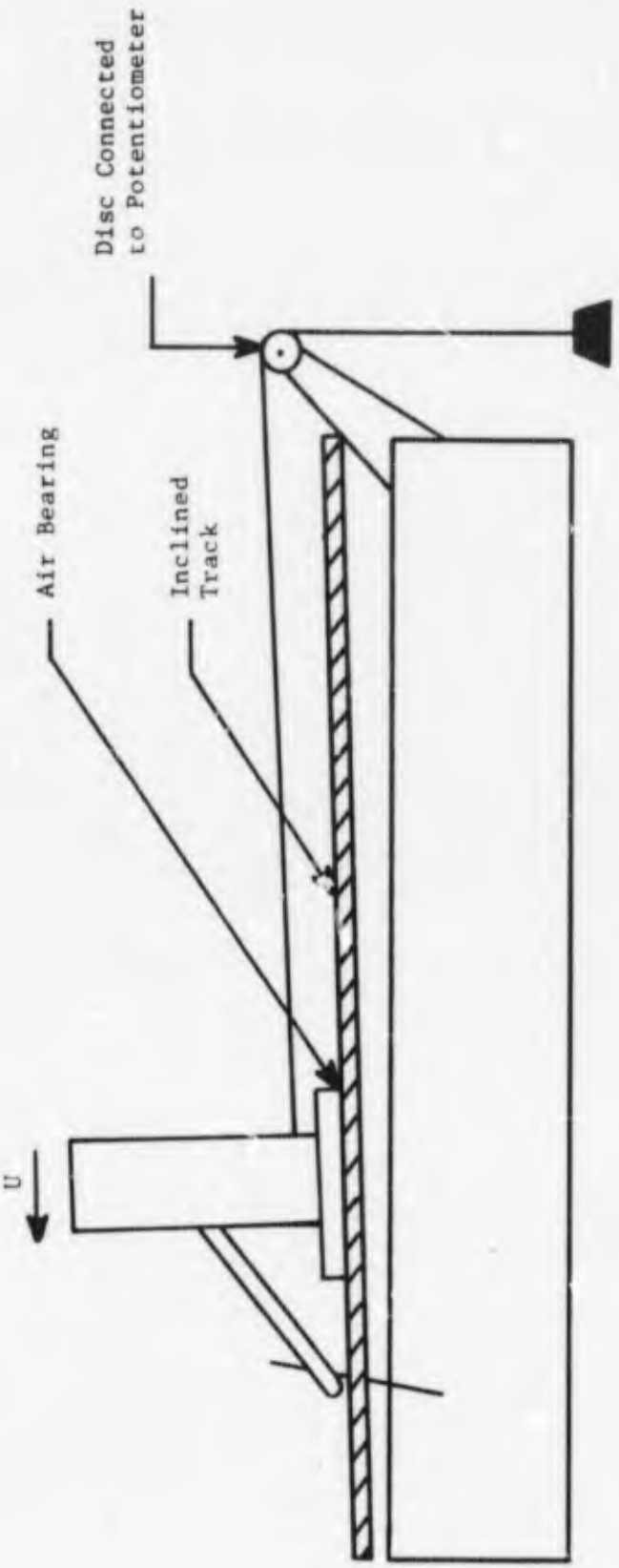

Figure 10: Schematic Showing Hot-Film Calibration Procedure.

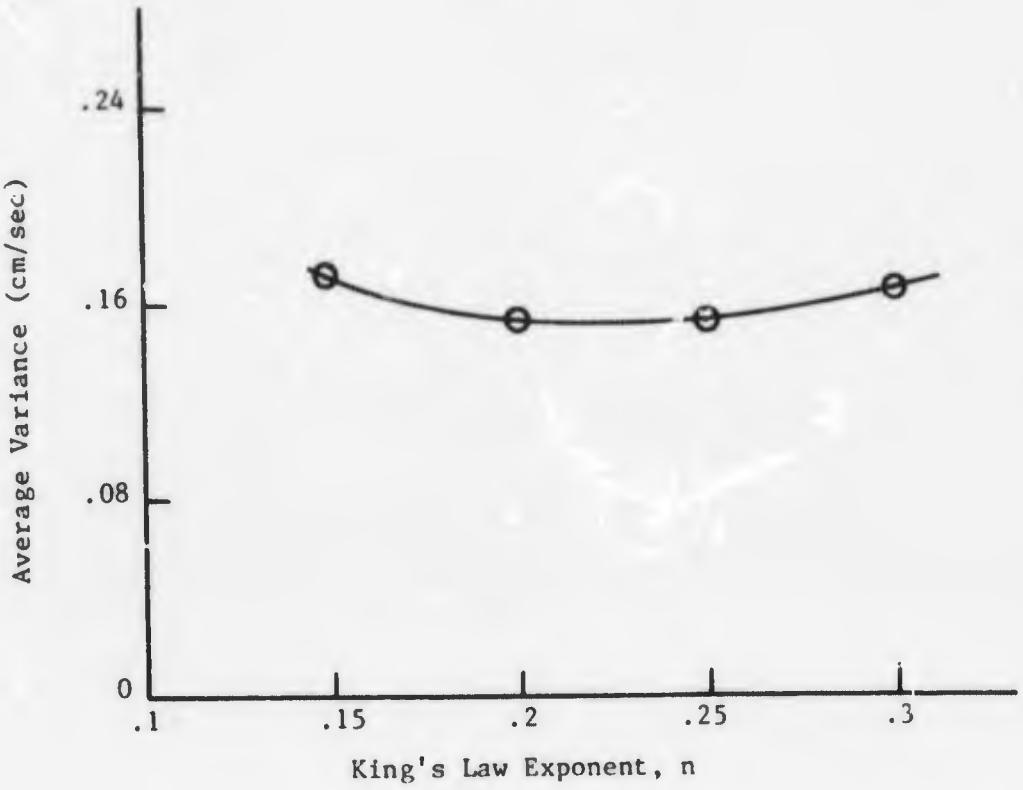

Figure 11: Effect of King's Law Exponent Upon Average Variance of Hot-Film Data.

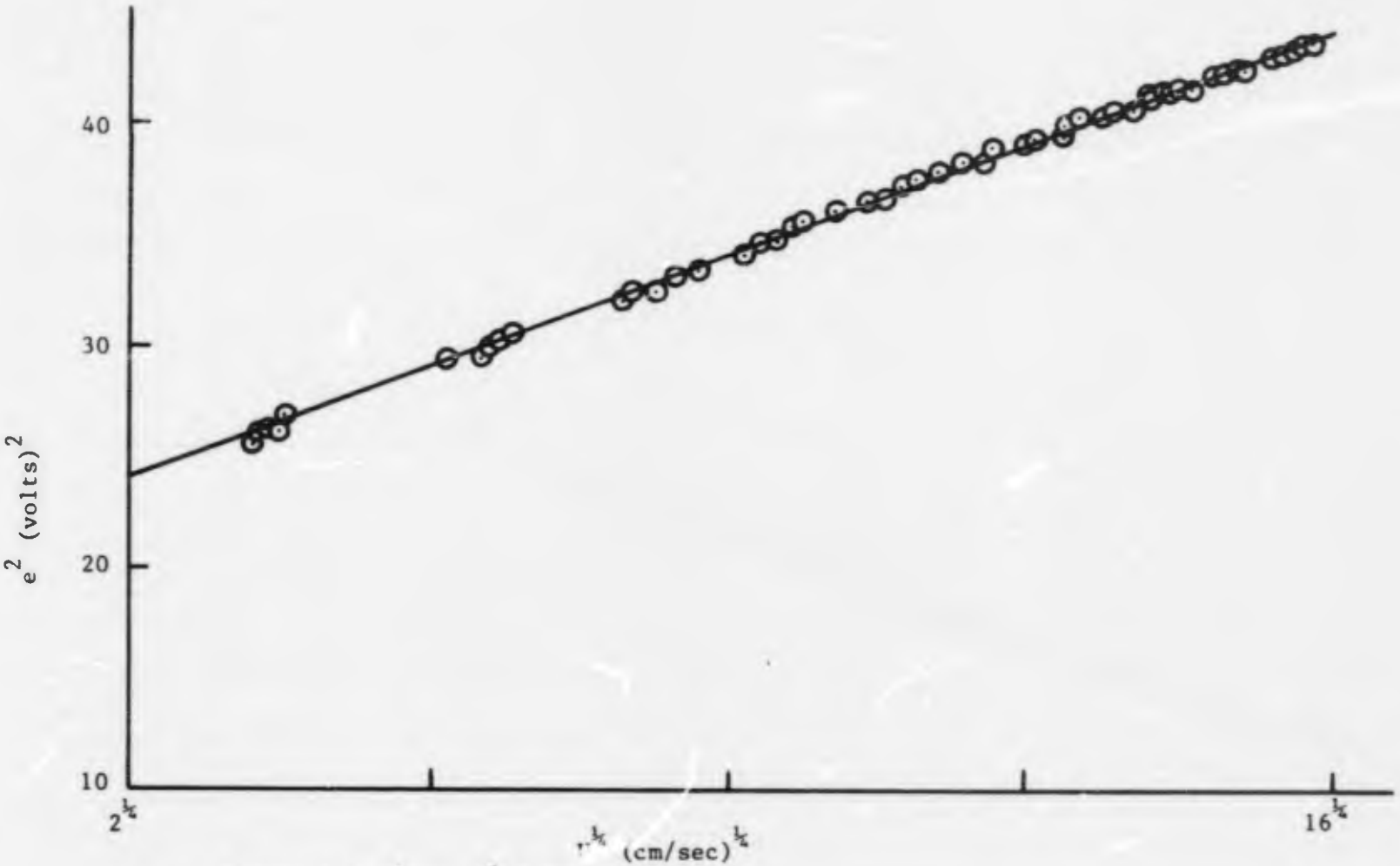

Figure 12: e^2 vs. $U^{\frac{1}{4}}$ Prior to a Test

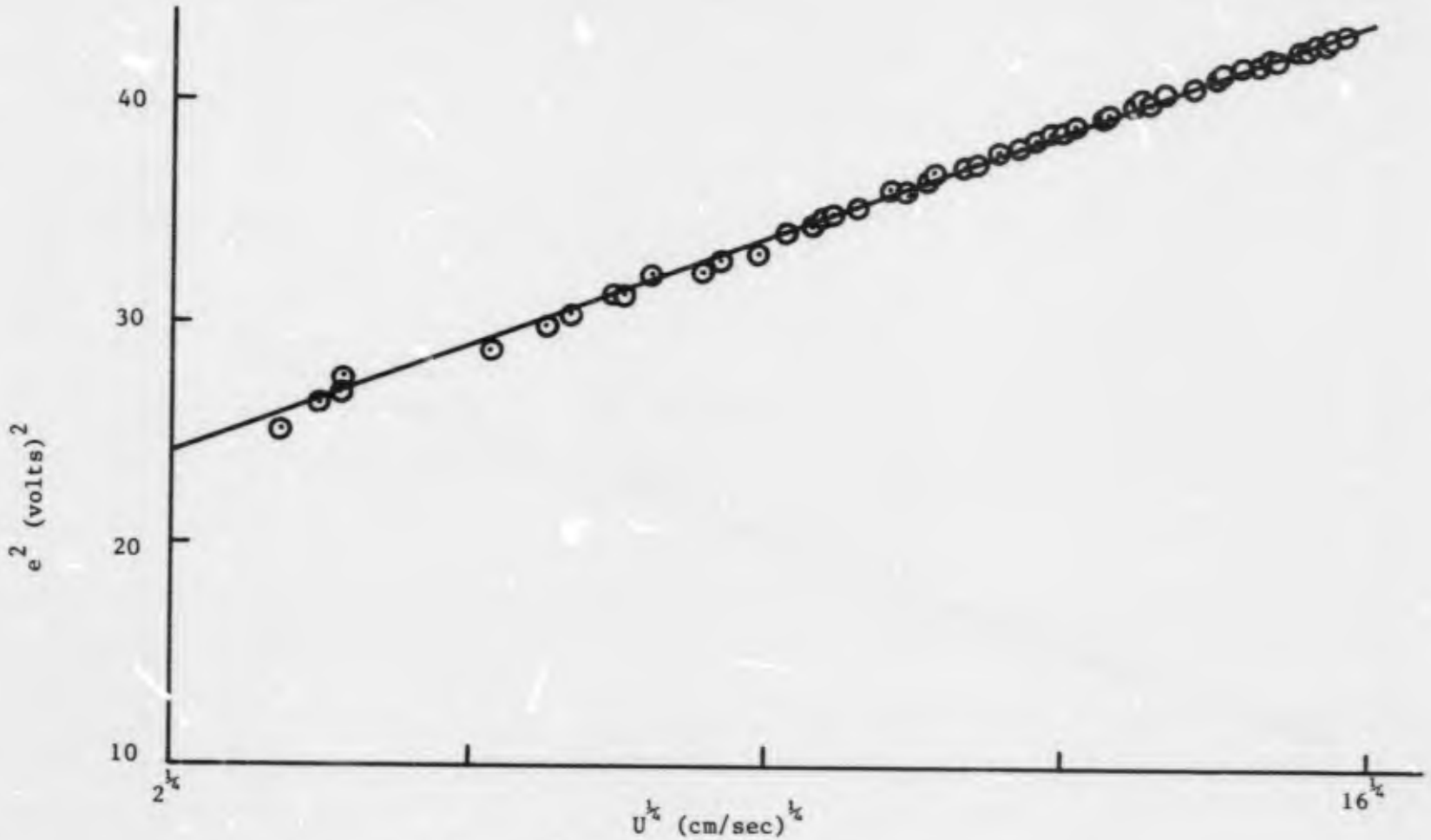

Figure 13: e^2 vs. $U^{1/4}$ Following a Test

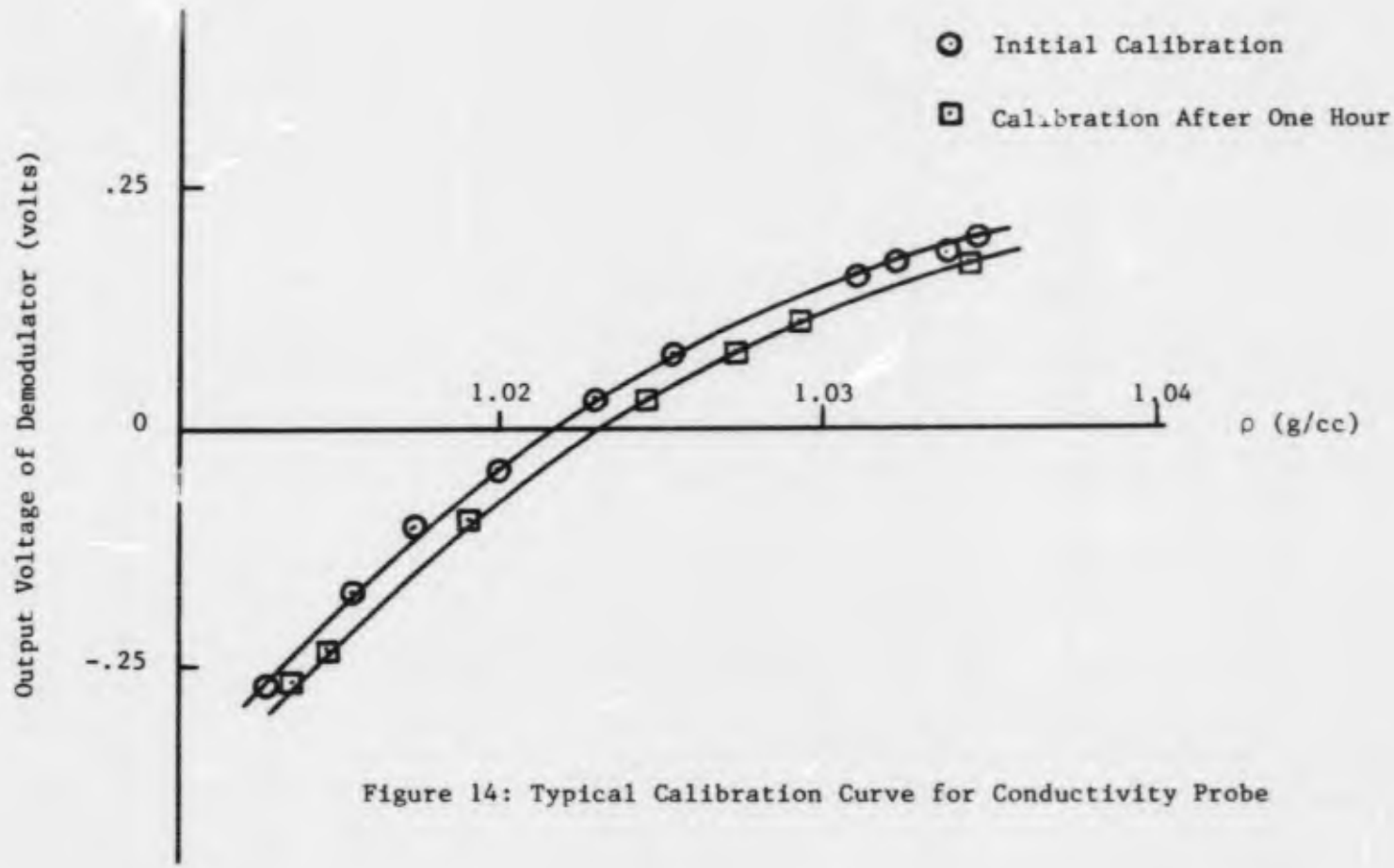

Figure 14: Typical Calibration Curve for Conductivity Probe

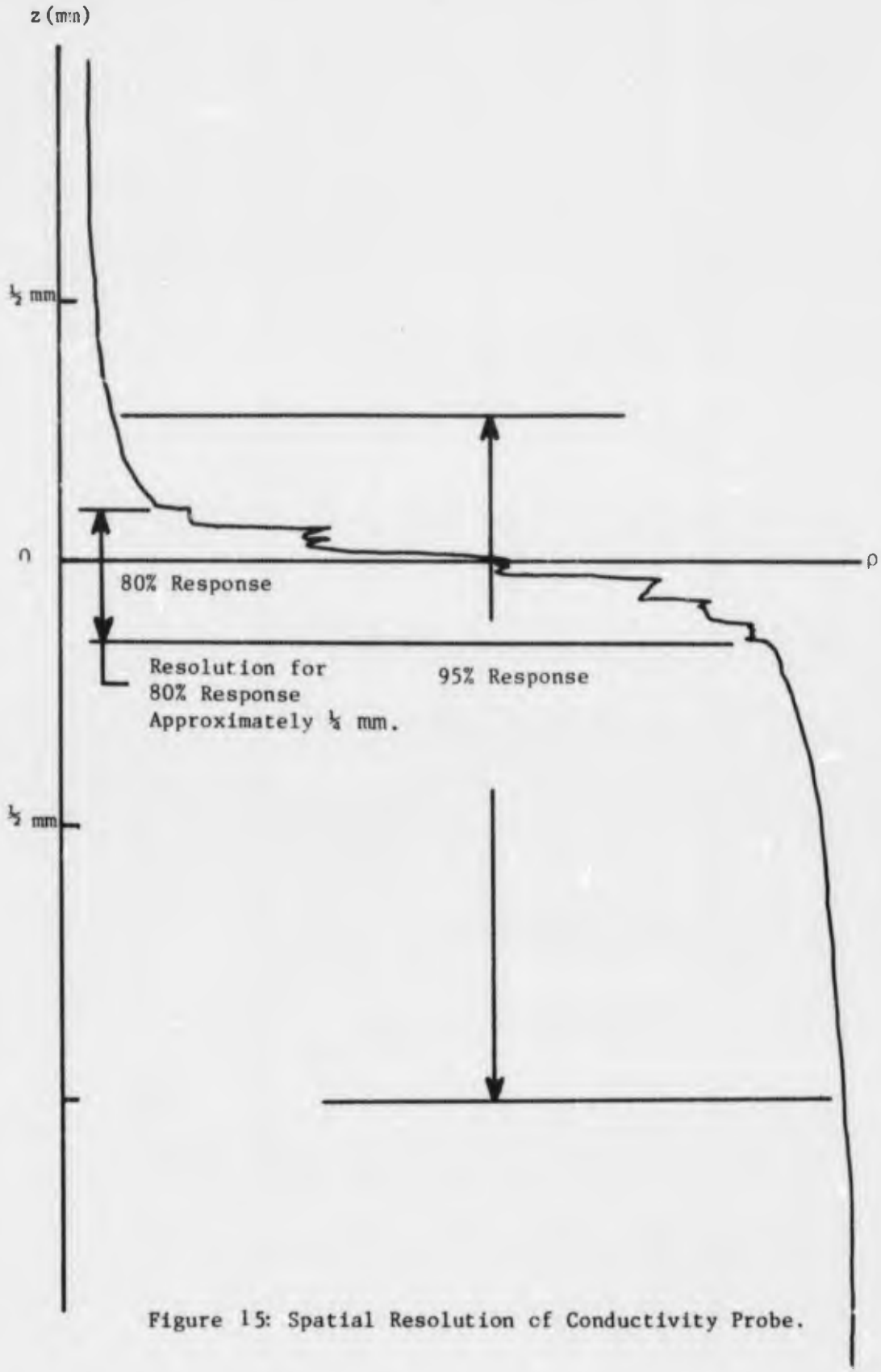

Figure 15: Spatial Resolution of Conductivity Probe.

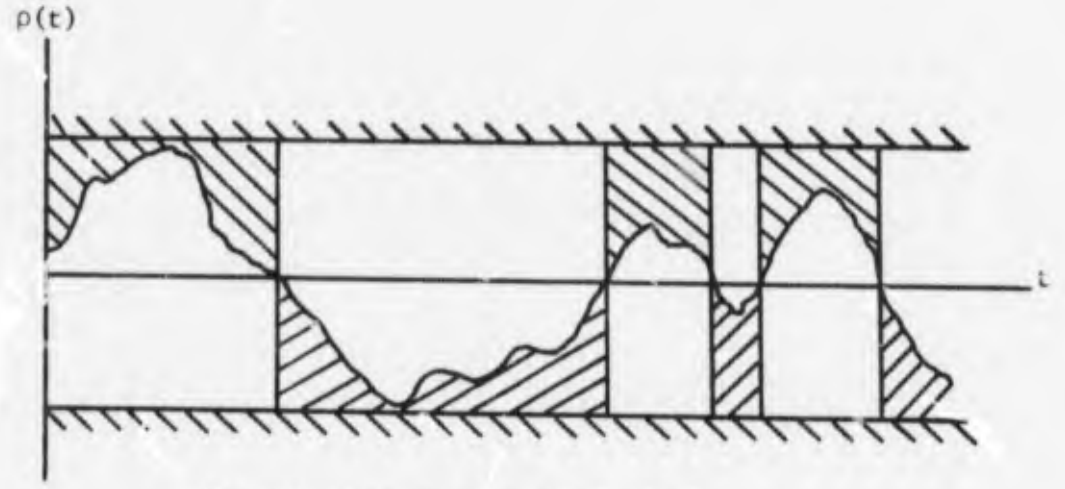

(a) Arbitrary Density Variations

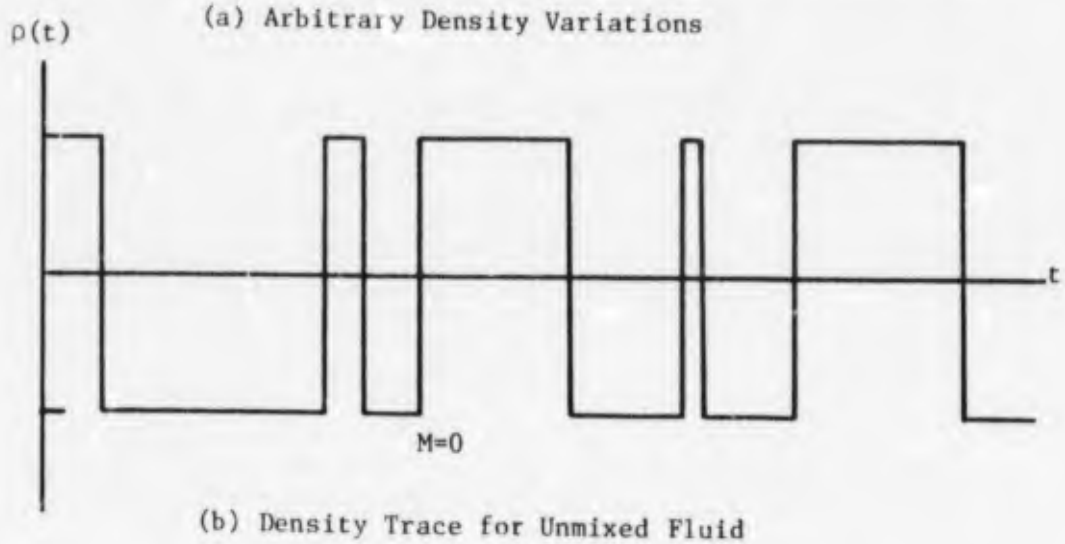

(b) Density Trace for Unmixed Fluid

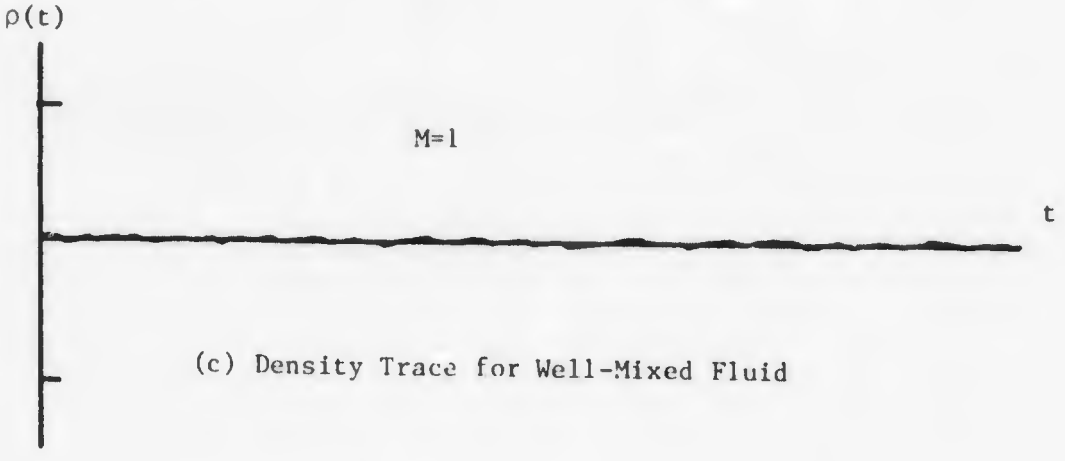

(c) Density Trace for Well-Mixed Fluid

Figure 16: Definition of the Mixedness

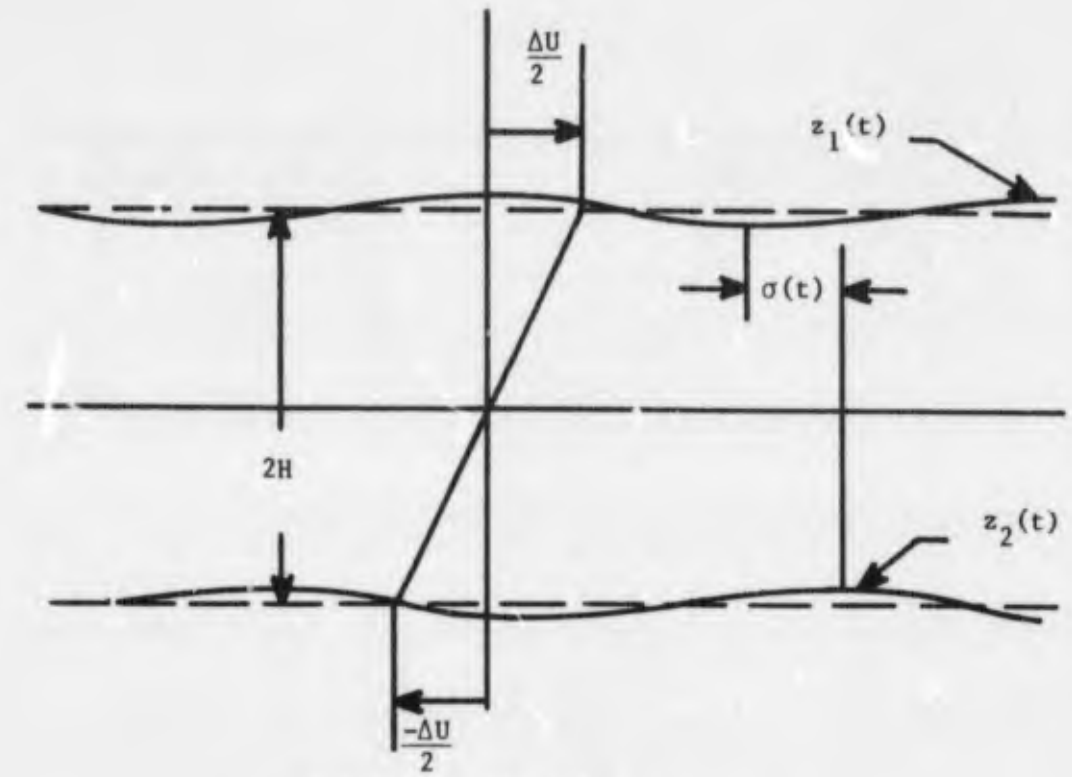

(a) Unstratified Case

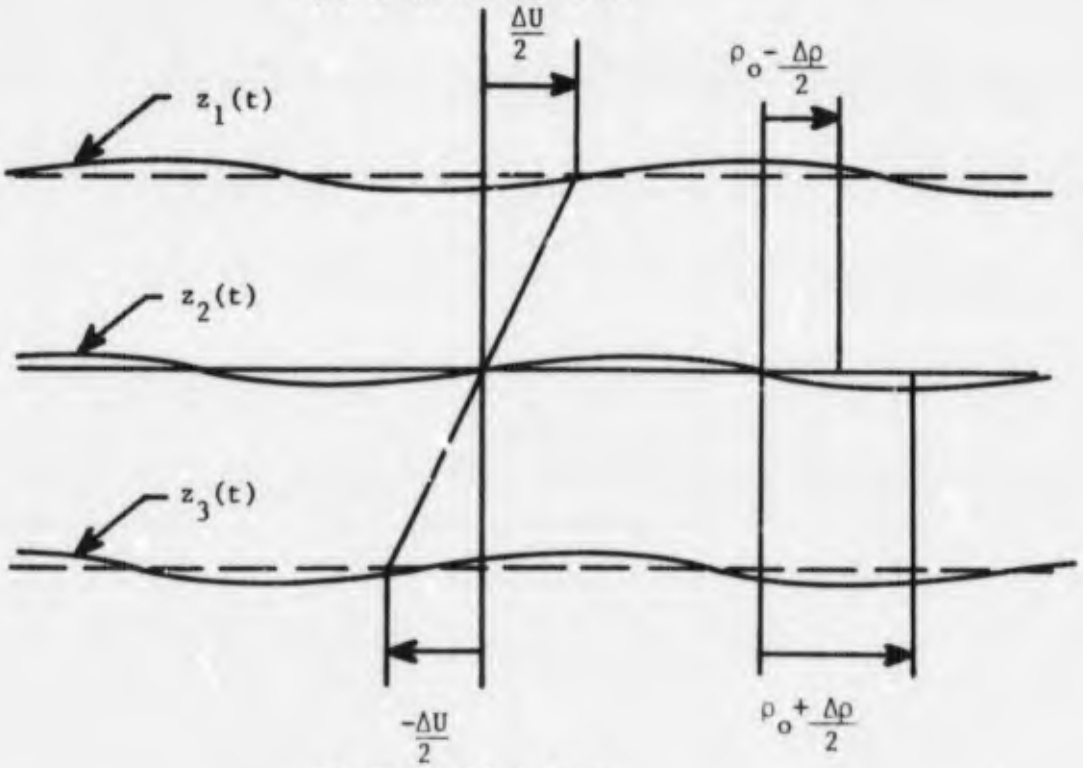

(b) Stratified Case

Figure 17: Schematic of Holmboe's Model

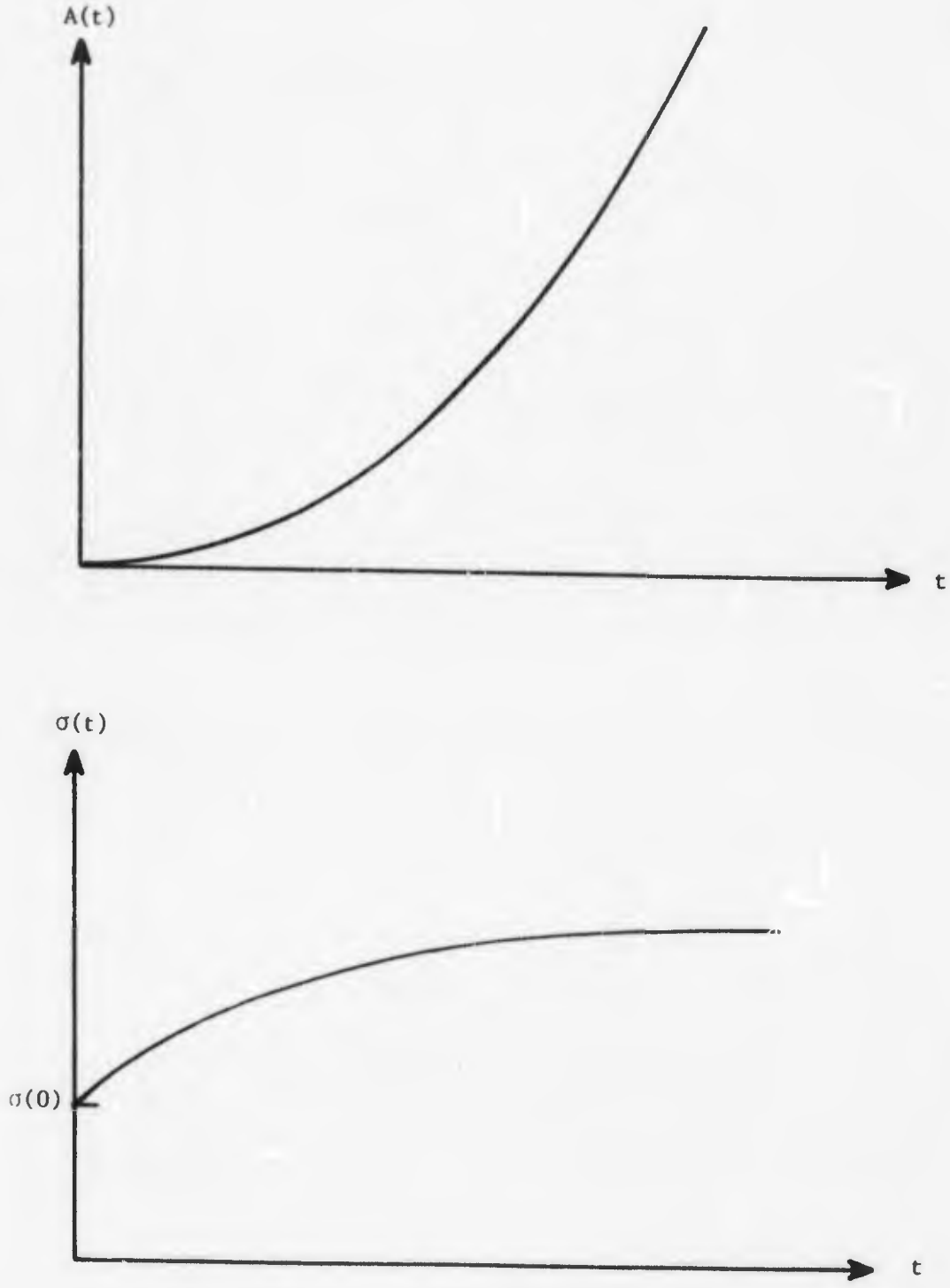

Figure 18: Time Variation of the Parameters σ and A From Holmboe's Model.

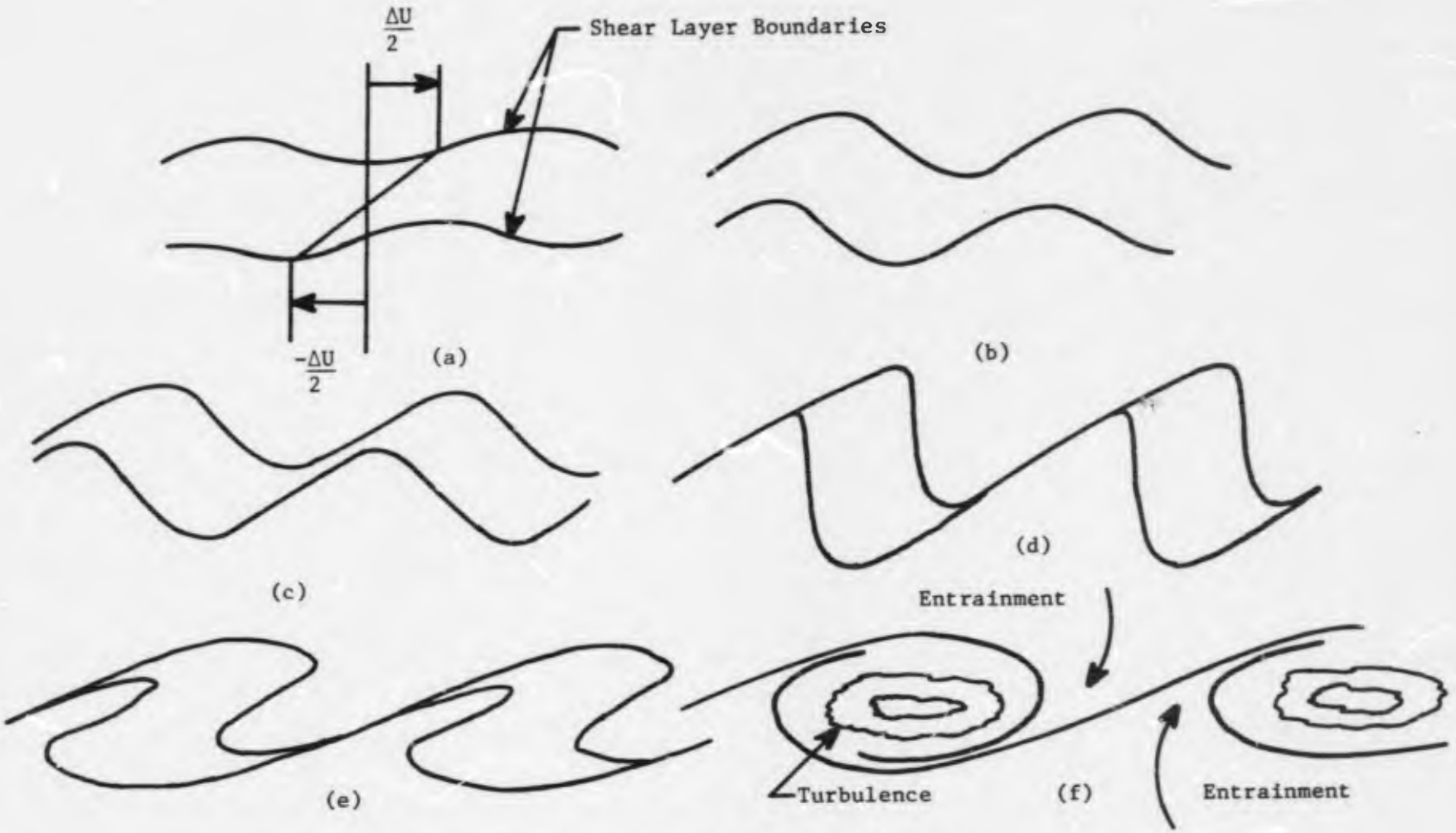

Figure 19: Conceptualization of Mode I Instability.

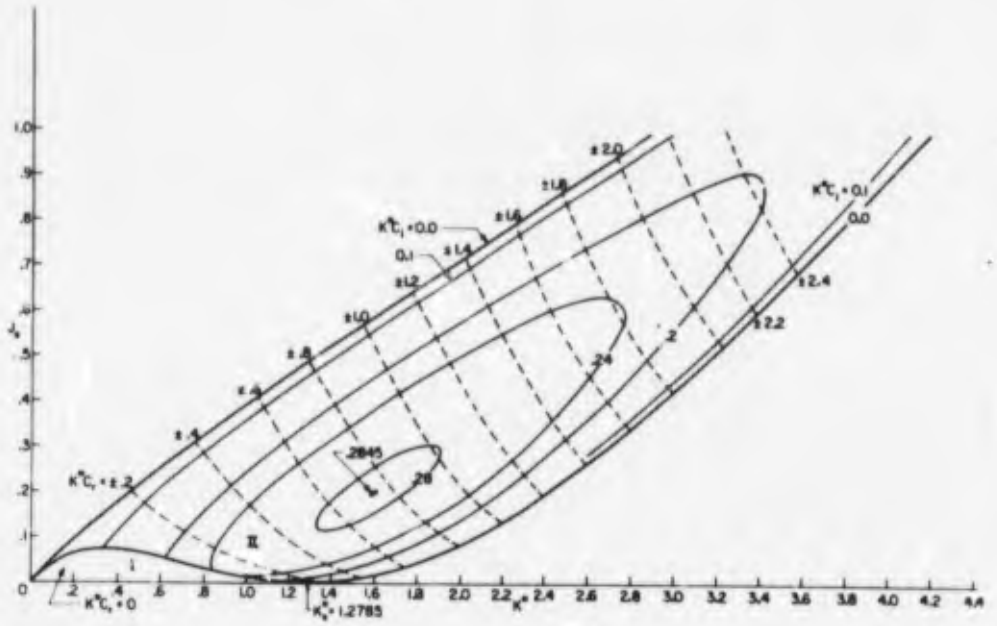

(a) Stability Diagram for Holmboe's Model.

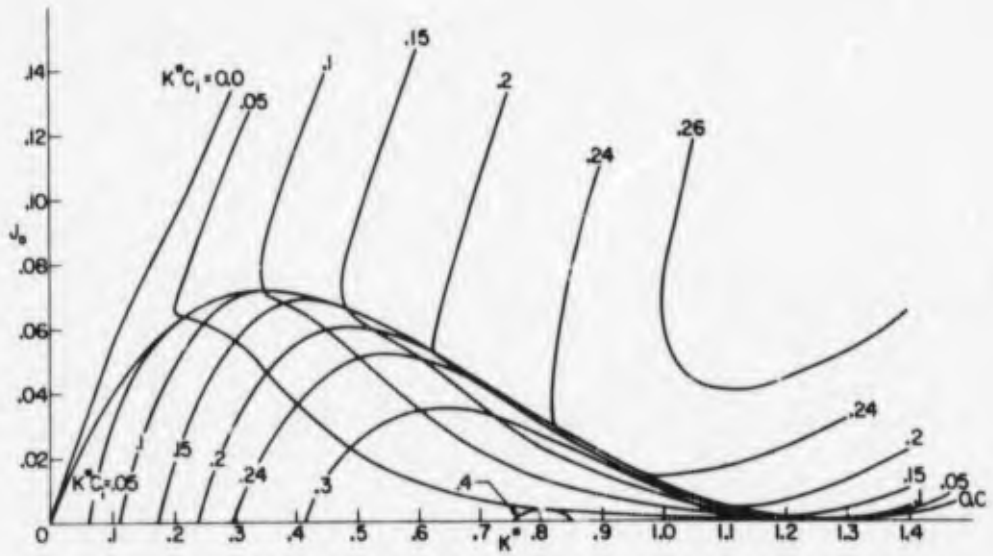

(b) Stability Diagram for Small Richardson Numbers.

Figure 20: Stability Diagram for Holmboe's Model.

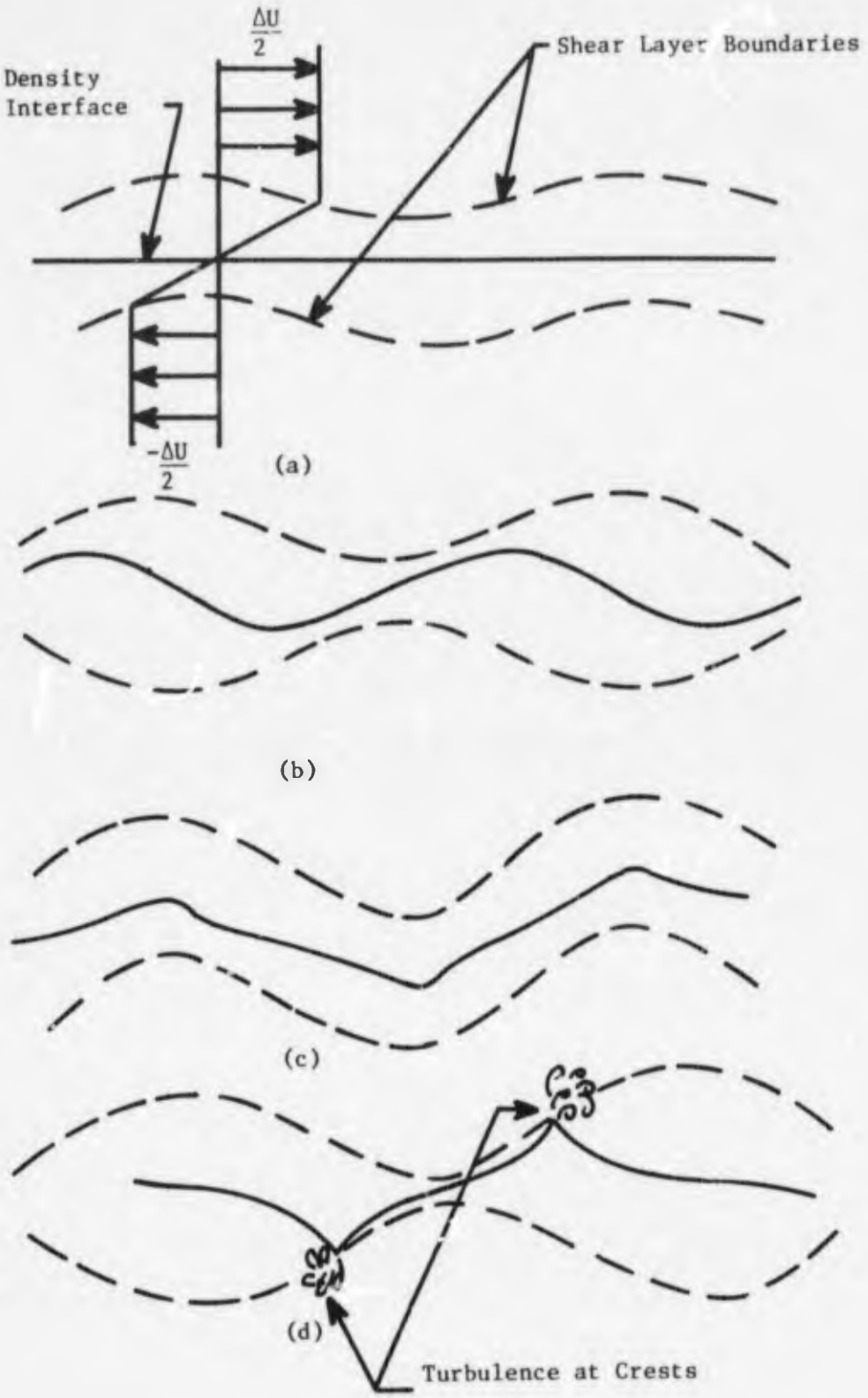

Figure 21: Conceptualization of Mode II Instability.

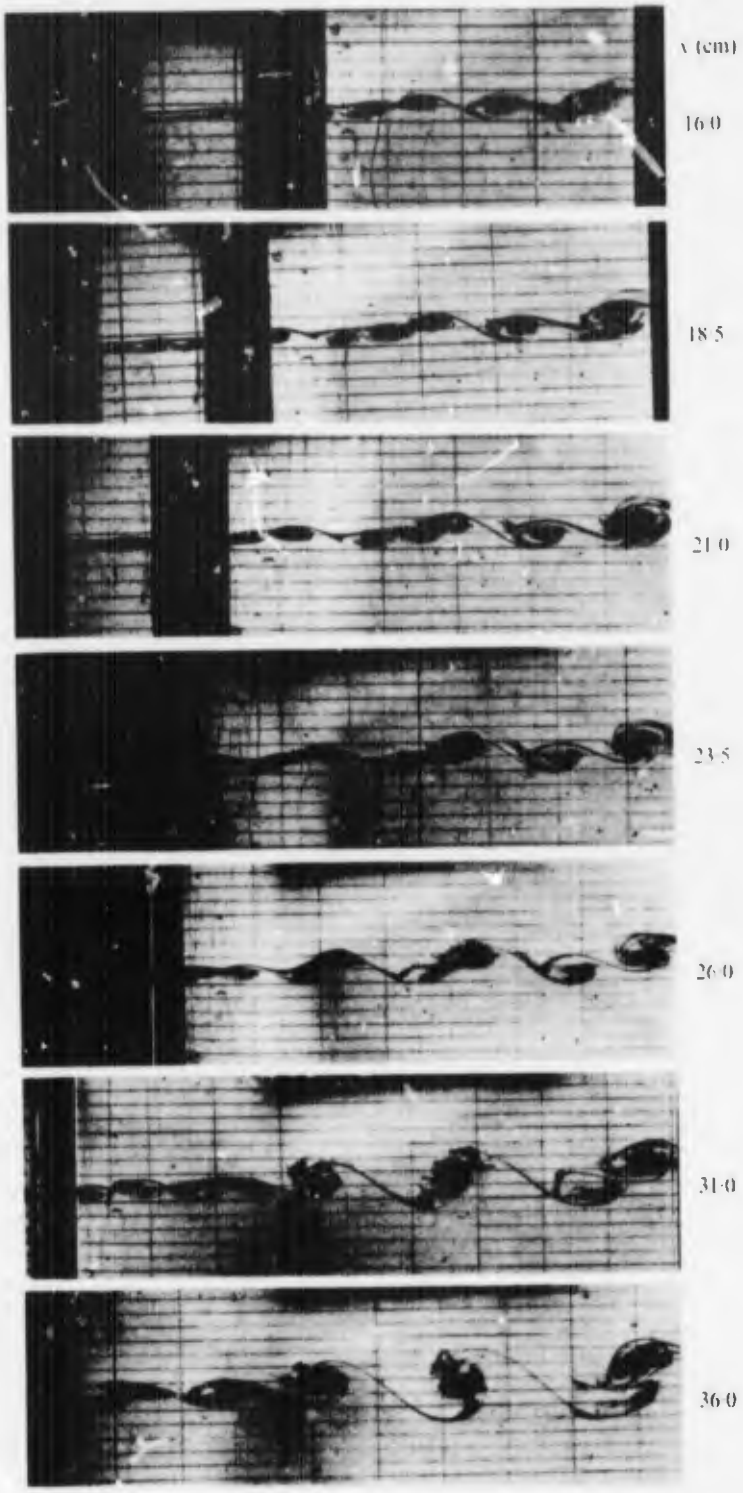

Figure 22: Dye Visualization Photographs for Unstratified Mixing Layer (from Winant and Browand (1974)).

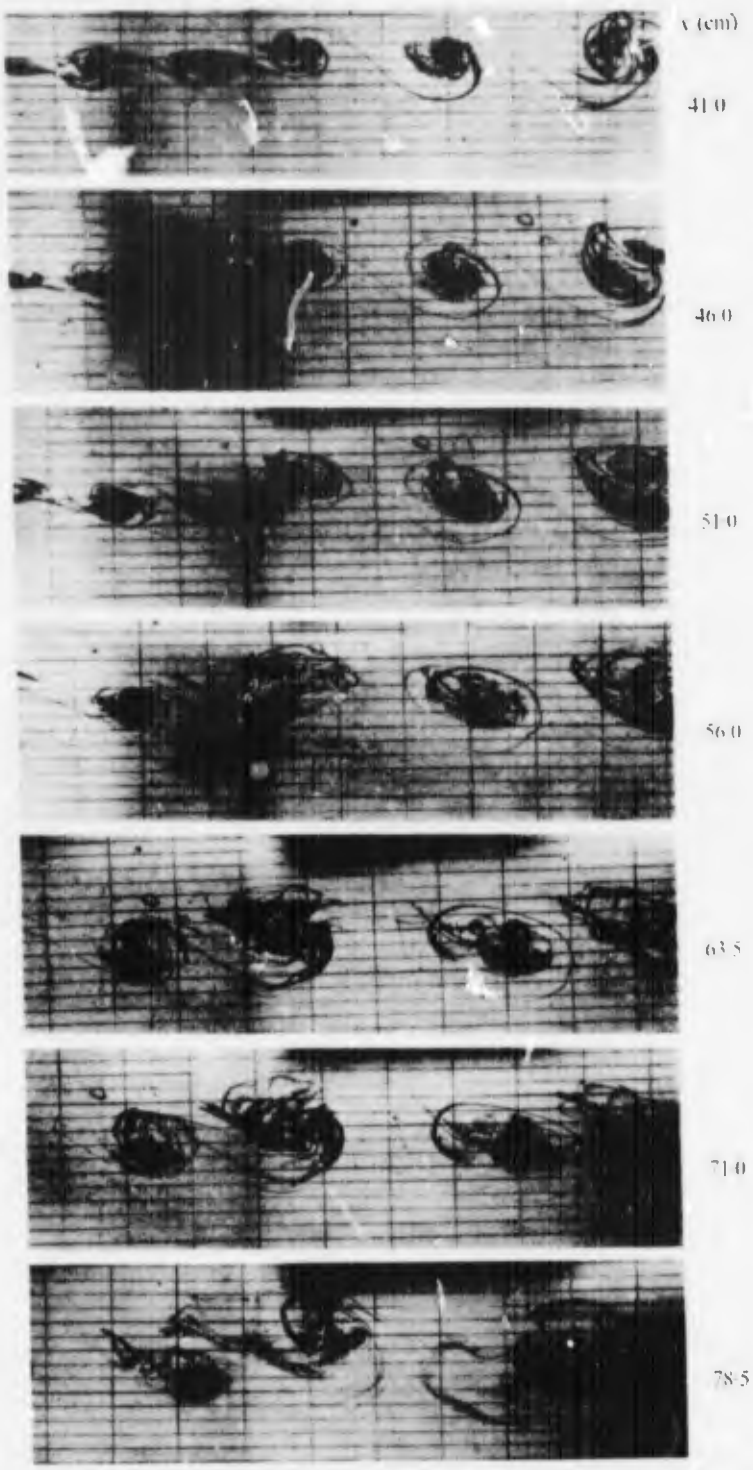

Figure 22: Dye Visualization Photographs for Unstratified Mixing Layer (from Winant and Browand (1974)).

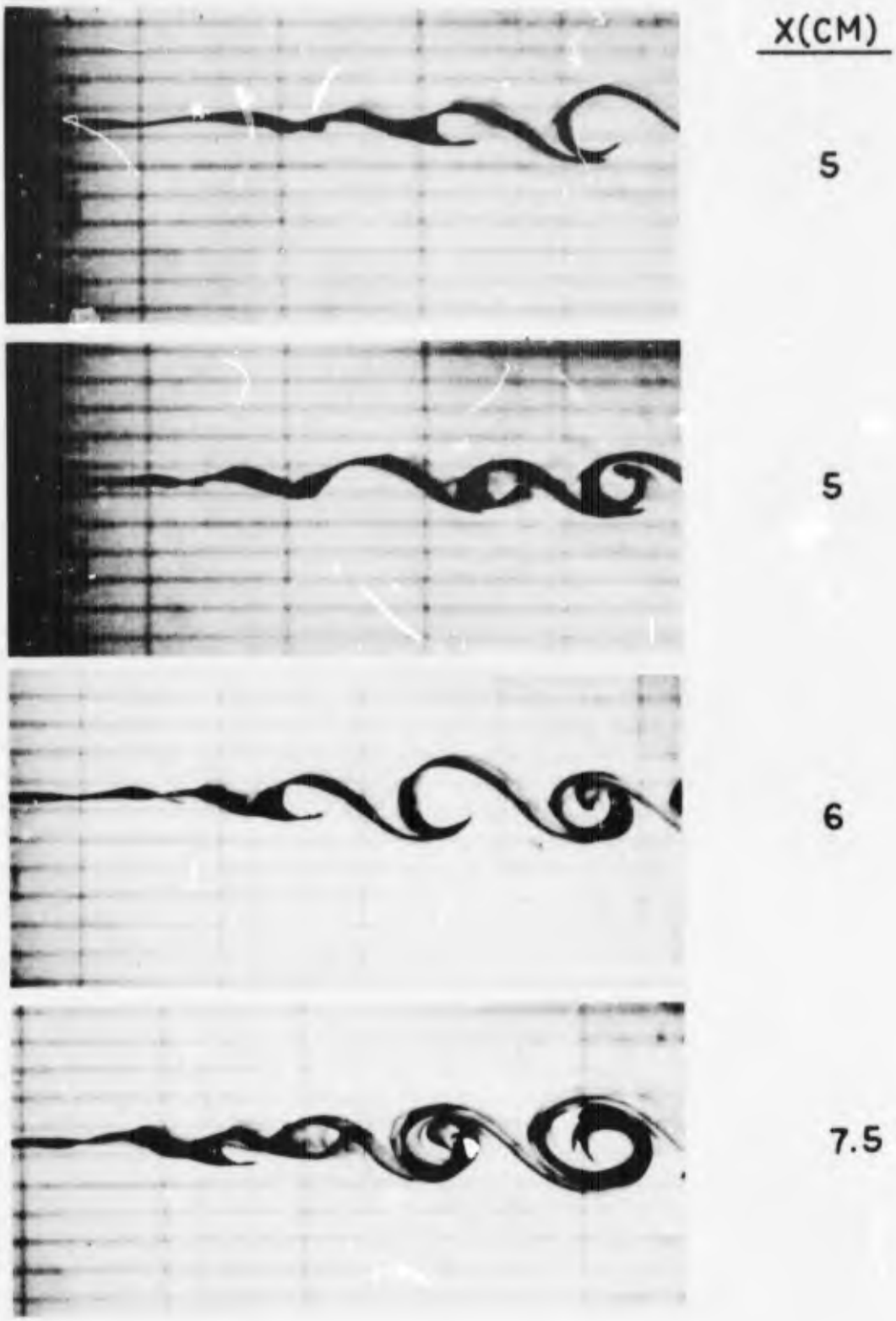

Figure 23: Flow Visualization Using Dye, $Ri_{h_o} = .04$.

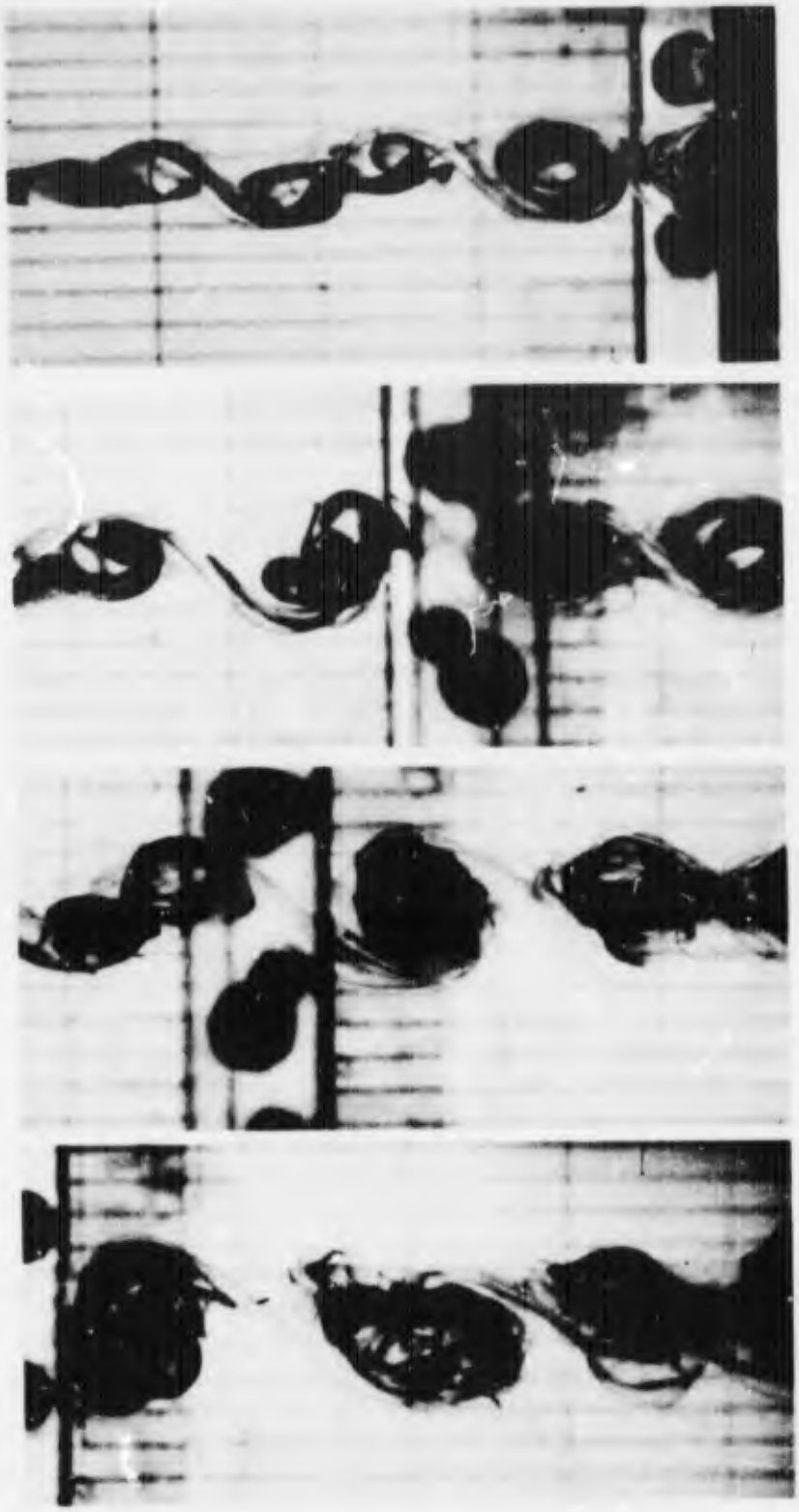

Figure 23: Flow Visualization Using Dye, Ri_{h_o} =.04.

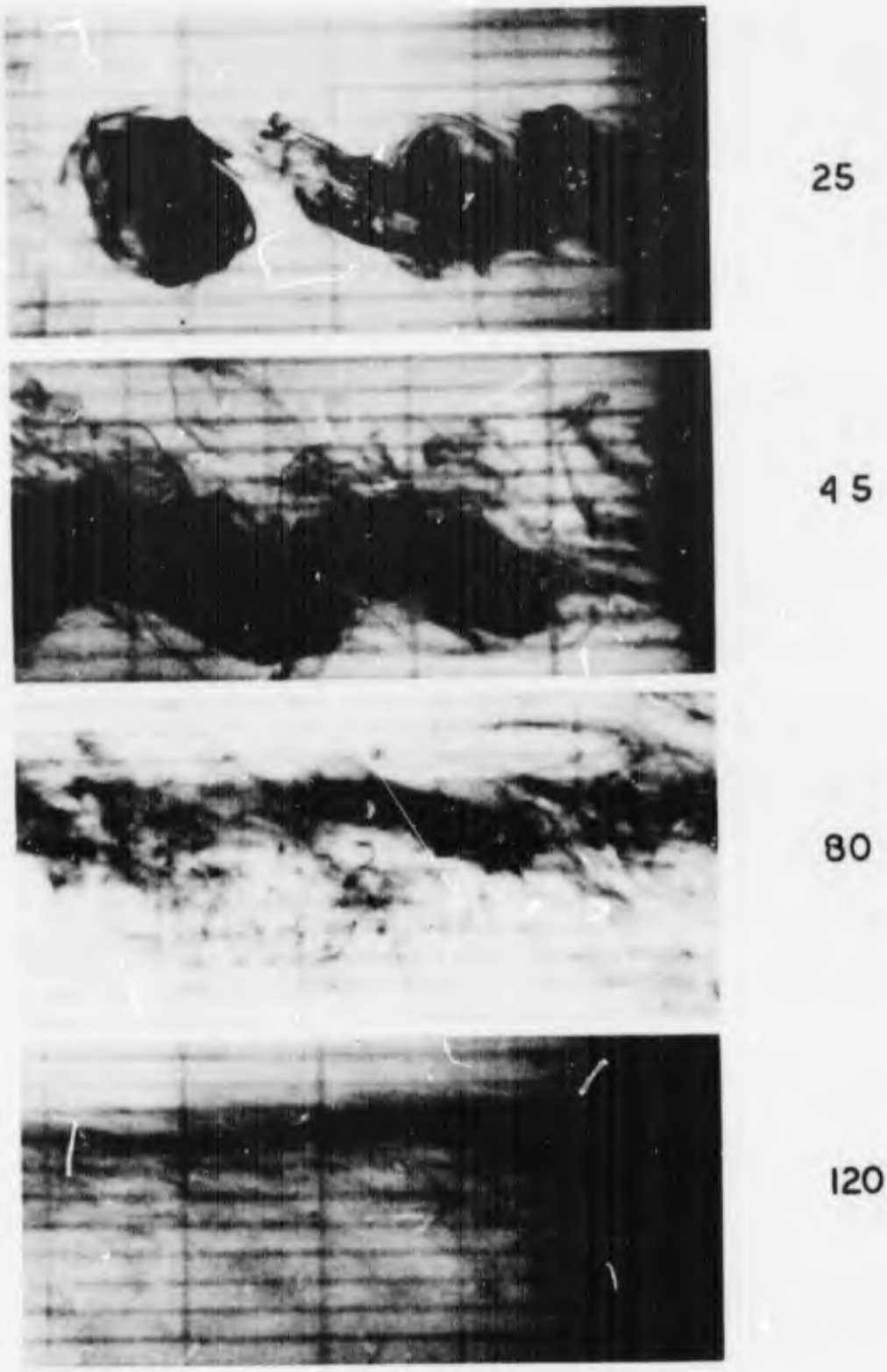

Figure 23: Flow Visualization Using Dye, Ri_{h_o} =.04.

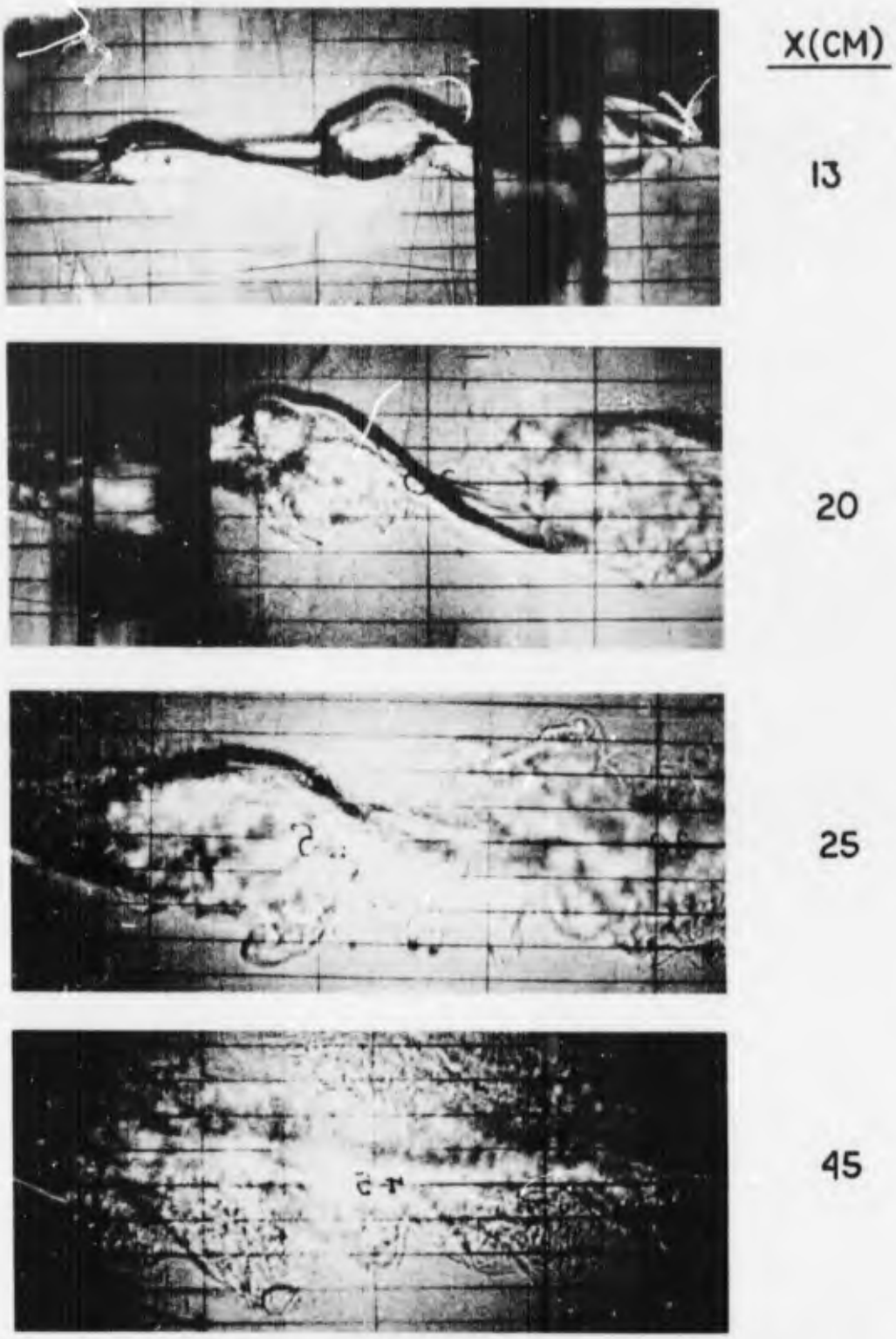

Figure 24: Flow Visualization Using Shadowgraph, Ri_{h_o} =.04.

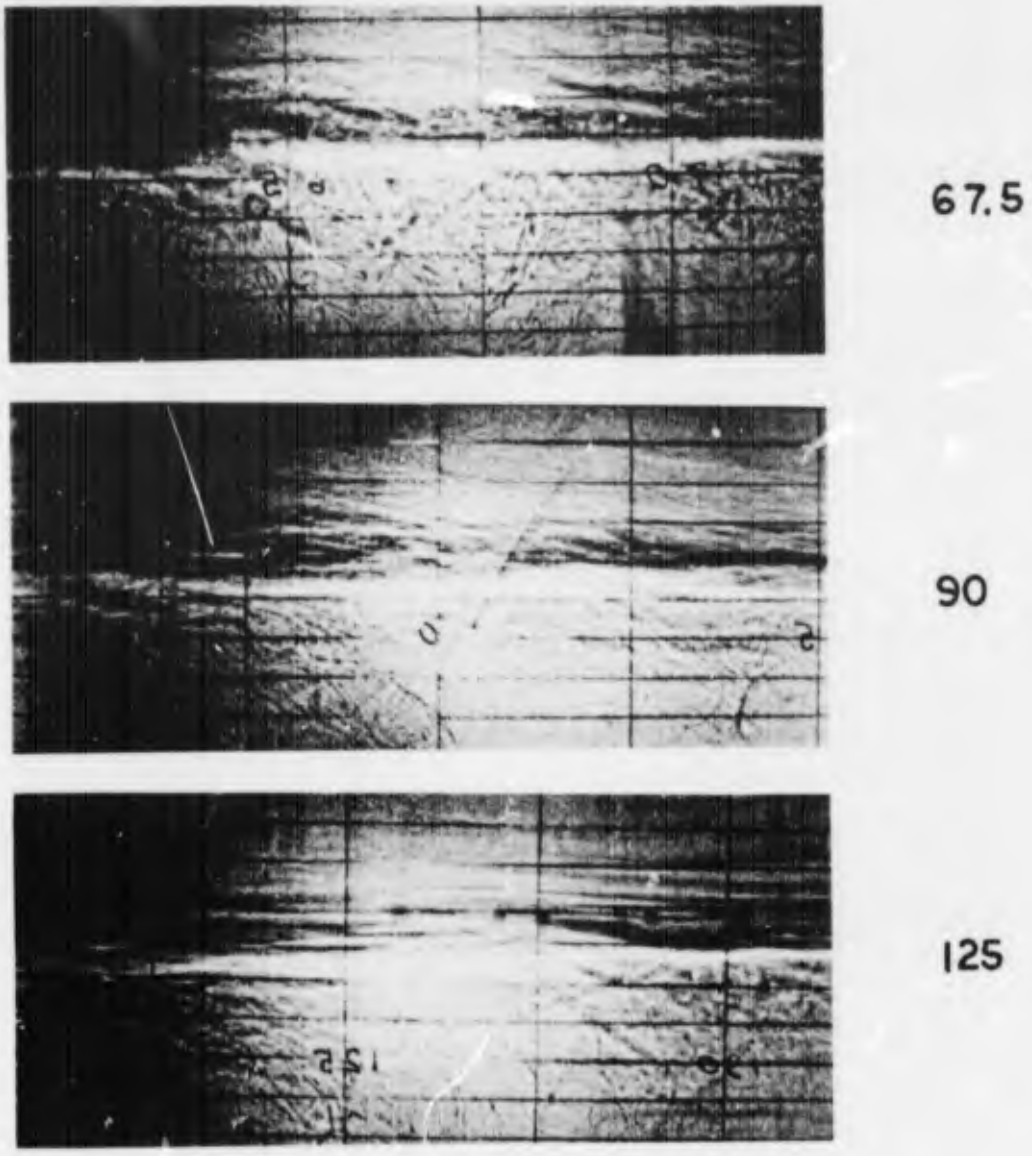

Figure 24: Flow Visualization Using Shadowgraph, Ri_{h_o} =.04.

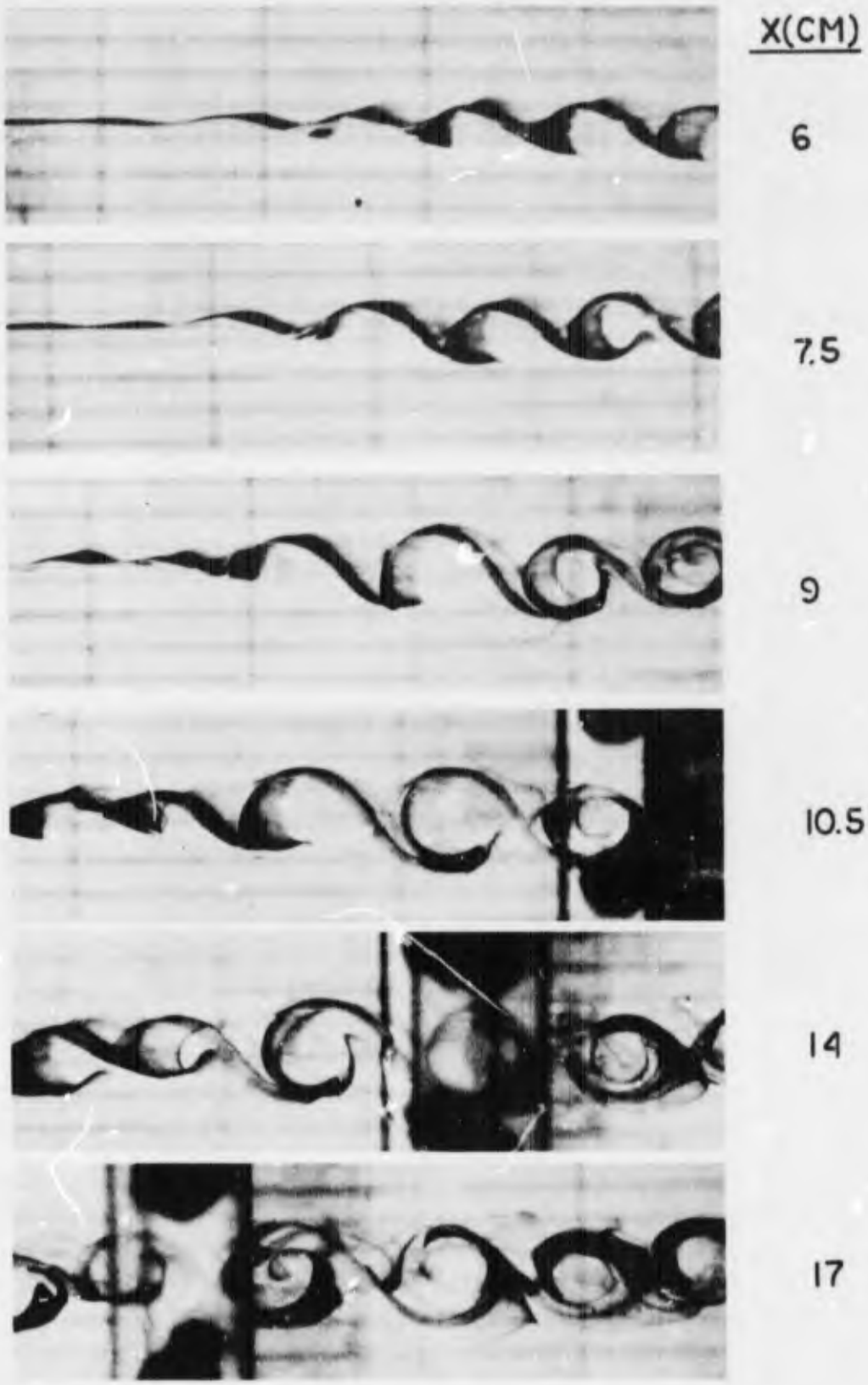

Figure 25: Flow Visualization Using Dye, Ri_{h_o} =.06.

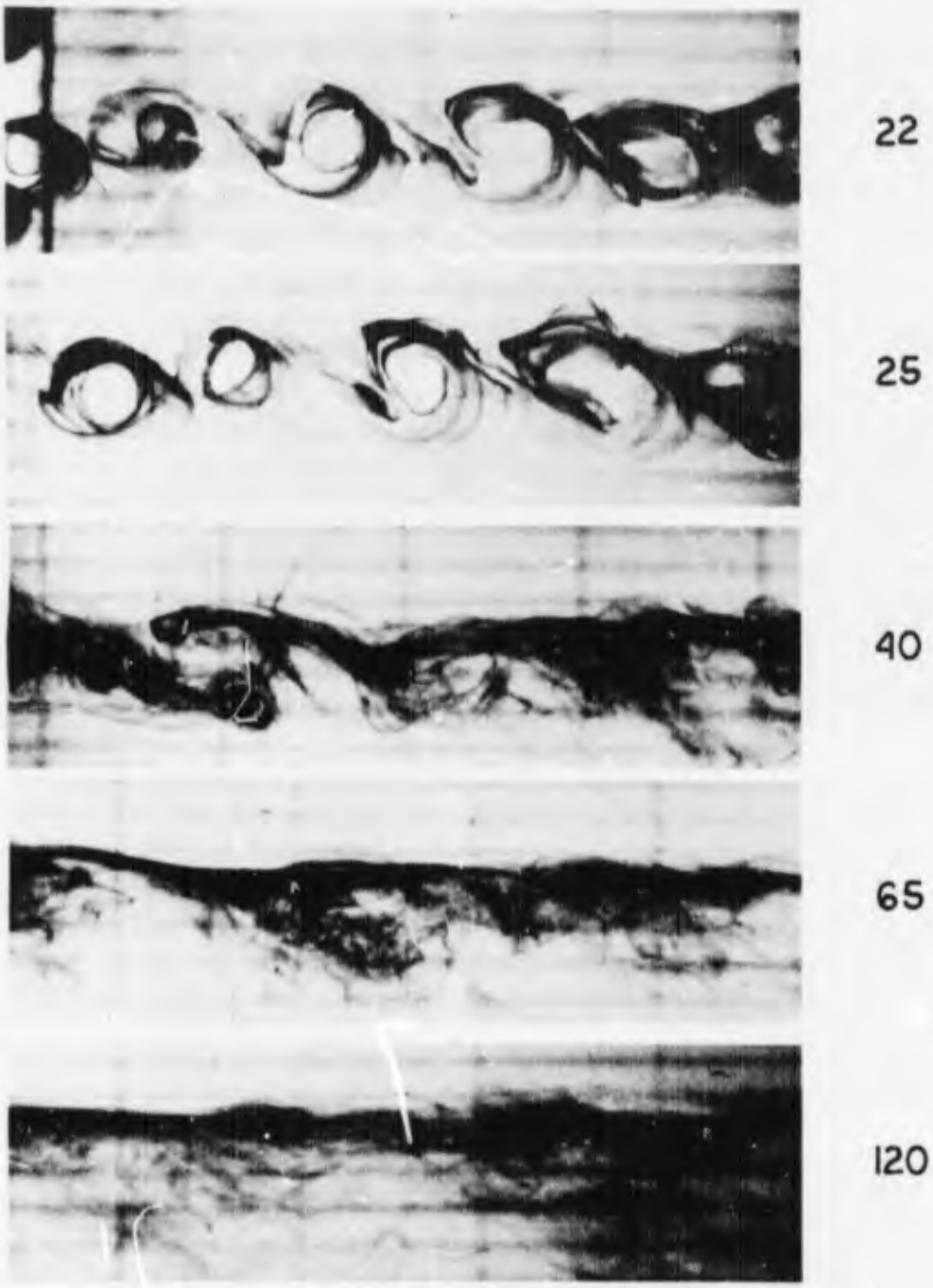

Figure 25: Flow Visualization Using Dye, Ri_{h_o} =.06.

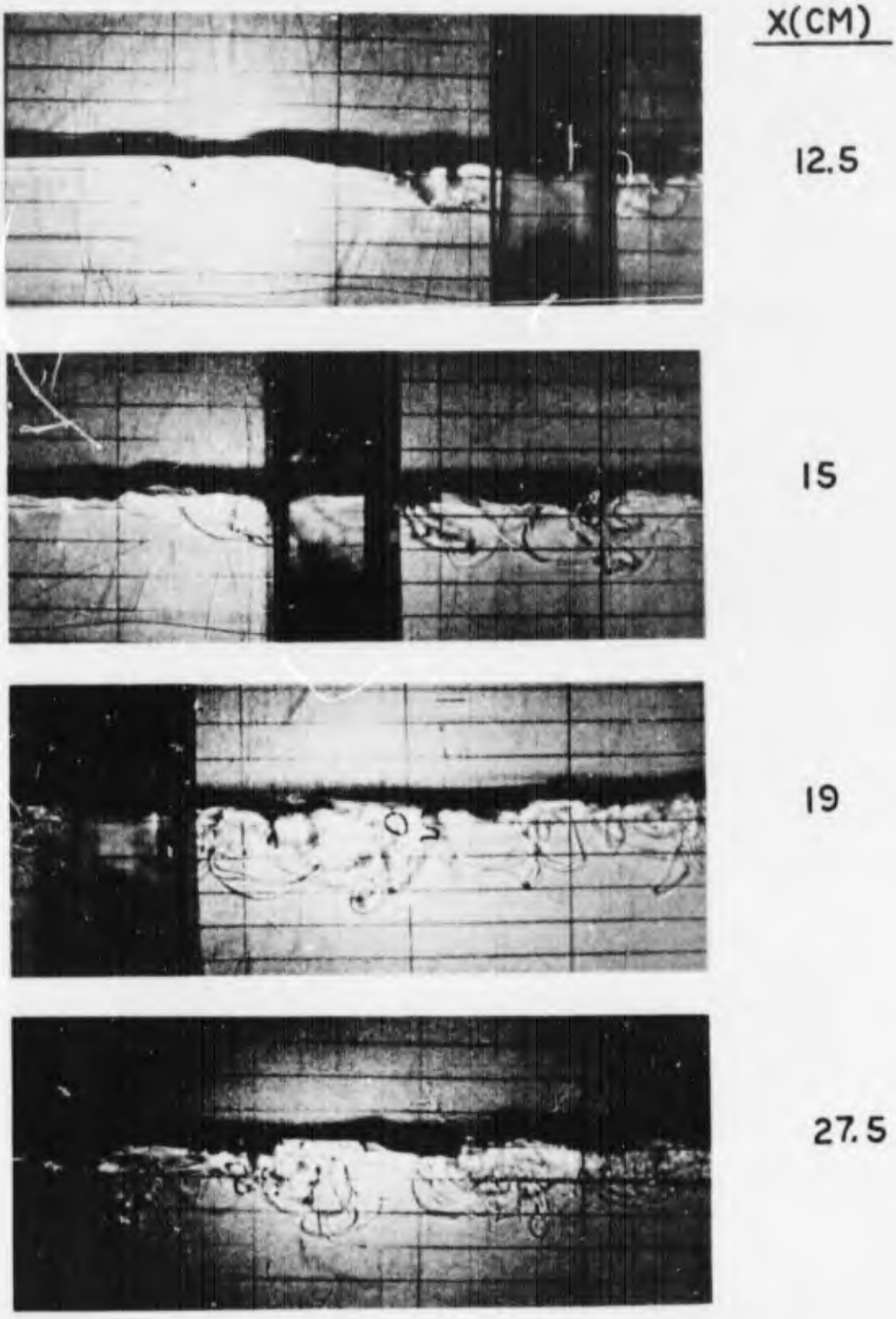

Figure 26: Flow Visualization Using Shadowgraph, Ri_{h_o} =.20.

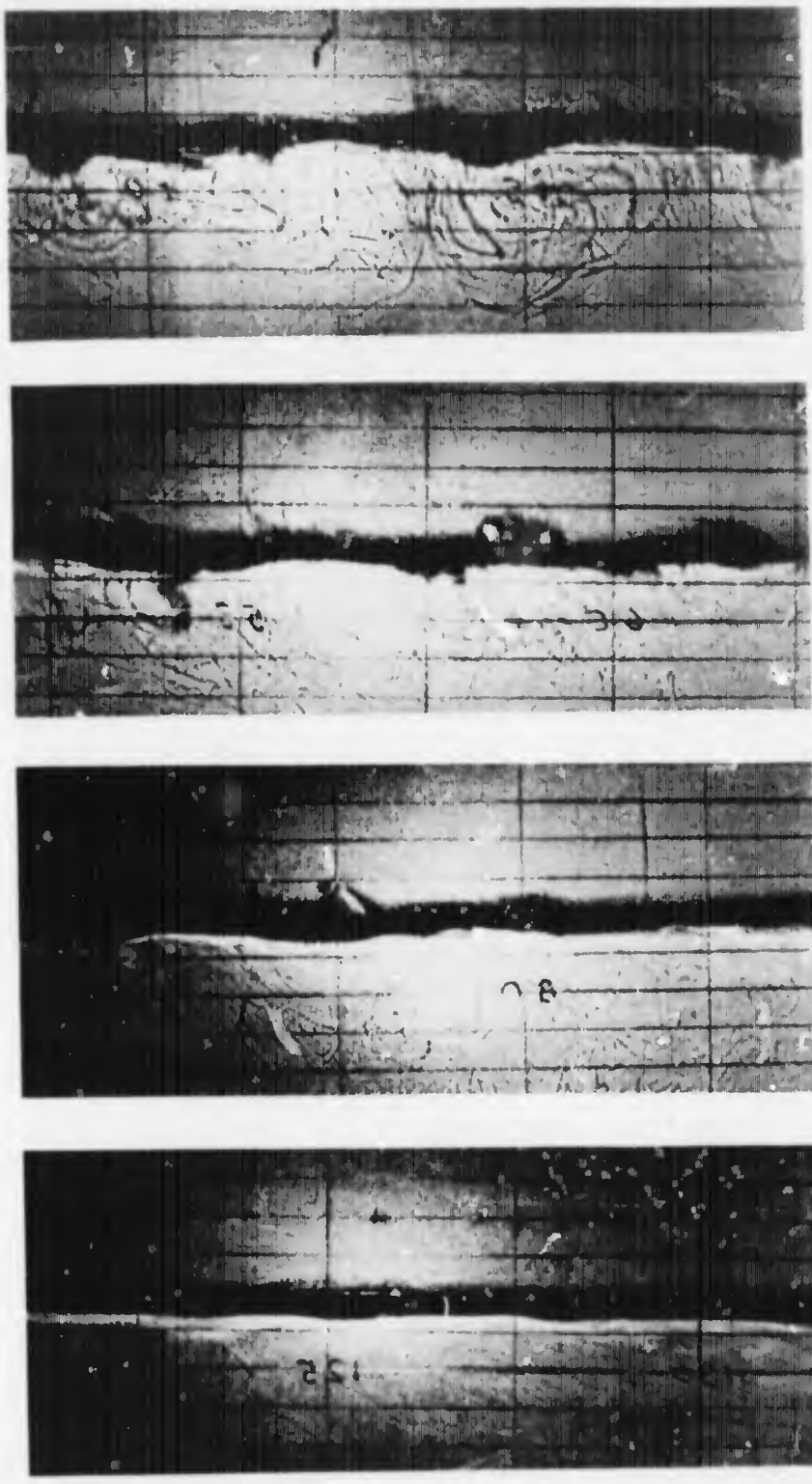

Figure 26: Flow Visualization Using Shadowgraph, $Ri_{h_o} = .20$.

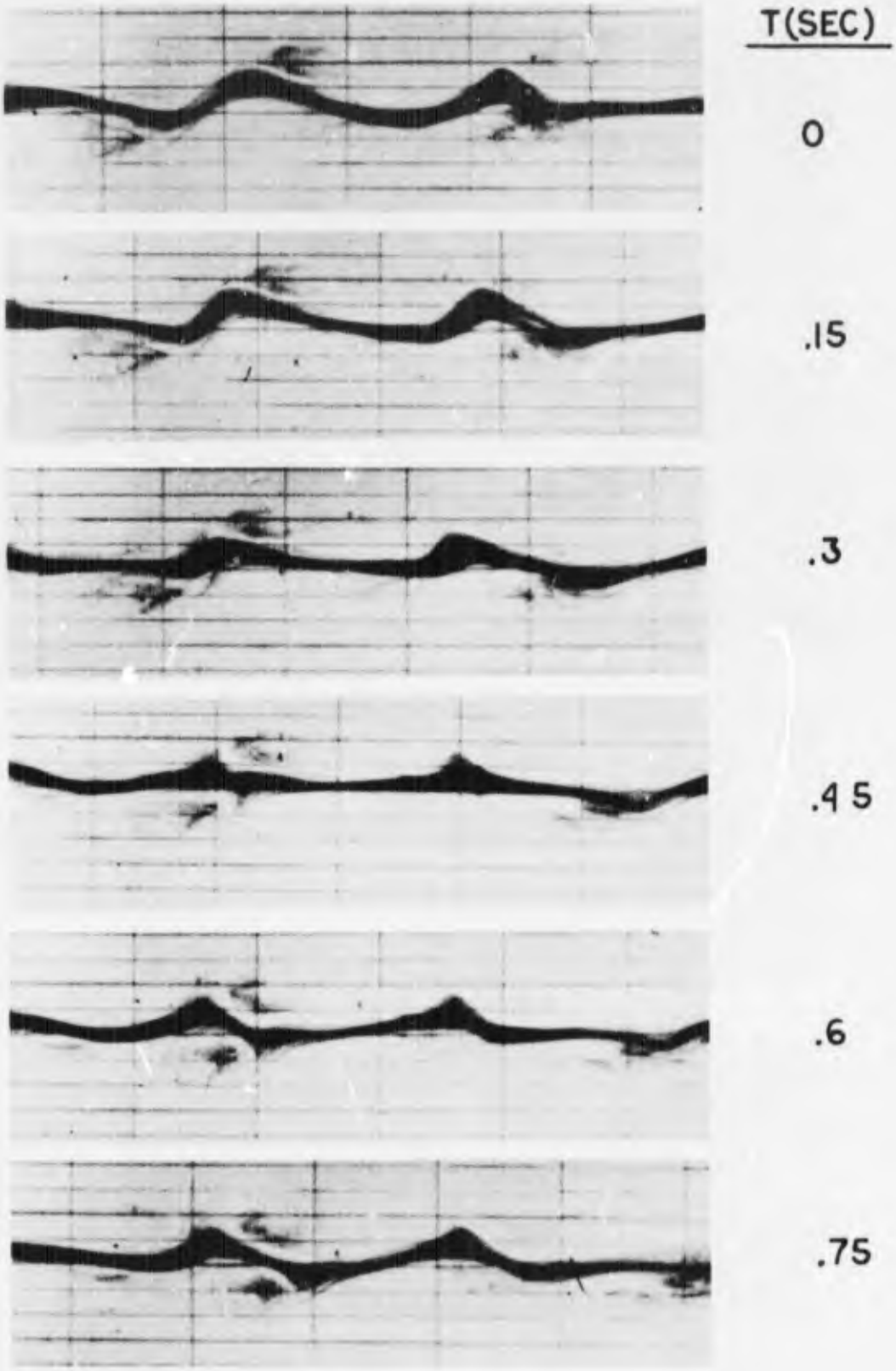

Figure 27: Dye Visualization of Mode II Instability.

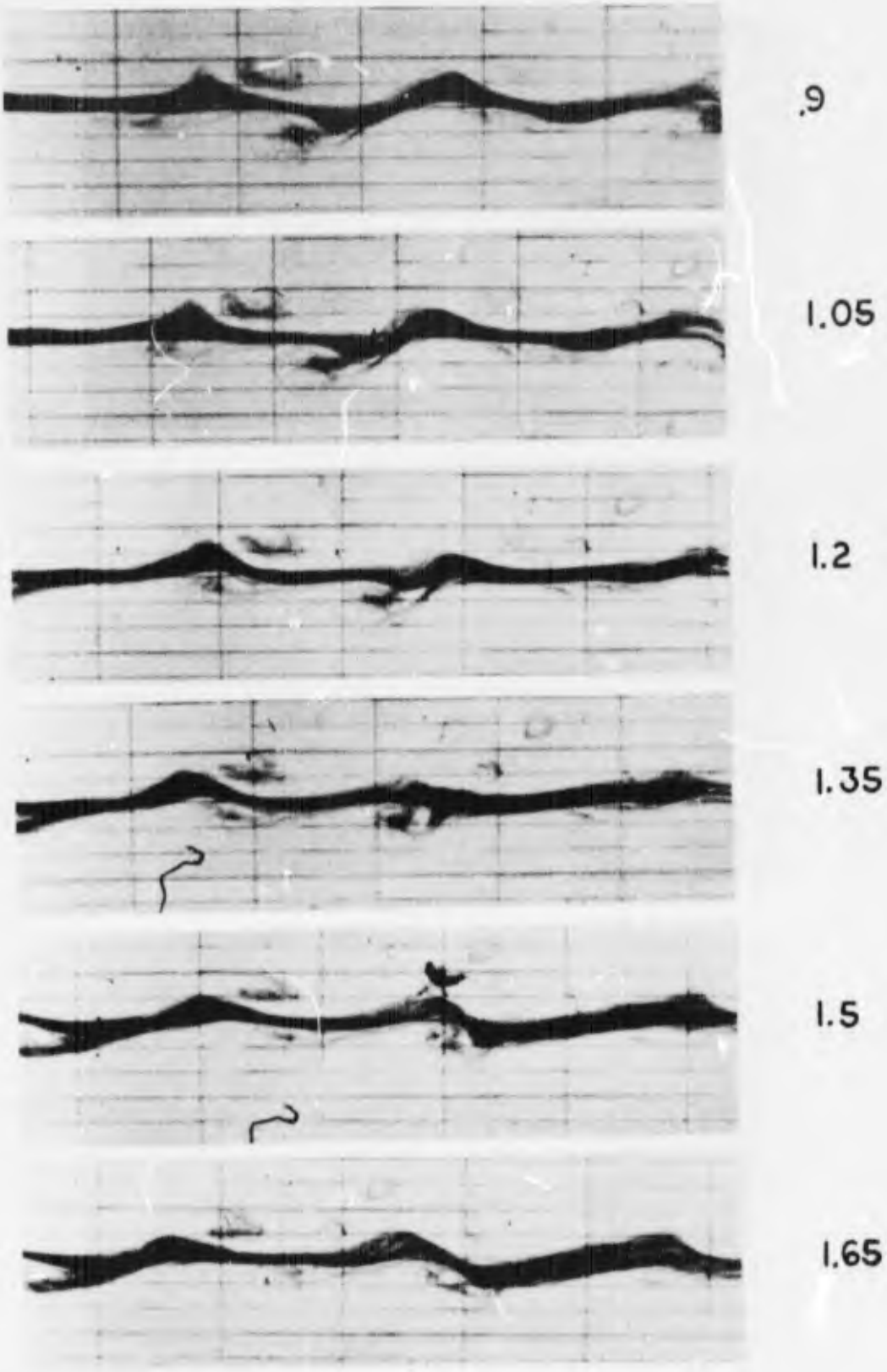

Figure 27: Dye Visualization of Mode II Instability.

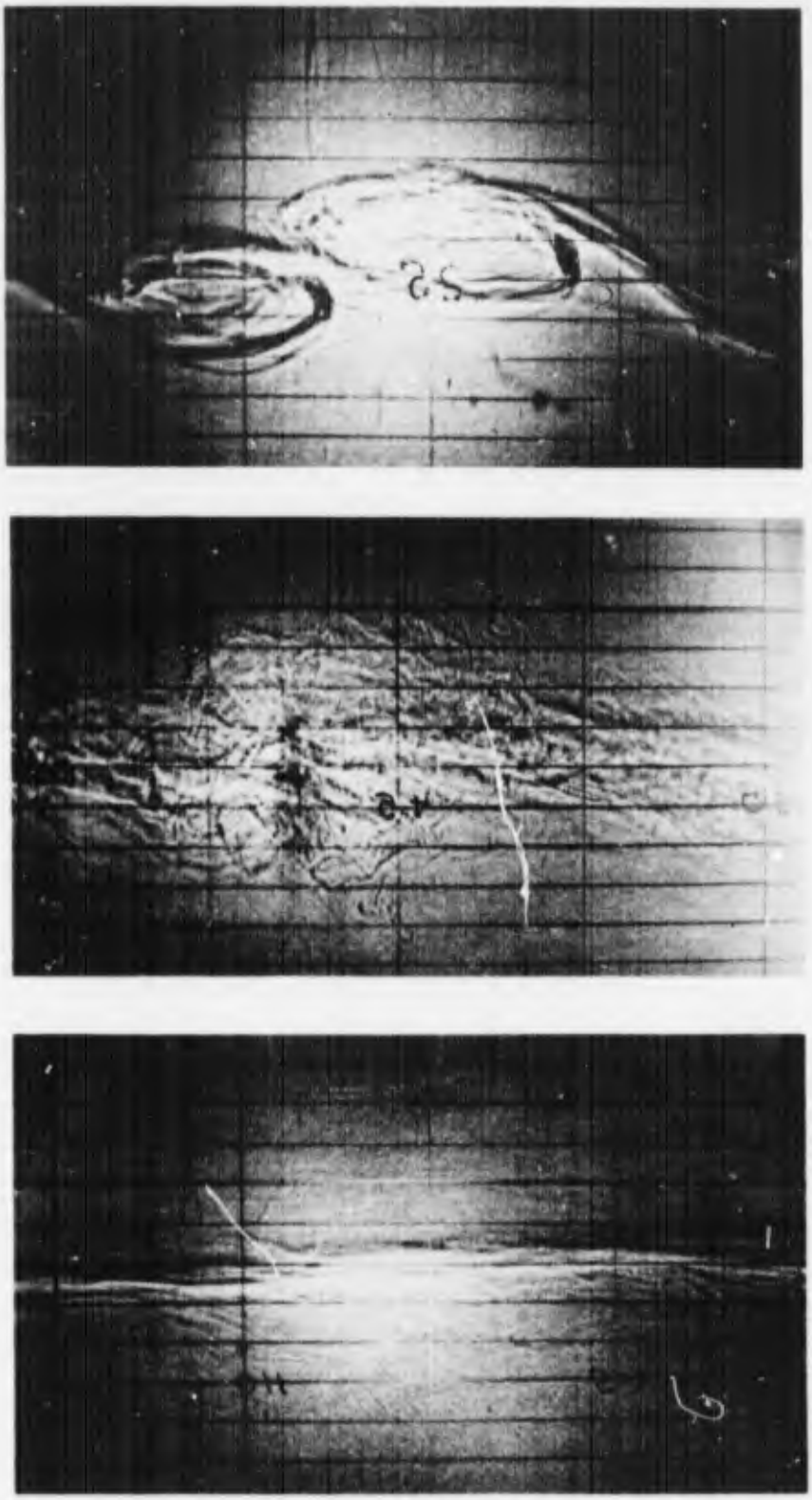

Figure 28: Flow Visualization Using Shadowgraph, Re_{h_o} =200.

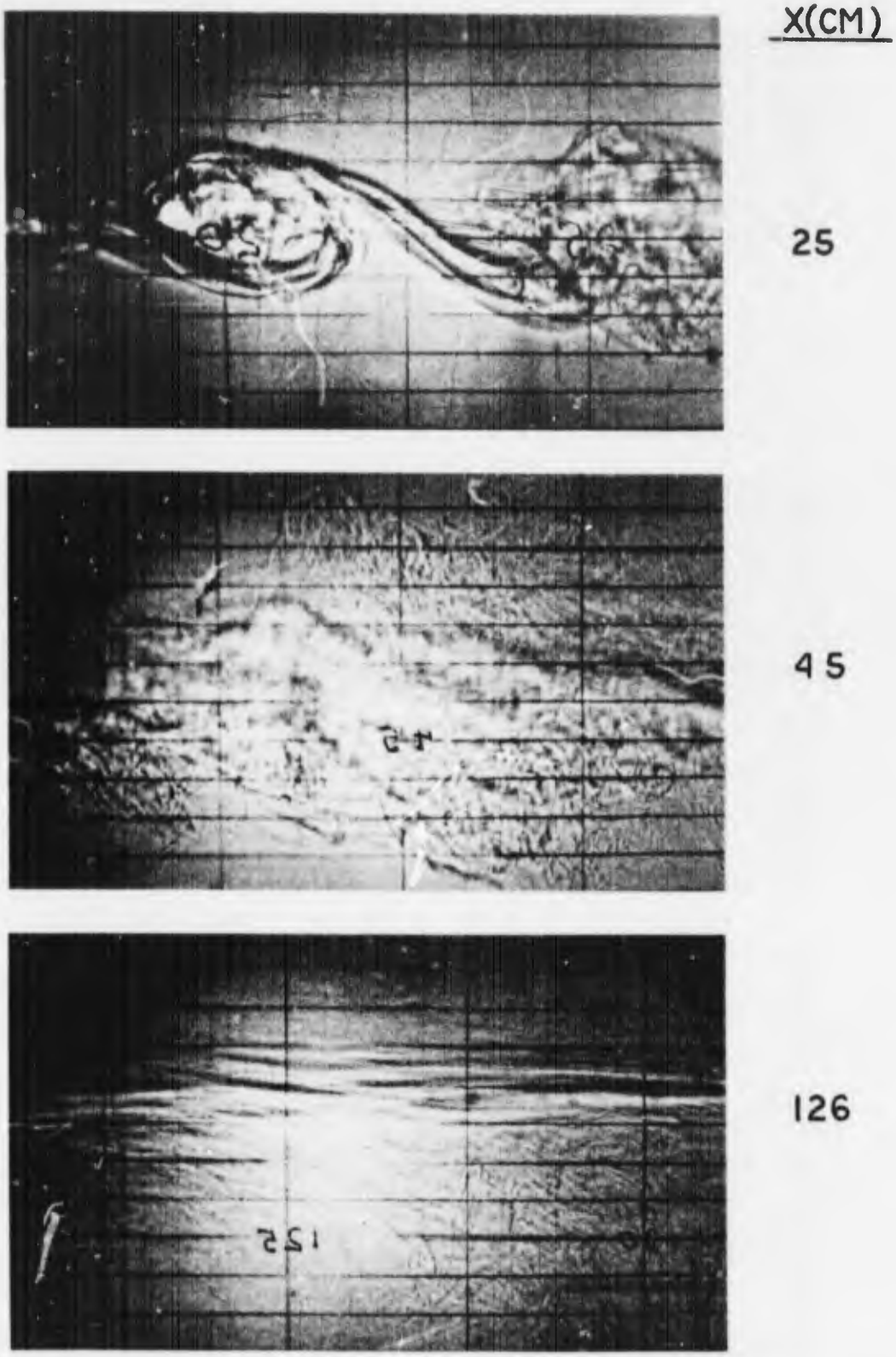

Figure 29: Flow Visualization Using Shadowgraph, Re_{h_o} =250.

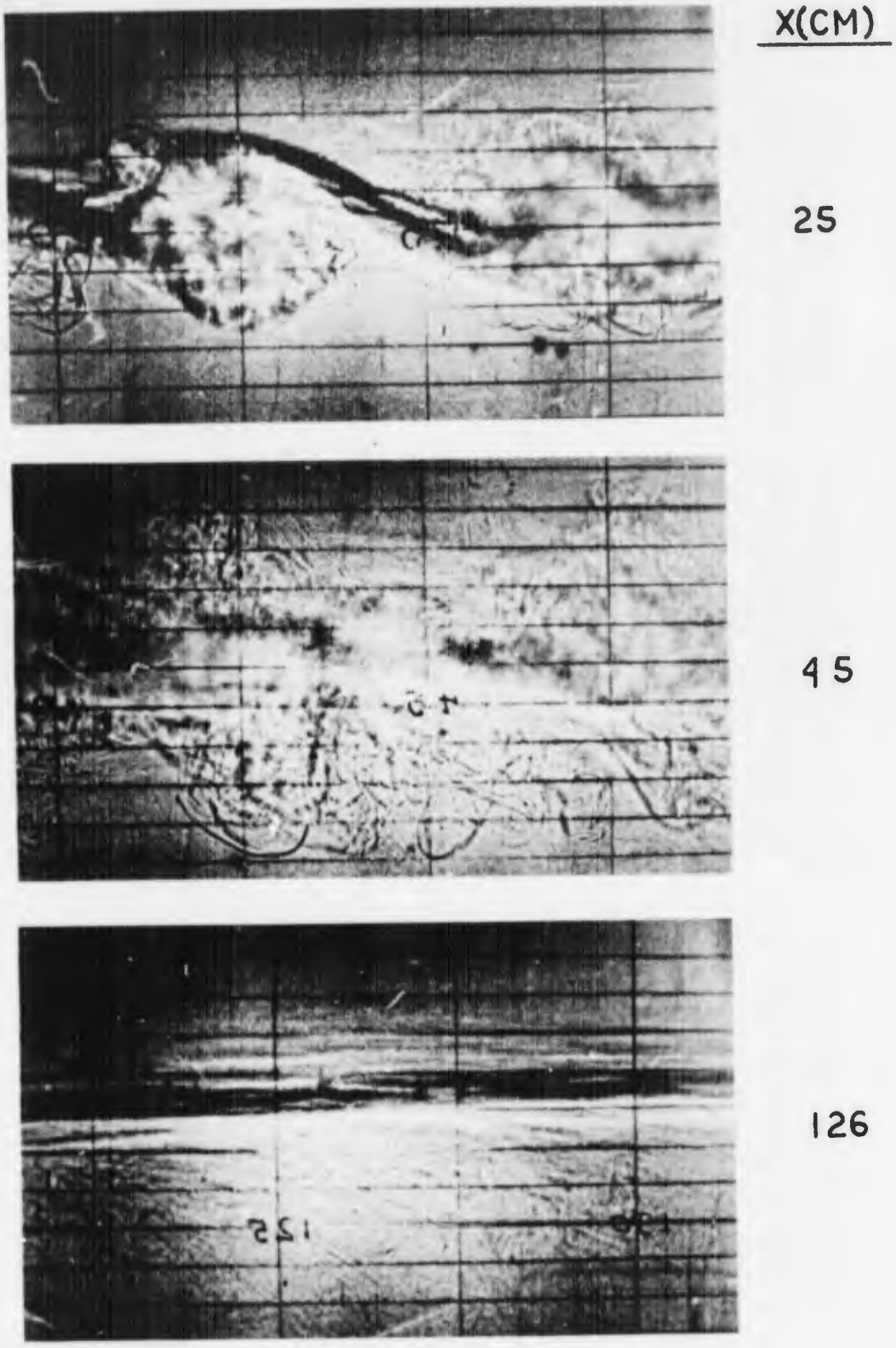

Figure 30: Flow Visualization Using Shadowgraph, Re_{h_o} =300.

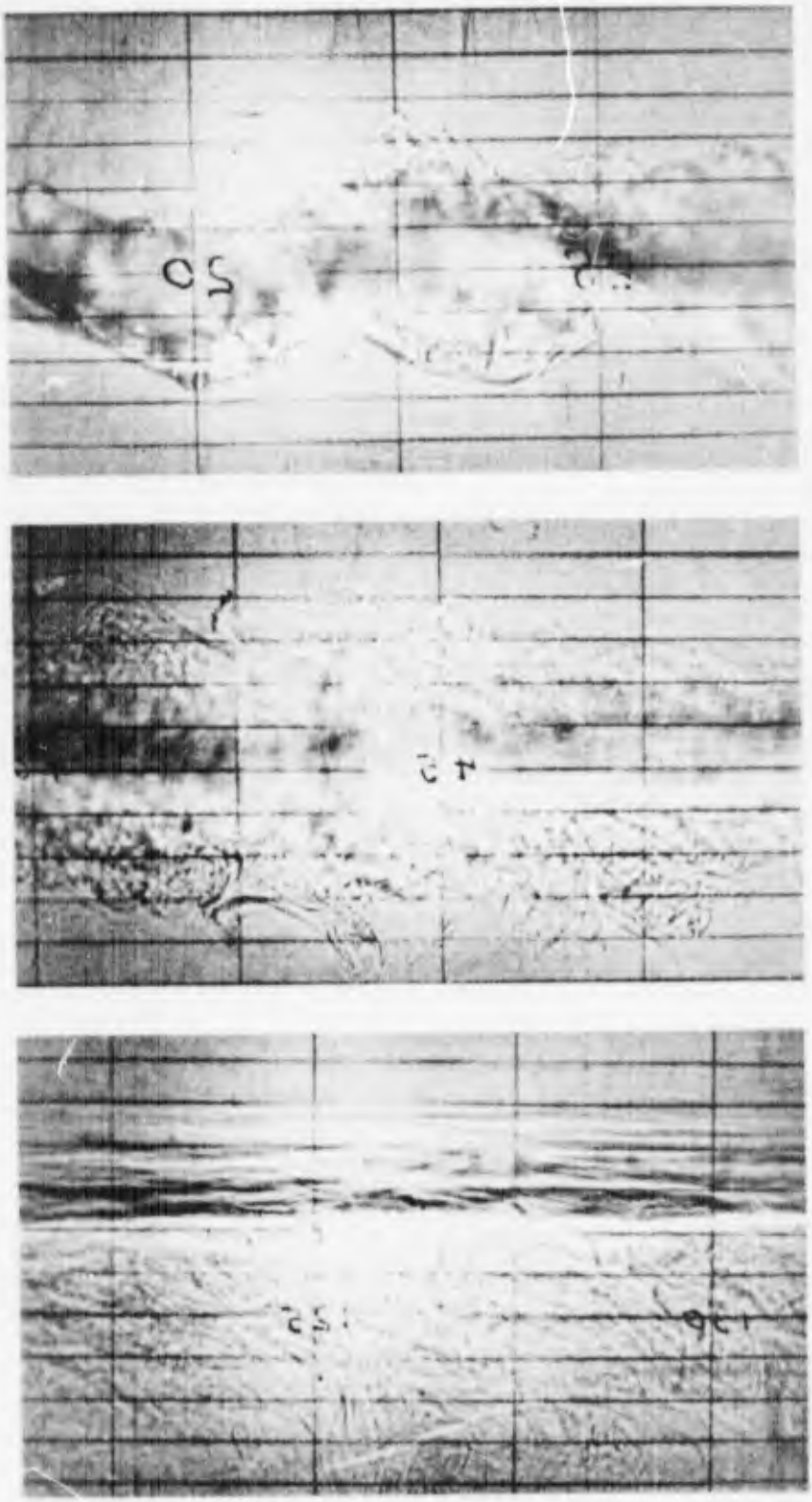

Figure 31: Flow Visualization Using Shadowgraph, Re_{h_o}=350.

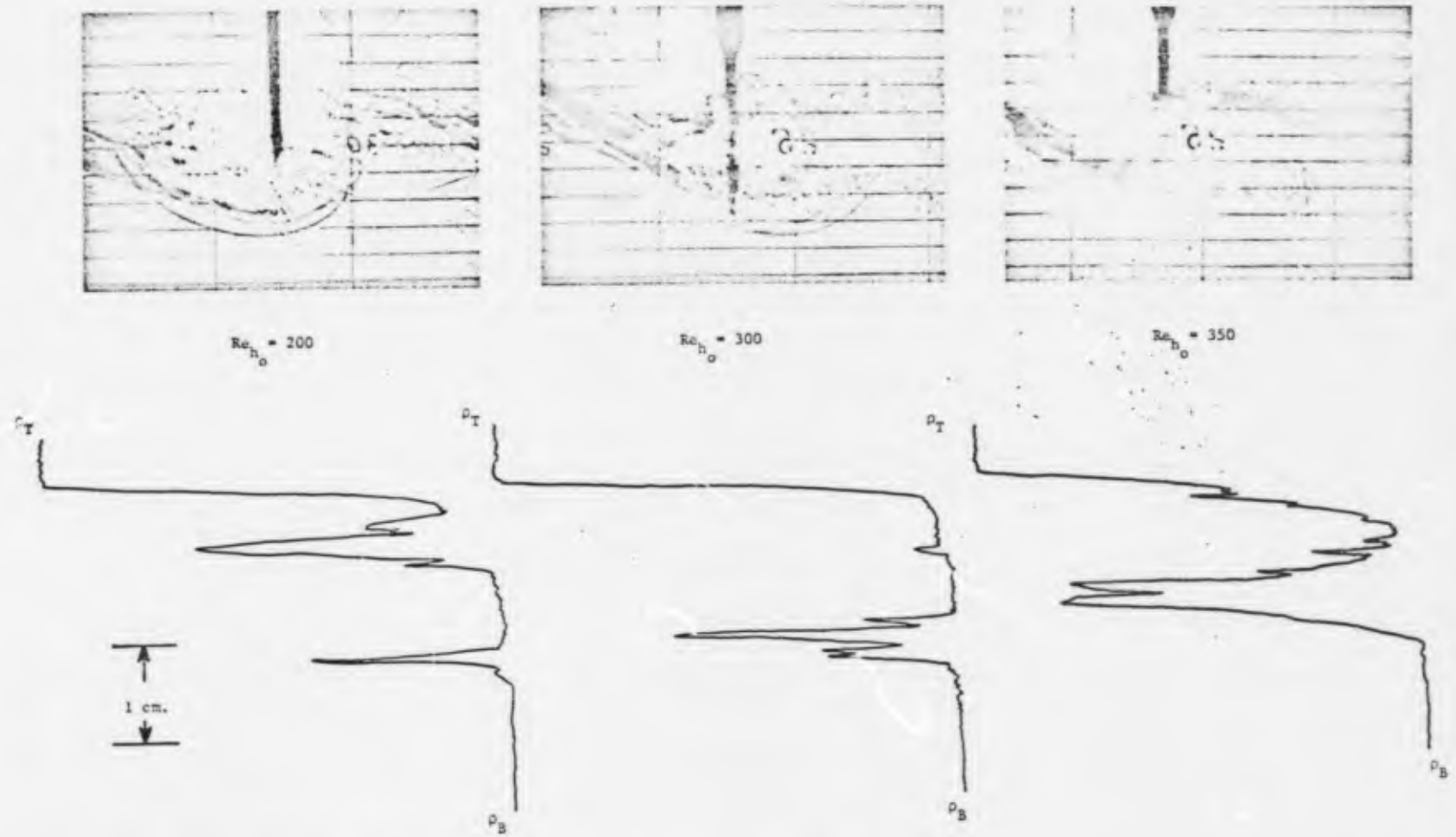

Figure 32: Instantaneous Vertical Distribution of Density, x= 25 cm.

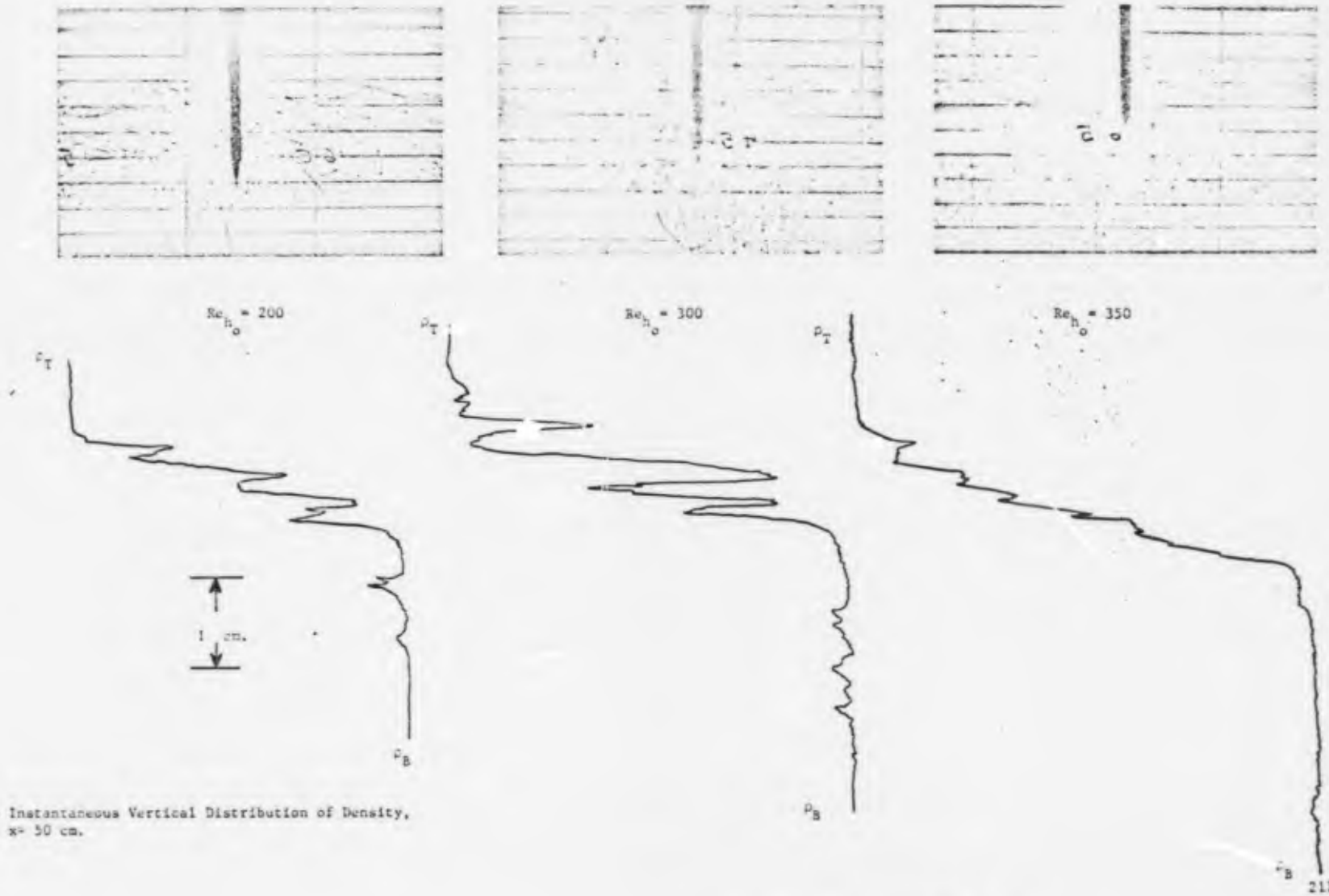

Figure 33: Instantaneous Vertical Distribution of Density, x= 50 cm.

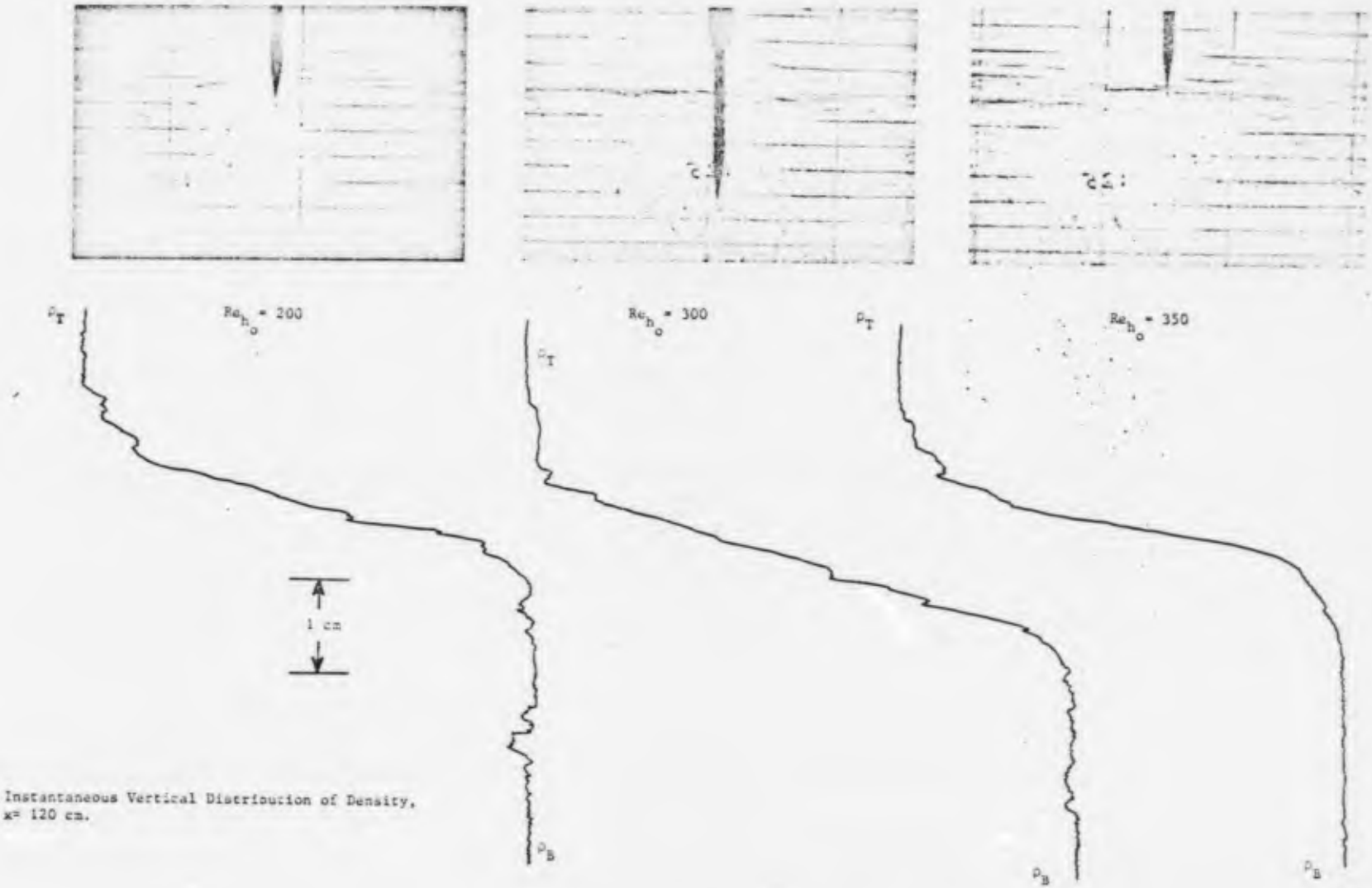

Figure 34a: Instantaneous Vertical Distribution of Density, x= 120 cm.

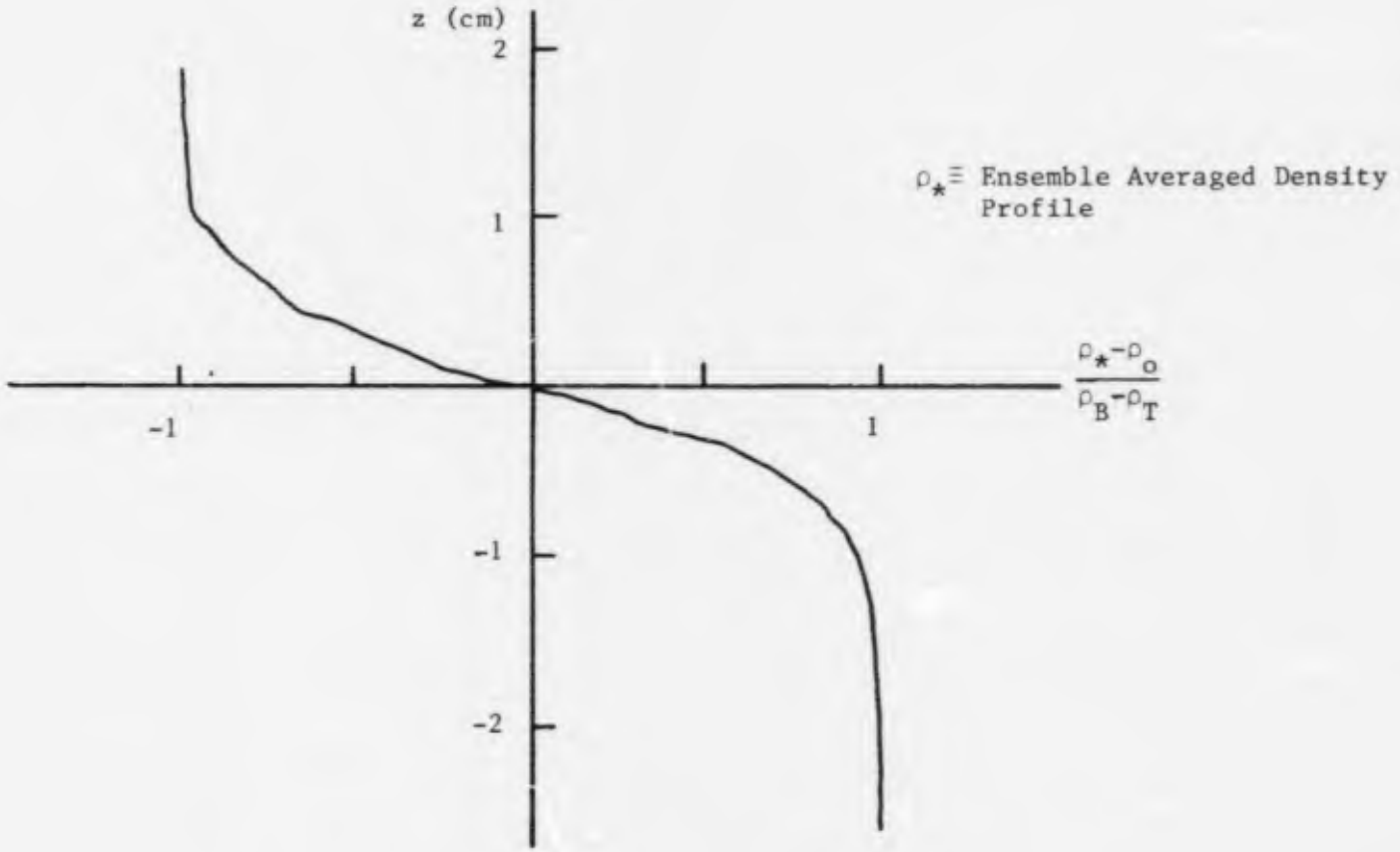

Figure 34b Instantaneous Density Profiles at x= 120 cm.

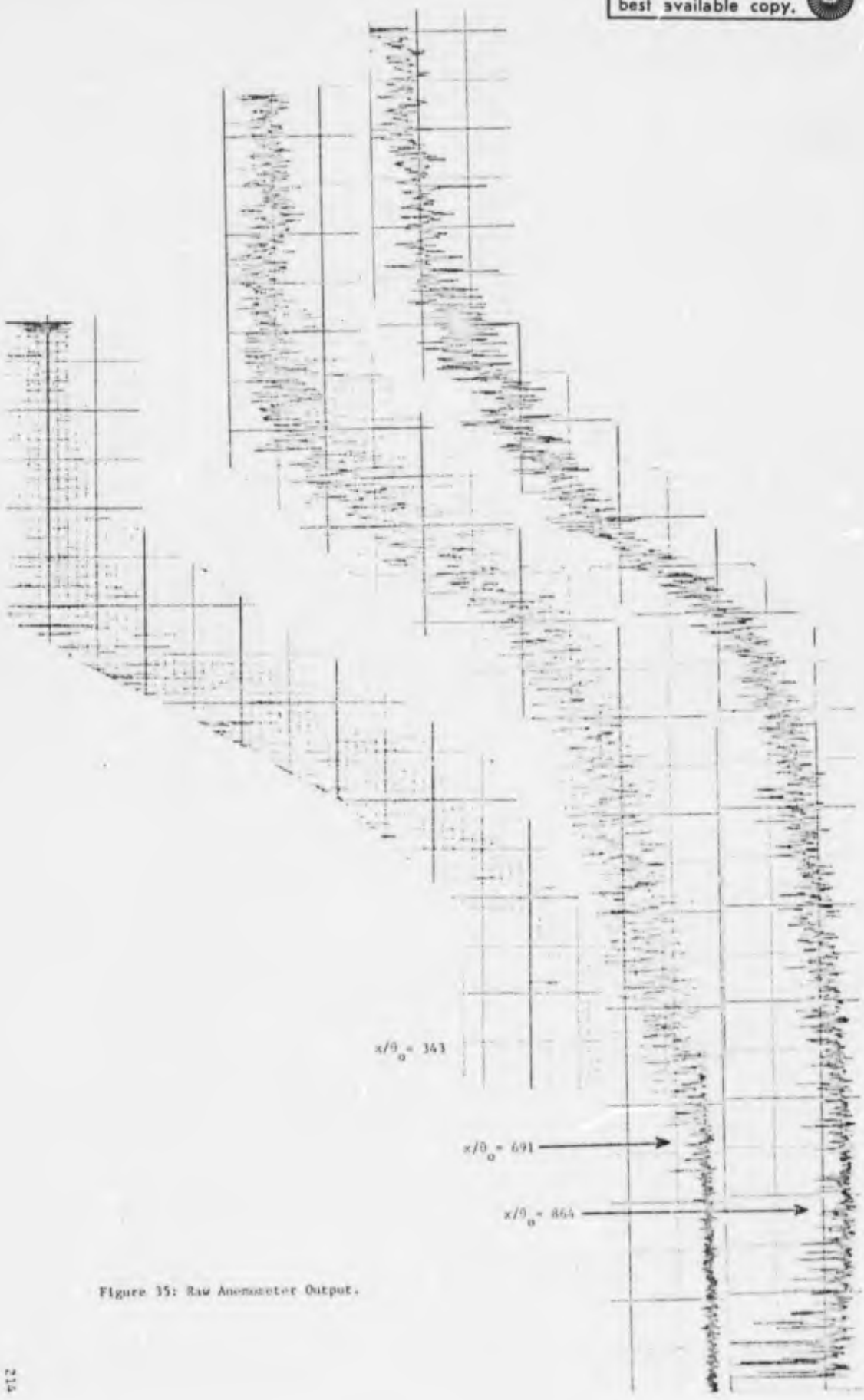

Figure 35: Raw Anemometer Output.

x/θ_o = 343

x/θ_o = 691

x/θ_o = 1723

Figure 36: Raw Conductivity Probe Output.

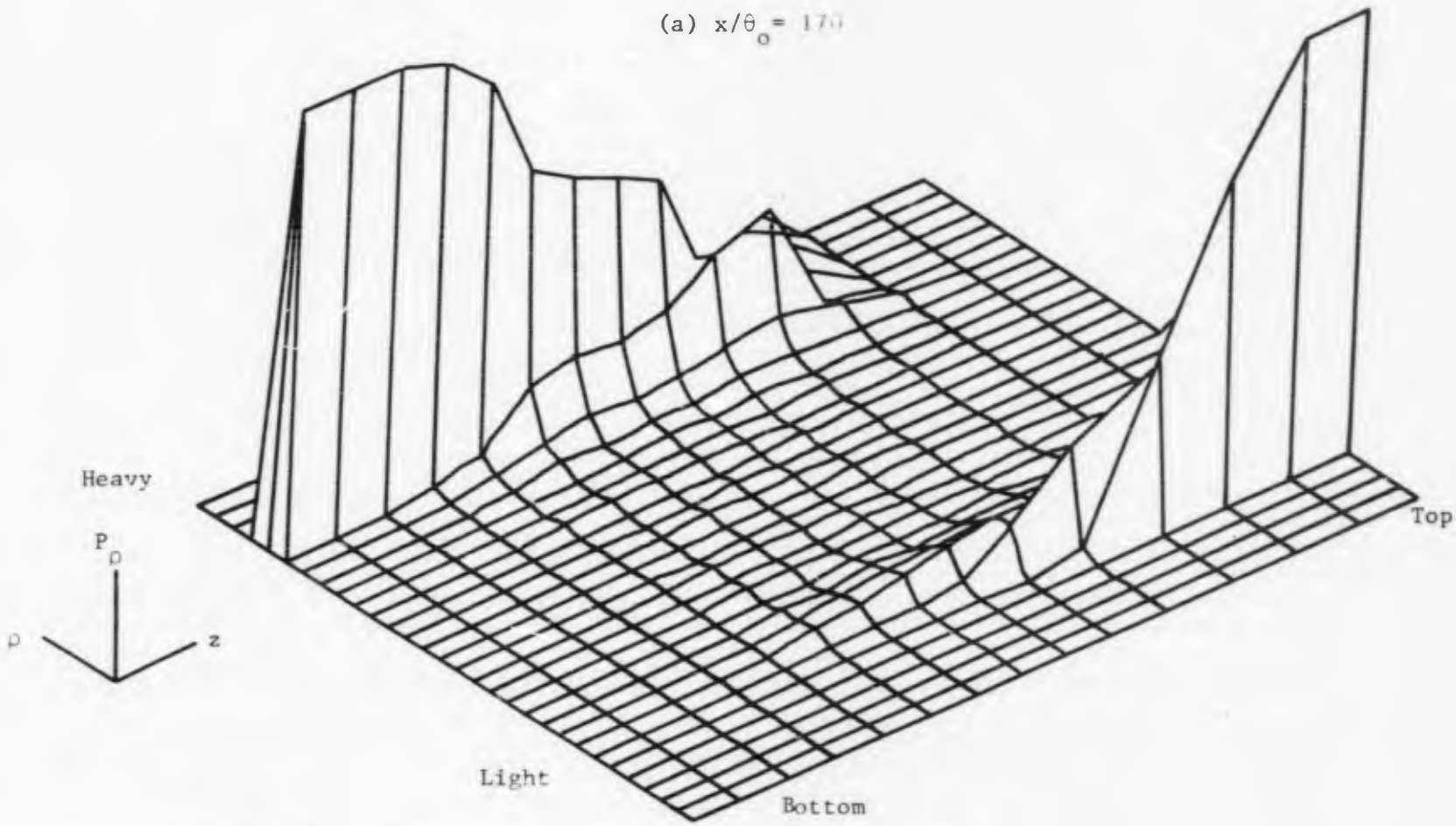

Figure 37: Probability Distribution Function $P_\rho(\rho,\rho+\delta\rho;z)$

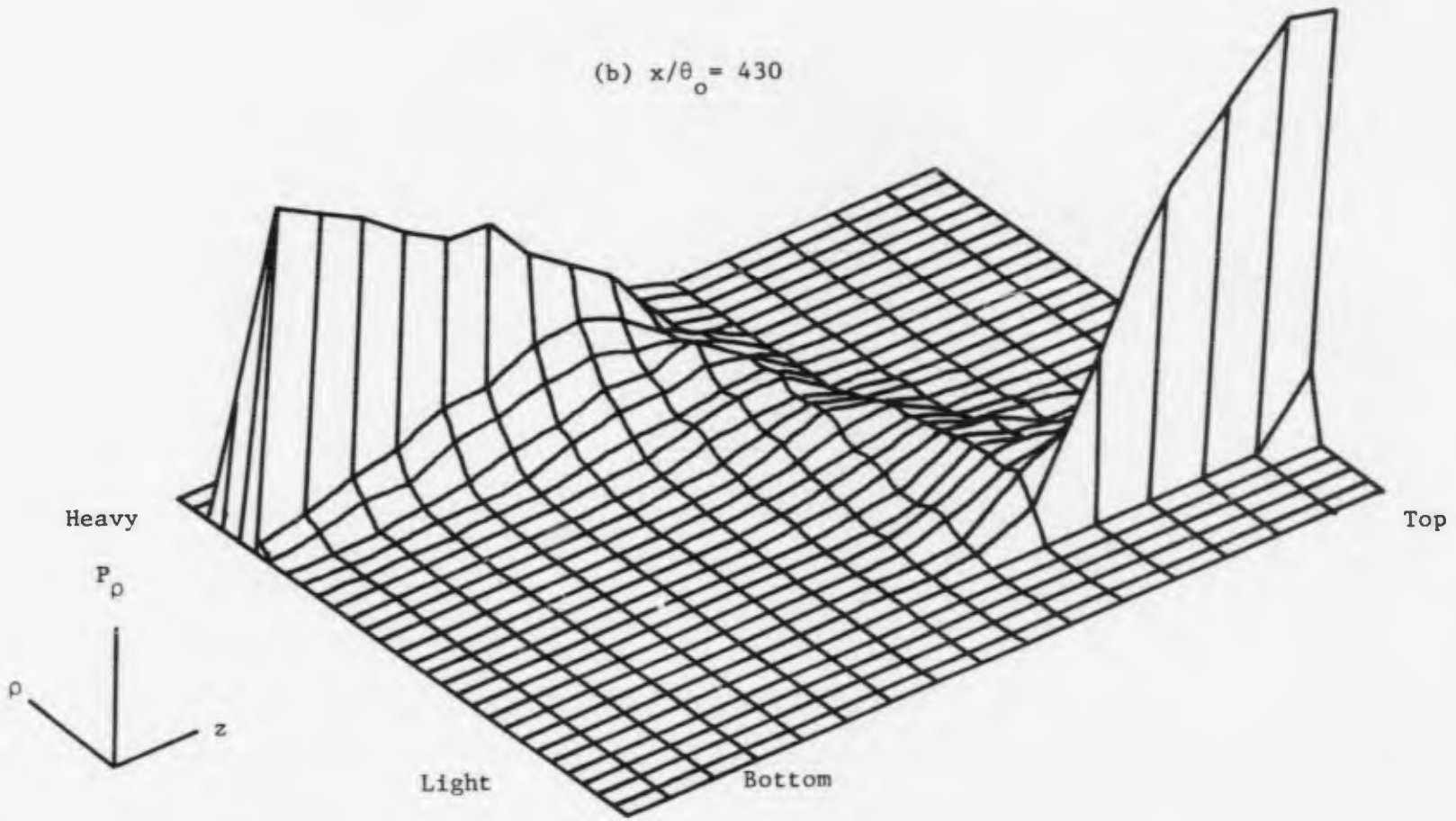

Figure 37: Probability Distribution Function $P_\rho(\rho,\rho+\delta\rho;z)$.

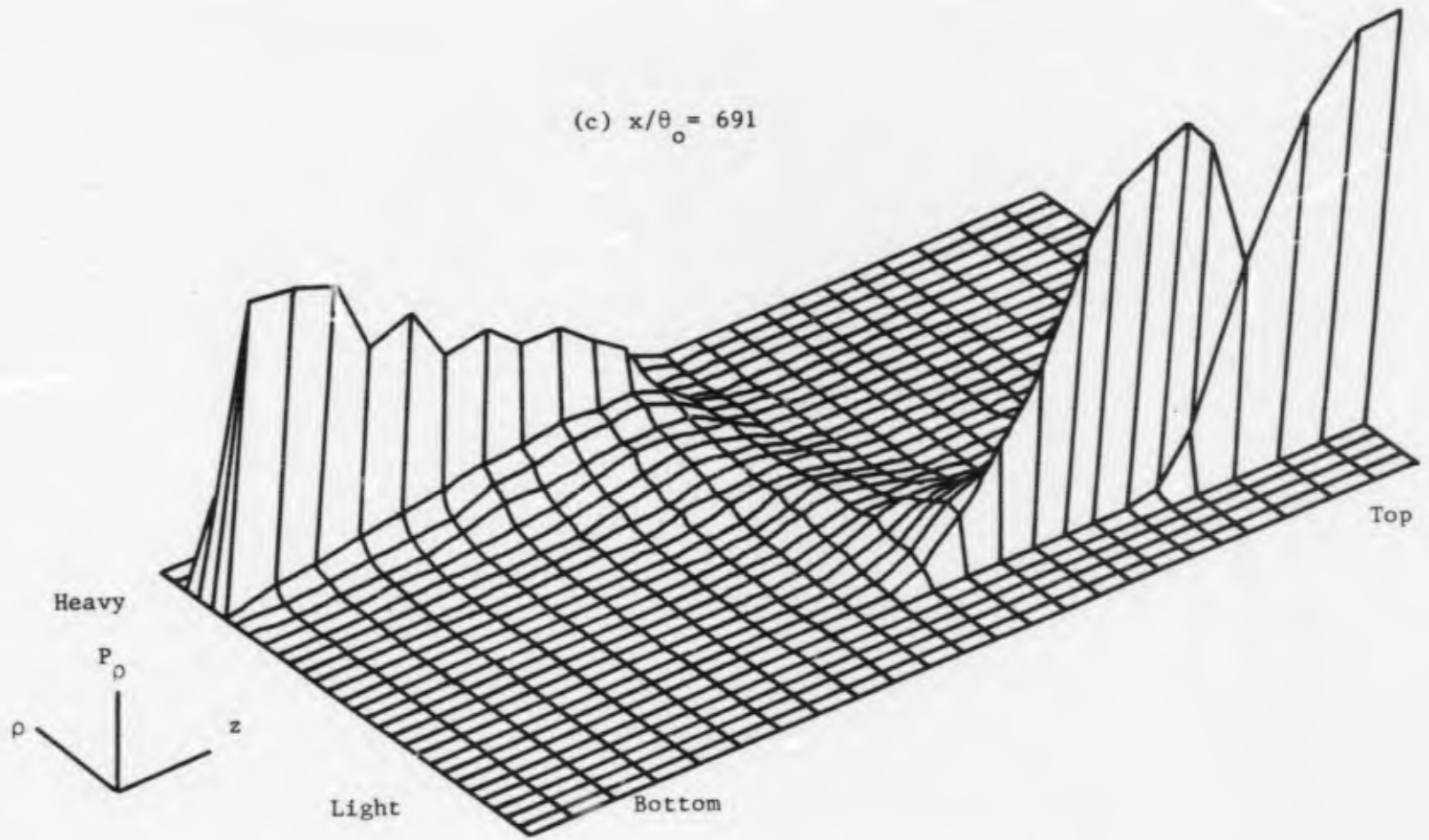

Figure 37: Probability Distribution Function $P_\rho(\rho,\rho+\delta\rho;z)$

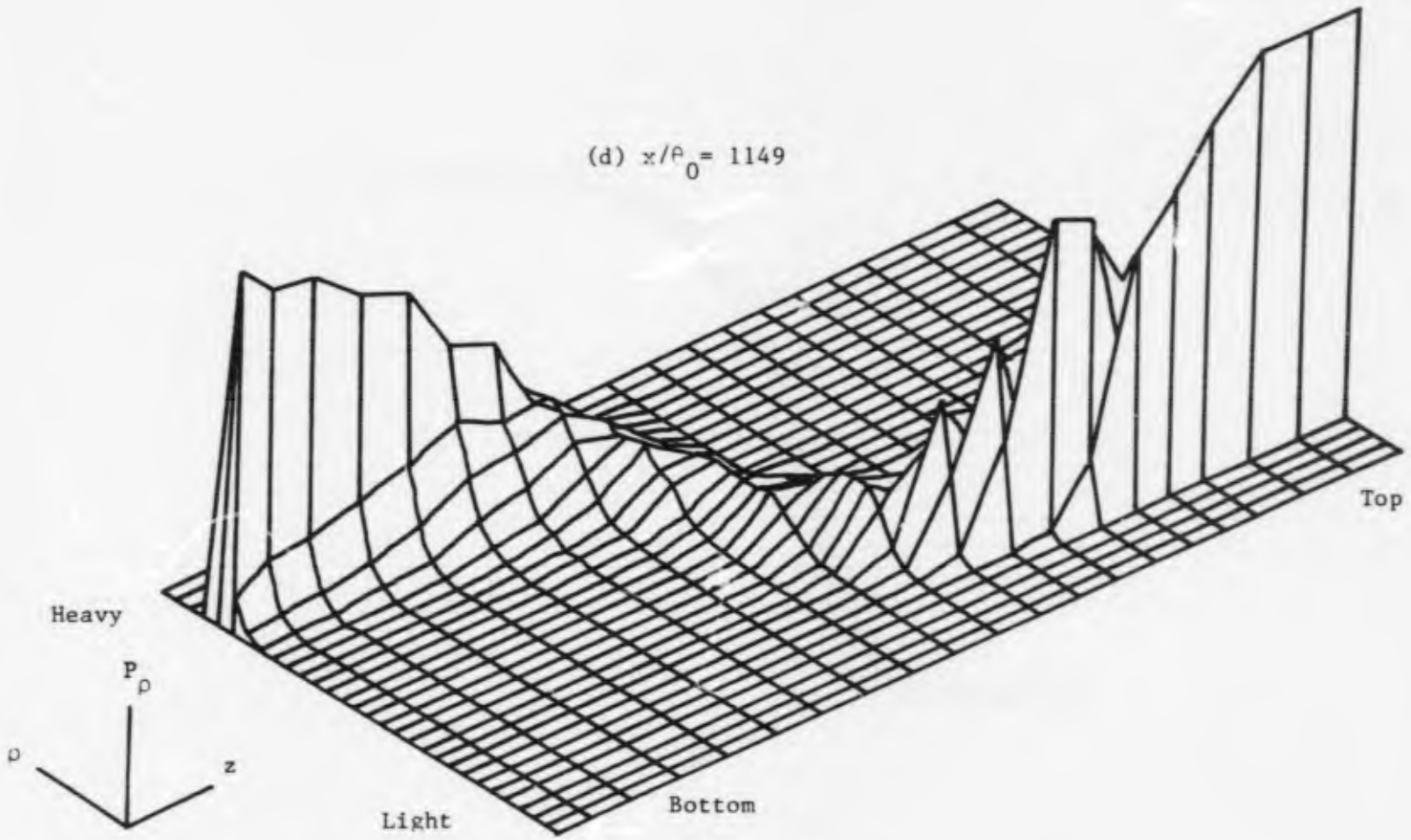

Figure 37: Probability Distribution Function $P_\rho(\rho,\rho+\delta\rho;z)$

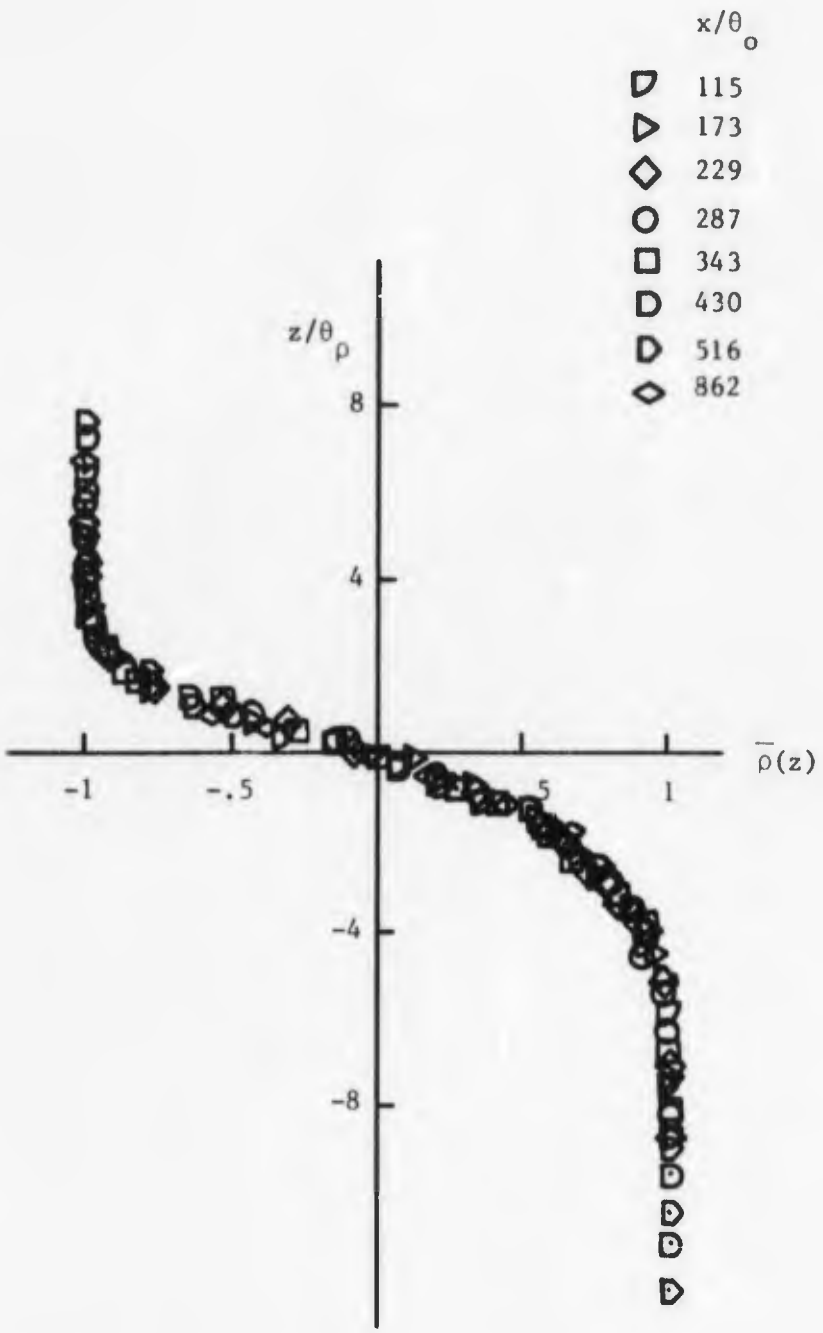

Figure 38: Mean Density Distribution.

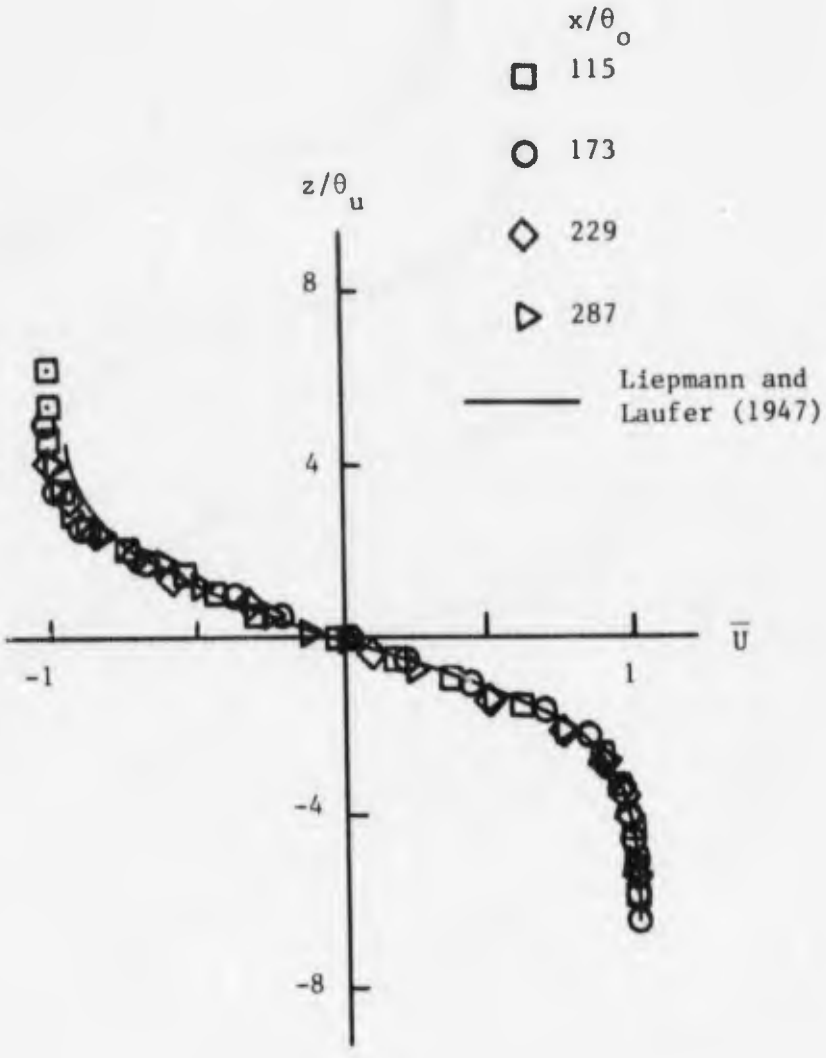

(a) $x/\theta_o < 300$

Figure 39: Mean Velocity Profile

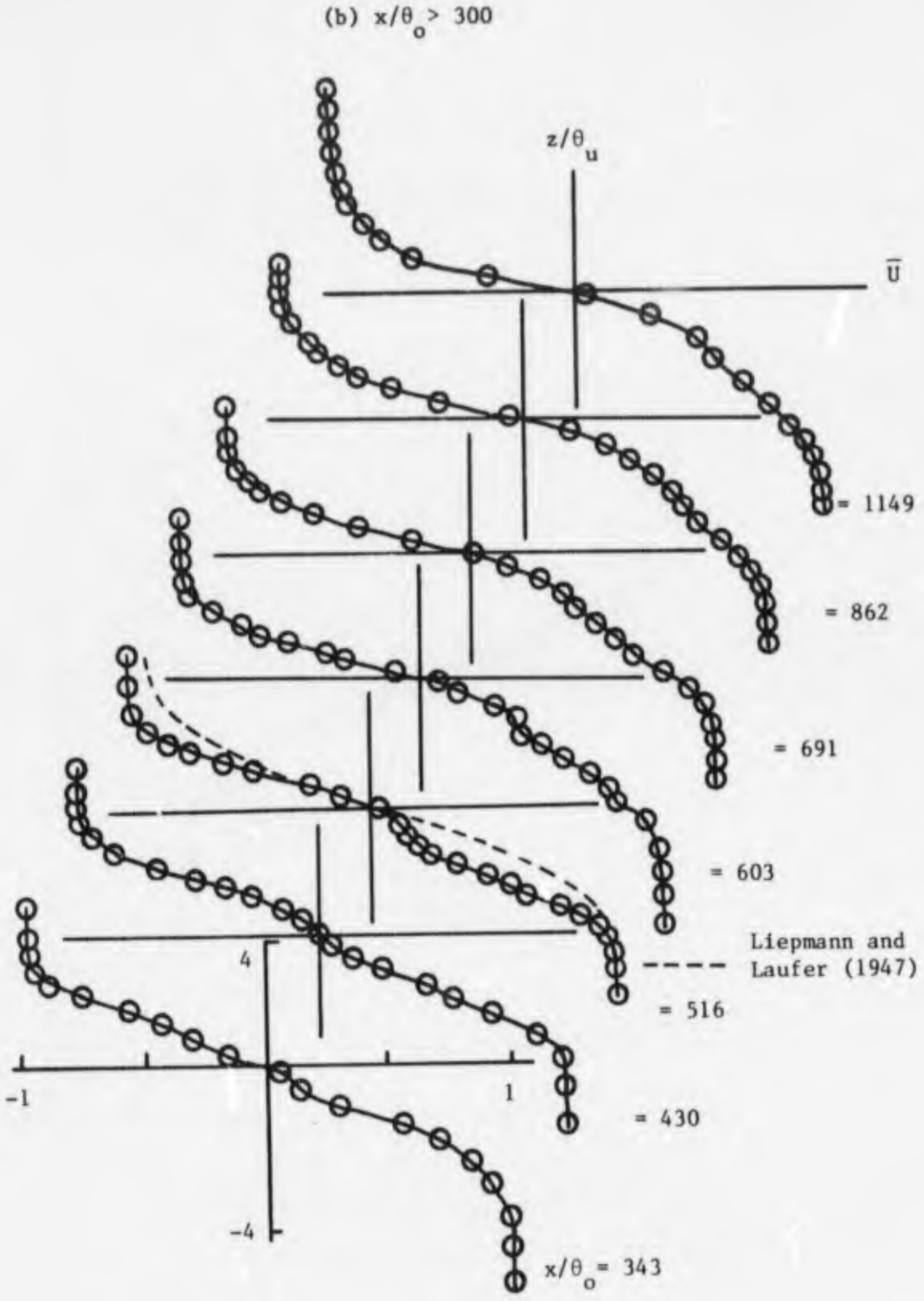

Figure 39: Mean Velocity Profile.

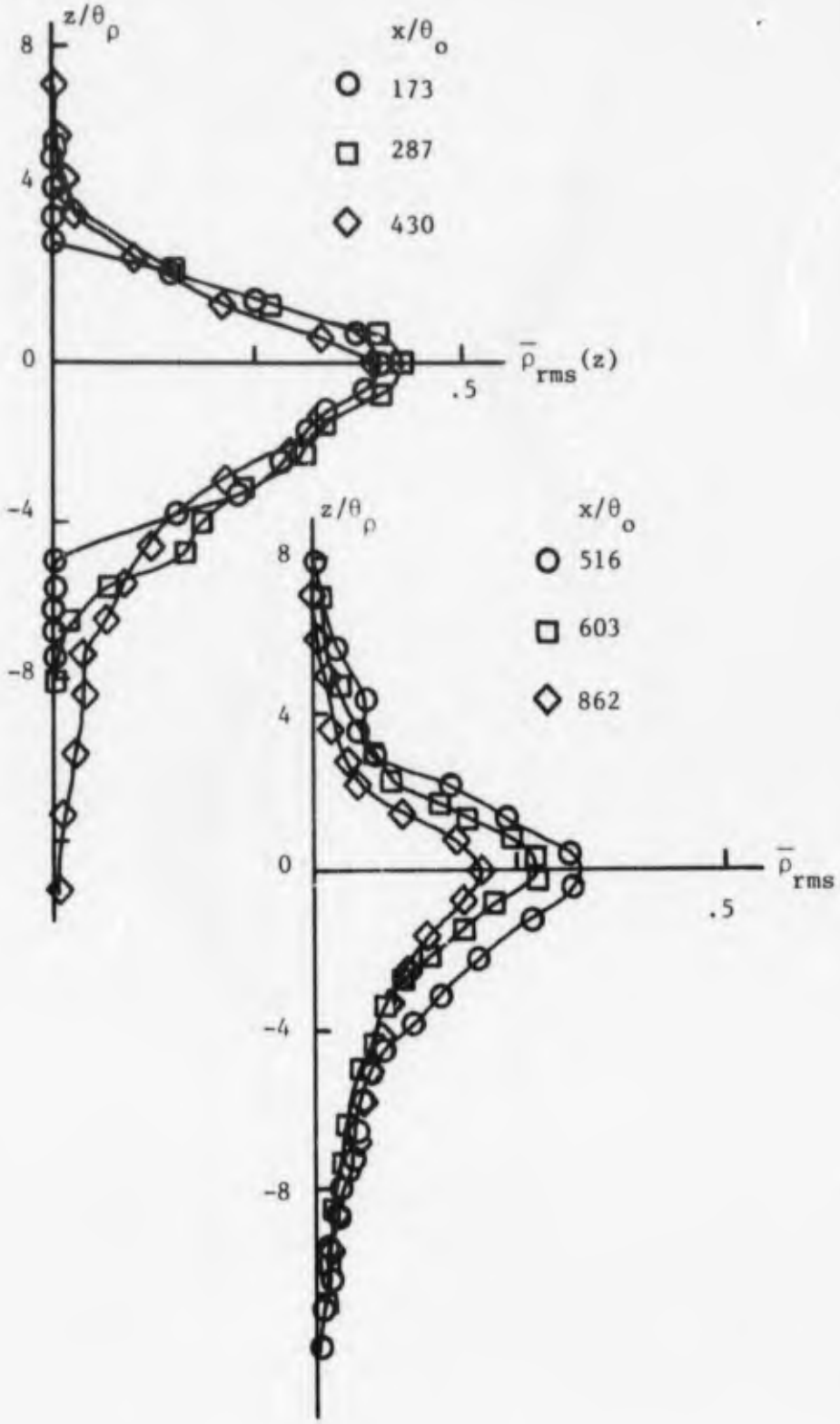

Figure 40: Normalized RMS Density Profile.

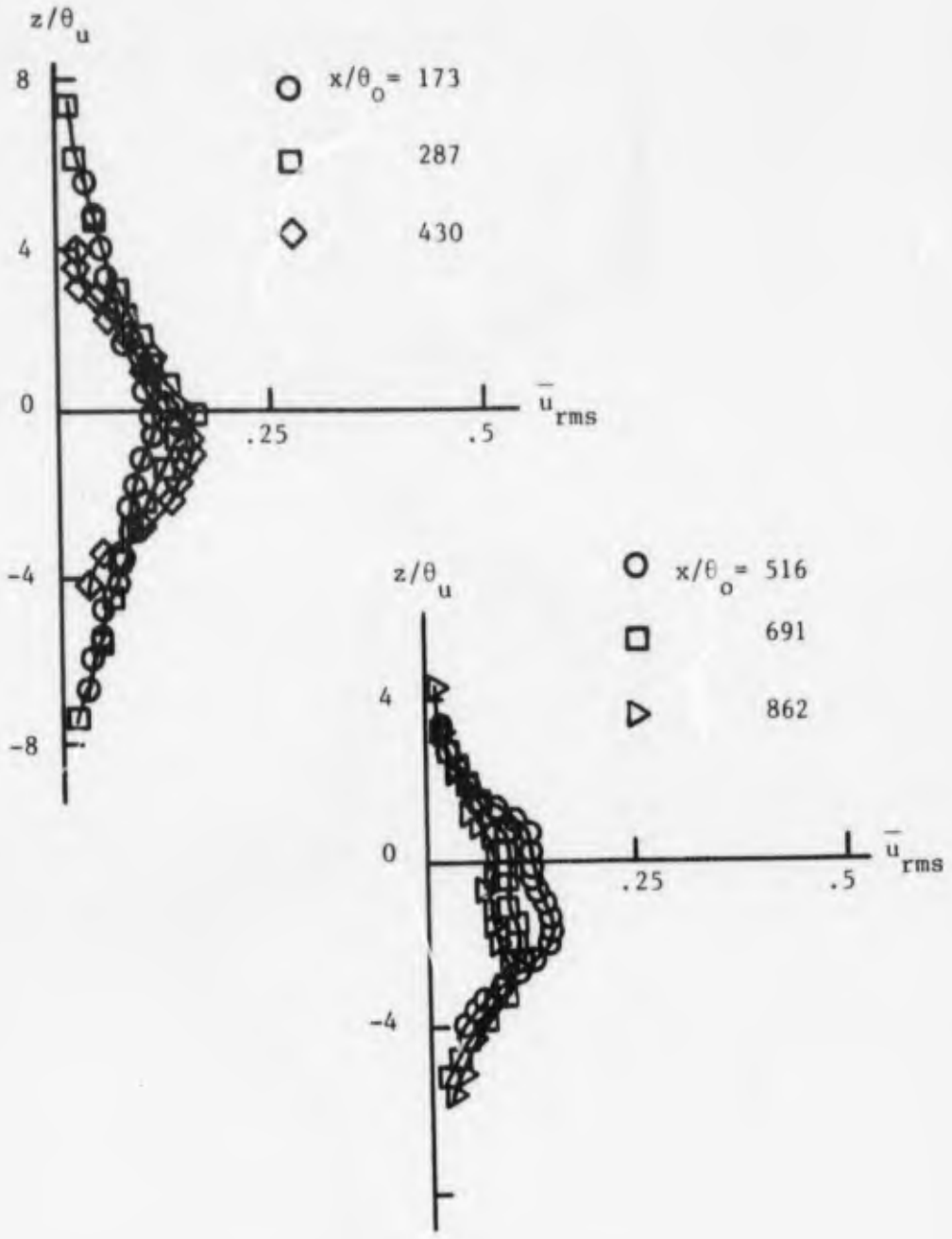

Figure 41: Normalized RMS Velocity Profile

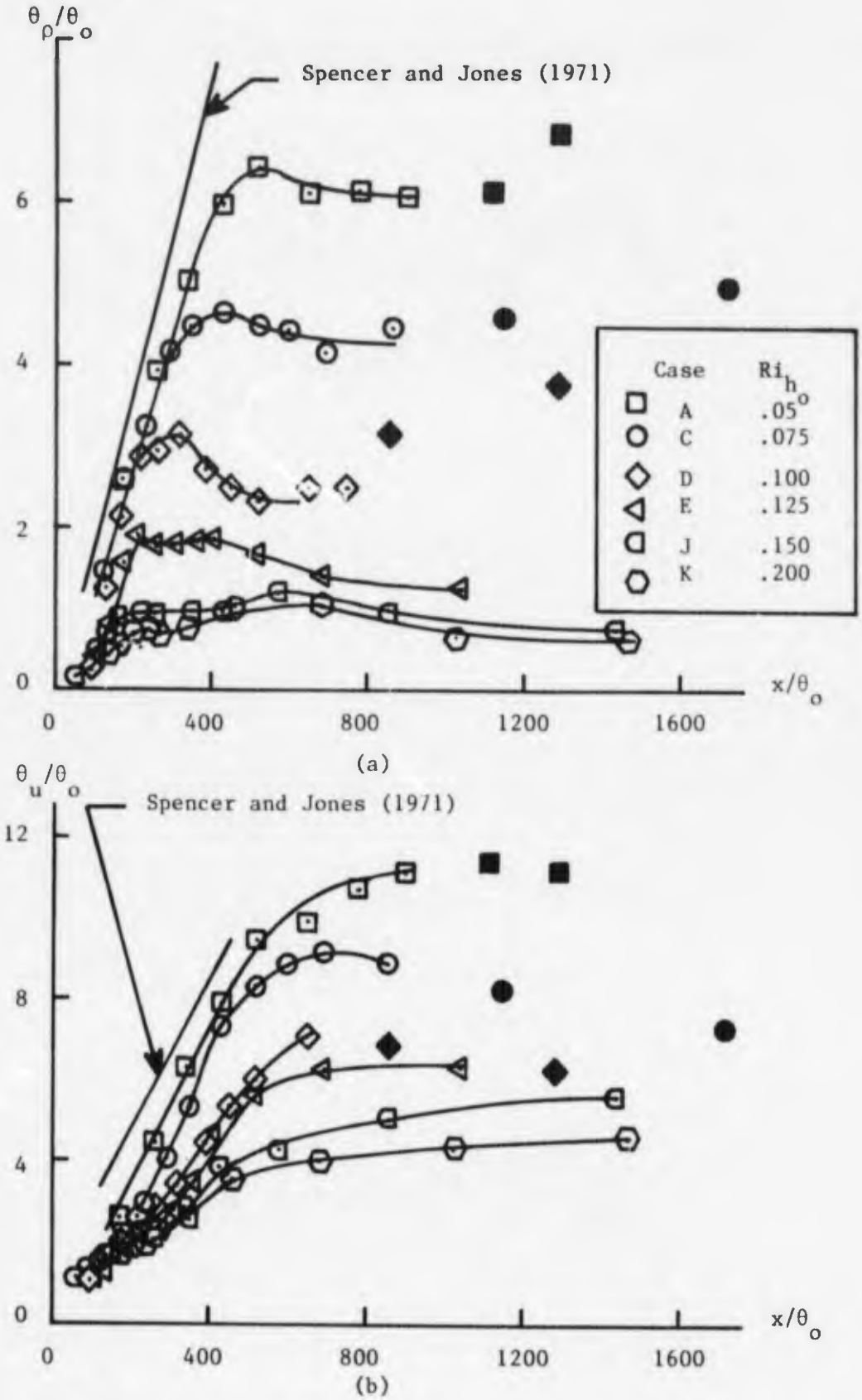

Figure 42: Effect of Ri_{h_o} upon $\theta_u(x/\theta_o)$ and $\theta_\rho(x/\theta_o)$.

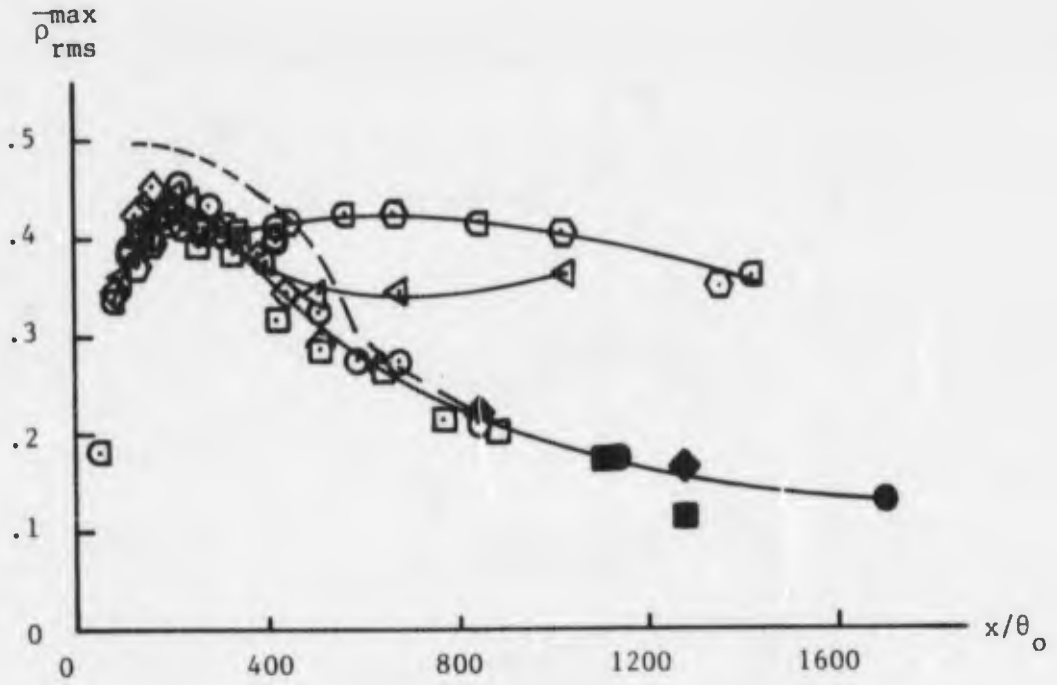

(a)

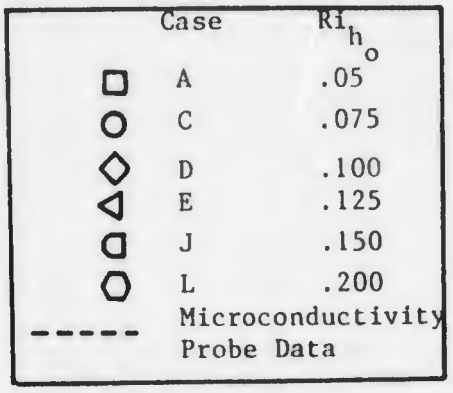

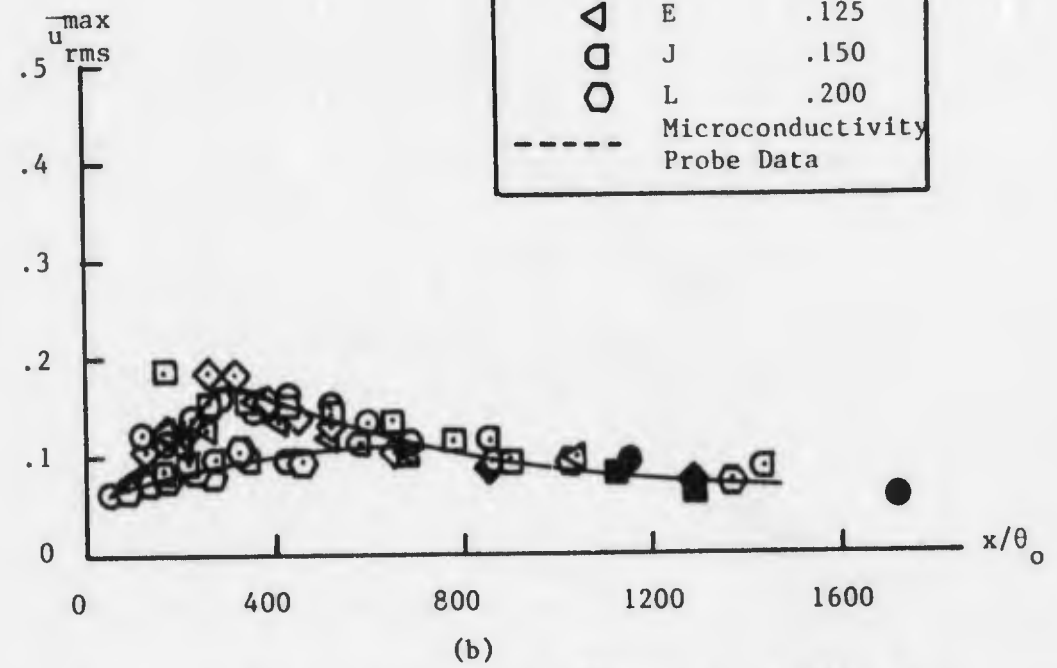

(b)

Figure 43: Effect of Ri_{h_o} upon $\overline{u}^{max}_{rms}(x/\theta_o)$ and $\overline{\rho}^{max}_{rms}(x/\theta_o)$.

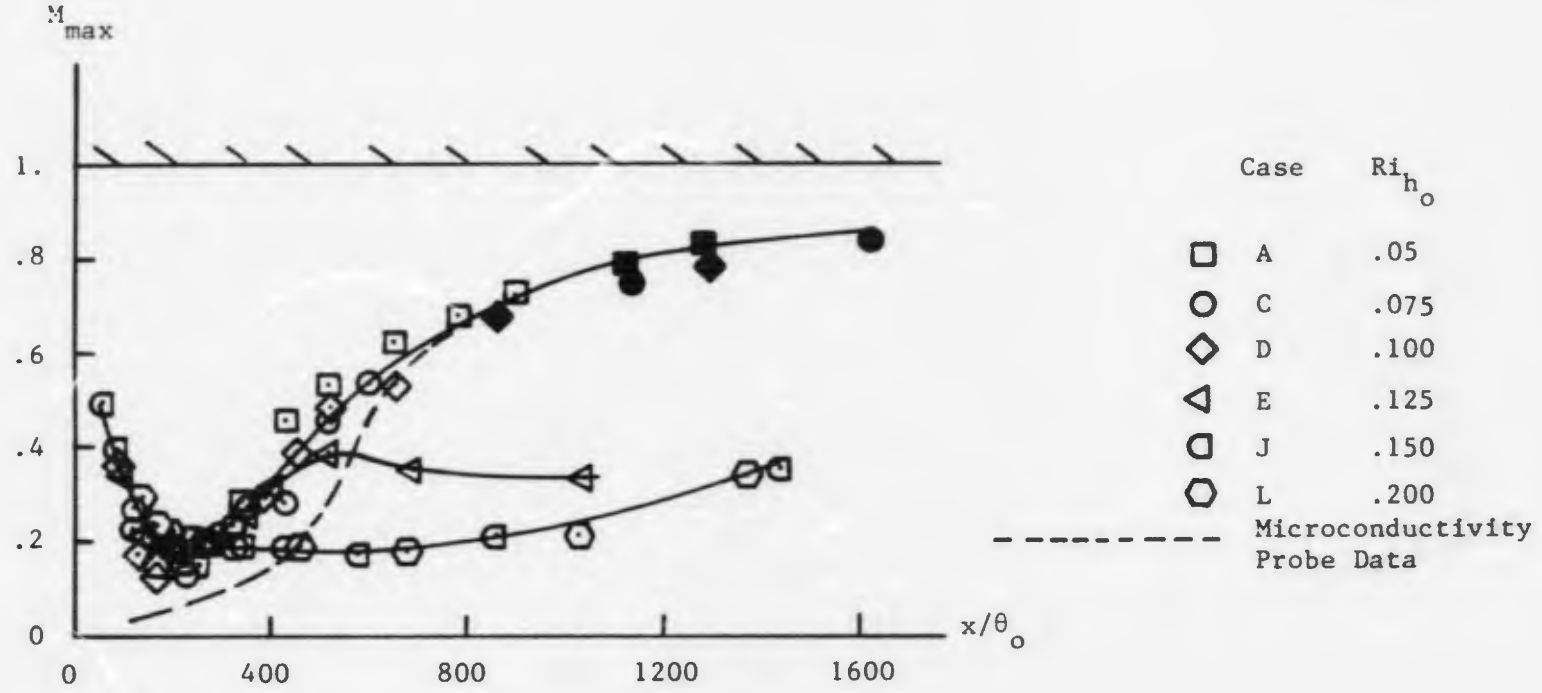

Figure 44: Effect of Ri_{h_o} upon $M_{max}(x/\theta_o)$.

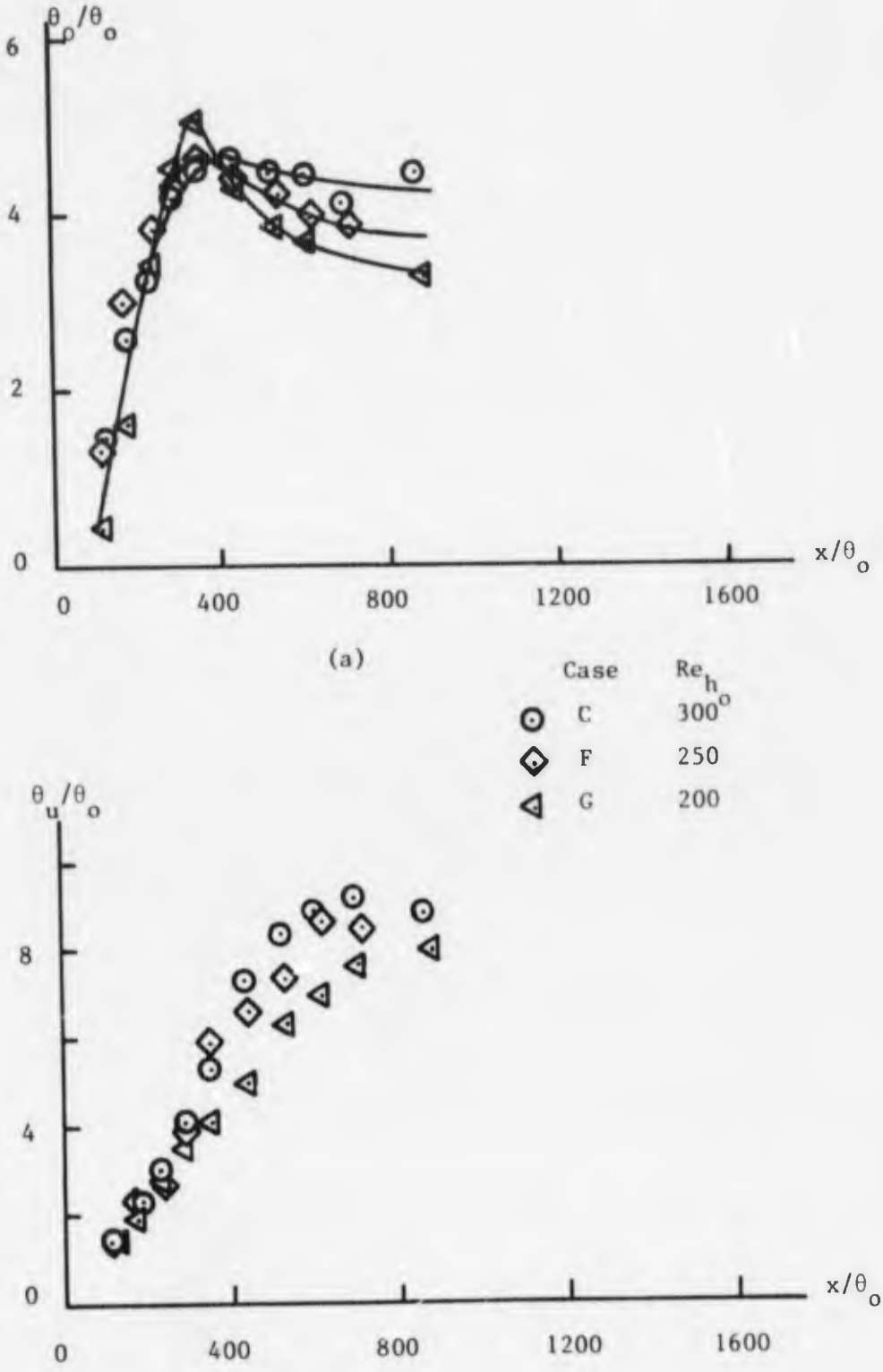

Figure 45: Effect of Re_{h_o} Upon $\theta_\rho(x/\theta_o)$ and $\theta_u(x/\theta_o)$.

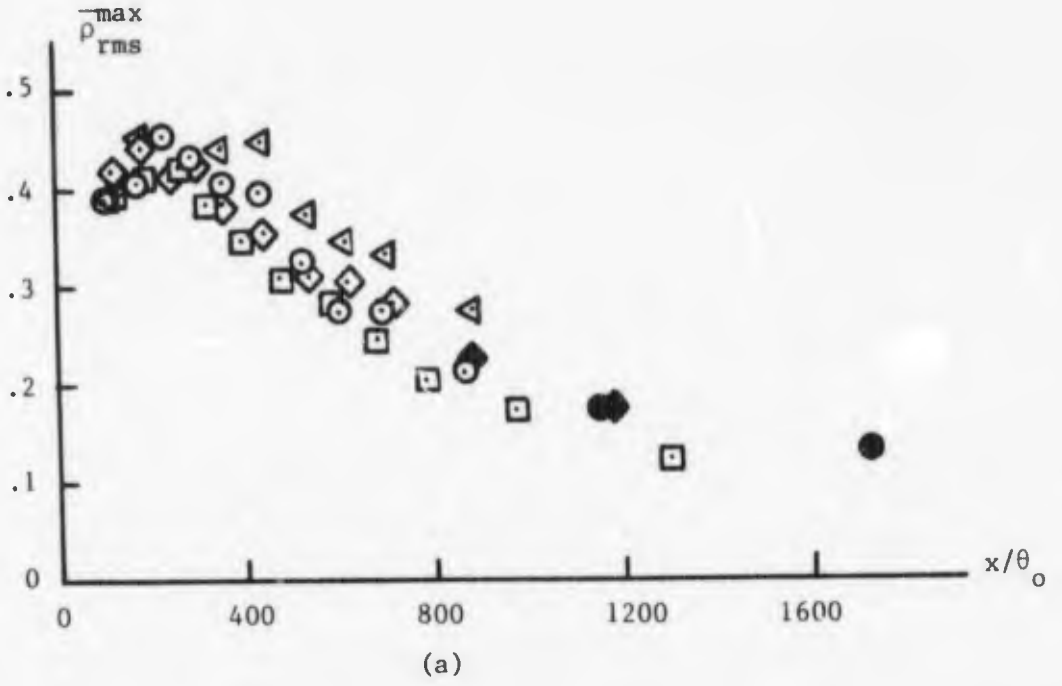

(a)

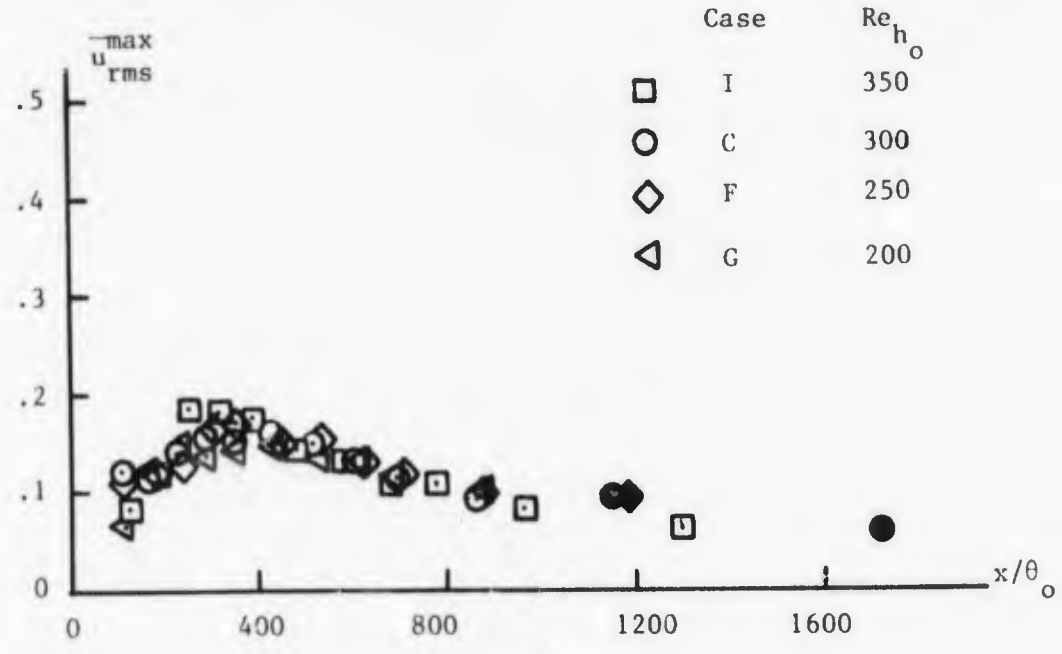

(b)

Figure 46: Effect of Re_{h_o} upon $\overline{\rho}^{max}_{rms}(x/\theta_o)$ and $\overline{u}^{max}_{rms}(x/\theta_o)$.

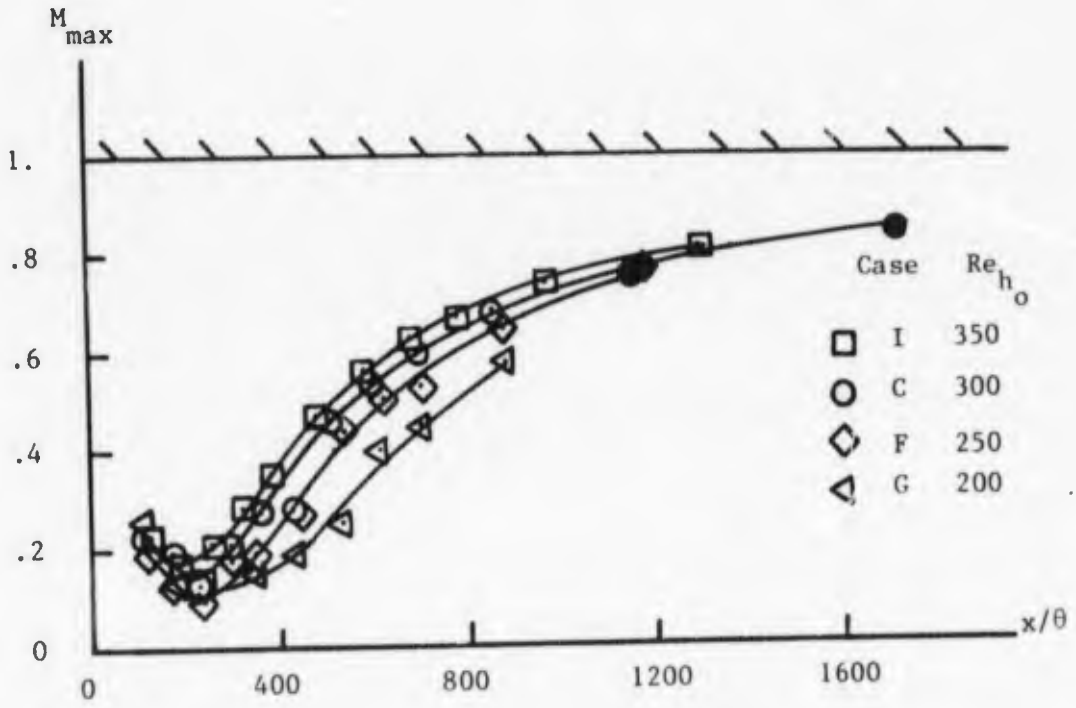

Figure 47: Effect of Re_{h_o} upon $M_{max}(x/\theta_o)$.

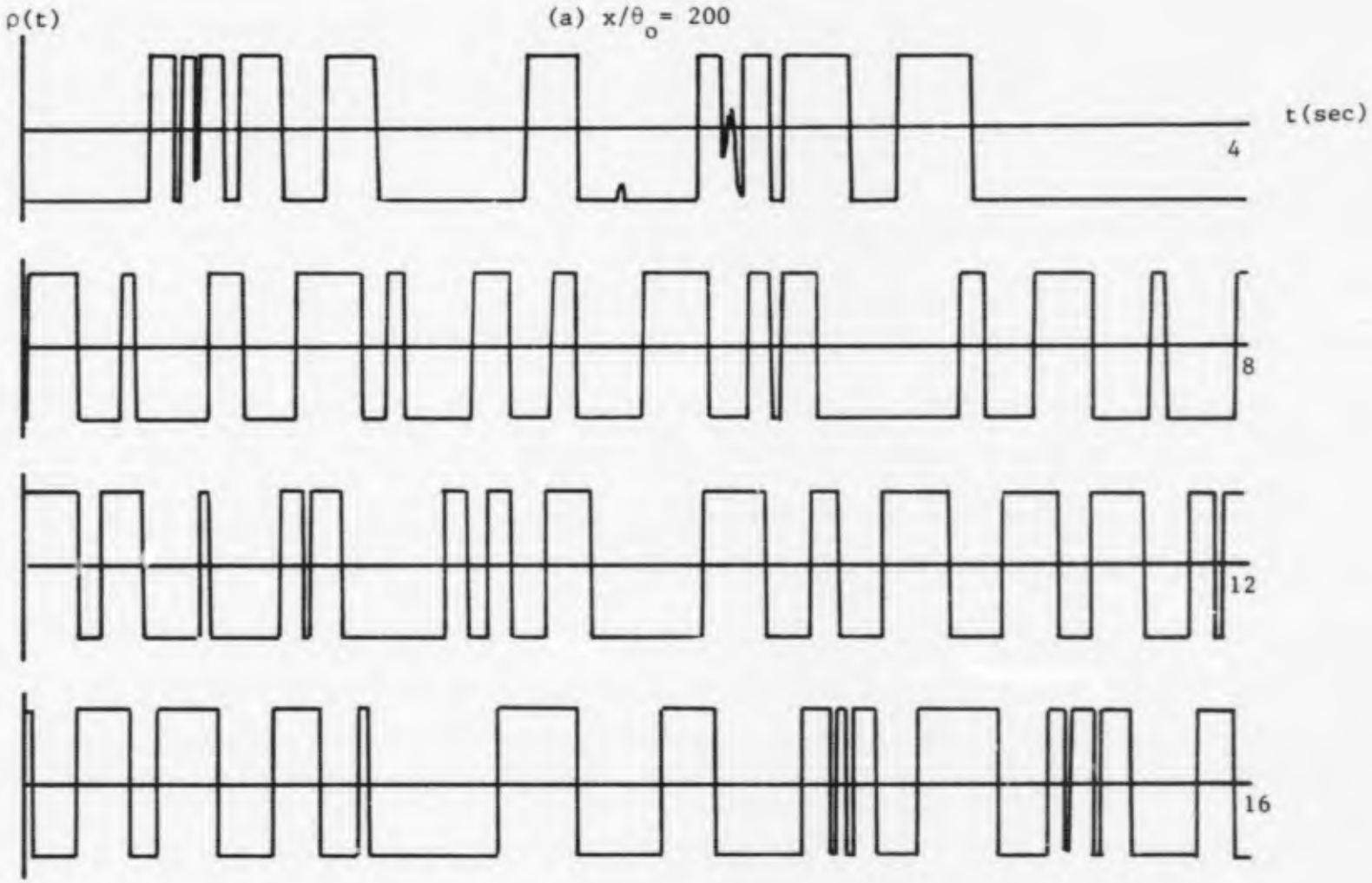

Figure 48: Raw Microconductivity Probe Data.

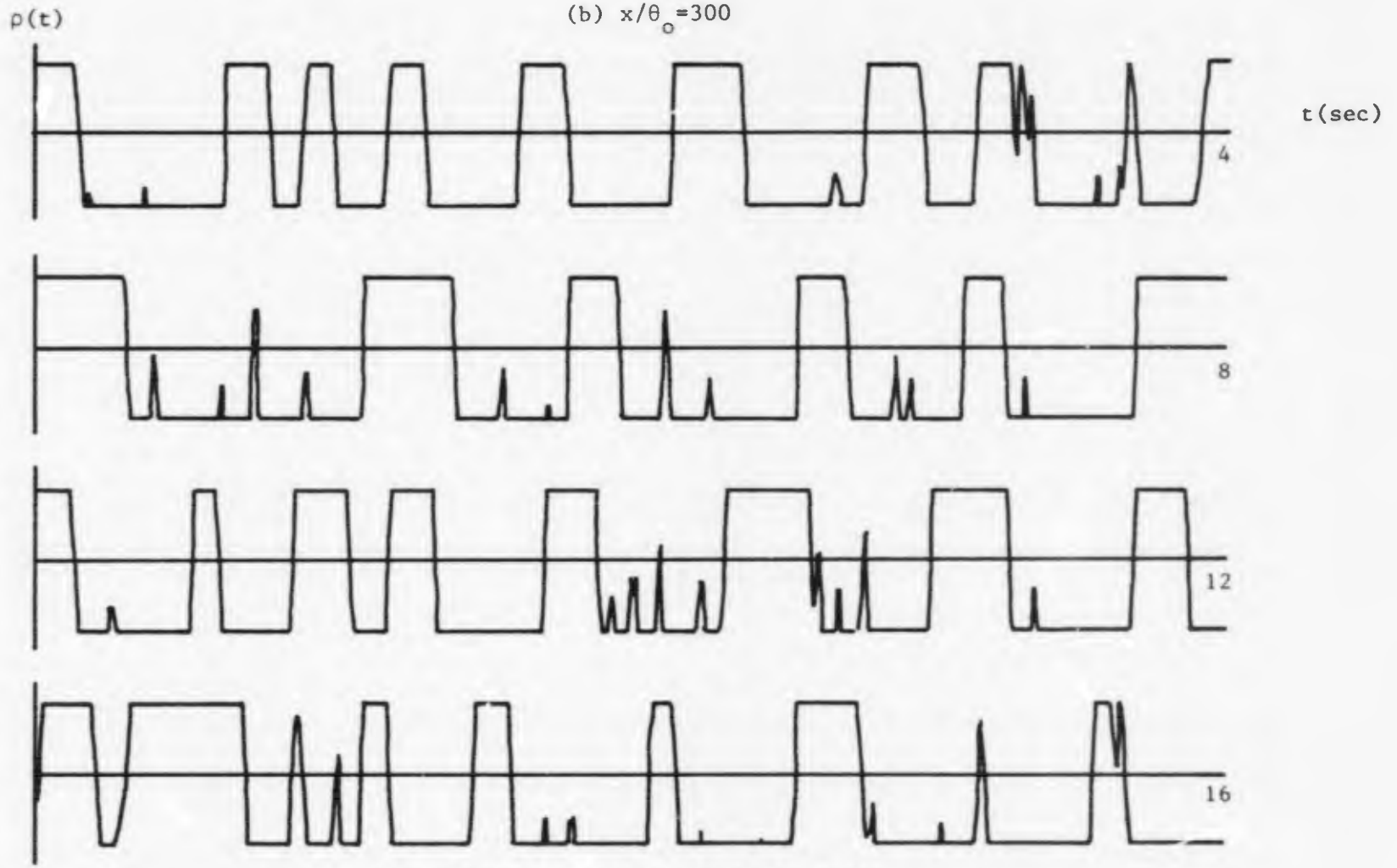

Figure 48: Raw Microconductivity Probe Data.

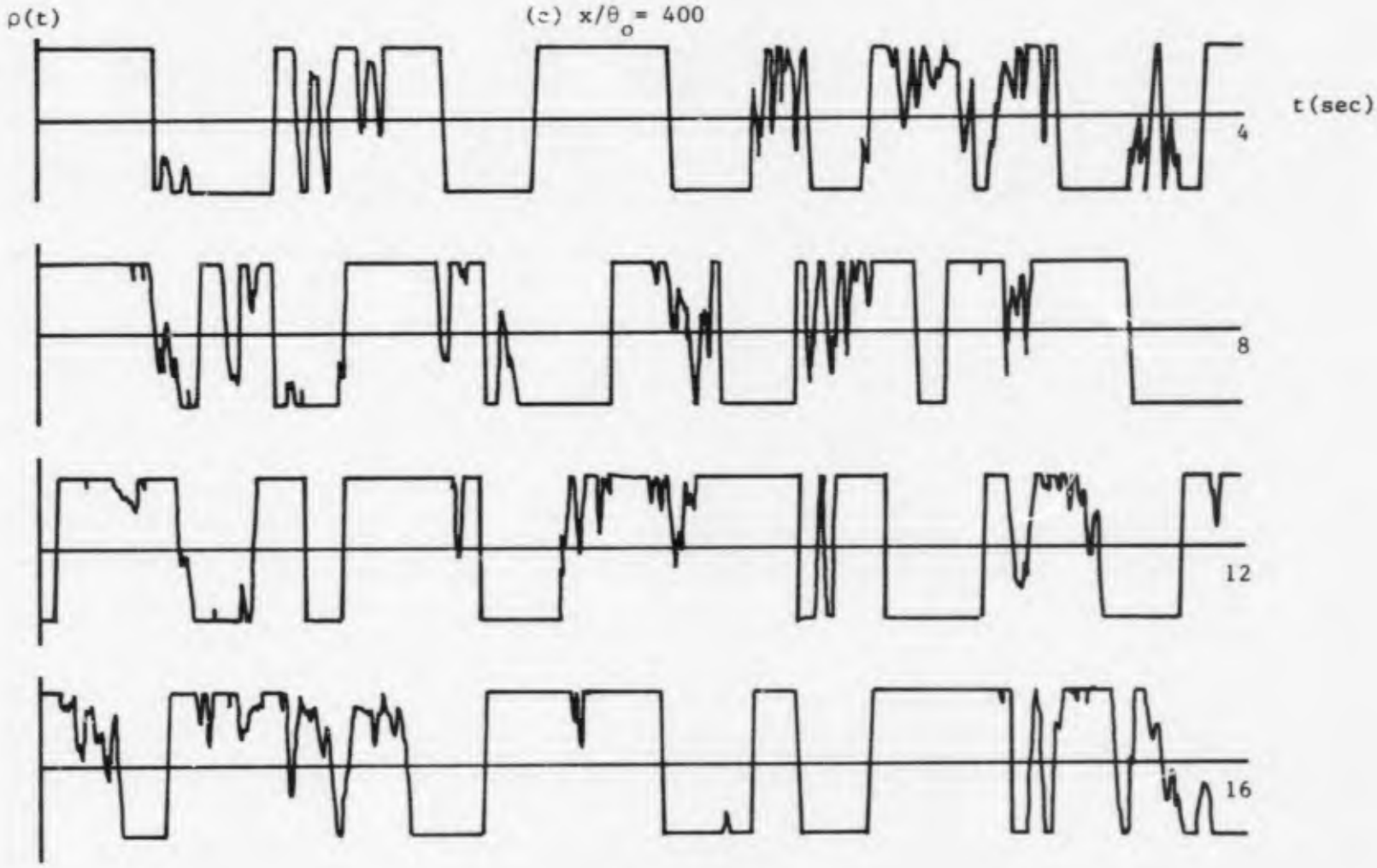

Figure 48: Raw Microconductivity Probe Data

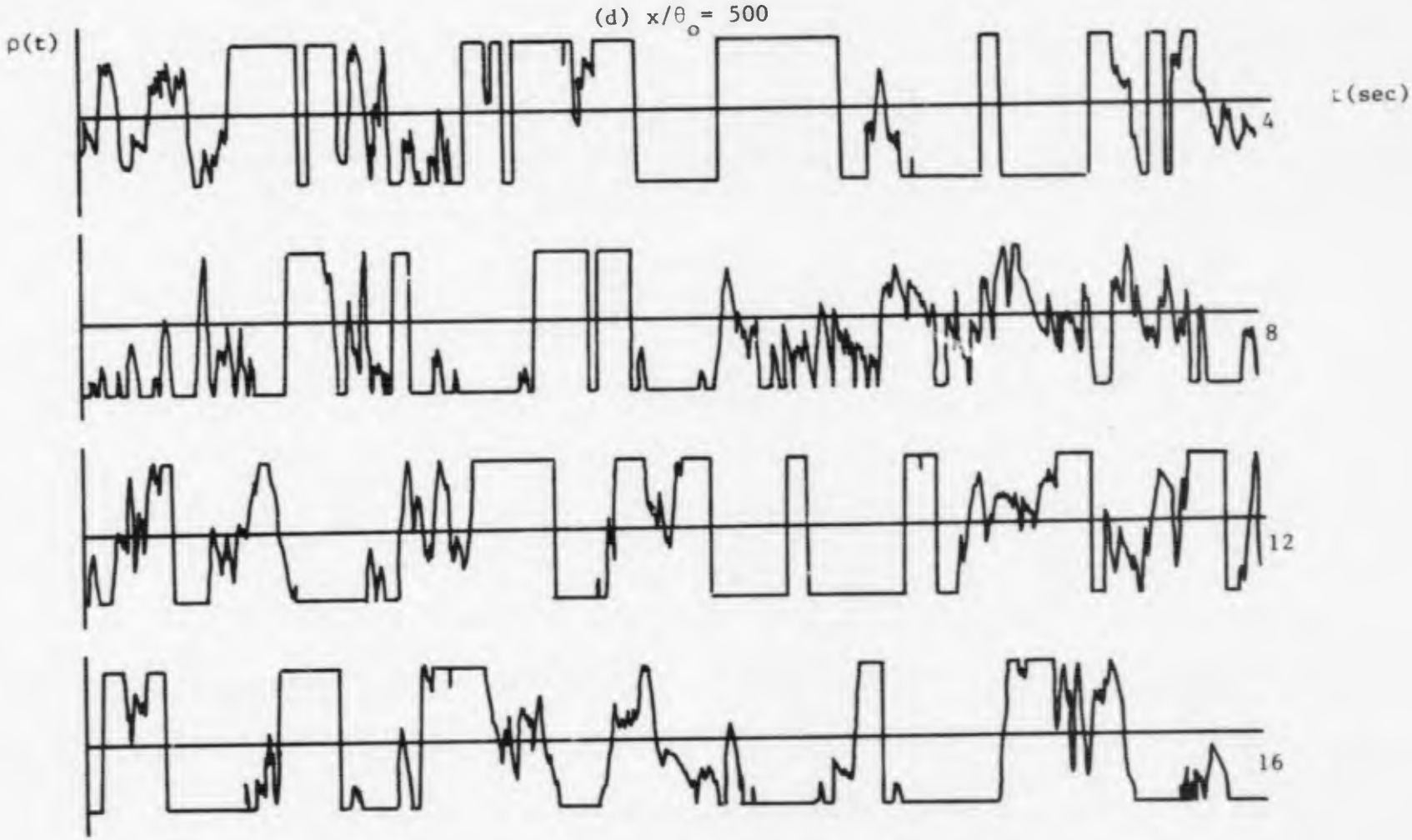

Figure 48: Raw Microconductivity Probe Data.

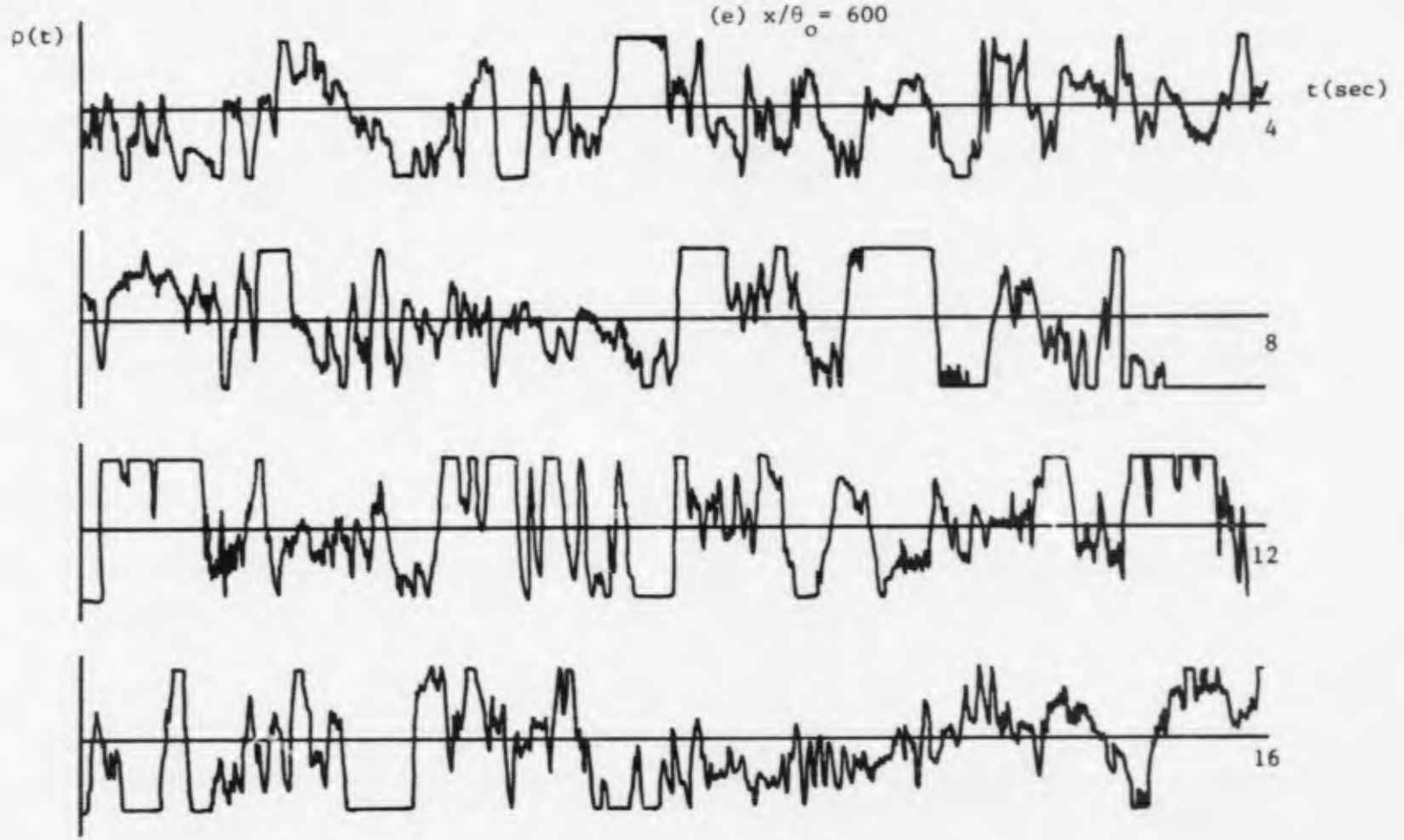

Figure 48: Raw Microconductivity Probe Data.

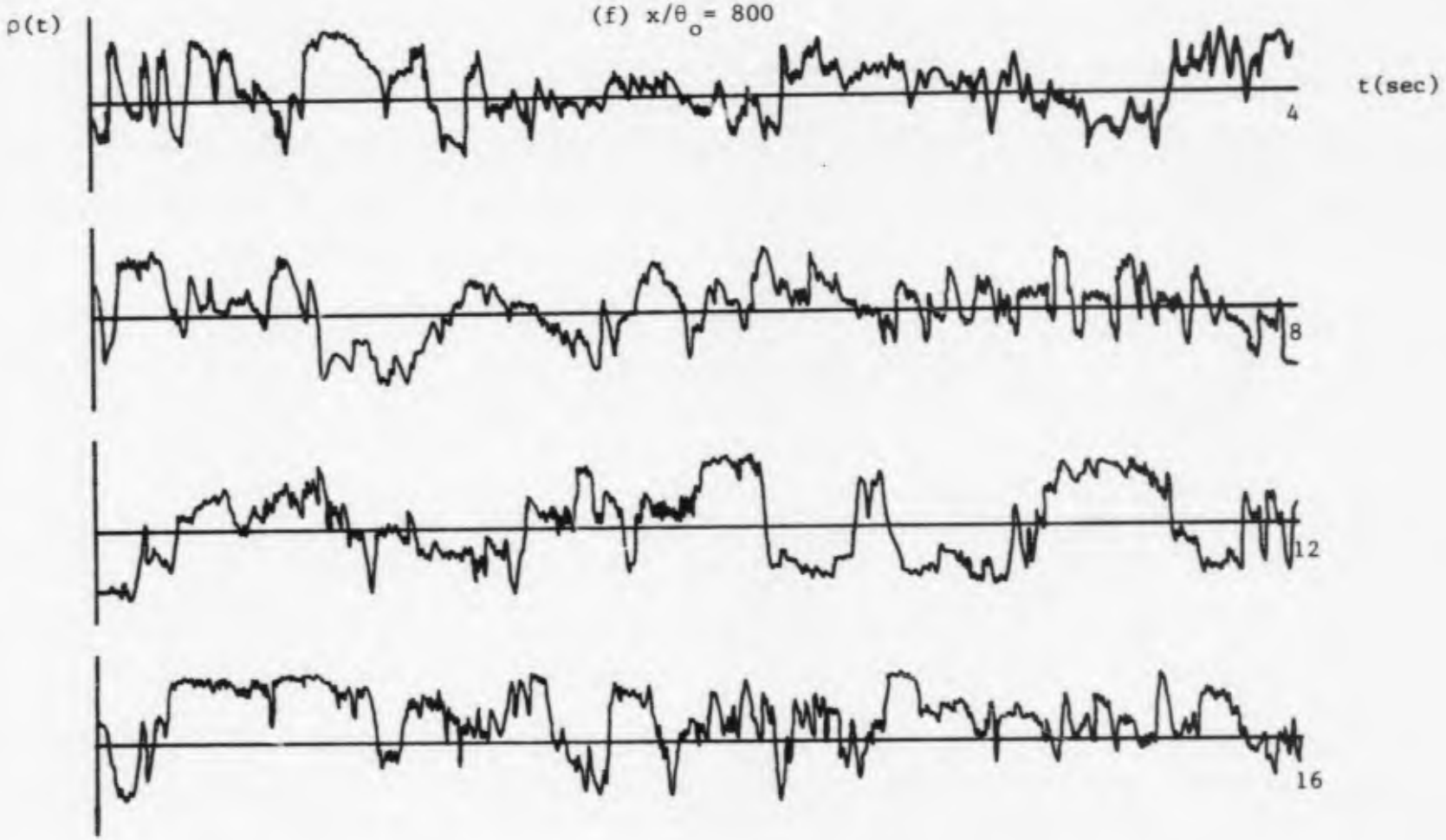

Figure 48: Raw Microconductivity Probe Data.

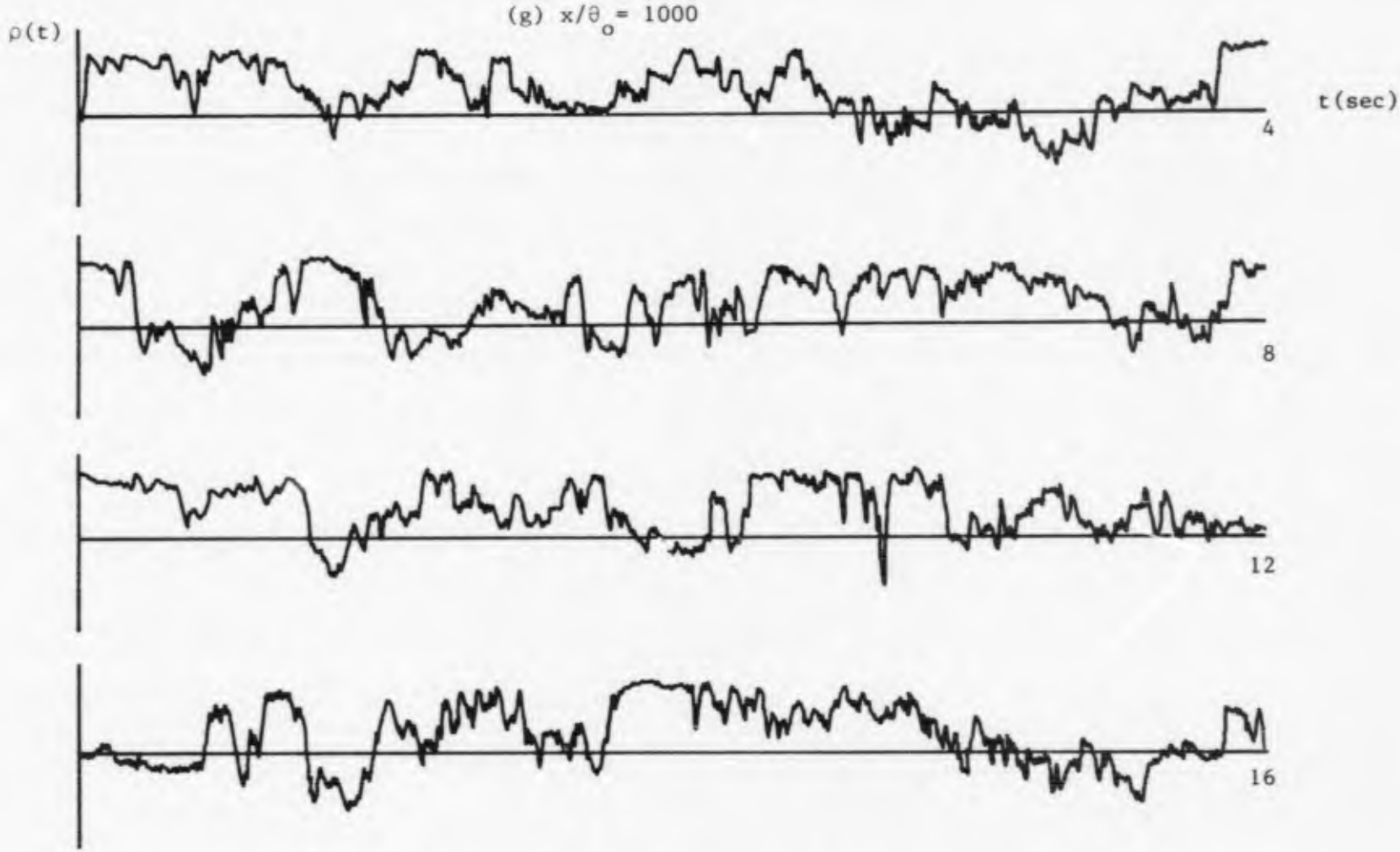

Figure 48: Raw Microconductivity Probe Data.

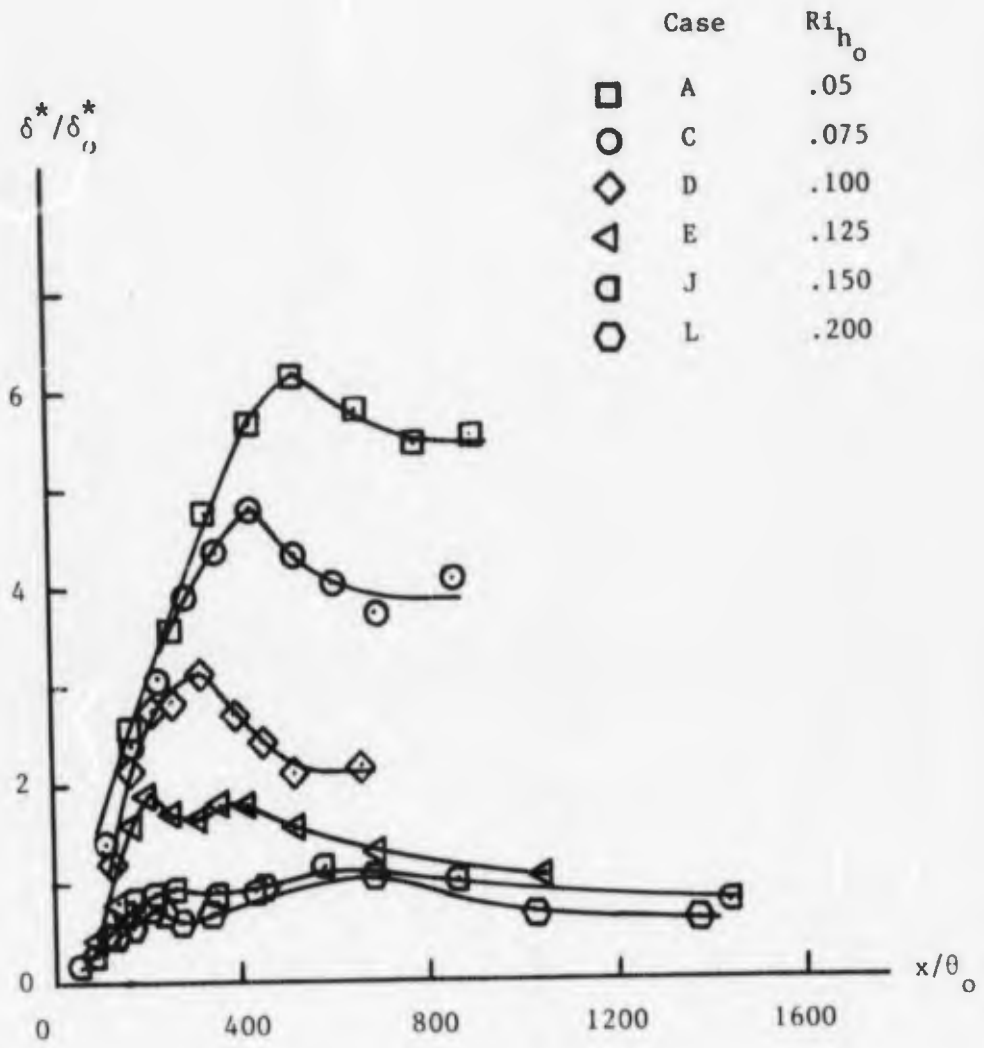

Figure 49: Effect of Ri_{h_o} upon $\delta^*(x/\theta_o)$.

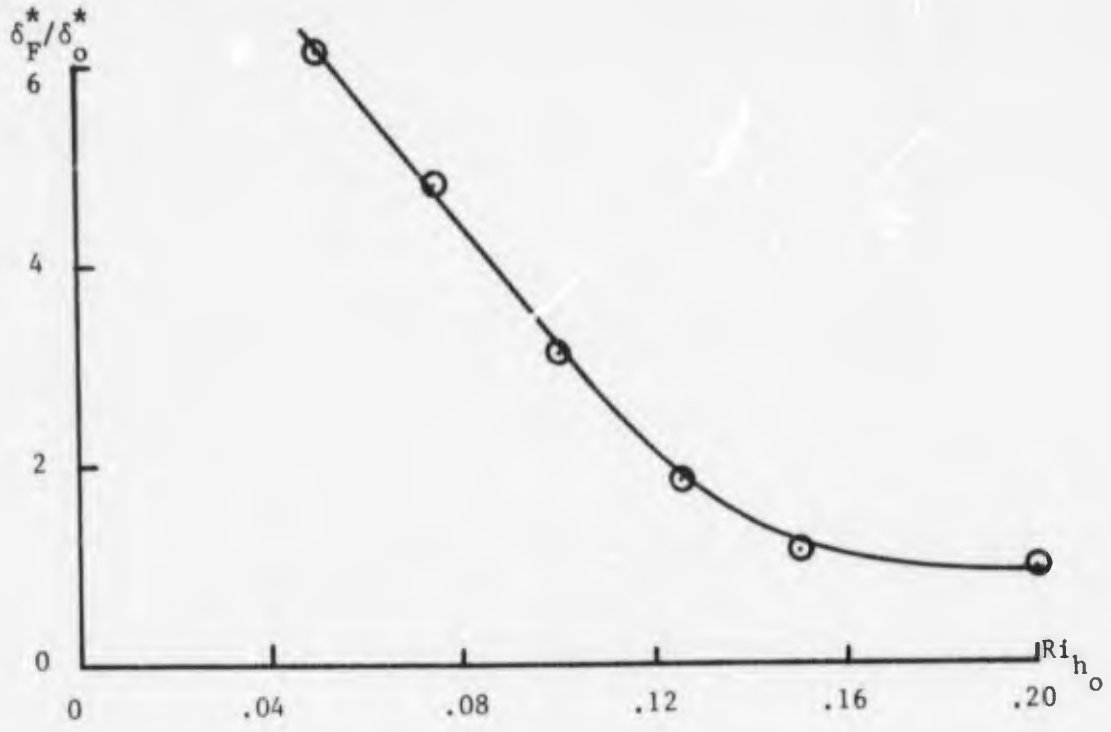

(a) δ_F^*/δ_o^* vs. Ri_{h_o}.

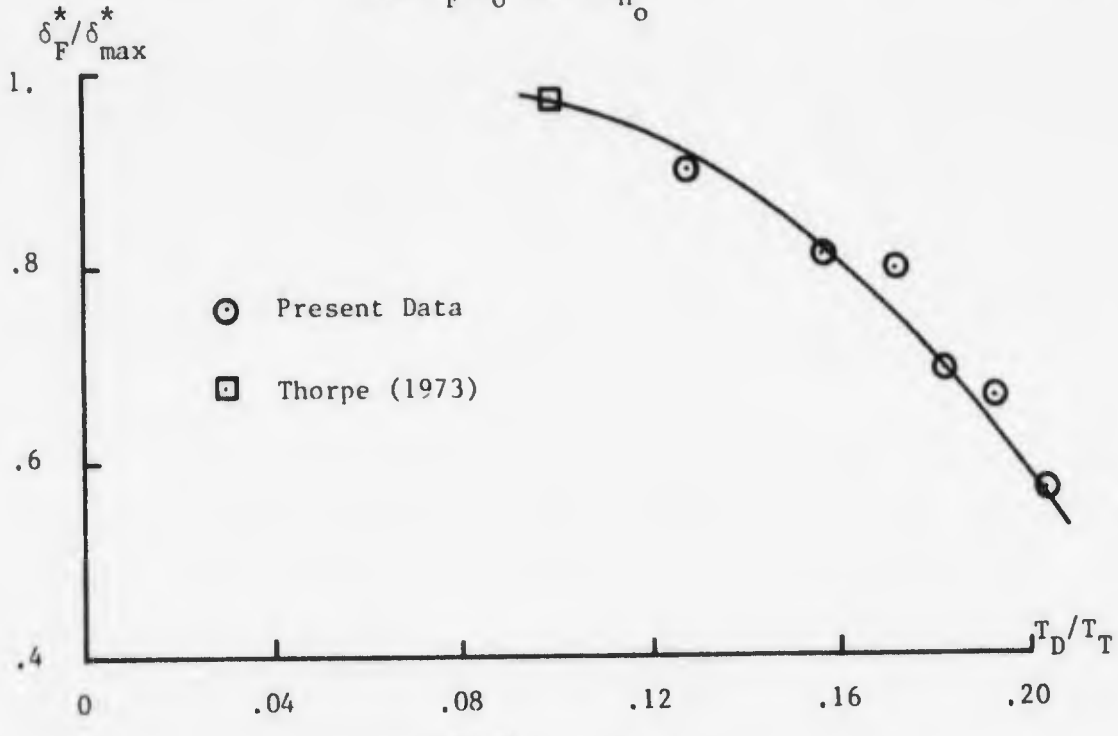

(b) $\delta_F^*/\delta_{max}^*$ vs. T_D/T_T.

Figure 50: δ_F^*/δ_o^* vs. Ri_{h_o} and $\delta_F^*/\delta_{max}^*$ vs. T_D/T_T.

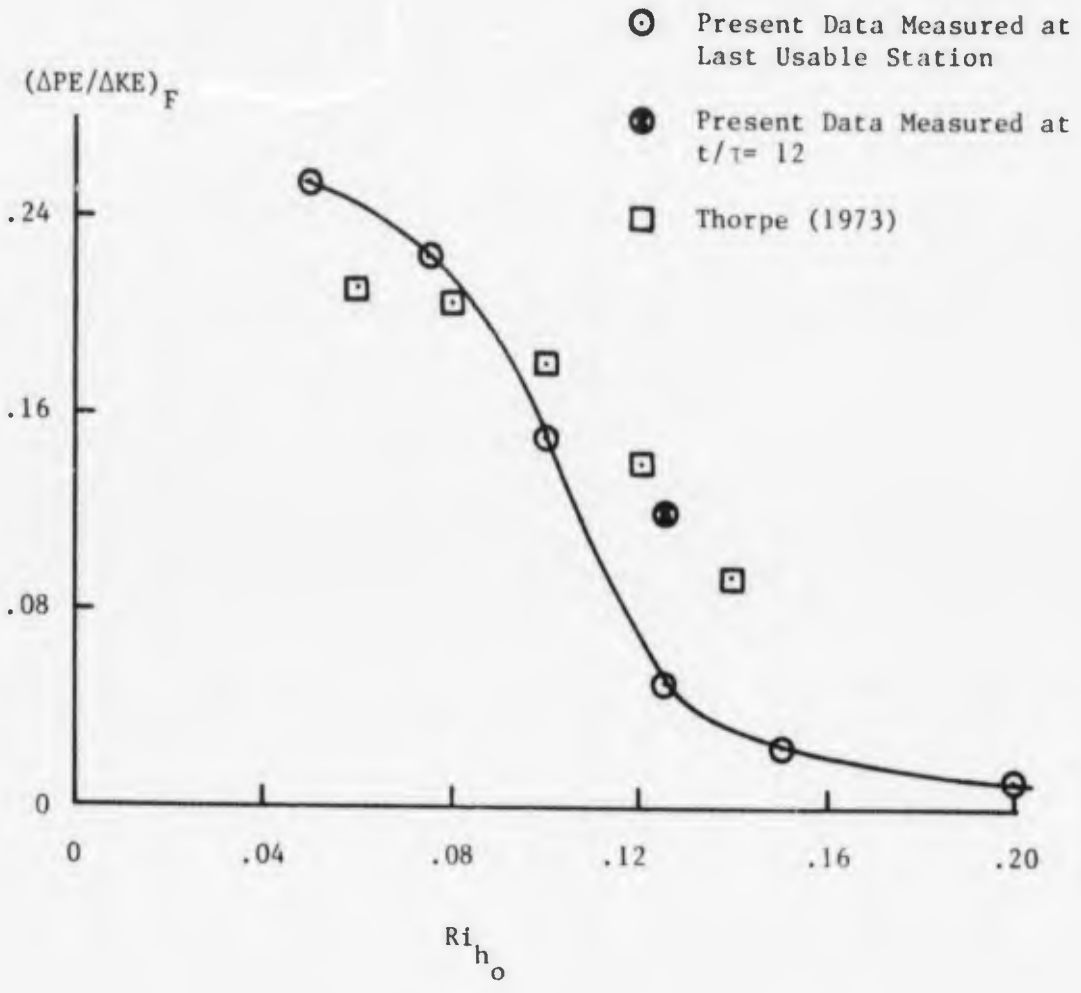

Figure 51: $(\Delta PE/\Delta KE)_F$ vs. Ri_{h_o}.

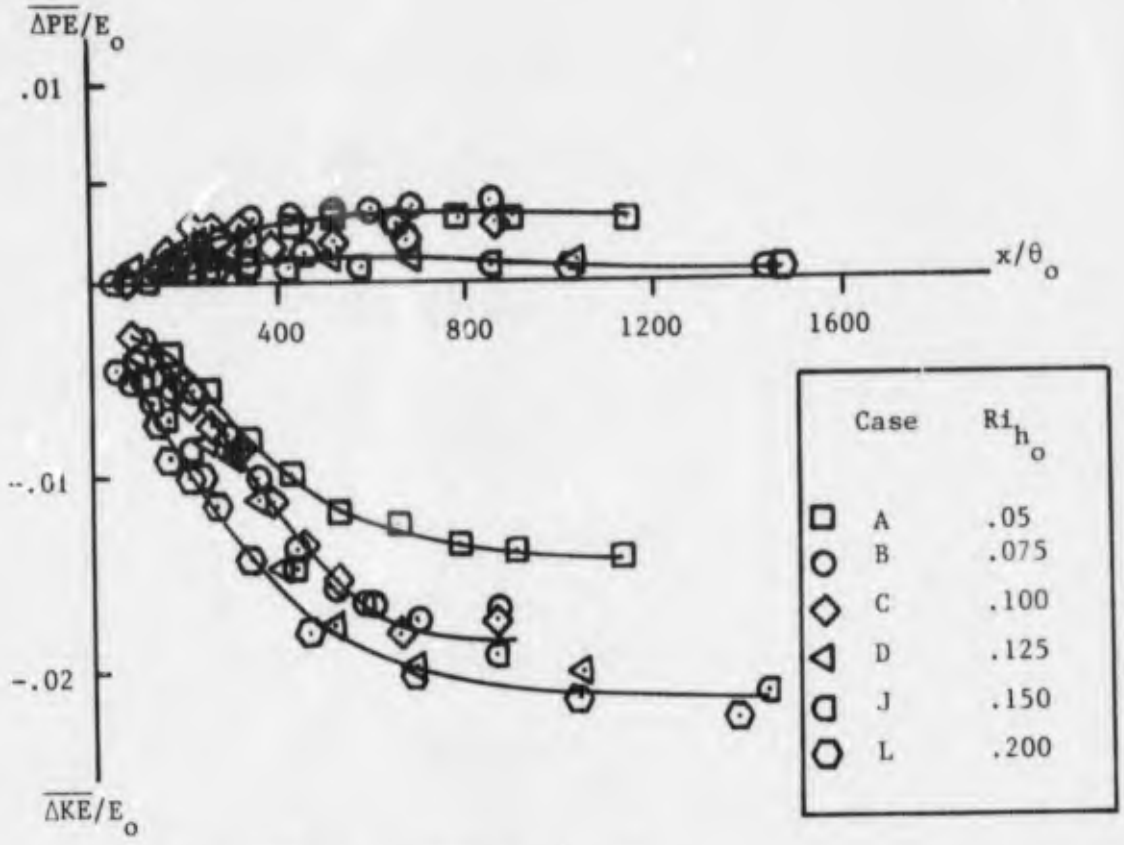

(a) $\overline{\Delta KE}(x)$ and $\overline{\Delta PE}(x)$ vs. x/θ_o.

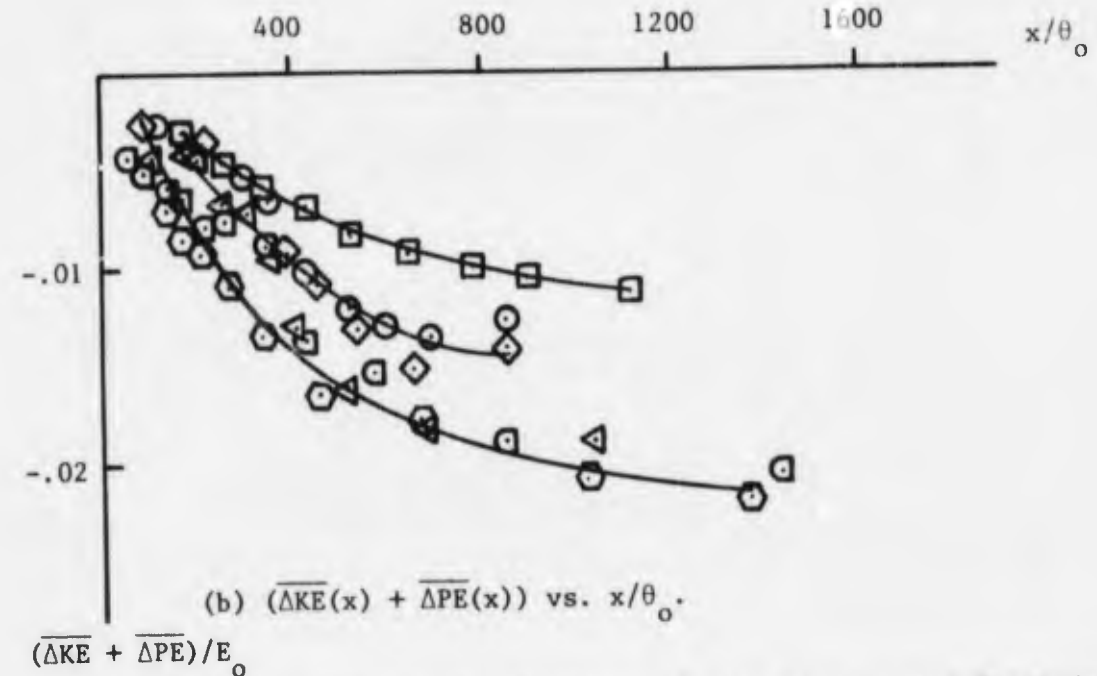

(b) $(\overline{\Delta KE}(x) + \overline{\Delta PE}(x))$ vs. x/θ_o.

Figure 52: Longitudinal Variation of Mean Kinetic and Potential Energy.

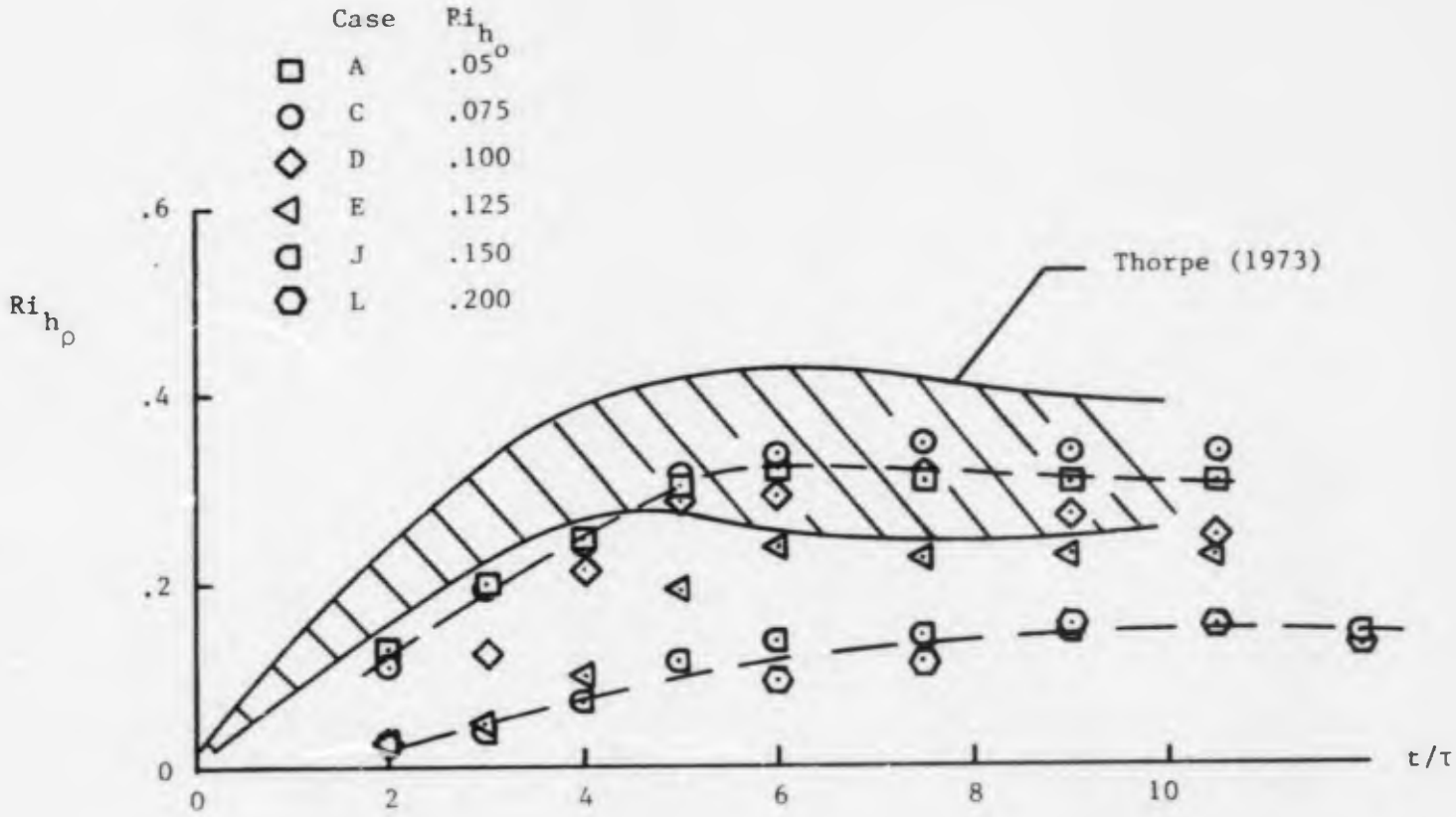

Figure 53 : Ri_{h_ρ} vs. t/τ for several values of Ri_{h_o}.

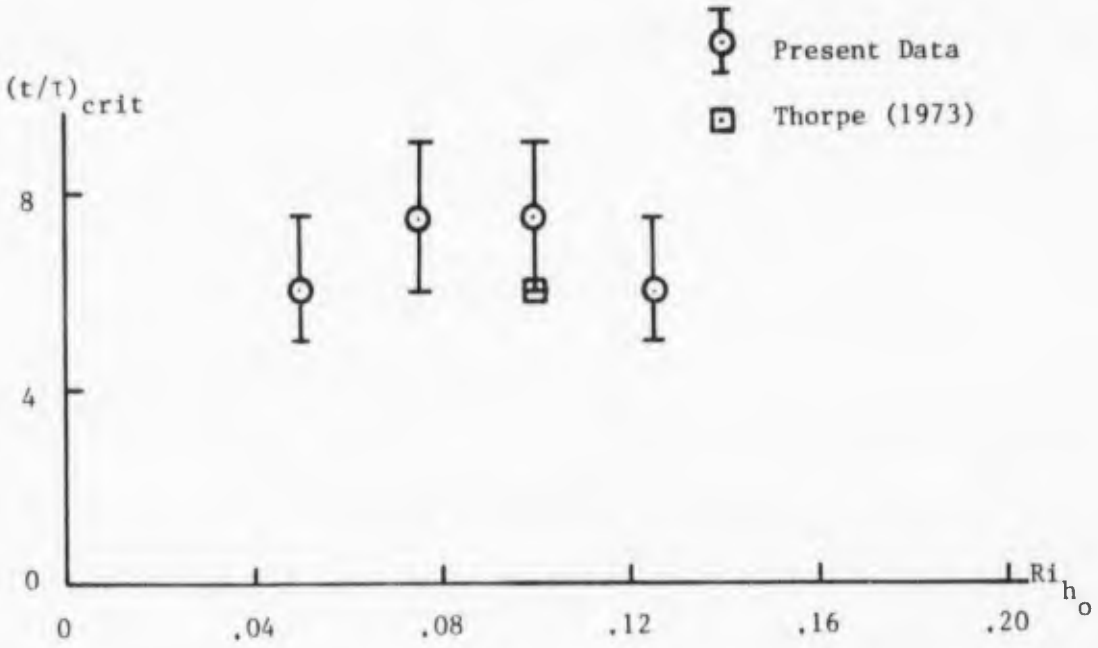

(a) $(t/\tau)_{crit}$ vs. Ri_{h_o}.

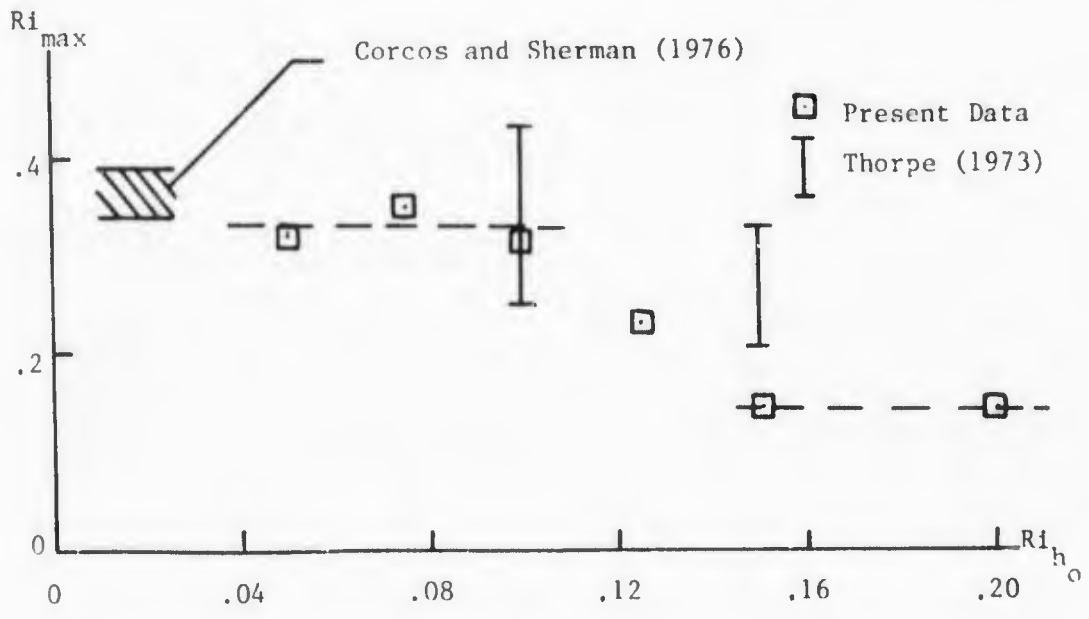

(b) Ri_{max} vs. Ri_{h_o}.

Figure 54: Ri_{max} and $(t/\tau)_{crit}$ vs. Ri_{h_o}

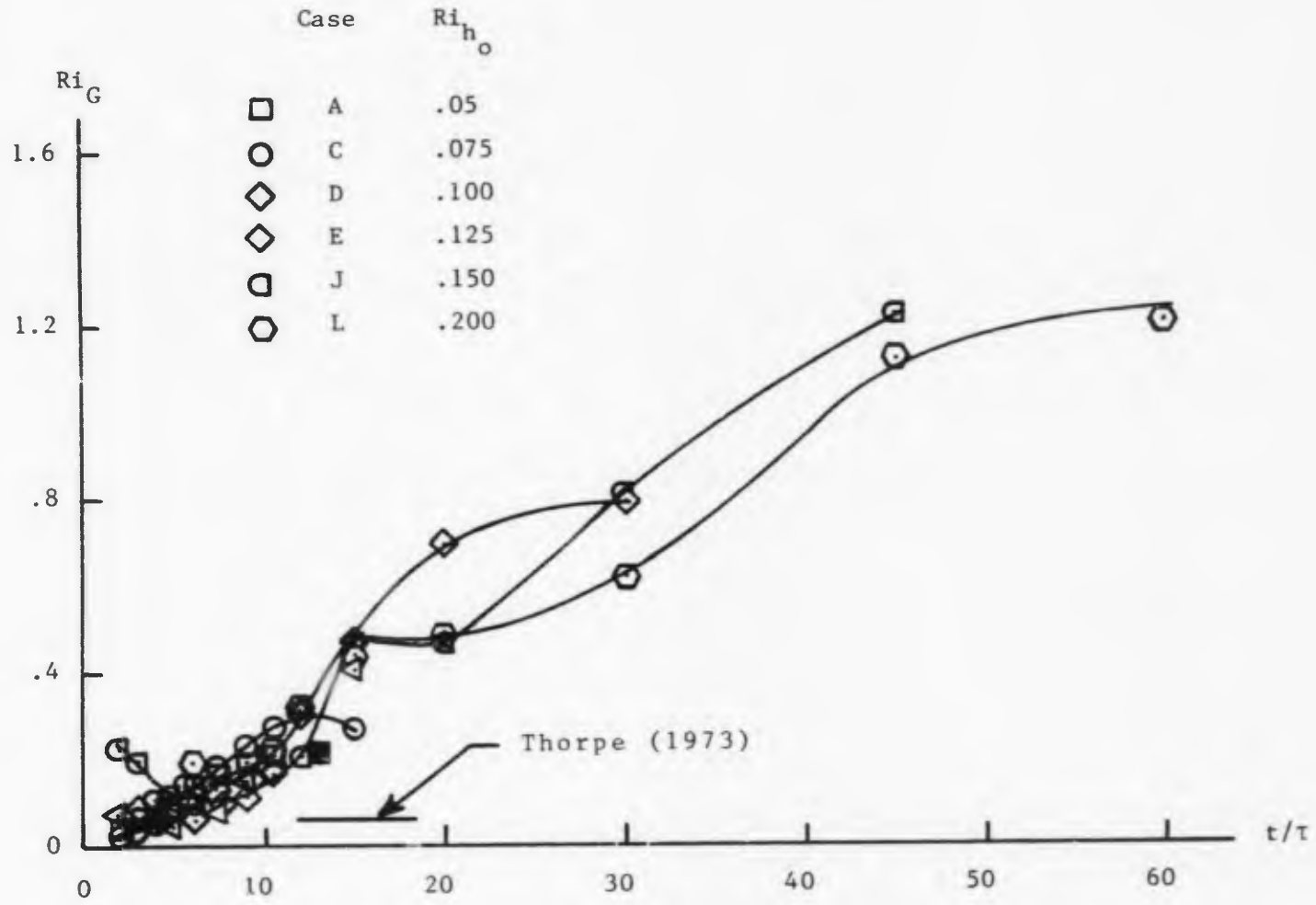

Figure 55: Ri_G vs. t/τ for several values of Ri_{h_o}.

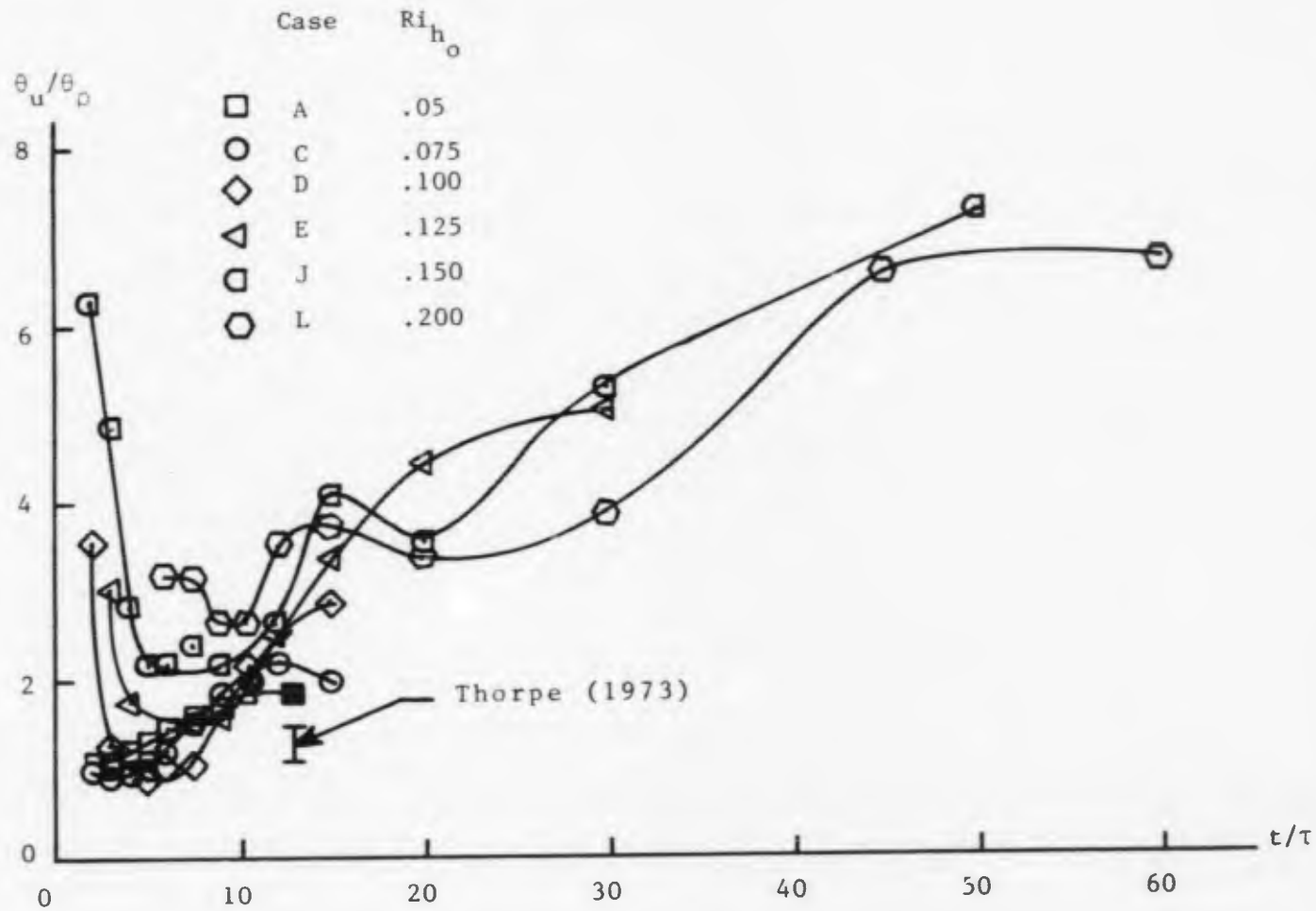

Figure 56: θ_u/θ_ρ vs. t/τ for Several Values of Ri_{h_o}.